Dipartimento di Medicina Molecolare e Traslazionale

Dottorato di Ricerca in

PRECISION MEDICINE

Settore Scientifico Disciplinare CHIM/08 Chimica Farmaceutica

Ciclo XXXVIII

SCREENING AND DEVELOPMENT OF SMALL MOLECULES TARGETING G-QUADRUPLEX NUCLEIC ACIDS

Supervisore:

Prof. ssa Alessandra Gianoncelli

Correlatore:

Dr. Giovanni Ribaudo

Dottoranda:

Margrate Anyanwu

Table of contents

Abstract (English)

The process of researching and developing new drugs has historically been among the longest and most expensive. To accelerate the identification of therapeutic targets in diseases such as tumors and infections, it was essential to develop computational techniques that have proven to be crucial for reducing the failure rate of the process.

Several thousand proteins have been identified, structurally resolved, and functionally annotated. Although thanks to the completion of the Human Genome Project, approximately 20,000 genes have been identified, including around 18,000 capable of coding for proteins. Of these, around 8,500 are predicted to be druggable targets, about 3,000 have already been targeted, and only 3% (approximately 700) have an approved drug molecule. In various contexts, among the proteins associated with diseases, many are defined as "undruggable" because they often lack binding sites for drugs or due to their inherently disordered nature. At the tumor level, the most well-known examples of these proteins are RAS and MYC, important targets of cancer therapies. Additionally, recent studies on the interactome suggest that there are up to 650,000 protein-protein interactions considered challenging in humans, given the large flat surfaces lacking the distinctive features typical of drug-target interaction sites. Therefore, alternative strategies are needed to inactivate these disease-related undruggable proteins. In this context, my primary work over the past three years has focused on non-canonical structures, specifically G-quadruplexes (G4s), which have been the subject of research on new ligands with antitumor properties. In this regard, my work has primarily focused on the application of computational techniques to study interactions and optimize molecules selective for G4s (*Chapter 2.4*).

Another therapeutic target investigated over the past three years is phosphodiesterase 9, which has been recognized as a crucial therapeutic target for treating central nervous system diseases. In this area, my work has mainly focused on database screening, interaction studies, and the identification of compounds that bind to PDE9A (*Chapter 3*).

Principally, computational studies have been enhanced by analytical techniques such as mass spectrometry, NMR spectroscopy, and high-performance liquid chromatography. The combination of these methods has created a synergistic effect that

has significantly improved and accelerated the process of identifying ligands targeting the therapeutic targets evaluated over the past three years.

Given the versatility of computational techniques, they have been utilized in various collaborations to investigate the interactions between ligands and targets (*Chapter 4*). Specifically, the analyzed ligands are of natural origin, which is particularly important for the research and development of new drugs due to their bioactive properties.

Abstract (Italian)

Il processo di ricerca e sviluppo di nuovi farmaci è storicamente tra i più lunghi e costosi. Per accelerare l'identificazione di bersagli terapeutici in malattie come i tumori e le infezioni, è stato essenziale sviluppare tecniche computazionali che si sono rivelate fondamentali nel ridurre i tassi di fallimento del processo nel corso degli anni.

Diversi migliaia di proteine sono state identificate, risolte strutturalmente e annotate dal punto di vista funzionale. Nonostante grazie al completamento del progetto Genoma Umano, siano stati identificati circa 20000 geni, tra cui circa 18000 in grado di codificare proteine; di queste, circa 8500 sono predette bersagliate da farmaci, circa 3000 sono già state identificate come tali e solo il 3% (circa 700) ha una molecola approvata come farmaco.

In diversi contesti, tra le proteine associate alle malattie, molte sono definite "non bersagliabili" perché spesso mancano di siti di legame per i farmaci o presentano una natura intrinsecamente disordinata. A livello tumorale, gli esempi più noti di queste proteine sono RAS e MYC, bersagli importanti delle terapie antitumorali. Inoltre, studi recenti sull'interattoma suggeriscono che in umani ci siano fino a 650000 interazioni proteina-proteina considerate impegnative, viste le grandi superfici piatte prive di caratteristiche distintive tipiche dei siti di interazione farmaco-bersaglio. Pertanto, sono necessarie strategie alternative per l'inattivazione di queste proteine intrattabili legate alle malattie e, in questo contesto, si colloca il mio lavoro principale svolto nei tre anni, durante i quali le strutture non canoniche, identificate come G-quadruplexes (G4s), sono state oggetto di ricerca di nuovi ligandi a fini antitumorali.

In questo, il mio lavoro si è principalmente concentrato sull'uso di tecniche computazionali mirate allo studio dell'interazione e all'ottimizzazione di molecole selettive per G4 (*Capitolo 2.4*).

Un altro target di cui mi sono occupata in questi tre anni è la fosfodiesterasi 9 (PDE9A), riconosciuta nel tempo come un bersaglio terapeutico importante nel trattamento delle malattie del sistema nervoso centrale. Anche in questo ambito, il mio lavoro si è principalmente focalizzato sullo screening di database, sugli studi di interazione e sull'individuazione di composti in grado di legarsi a PDE9A (*Capitolo 3*).

In particolare, il lavoro computazionale è stato rafforzato dall'uso di tecniche analitiche quali la spettrometria di massa, la spettroscopia NMR e la cromatografia liquida ad alte prestazioni. La combinazione di queste tecniche ha generato un effetto sinergico che

ha migliorato e accelerato significativamente la velocità di identificazione dei ligandi targeting i bersagli terapeutici valutati negli ultimi tre anni.

Data la grande versatilità delle tecniche computazionali, sono state impiegate in diverse collaborazioni per esplorare le interazioni tra il ligando e il bersaglio (*Capitolo 4*). In particolare, i ligandi analizzati sono di origine naturale, un aspetto particolarmente rilevante nella ricerca e nello sviluppo di nuovi farmaci, grazie alle loro proprietà bioattive.

1. Research and development of new drugs: innovative approaches

Drug discovery research is a complex, multidisciplinary process aimed at identifying and developing new therapeutic agents to treat diseases. It involves several stages, each requiring significant scientific expertise, technological advancements, and considerable financial investment.

The process begins with target identification, in which researchers study disease mechanisms to pinpoint "druggable" macromolecules, such as nucleic acids, proteins, or protein-protein interactions involved in the disease of interest [1]. This step typically occurs in Academia, where basic research involving bioinformatics, genetics, expression profiles, *in vitro* cell-based assays, and functional screening techniques is used. To demonstrate its involvement, a pharmacological validation is performed by testing small molecules or biologics to define their ability to modulate the target effectively [2,3]. This phase is crucial, as it involves identifying hits, or compounds that exhibit promising biological activity against the therapeutic target, which usually have a micromolar-range (μM) affinity constant, low selectivity, and activity for the tested target. However, they often face limitations related to their pharmacological profiles, such as suboptimal pharmacokinetics (PK) and pharmacodynamics (PD). After identification of the hits, they undergo structural modifications to enhance their activity, selectivity, and PK/PD properties. These optimized compounds, known as leads, exhibit greater potency (typically in the nanomolar range, nM) and improved drug-like profiles. This change is also known as the hit-to-lead step [4]. Following lead optimization, the compounds progress to the preclinical testing stage, where their safety and efficacy are evaluated using *in vitro* systems (such as organoids) and animal models [5,6].

After preclinical validation, a selected group of promising compounds advances to clinical trials, which include several phases from I to III. About 70% of drugs pass Phase I, approximately 33% succeed in Phase II, and 25-30% reach Phase III [7].

After completing clinical trials, a New Drug Application is submitted to regulatory agencies, such as the Food and Drug Administration (FDA) or the European Medicines Agency, for approval. These agencies thoroughly review safety data to decide if the drug is ready for the market. Only about 0.02% of drug candidates ultimately get approved. Once approved, the drug becomes available to patients, and ongoing monitoring continues to track long-term side effects and effectiveness in larger patient groups (**Figure 1**).

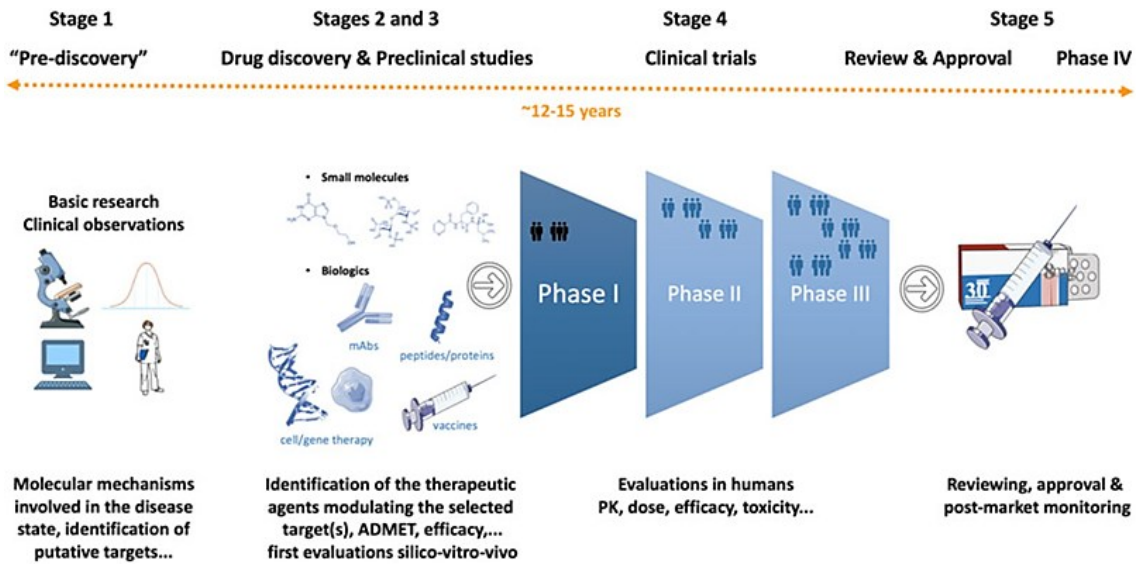

Figure 1. Overview of the drug discovery and development process. Adapted from [6]

1.1 Computer-Aided Drug Design

Discovering new drugs has always been a long and expensive process, with a significant risk of failure. Adding to the difficulty of this situation is the fact that the magnitude of the chemical space that needs to be investigated is enormous. Chemical space is a fundamental concept in cheminformatics and molecular design since it is used to analyze, study, and visualize the chemical diversity of all types of compounds within the "chemical universe", which includes every compound that can or could exist [8]. For example, it is estimated that chemical space contains nearly 10^{60} potentially existing compounds [9,10].

These amplitudes within the chemical space are impractical to investigate, particularly from an experimental perspective. Despite contemporary technologies, such as high-throughput screening (HTS), capable of rapidly evaluating hundreds of thousands of compounds weekly, their capacity will ultimately fall short of the magnitude required to exhaustively explore the entire chemical space concerning the identified therapeutic target [4,11].

The virtualization of these processes led to the implementation of high-throughput virtual screening (HTVS) that is now a key strategy for discovering new compounds [12]. Comparing the number of compounds analyzed by HTS and HTVS, the latter stands out for its ability to process several million compounds per week, leveraging only computational power and speed achievable, given the growing availability of modern

graphical processing units [13]. Over the last four decades, these events have led to the introduction of computational approaches in the drug discovery process, creating a new branch known as Computer-Aided Drug Design (CADD) to improve the efficiency and effectiveness of drug discovery [14]. To minimize error rates and reduce the financial burden associated with drug discovery and development, HTVS has been strategically integrated to enhance the early stages of the process, leading to compounds such as saquinavir and Tamiflu [15].

Although CADD aims to simplify and improve the process of researching and developing new drugs, it has some limitations. Many CADD techniques often rely on predictive models that may oversimplify the complexities of biological systems. Without proper context and experimental evidence, these models can yield misleading results. Therefore, results generated through CADD are consistently tested through follow-up experimental studies [16].

In recent years, advances in structural biology and the rapid growth of computational power have enabled us to gain insights into three-dimensional (3D) data on biomolecules and to reduce the time needed to simulate them in a virtual environment. Additionally, many databases, both free and commercial, that contain various types of potential ligands are available. Another breakthrough in CADD has come from integrating artificial intelligence (AI) and machine learning (ML), which have unlocked new levels of accuracy, speed, and understanding of molecular interactions [17]. Today, these methods allow for processing large datasets and discovering complex (often hidden) patterns, which aid in predicting drug responses based on the properties of both ligands and their targets [18,19]. The way a computational chemist approaches a pharmacological problem can be complex, but the key factor influencing the method is the amount of data available in the specific case. In particular, one of the most crucial factors is whether experimental structural information about the target is accessible [20]. Depending on this, CADD methods can be classified into two categories: structure-based drug discovery (SBDD) and ligand-based drug discovery (LBDD). SBDD uses 3D structures of targets to identify ligands that can be selective and active binders. In contrast, LBDD does not need structural data about the target; instead, it relies on information about the ligands' physicochemical properties or biological activities to discover new compounds with similar or better features.

1.1.1 Structure-based Drug Design (SBDD)

3D models needed for the SBDD approach can be acquired experimentally or through predictive methods. Following the completion of the Human Genome Project and advancements in bioinformatics, the speed and success rate of drug development using SBDD have increased significantly [21]. One of the key factors is having experimental structural information about the target [16], and this can be achieved through various techniques, with nuclear magnetic resonance (NMR), X-ray crystallography (X-ray), and cryogenic electron microscopy (cryo-EM) [22].

On the other hand, when no experimental data are available, bioinformatics techniques can help in modelling and predicting 3D structures. Several methods, including homology modeling, *ab initio* folding, and threading, are used. For instance, homology modelling builds a predictive 3D model by finding closely related homologs of the target protein [23,24]. Due to the relevance of this approach, various computational tools have been developed to support homology modeling, including Phyre, I-TASSER, HHpred, and Robetta [25–28].

Recently, the rise of AI has revolutionized the field of structural prediction for biological targets. A key innovation in this area is AlphaFold4, which builds on the capabilities of its predecessor, AlphaFold3, which was more focused on predicting the structures of monomeric proteins. AlphaFold4 takes its functionality to the next level by modeling interactions between targets and a wide range of biomolecular partners, including nucleic acids, proteins, small molecules, ions, and modified residues [29–32], further broadening the range of possible starting points for SBDD applications [33,34].

While this tool is a significant advancement in structural prediction, it also has certain limitations. For example, it struggles to account for the effects of point mutations and highly dynamic structures, primarily due to the limited data available in existing repositories [35].

Target-ligand interaction is a crucial requirement for drug activity. Therefore, another critical step in using the SBDD approach is identifying the binding site, especially when dealing with proteins as therapeutic targets. When 3D structures come from resolution experiments, the binding site is identified from cocrystal structures of the targets. If this information is unavailable, *in vitro* mutagenesis experiments are usually performed to determine the ligand's binding site [36,37]. However, biological experiments are time-consuming and require substantial equipment, materials, and labor. Due to this, since the

1990s, accurate and efficient computational methods for target-ligand interaction, such as DeepPocket [38] and NucBind [39], have been developed [40–43].

Molecular Docking

In drug discovery and development, identifying hit and lead compounds is crucial. The most widely used technique in modern CADD is molecular docking, which nowadays enables screening billions of small molecules against the investigated biological target [44].

The primary goal of molecular docking is to determine the optimal conformation of a molecule that binds to another to form a stable complex. In this case, 3D information concerning the investigated target needs to be known *a priori,* and as previously mentioned, experimentally resolved high-resolution 3D models of investigated targets can be retrieved from public repositories (e.g., PDB), or if this is not available in data repositories, this could be predicted by computational means.

Molecular docking methods consist of two main components: conformational search algorithms and scoring functions. Conformational search algorithms primarily aim to identify all possible orientations and conformations of the target molecule in combination with the ligand. These can be grouped into systematic search methods, including conformational search algorithms, fragment-based methods, and database searches. Conformational algorithms gradually alter the ligand's degrees of freedom by including torsional, rotational, and dihedral angles throughout the search [45]. Then, fragment-based methods divide the ligand into small fragments, which are individually docked during the molecular docking process to form bonds with each other or with the target. Subsequently, the best-performing fragment is used to generate the final ligand conformation (also known as the *pose*). Lastly, database search enables the creation of numerous reasonable conformations of every molecule already recorded in the database, which are then docked as rigid bodies [46]. Unlike systematic methods, random or stochastic methods are present. Approaches such as the one relying on Monte Carlo sampling randomly place ligands in the search space, assign a score, and iteratively generate new conformations until it finds the most favorable pose [47]. On the other hand, genetic algorithms simulate evolution by starting with a population of ligand conformations (genes), scoring them for fitness, and then combining the best poses with favorable traits from the rest to create improved conformations until it reaches the optimal pose [48].

Then, in addition to the implied method, docked ligands are evaluated using scoring functions that assess their binding potential. These functions measure the strength of interactions between a ligand and the investigated target by considering the conformational strain, electrostatic interactions, and steric hindrance of a ligand when it is bound to its target [49–51]. Several types of scoring functions were implemented over the years, and nowadays, four main groups are available. The force-field-based scoring functions represent the earliest set of equations developed in the 1970s to assess ligand-target interactions and estimate binding strength, accounting for both bonded (intramolecular) and non-bonded (intermolecular) terms. The intermolecular forces are described using Lennard-Jones (LJ) potentials for van der Waals (VdW) interactions and distance-dependent dielectric functions for electrostatic (Coulomb) interactions (see *Equation 1*).

$$\Delta G_{binding} = \Delta E_{vdW} + \Delta E_{electrostatic} + \Delta E_{Hbond} + \Delta E_{desolvation} \quad (1)$$

These terms can be derived from experimental and *ab initio* quantum mechanical calculations. Since these interactions typically occur in water, desolvation energies of ligands and targets are modeled using implicit solvation methods such as the Generalized Born Surface Area or Poisson-Boltzmann Surface Area [52]. Some of the software available nowadays, based on these scoring functions, include DOCK and DockThor [53,54].

Another type of scoring function, such as the empirical scoring functions, relies on repeated linear regression analysis of a prepared set of complex structures using protein-ligand complexes with known binding affinities. These complexes include functional groups and various interactions, such as the N–O hydrogen bond, O–O hydrogen bond, salt bridge, and stacking of aromatic rings. In this context, techniques like LUDI score, ChemScore, and AutoDock scoring are used for this analysis [46,50,55]. Furthermore, knowledge-based scoring functions assume that target-ligand contacts exhibiting higher statistical frequencies are associated with favorable interactions. By utilizing a structural database, the frequencies of atom pair interactions within complexes are calculated and converted into energy terms. During the docking assessment, the energy contributions from all atom pairs within the target-ligand complex are summed to determine the overall score of the predicted docking pose. By using this approach, the complex physical interactions are simplified by considering many atom-pairwise terms in the complex. Molecular

docking tools such as DrugScore and GOLD rely on these types of scoring functions [49,56]. Finally, ML scoring functions combine modern quantitative structure-activity relationship (QSAR) techniques with information on target-ligand interactions. QSAR has historically been used to model different physicochemical, biological, and pharmacological properties of small molecules within computational medicinal chemistry. By describing ligand, receptor, and interaction characteristics with specific descriptors, advanced ML techniques can create statistical models that forecast target-ligand binding scores. Unlike traditional methods, these scoring functions do not rely on a fixed functional form, allowing them to implicitly account for intermolecular interactions that are tough to model explicitly. Over the past few years, ML scoring functions have seen significant improvements in predicting binding affinity [57].

A general molecular docking workflow comprises six main steps (**Figure 2**).

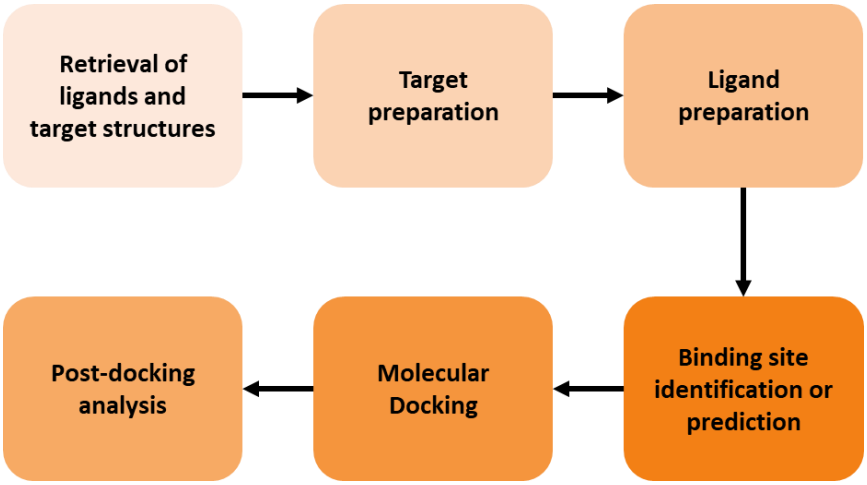

Figure 2. A prototype flow chart of a molecular docking study.

The first step in molecular docking involves obtaining digital representations of both the ligands and the target structures. This initial step is essential, as the accuracy and quality of retrieved structural models directly impact the reliability of the results. Experimentally determined target structures are preferred and are readily accessible from public databases, such as the Protein Data Bank (PDB) (https://www.rcsb.org/) and the Swiss-Prot Knowledgebase (http://expasy.org/sprot). Alternatively, predictive tools such as AlphaFold4 and I-TASSER can be used when the target's structural properties cannot be resolved [29,58]. Once the 3D structure is obtained, ligands can be retrieved from chemical repositories (public or commercial) such as PubChem [59], ZINC [60], and COCONUT

[61]. If a desired ligand is not available in these databases, molecular chemical drawing programs such as ACD/ChemSketch can be used to construct the compound's structure manually [62].

After acquiring the target structure, this needs to be filled with missing atoms or residues, energetically minimized to resolve potential steric clashes, adjusted to reflect physiological conditions by adjusting the protonation states of ionizable groups, and ensured to have proper electrostatic interactions [63]. Furthermore, in the case of experimentally derived structures, solvent molecules and coadjutant components are removed from the structure [46]. Once these steps are completed, the structure of the target receptor becomes a valid starting point for a successful molecular docking-based study [64]. Since the target structure requires preparation, the same principle applies, and ligands need to be prepared as well. Due to the relevance of protonation states, charge distribution, and geometries in binding with targets, optimizing these features to achieve the most suitable structures from a physicochemical standpoint is crucial.

Furthermore, one of the requirements for running a molecular docking analysis is defining a search space (x, y, z) where the ligand's geometry is explored using search algorithms. Depending on the type of search space defined, molecular docking is divided into blind docking and site-specific docking. The volume of the *site-specific* confines the search space to a specific area of the target (**Figure 3A**) while the volume in a *blind* molecular docking includes the entire surface of the model under investigation (**Figure 3B**). Once the search space coordinates are defined, the analysis is ready to be performed. According to the adopted tool, ligands can result in a set of different conformations identified during the experiment, which are then ranked according to their docking score (ΔG), expressed in kcal/mol.

As with any technique, validating the protocol is essential. In molecular docking, this process is called *redocking* and is operable when co-crystallized ligands are available within the structure of the target [65]. The co-crystallized ligand from the target is used to determine the Root-Mean-Square Deviation (RMSD) value, expressed in Å (10^{-10} m), which allows for measuring the difference in atomic coordinates between docked and experimental coordinates. When RMSD values are below 2.0 Å, the docking protocol is highly reliable since it accurately reproduces the original ligand's orientation. Values between 2.5 and 3 Å indicate an acceptable level of precision, with some minor deviations. However, if the RMSD exceeds 3 Å, the protocol is inaccurate, making it unsuitable for

reliable predictions. In such cases, adjusting the docking parameters and repeating the process is recommended to improve the model's accuracy. Once that RMSD has been calculated, the analysis with the set of investigated ligands can be done.

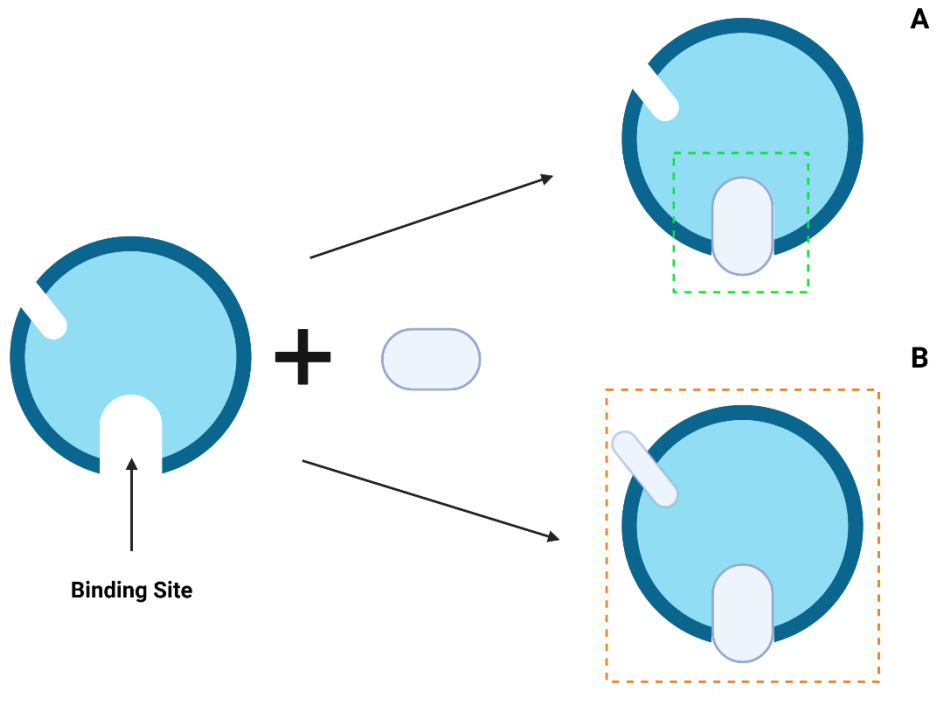

Figure 3. Graphical representation of a site-specific (green dashed box, A) and a blind search box (orange dashed box, B) contouring all the putative binding sites in which ligand poses could be generated during the molecular docking process.

Molecular dynamics

One of the features of the investigated therapeutic targets (i.e., proteins and nucleic acids) in drug discovery applications is that they are highly dynamic systems, thereby making difficult to capture through classical molecular docking analyses due its property in treating the targets as rigid bodies; exceptions are made for induced-fit docking which introduces degrees of freedoms for accounting the flexibility in both ligands and targets.

In CADD, molecular dynamics (MD) has brought significant support in hit and lead identification/optimization, providing relevant insights [66,67]. Since the late 1980s, MD has been used to accurately evaluate the stability and dynamic properties of molecular systems over time, considering full atomic flexibility and explicitly incorporating solvents (i.e., water molecules). This allowed for detailed information on the structural properties, fluctuations, conformational transitions, dynamic behavior, and thermodynamic characteristics of macromolecular targets and their complexes [56].

MD is a complex technique that calculates the force (F) exerted on each atom in a biomolecular system (like a target surrounded by solvent) based on the positions of all atoms. This information is then used to predict the position of each atom over time, typically using Newton's equation of motion. The process moves forward in time, repeatedly calculating the forces on each atom and updating their positions and velocities. The resulting trajectory is essentially a 3D animation showing the atomic-level configuration of the system at every point during the simulation [67]. Performing these simulations yields several advantages, including the ability to capture the position and motion of every atom at every point in time and the ability to fully control the simulation, as the conditions are precisely known (**Figure 4**).

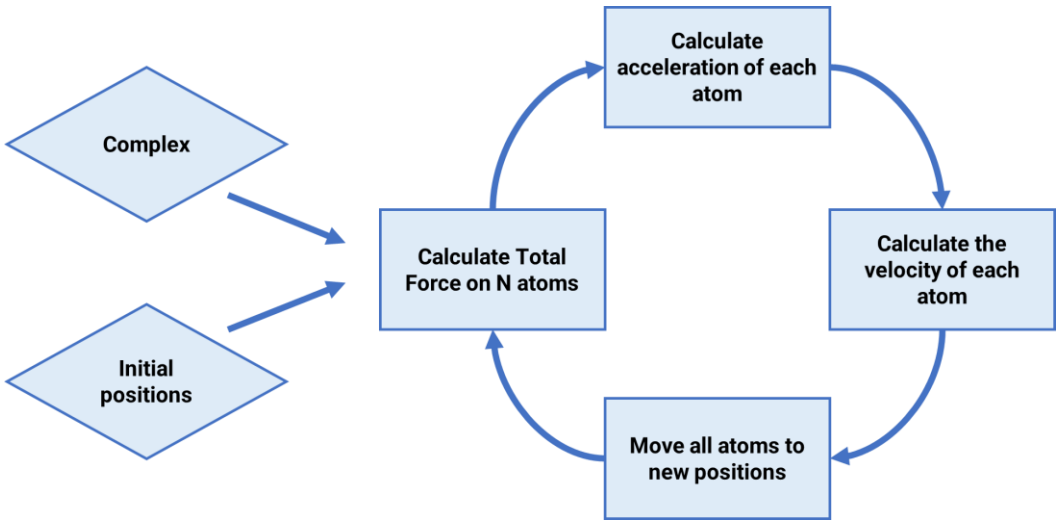

Figure 4. General workflow of Molecular dynamics simulation.

When discussing MD, it is crucial to emphasize the concept of ergodicity. MD simulations are based on the ergodic assumption, which states that the average of a property over all possible states is equivalent to the average over time, making it possible to perform MD simulations of real-world behavior within a realistic timeframe [68].

The initial step in performing an MD simulation is to obtain structures, which can be obtained from either experimental data (such as a crystallized model) or a computational model (complexes derived from molecular docking). As in molecular docking, also in this case, a virtual space (box) that surrounds the investigated complex needs to be defined. Since the goal of running MD simulations during CADD is to mimic real-life events, solvent molecules are added to the systems. In most cases, salt concentrations are implemented in the simulation box, and charges present in the studied complexes are neutralized by adding counterions, such as Na^+ and Cl^-, which replace the solvent

molecules. Once the system has been built, an energy minimization step is performed to lower its initial potential energy to remove steric clashes (**Figure 5**).

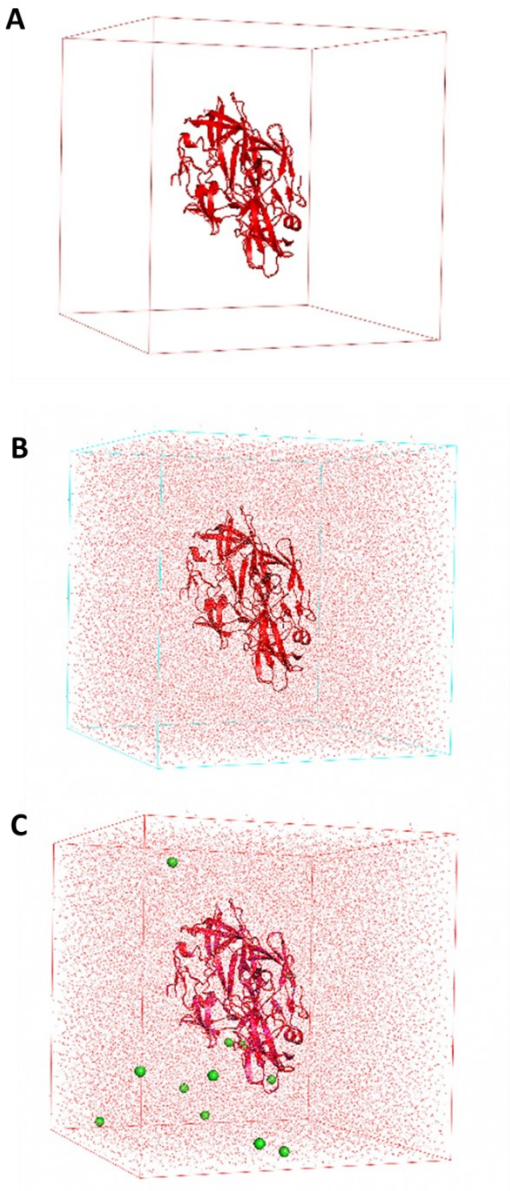

Figure 5. Examples of a molecular system in which the complex is inserted in a cubic virtual box (A), surrounded by water molecules (red dots, B). Then counterions and salt molecules are added (green spheres, C).

Once the system is ready, an appropriate Force Field (FF) and initial velocities are assigned to the atoms to determine the system's motion at the end of the simulation. This step is accomplished using the Maxwell-Boltzmann distribution at the temperature of interest, after which the initial velocities, V_i, are adjusted for the subsequent steps. Then, the equilibration step is performed to bring the system to equilibrium, considering temperature, volume, and pressure parameters.

In classical MD, quantum mechanical properties of atoms are ignored, and molecules are simplified as balls (representing atoms) connected by elastic sticks (representing bonds). Although this may be seen as a limitation due to the level of approximation, it enables the study of molecular mechanisms related to therapeutic targets, such as proteins and nucleic acids.

There are several types of FFs available for performing MD, and their use is based on different aspects, i.e., the type of macromolecule under investigation. The most used are CHARMM, AMBER, OPLS, and GROMOS [69–72]. Generally, in FFs, the expression of potential energy of contributing terms can be divided into two main categories: bonded and non-bonded interactions. In bonded interactions (E_{bond}), the stretching term considers the sum of all the 1-2 interactions (bonds), and the bending terms are the ones that consider angles formed by atoms in the molecules (1-3 interaction). Then, the torsion term describes the dihedral angles present in a 1-4 connection in a molecule. Furthermore, the cross term is given by the interaction of the previous bonded interactions, introducing a layer of complexity in the representation of the molecules (see *Equation 2*).

$$E_{bond} = E_{str} + E_{bend} + E_{tors} + E_{cross} \quad (2)$$

In contrast, non-bonded interactions ($E_{\text{non-bond}}$) account for interatomic forces separated by three or more bonds (e.g., 1–3, 1–4, 1–5, and beyond). These can be divided into VdW and electrostatic interactions (see *Equation 3*). Non-bonded interactions are also defined as paired interactions since the final $E_{\text{non bond}}$ highly depends on the distance between the pair of atoms (N). This aspect leads to a computational time of $O(N^2)$, which in big systems results in high computational time.

$$E_{non-bond} = E_{vdw} + E_{el} \quad (3)$$

VdW interactions encompass both attractive and repulsive forces between non-bonded atoms, and their magnitude depends mainly on the interatomic distance. Overall, E_{VdW} is positive at short distances due to repulsion, slightly negative at intermediate ranges due to attraction, and gradually tends toward zero as atoms move farther apart. These interactions can be modeled using LJ potentials, where a cut-off distance can be introduced to facilitate and speed up calculations by ignoring negligible VdW interactions.

Then, electrostatic interactions, primarily driven by fluctuations in electronic clouds that generate positive and negative charged regions, are represented using an electrostatic term expressed by the Coulomb potential. Since this term is also highly computationally demanding, cut-off values can be applied to ignore interactions beyond a specific range and manage long-range interactions. Being able to manage non-bonded interactions is pivotal, as these drive a whole set of events in therapeutic targets, such as the folding and stability of macromolecules, ligand binding, enzymatic activities, and solvent interactions [73].

Since MD simulations aim to reproduce the behavior of atoms in real-world systems, key physical properties, such as temperature (T), pressure (P), and volume (V), must be considered. The combination of these conditions in this context is known as the *thermodynamic ensemble* and is essential for deriving the thermodynamic properties of the system under investigation. Different thermodynamic ensembles represent varying levels of interaction between the system and its environment, ranging from a completely isolated system, such as the microcanonical ensemble (NVE), to fully open systems. The chosen ensemble should accurately reflect the physical conditions of the process being simulated. Given that the NPT ensemble is predominantly used in this thesis project, a detailed description of both is provided below. In the isothermal-isobaric canonical ensemble NPT, the number of particles (N), V, and T are conserved during the simulation. This allows the system to exchange heat with its surroundings and maintain a stable temperature as if it were placed within a thermostat, thus ensuring the realistic behavior of atoms and simulating temperature-dependent processes.

In this context, virtual thermostats implement a scale factor λ that can assume values greater than or less than 1, which is used to scale velocities and maintain a target temperature. Several thermostats are based on this concept, and for instance, Nosè-Hoover thermostat is considered very accurate and reliable in the context of classical MD simulations [74].

Furthermore, pressure is a driving parameter in many real-life events, which is why its simulation became an essential aspect to consider over the years. For this reason, a series of barostats were implemented following the rationale of thermostats. In this case, pressure control is achieved by rescaling V of the system. Many barostats have been implemented over the years. Still, the Martyna-Tobias-Tuckerman-Klein (MTTK) barostat is a particularly suitable choice for simulating the NPT ensemble using the Nosé-Hoover algorithm. This extends Newton's equation of motion by introducing variables that

simulate the presence of virtual pistons, rescale the volume of the simulation box, and allow for the maintenance of a constant pressure [75].

Since one of the primary goals of MD simulations is to capture realistic environmental conditions, bulk properties must also be accounted for. These are achieved through the boundary effect created by the Periodic Boundary Conditions (PBCs), which enable the simulation of an infinite system by considering multiple repetitions of the initial finite system. According to the simulation's goal, the periodic box size and shape need to be selected from a notable variety of options (i.e., a cubic periodic box, which is the most intuitive). However, in some cases (especially in the presence of globular complexes), working with cubic boxes leads to an inefficient amount of water molecules, which increases the computational cost. The optimal setup for simulation would involve a macromolecule encased in a sufficiently large sphere of solvent, as in the case of octahedral, dodecahedral, and triclinic boxes [76].

Despite their crucial importance, using PBCs in MD simulations could lead to issues where atoms interact with themselves or with other copies of the atoms. Furthermore, it is necessary to consider that non-bonded interactions must be calculated. To avoid this, the minimum image convention is employed, ensuring each atom interacts only with the nearest image of other atoms across periodic replicas [77]. Since long-range interactions still need to be considered, a cut-off radius is introduced to reduce calculations and prevent a particle from interacting with its own periodic image. For instance, in a cubic simulation box, this radius should not exceed half the box length to maintain physical accuracy. Additionally, it is essential to consider how the cut-off affects the calculation, as the potential energies computed at each step are truncated, thereby reducing the simulation's accuracy. VdW interactions decay quickly to zero, introducing minimal error when the cutoff is applied. However, electrostatic interactions decay slowly, and abruptly truncating these potentials could cause significant errors that need correction, which is achieved by the use of Particle mesh Ewald summation [78].

Then the integration of Newton’s equation of motion occurs thanks to a set of algorithms known as integrators, such as the most known Verlet integrator, in which the current positions r(t), accelerations a(t), and the positions from the previous step $r(t - \delta t)$ are used to obtain the positions in the next step $r(t + \delta t)$. As for any techniques, optimizations were done, and the Velocity Verlet method and Leapfrog were implemented [79,80].

After completing the simulation, specific metric parameters are used to evaluate its quality and identify key system characteristics, such as stability, flexibility, and compactness. The stability of an MD simulation is typically assessed using RMSD, whose interpretation differs slightly from that in molecular docking. In MD simulations, RMSD monitors the structural deviation of molecules over time by calculating the value of each frame versus the desired reference frame. Another useful parameter for analyzing molecular dynamics simulations is the Root Mean Square Fluctuation (RMSF), which tracks how much each atom, usually the α-carbon (C_α) in proteins, moves from its average position during the simulation [81]. This analysis is particularly useful for identifying and characterizing structural domains within the target, as regions with higher fluctuations often point to more flexible or dynamic segments. Another key parameter in MD analysis is the Radius of Gyration (RoG), which assesses the overall spatial distribution of a molecule by showing the RMS distance of all atoms from their shared center of mass. By examining RoG during a simulation, valuable insights into molecular compactness due to putative folding and unfolding events can be obtained (**Figure 6**).

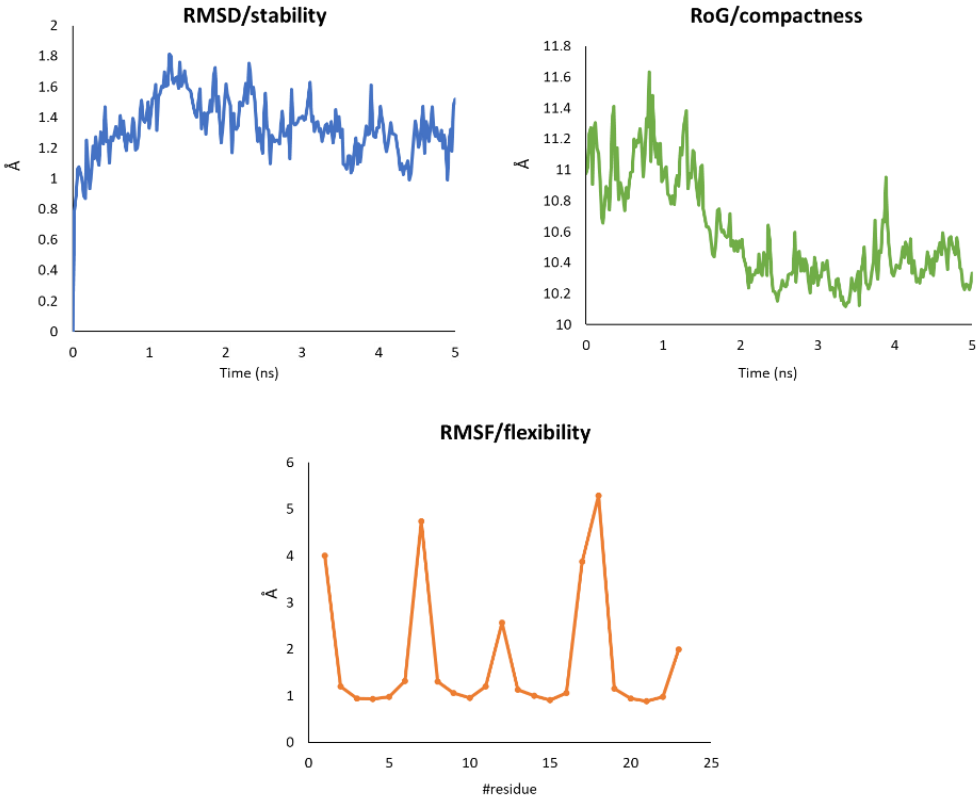

Figure 6. Graphical representation of RMSD, RMSF, and RoG data from a molecular dynamics simulation of 5 ns.

1.1.2 Ligand-based Drug Design (LBDD)

Ligand-Based Drug Design (LBDD) is a computational strategy that uses information about existing small molecules that bind to biological targets to create and refine new drug candidates. Additionally, when there is no structural information available about targets or if further insights are required to advance drug discovery research, ligand-based drug design is employed. Unlike SBDD, LBDD draws insights from the known properties and behaviors of active ligands to guide the design and discovery of new compounds [82]. The set of LBDD techniques encompasses various methods; however, this thesis will focus on explaining similarity-based and pharmacophore modeling [83].

Pharmacophore

At the end of the 19th century, the concept of pharmacophore arose when Langley first suggested that drug compounds might act on specific receptors [84]. Then, the discovery of Salvarsan by Paul Elrich led to the idea of drug-target selectivity. Subsequent experiments, including the model "lock and key" proposed by Fisher [85], were conducted, defining that drug-target interaction is driven by chemical bonds established in the complex [86]. Hence, the term pharmacophore was coined to describe the ensemble of steric and electronic features necessary to ensure the optimal molecular interactions between a ligand and a specific biological target structure and to trigger or inhibit its biological response [86–88].

Chemical features of molecules are described as pharmacophoric properties, virtually characterized as geometric entities such as spheres, vectors, and planes. Many of these features exist, but the most used include hydrophobic areas (H), hydrogen bond donors (D), hydrogen bond acceptors (A), positively and negatively ionizable groups (PI/NI), aromatic groups (R), metal-coordinating regions, and exclusion volumes (XVOL) (**Figure 7**).

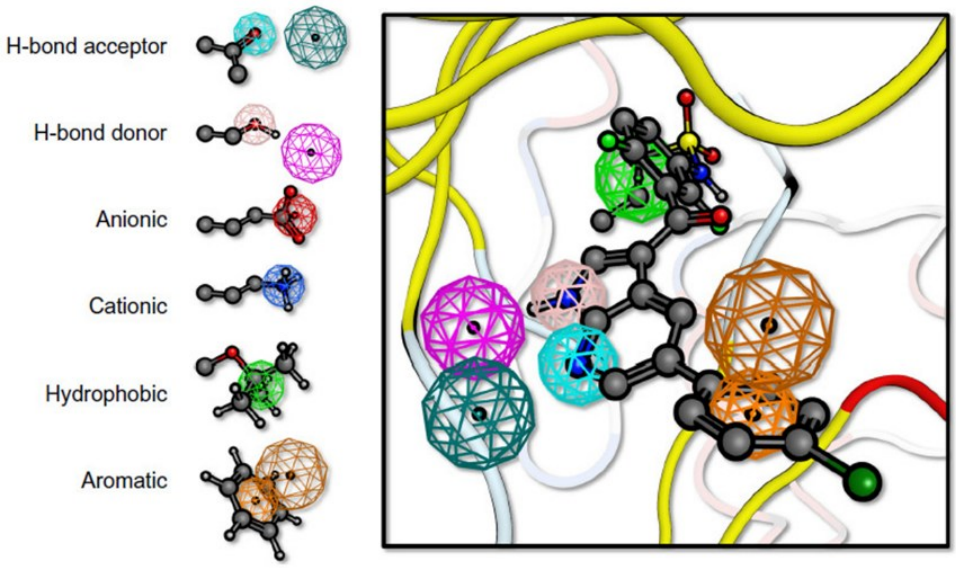

Figure 7. Pharmacophoric features. Geometric entities represent the main pharmacophoric feature types. Image from [89]

The general workflow of pharmacophore modeling involves the use of two datasets: a training set and a test set. The training set can vary in complexity, depending on the algorithm used and the available data. It can range from a basic set with at least two active compounds to a more complex set with multiple compounds showing different activities. The test set should include a combination of structurally diverse active and inactive compounds, preferably experimentally confirmed, to gather information on biological activity (i.e., EC_{50}/IC_{50} and K_d). If inactive ligands are unknown, decoy molecules can be used, available from sources such as the DUD (Directory of Useful Decoys) or generated using services such as DUD-E [90]. Molecules for dataset construction can be obtained from chemical databases such as OpenPHACTS, ChEMBL, or DrugBank for target-based activity compounds, and from ChEMBL, PubChem Bioassay, and Tox21 for inactive molecules.

After preparing all ligands to explore the conformational space and identify low-energy conformations, the goal is to find the bioactive conformation. Then, alignment of all conformers is done to ensure a good representation of the pharmacophoric space. After this, a pharmacophore model can be generated and evaluated based on its ability to distinguish active compounds from inactive ones. Those with the best performance in this initial screening are chosen for further testing and refinement using a dedicated test set. Before using them in real-world applications, these models must undergo validation to ensure their reliability and predictive accuracy by using four key metrics. Sensitivity

measures how well the model detects active compounds, specificity measures its ability to correctly reject inactive compounds, and the enrichment factor assesses the model's ability to prioritize active compounds relative to their prevalence in the entire screening set.

Here, other statistical parameters are used. The Receiver Operating Characteristic (ROC) curve, which plots sensitivity versus 1-specificity (false-positive rate), visually represents a model's ability to enrich results. Another key metric is the Area Under the Curve (AUC), which gives a numerical evaluation of a model's predictive performance. AUC values range from 0 to 1, with 1 indicating perfect recognition of active compounds, 0 showing complete recognition of inactive ones, and 0.5 representing performance equal to random guessing [91]. Several software tools can be used to generate pharmacophore models, with PHASE being a widely used platform in this field [92]. After this evaluation, compound libraries are screened, and those that best match the pharmacophore model are more likely to undergo experimental validation, during which *in vitro* and biophysical assays are performed to verify whether the predicted interactions hold true in real biological systems.

1.2 Mass spectrometry

While drug discovery and development have accelerated in recent years in identifying new active compounds, the development and optimization of confirmatory techniques for discovering new ligands, along with the study of complexes formed with targets, have also seen significant progress. Analytical techniques are now used as confirmatory steps because they help verify the evidence obtained during the *in silico* phase, thereby reducing the risk of failure in later stages, such as *in vitro* testing of selected ligands. Among the analytical techniques employed in drug discovery, mass spectrometry (MS) stands out as one of the most versatile, as it exploits the mass (m) and charge (z) of the investigated ions.

MS analysis begins with ionization, where the samples are ionized using various methods. The speed of the ions inside the instrument is affected by applying a voltage, which causes them to be evaluated according to their mass.

The first component in MS analysis is the source, the area where the sample is inserted and ionized. Insertion of the sample can occur in different ways, for instance, by coupling the MS with gas and liquid chromatography. Depending on the type of sample and instrument, various ionization methods are employed, including chemical ionization, matrix-assisted laser desorption/ionization, and electron spray ionization (ESI).

Electrospray ionization (ESI)

Electrospray ionization (ESI) nowadays is one of the most widely used techniques in the field of biomolecular investigations. This technique is a soft ionization method where liquid samples are exposed to strong electric fields. This exposure causes an event like electrophoresis, leading to the movement of ions in the sample, which are pulled toward the tip of the source. Then, the presence of a gas flow at atmospheric pressure leads to a droplet fission event. In this process, the solvent evaporates until the radius of the droplets decreases to the Rayleigh limit, resulting in the isolation of target ions, which are then desolvated in the gas phase [93]. One of the advantages of using ESI as an ionization technique is its compatibility with inlets that operate with volumes in the order of microliters (μL), allowing for the use of small sample amounts. Nanoelectrospray ESI (nanoESI), a refined variant of ESI, exploits narrow-bore emitters (orifices with a diameter that ranges from 1 to 10 μM) with an nL/min flow rate compared to a μL/min flow rate in conventional ESI (**Figure 8**).

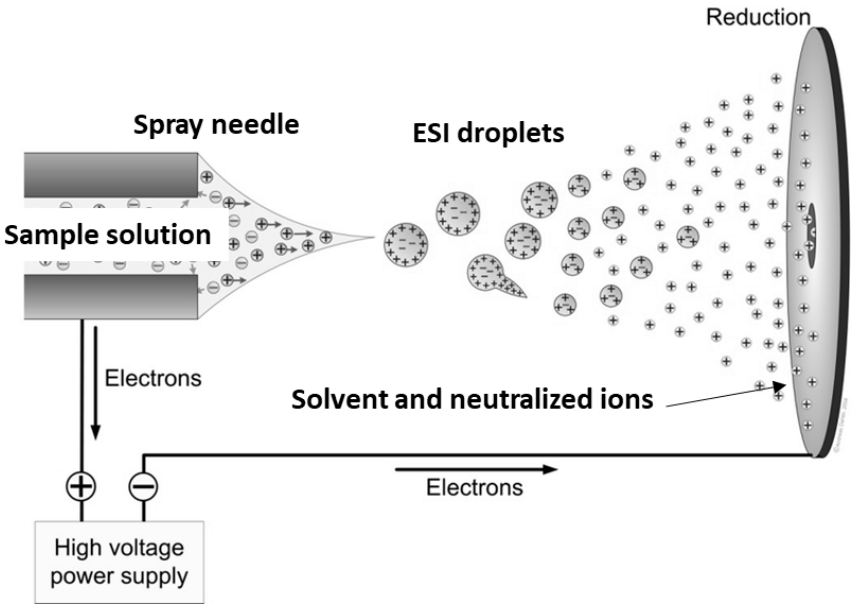

Figure 8. Schematic representations of ESI. Adapted from [94].

Mass analyzers

Mass analyzers are the second component in an MS analysis. In this region of the instrument, ions are separated based on their m/z ratio, and the output is then sent to the detector. As with ionizers, there are various mass analyzers. The most used are the quadrupole, the time-of-flight (TOF), and the ion trap.

One of the most used mass analyzers is the quadrupole, which consists of four metal rods inside a vacuum chamber. A radio frequency (RF) and a direct current (DC) are applied to these rods in an alternating manner to isolate and direct the desired ions according to their m/z. Due to their robustness, affordability, and good scan speed and sensitivity, quadrupoles are widely used nowadays (**Figure 9**).

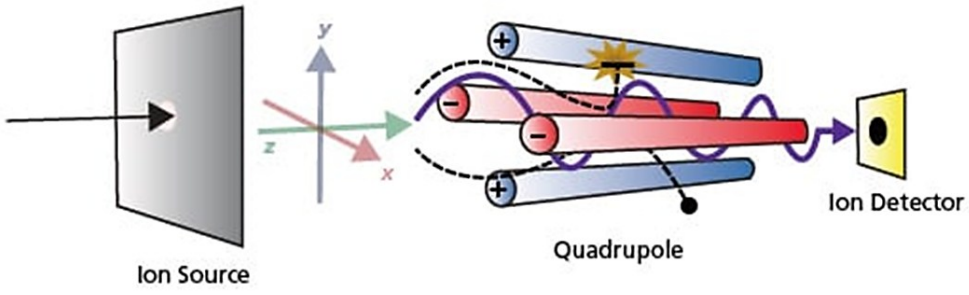

Figure 9. Schematic representation of a quadrupole system. Adapted from [95].

In the case of TOF mass analyzers, the principle relies on measuring the time of flight, where the ions to be analyzed are accelerated by an electric field of known strength. The acceleration of the ions inside the drift tube occurs at a constant kinetic energy; their velocities vary inversely with their mass, so the lighter ions reach the detector first. The time it takes for the particle to arrive at a detector placed at a known distance is then measured. Since the ion's velocity depends on the m/z ratio (heavier particles move more slowly), it can be calculated from this time and the known experimental parameters (**Figure 10**).

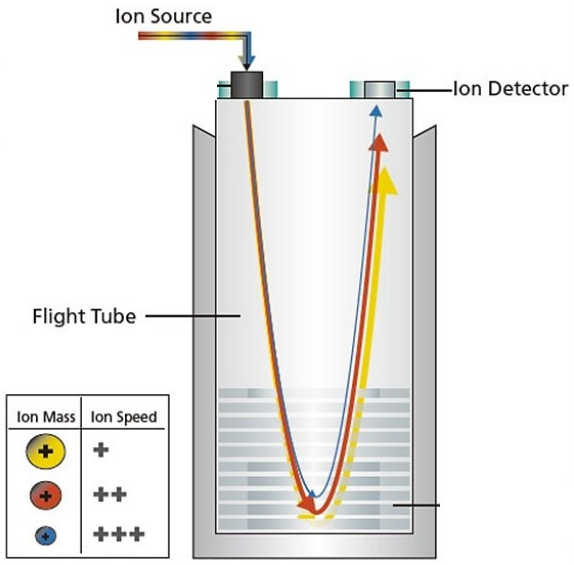

Figure 10. Schematic representation of a TOF system. Adapted from [95].

Quadrupole Ion Trap Mass Analyzers

This analyzer operates on principles similar to those of the quadrupole analyzer described earlier. It uses an electric field to separate ions based on their m/z ratios. The device has a ring electrode set to a specific voltage, with grounded end cap electrodes. Ions enter between the electrodes through one end cap. Inside, the electric field generated by the electrodes causes ions with specific m/z values to orbit around the electrodes. As the RF voltage increases, heavier ions become more stable in their orbits, while lighter ions are less stable and tend to collide with the wall. These collisions prevent lighter ions from reaching and being detected. There are two types of quadrupole ion traps: 3D and 2D.

3D ion traps operate similarly to quadrupole mass analyzers but with different setups. In a 3D ion trap mass analyzer, two hyperbolic metal electrodes (end caps) face each other, with a ring electrode positioned between them. Ions get trapped between the

electrodes because of the applied oscillating RF voltage and static DC. Selective ejection and detection of ions with specific m/z ratios happen by adjusting the RF voltage.

A 2D ion trap (also called a linear trap) uses quadrupole rods with electrodes on each end to facilitate ion trapping. This allows it to be used as either a quadrupole mass filter or as an ion trap. The selected ions are ejected either radially or axially (**Figure 11**).

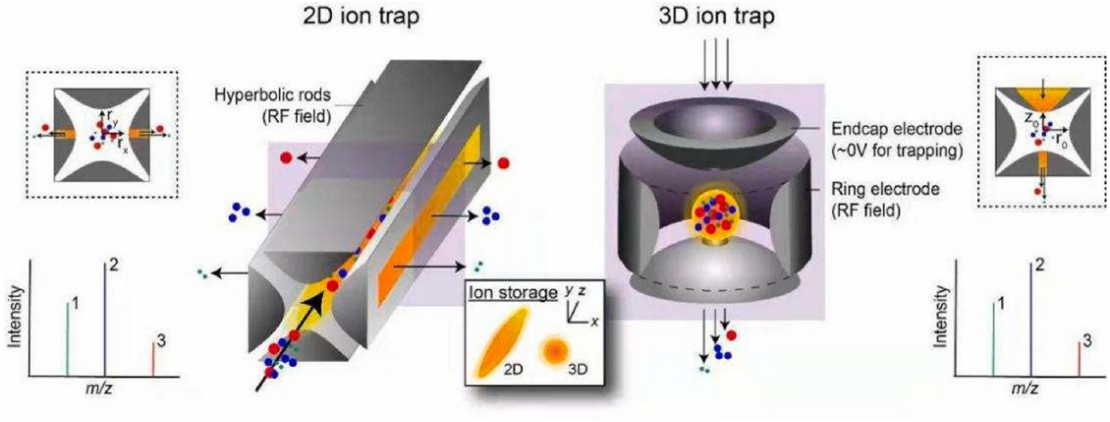

Figure 11. 2D and 3D ion trap working diagram. Image from [96].

Ion Mobility Mass Spectrometry

Ion mobility mass spectrometry, an evolution of MS, was used to study biomolecular complexes in drug discovery since the 1960s, when McDaniel combined these systems to develop new resolving methods. IM spectrometry measures the time with which an ion, in the presence of a weak electric field, takes to travel the length of the drift tube. By knowing the length (L) of the drift tube and the drift time of the ion, it is possible to calculate the steady-state velocity of drift (V_d) of the ion, which, in the case of analyses made with drift tubes, is a linear function of the applied electric field (E). From here, the constant *K*, known as the mobility of the ion that represents the drag force from the drift gas versus the driving force of E, is obtained. When IM is coupled with mass spectrometry (IMMS), MS serves as a detection system in which the arrival time distribution is calculated. Although these hybrid systems boosted the power of detection in the field of drug discovery, specific attention was needed at the interface between IM and MS. Since the 1990s, the introduction of the RF confining ion traps and ion funnels in IM systems significantly improved performances, and trapped ion mobility mass spectrometry (TIMS) was introduced in 2011 by Park and his coworkers [97,98].

In TIMS, the mobility of ions (*K*) is defined to be the V_d that the ion has under the influence of E, in which:

$$V_d = KE$$

For this reason, K is a variable related to the interaction of the ion with the drift gas, resulting in several dependencies due to the type of gas, temperature, pressure, composition, polarizability of the gas, and the size and shape of the ion. To establish K as a reproducible and comparable parameter within the scientific community, a standardized value, K_0, was introduced, accounting for all previous conditions [99].

$$K_0 = K * \left(\frac{p}{p_0}\right) * \left(\frac{T_0}{T}\right)$$

Furthermore, K_0 can be related to the m/z and the Collision Cross Section (CCS), which can be defined as the rotationally averaged ion surface area (usually expressed in Å²).

$$CCS = \frac{3ze}{16}\left(\frac{2\pi}{\mu k_B T}\right)^{\frac{1}{2}} \frac{1}{K_0}$$

Where z is the charge on the ion, e is the elemental charge, K_b is Boltzmann's constant, and μ is the reduced mass.

Conceptually, TIMS constitutes an inversion of the traditional IMS experiment since it uses an E to hold ions stationary against a moving gas. TIMS enables a bidimensional separation, making it suitable for various applications such as proteomics, metabolomics, and the study of nucleic acid complexes.

In the TIMS funnel, ions generated mainly by ESI or nanoESI are introduced, and here, ions move in the same direction as drifting gas molecules. In contrast, E is applied in the opposite direction, slowing the ions. When an equilibrium state is achieved, an ion of a specific size (with a corresponding *K*) is trapped in a region where the electric force V_d equals the carrier gas velocity V_g, where $V_d + V_g = 0$, with V_d directly proportional to *K* and E. Then, the second part is where the m/z of the separated ions is detected. This is done via the mass spectrometer, usually a quadrupole TOF (Q-TOF) instrument, which enables the separation of ions derived even from large biomolecular assemblies along the m/z axis.

These two regions in TIMS allow for the production of both a mobilogram (ion current versus ion mobility) and a mass spectrum (ion current versus m/z), making TIMS a bidimensional separation method that offers insights into molecule shapes and sizes, information that is not available from traditional MS instruments (**Figure 12**).

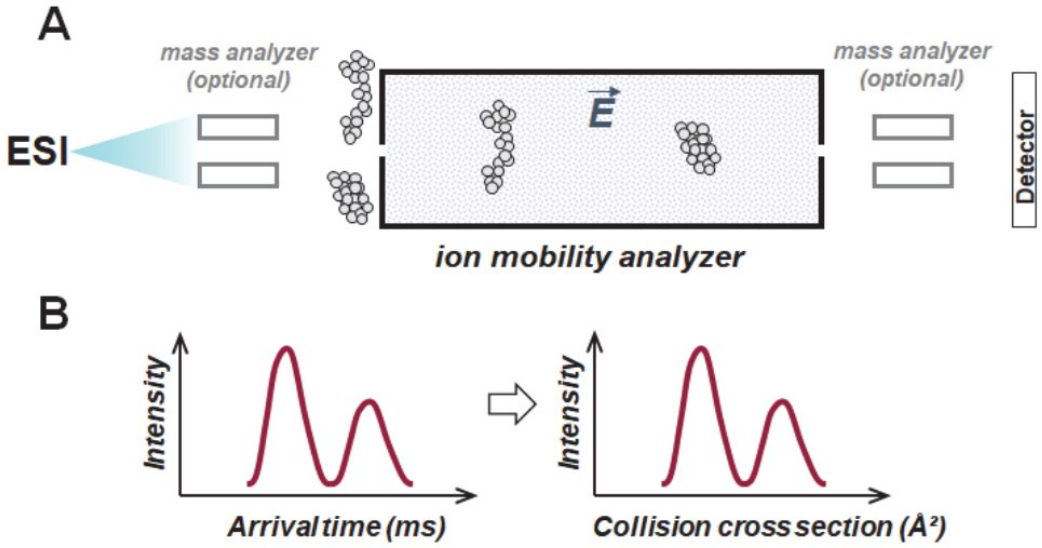

Figure 12. A) Schematics of an ion mobility spectrometer, here with a drift tube analyzer. The most compact ions travel faster and reach the detector earlier than the more extended ions (assuming they have the same mass and charge). B) A typical ion mobility spectrum: ion counts as a function of the time elapsed between the pulsing in the mobility analyzer and the detector. The arrival time distributions can be converted into CCS distributions. Image from [100].

One of the most attractive aspects of IMMS, particularly of TIMS, is the ability to measure the CCS values of biomolecular entities. Experimentally determined CCSs facilitate the comparison of actual measurements with those predicted by *in silico* simulations, providing a comprehensive view of the analyte's structure.

Calculating theoretical CCS values usually requires simulating the collisions and long-range interactions between drift gas molecules and analyte ions at different levels of detail, as these factors influence the *K* value. In this, CCS values on themselves do not provide information on the structures, but comparing them to known systems can reveal which ensembles the user is working with.

In this, *in silico* analyses are fundamental, as they allow the creation of 3D molecular models, the calculation of their theoretical CCS, and, finally, the comparison with experimentally derived values. In this context, CCS prediction techniques are categorized into three groups: Project Approximation (PA), Trajectory Methods (TM), and Exact Hard Sphere Scattering (EHSS). In PA, CCS values are determined by projecting the ion onto a surface and averaging across all possible orientations, based on an all-or-none interaction assumption [101]. A more sophisticated method uses the EHSS technique, which models the drift gas's trajectory as it approaches and interacts with the analyte ion (depicted as a set of rigid spheres). It accounts for momentum transfer during collisions,

based on impact and scattering angles [102]. Additionally, to enhance calculation precision, long-range interaction potentials and polarization effects were included. This resulted in TM methods that simulate thousands of buffer gas-ionic collision molecules governed by a relevant interaction potential [103].

MOBCAL is one of the most widely used TM-based CCS prediction tools. Originally designed to analyze small metal-ion clusters and fullerenes, it was later adapted to biomolecular research through IMMS applications. Consequently, MOBCAL has also been utilized in drug discovery, though it faces some limitations in this area [102]. Because calculating the CCS of larger biomolecular targets (>100 kDa) requires extensive computational resources, new tools became necessary, particularly for biomolecules other than proteins, such as nucleic acids. This was the case of the collision simulator for ion mobility spectrometry (CoSIMS), a TM-based tool developed by Myers and coworkers at University of Albany [104]. The generation of the geometrical space used for CCS calculations is one of the most crucial aspects in CoSIMS. Biomolecular targets with different natures, such as proteins and nucleic acids, also differ in shape (proteins tend to be mainly globular, while nucleic acids are more elongated). Therefore, treating elongated shapes as globular leads to significant approximation errors, resulting in biased CCS values. In this context, CoSIMS was used to dynamically modify the geometric interaction space based on the analyte's topology, thereby enhancing accuracy for elongated molecules such as nucleic acids [105] (**Figure 13**).

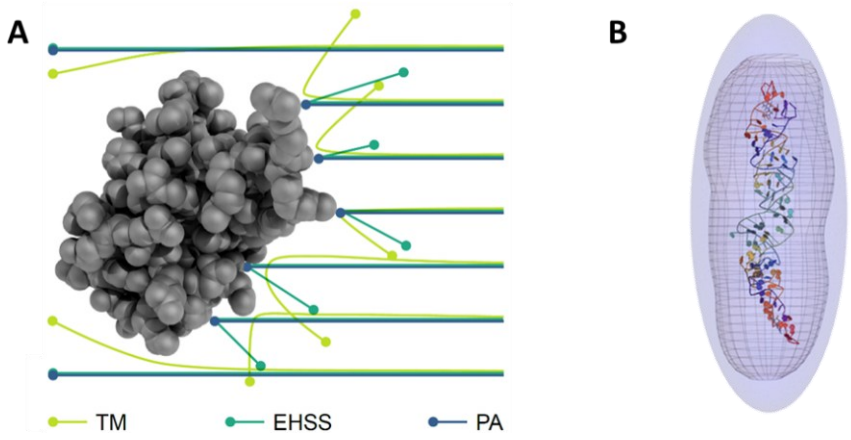

Figure 13. A) The principal operation and differences between the main classes of CCS calculation methods. TM traces the probe particles' trajectories, whereas EHSS and PA only regard direct contact between probes and analyte. The EHSS considers (multiple) scattering after initial collision, whereas PA only differentiates between hits and misses, and estimates CCSs from the fraction of hits. B) CoSIMS approximation. Adapted from [105,106].

1.3 Nuclear Magnetic Resonance

Nuclear magnetic resonance (NMR) spectroscopy is a non-destructive characterization technique used for various analyses, including the structural characterization of small molecules and macromolecules, as well as the study of their interactions. NMR was first described and measured by Isidor Rabi in 1938, building on the Stern-Gerlach experiment. In recognition of this work, Rabi received the Nobel Prize in Physics in 1944 [107]. Rabi, along with Bloch and Purcell, who received the Nobel Prize in 1952, discovered that magnetic nuclei like ^{1}H and ^{31}P could absorb RF energy when placed in a magnetic field if the RF is specific to that type of nucleus. This absorption occurs when nuclei are in resonance. Due to variations in local magnetic fields, different groups of atomic nuclei within a molecule resonate at various frequencies in the same external magnetic field. By examining differences in these resonance frequencies, scientists were able to gain important chemical and structural information about molecules, opening a new approach to the field of drug discovery. The principal components of an NMR spectrometer (**Figure 14**) are the magnet, the NMR console, and the workstation. The magnet is responsible for generating a strong magnetic field, and this aligns the nuclear spin of the atoms. The magnets used nowadays are usually made from superconducting materials and thus require a very low temperature to perform.

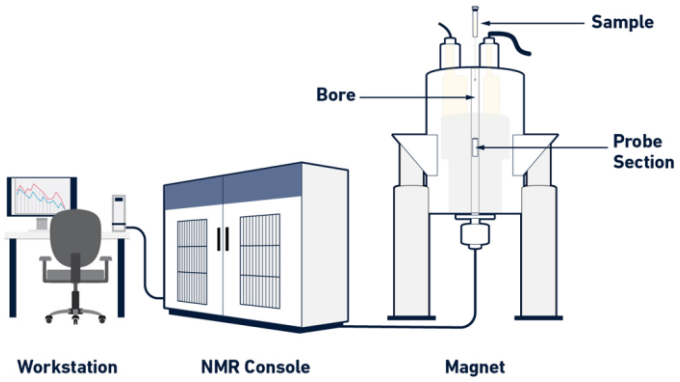

Figure 14. General design of an NMR spectrometer with its principal components. Image from [108]

For this reason, NMR spectrometers incorporate a cooling system (**Figure 15**) which consists of an inner jacket filled with liquid helium, which is cooled further by an outer coat containing liquid nitrogen. Additionally, the setup includes multiple layers of thermal insulation materials for efficient temperature control.

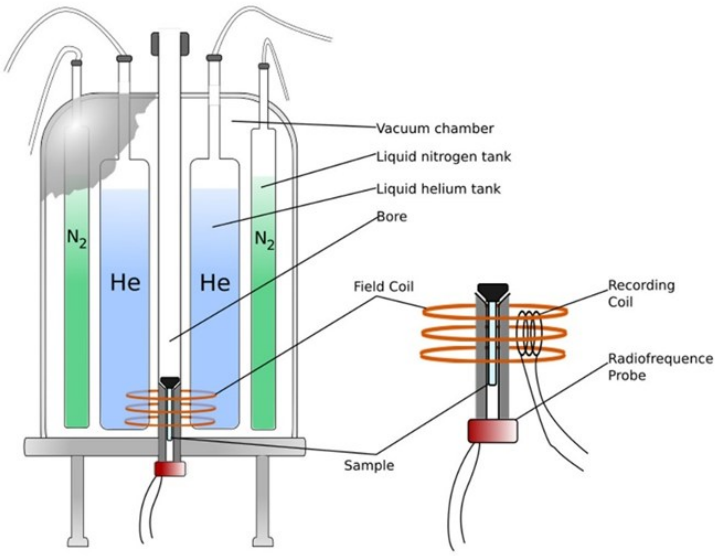

Figure 15. Internal components of an NMR spectrometer, including a detailed view of the probe. Image from [108].

Inside the magnet, the probe is present, and the sample is introduced into an environment surrounded by a series of magnetic coils that irradiate RF pulses, detect, and collect the NMR signal. Furthermore, they allow control of the magnetic field homogeneity and the application of pulse gradients that are used in some NMR experiments [109].

The NMR console manages all experimental conditions and allows for setting up and modifying every parameter of the NMR experiment using the workstation. This system is also used for the acquisition and application of the Fourier transform, which leads to the free induction decay (FID) being expressed as a time variable in the frequency domain (**Figure 16**).

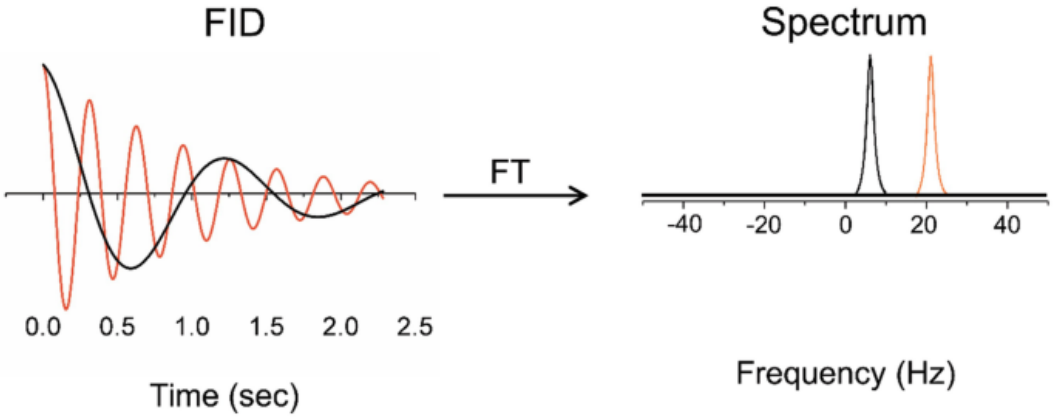

Figure 16. Illustration of the Fourier transform. Image from [110].

The spectrum is composed of a series of peaks with varying intensities, determined by a magnitude known as chemical shift. Chemical shift derives from the Larmor frequency and provides information about the local electronic environment of atoms in molecules. The Larmor frequency is an intrinsic property of atomic nuclei that are immersed in a magnetic field, which is proportional to the intensity of the magnetic field and depends on the gyromagnetic ratio of the particle. As anticipated, the analysis of peaks allows for the determination of molecular structure, chemical bonding, and interactions within a ligand, making NMR spectroscopy a powerful tool in structural elucidation and molecular characterization [111].

Saturation Transfer Difference experiment

The Nuclear Overhauser Effect (NOE) is defined as the change in the intensity of one resonance when another resonance is saturated [112]. In an NMR spectrum, a change in the integrated intensity (positive or negative) of one NMR resonance occurs when another is saturated by irradiation with an RF field. The shift in resonance intensity of a nucleus is a consequence of the nucleus being close in space (with a limit of 4 or 5 Å) to those directly affected by the RF perturbation. This feature, its spatial dependence, makes NOE extremely powerful for characterizing molecular stereochemistry and conformation. In fact, NOE is completely independent of the nature of the covalent bonding network between the two interacting spins.

An application of the NOE effect is the Saturation Transfer Difference (STD) experiment. The STD-NMR experiment relies on the exchange between bound and free states of a weak-binding ligand. In this context, the dissociation constant (K_d) should be from 10^{-8} mol/L to 10^{-3} mol/L. A low K_d value indicates that the two molecules are strongly attracted to each other, and only a low concentration of the ligand is needed to saturate the receptor. In contrast, a higher K_d value shows that a higher concentration of the ligand is necessary to saturate it. Fundamentally, an STD experiment involves subtracting a spectrum where the receptor is selectively saturated (on-resonance spectrum, obtained by irradiating a region of the spectrum containing only the receptor resonances, I_{SAT}) from one recorded without receptor saturation (off-resonance spectrum, I_0). In the resulting difference spectrum ($I_{STD}=I_0 - I_{SAT}$), only the signals of the ligand that received saturation transfer from the macromolecule, *via* spin diffusion and through the NOE, will remain. Compounds that do not bind to the receptor will not undergo saturation transfer; their

signals will remain equally intense in both on-resonance and off-resonance spectra, and as a result, no signals will appear in the difference spectrum for non-binding molecules. The intensity difference due to saturation transfer serves as an indicator of binding. For a molecule that binds to the receptor, only the signals of hydrogens in close contact with the receptor (within 5 Å) and receiving magnetization transfer will appear in the difference spectrum. The closer the hydrogens are to the macromolecule, the more intense their signals will be due to more efficient saturation transfer [113] (**Figure 17**).

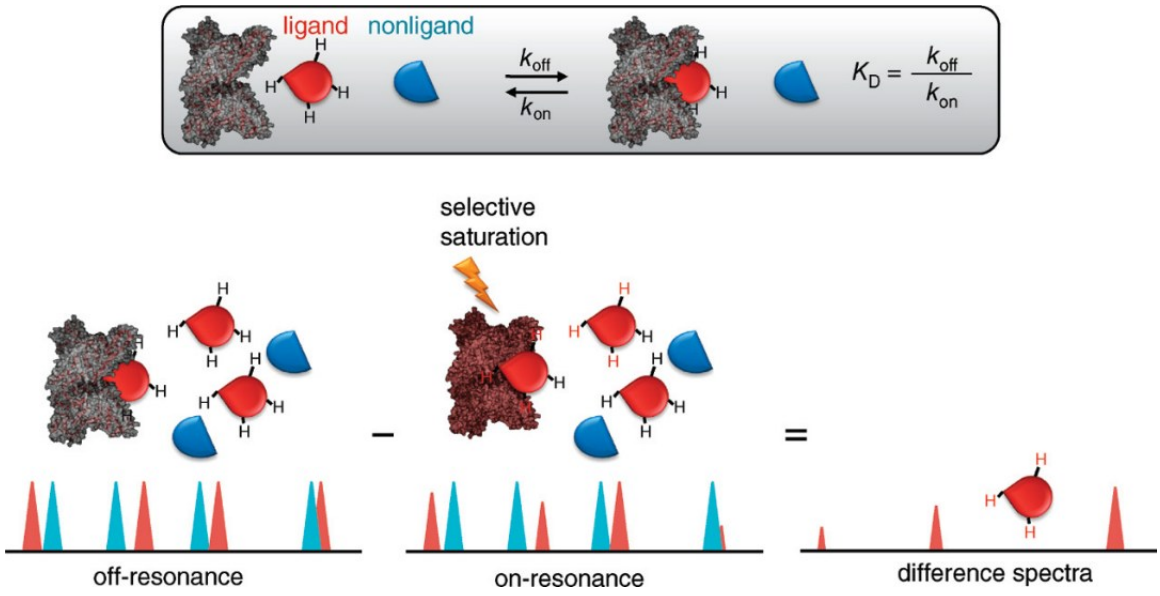

Figure 17. Scheme of the STD-NMR experiment. The exchange between free and bound ligand allows intermolecular transfer of magnetization from the receptor to the bound small molecule. Image from [113].

2 Main project: Developing ligands targeting G-quadruplexes

2.1. Introduction to nucleic acids and G-quadruplexes

Traditional drug discovery mainly involves the use of small molecules that can interact with identified protein targets, thereby modulating their functions. Although the tools for developing these compounds are more common and primarily stick to classical pharmacokinetic and pharmacodynamics rules, targeting proteins means targeting only a small fraction (20%) of the effectively translated proteins [114].

DNA was discovered in 1869 by Swiss biochemist Friedrich Miescher. In the 1930s, researchers identified the four DNA bases and the sugar deoxyribose, giving rise to the name deoxyribonucleic acid (DNA).

DNA is a polymer composed of nucleotides, each containing a five-carbon sugar (deoxyribose), a phosphate group, and a nitrogenous base. The bases include adenine and guanine (which are purines with two rings), as well as cytosine and thymine (pyrimidines with one ring). In each nucleotide, the base attaches to the 1′ carbon of deoxyribose through an N-glycosidic bond, while the phosphate connects to the 5′ carbon of the sugar moiety. In a DNA strand, nucleotides are linked by phosphodiester bonds, which connect the 3′-hydroxyl of one sugar to the 5′-phosphate of the next, establishing a direction: one end has a free 5′ phosphate group, and the other has a 3′ hydroxyl group (**Figure 18**).

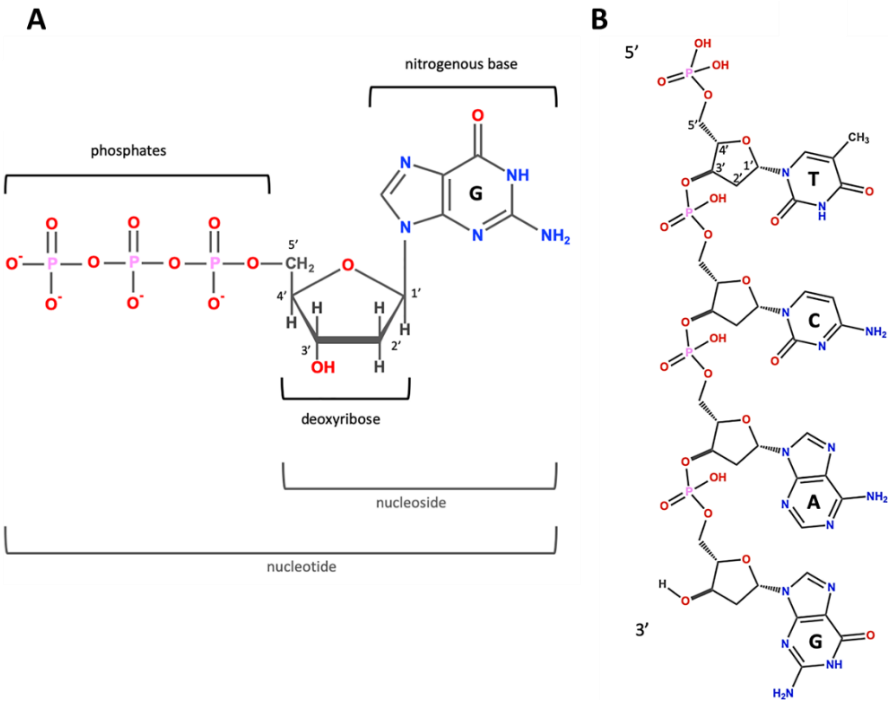

Figure 18. A) Depiction of a guanosine triphosphate. B) DNA strand containing four nucleotides with the nitrogenous bases thymine (T), cytosine (C), adenine (A), and guanine (G), respectively. Adapted from [115].

Once the importance of DNA was confirmed, research aimed at resolving its 3D structure. At King's College London, Rosalind Franklin and Maurice Wilkins used X-ray diffraction to suggest that DNA had a helical shape, with Franklin producing a clear diffraction image [116]. Meanwhile, at Cambridge, James Watson and Francis Crick used model building and data, including Franklin's image findings, to determine the double helix structure of DNA [117].

From this discovery, much information was achieved, leading to the understanding that DNA generally folds as a double-stranded (ds) helix with the two strands running in opposite directions (from 5′ to 3′ and the other from 3′ to 5′). Generally, strands are right-handed, and A-T and C-G are held together by Watson-Crick hydrogen bonds (**Figure 19**).

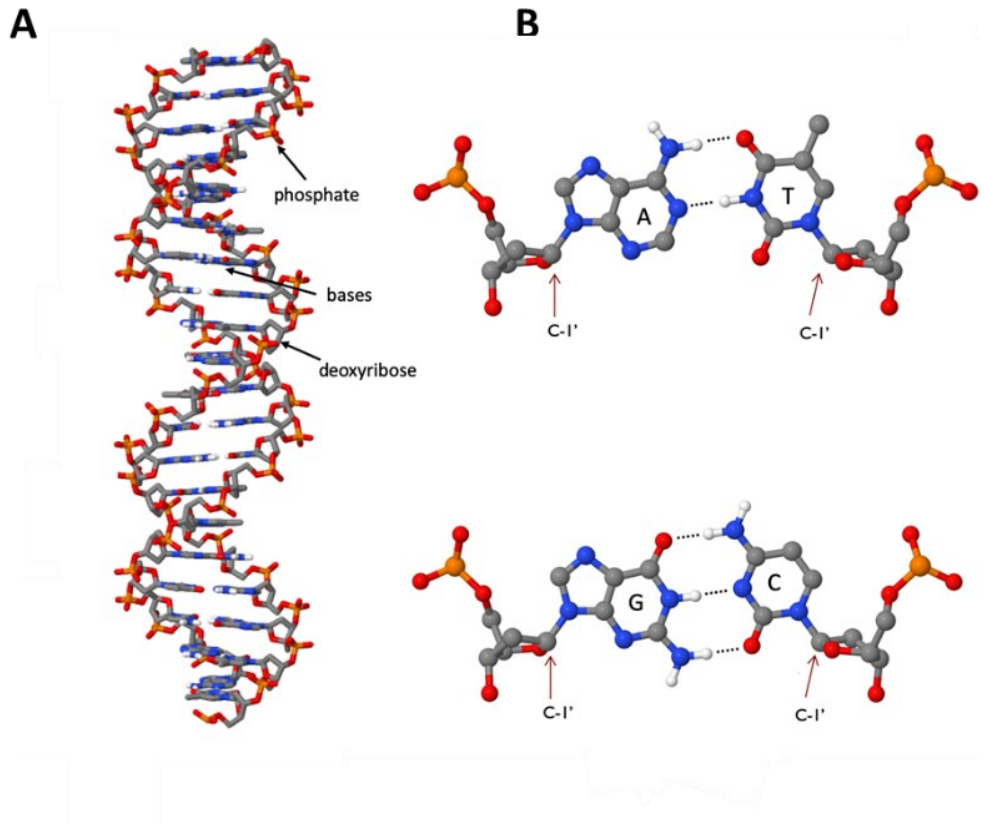

Figure 19. A) The DNA double helix, with the sugar phosphate backbone on the outside and the nitrogenous bases in the middle. (B) An A-T and a G-C base pair with the C1' of the deoxyribose indicated by the arrow. The dotted line indicates the hydrogen bonds between the base pairs. Adapted from [115].

Another essential nucleic acid is ribonucleic acid (RNA), which plays a pivotal role in cell life by serving as a messenger of genetic information and facilitating protein synthesis. From the structural point of view, RNA is very similar to DNA. As DNA, RNA is generally composed of a single chain, and the composing sugar is 5-carbon ribose, followed by the presence of a nitrogenous base and a phosphate group. In the case of RNA,

the phosphate group is linked to the nitrogenous base through the 1’ carbon, and the nitrogenous base composition is different since the T present in DNA is replaced by uracil (U) (**Figure 20**) [115].

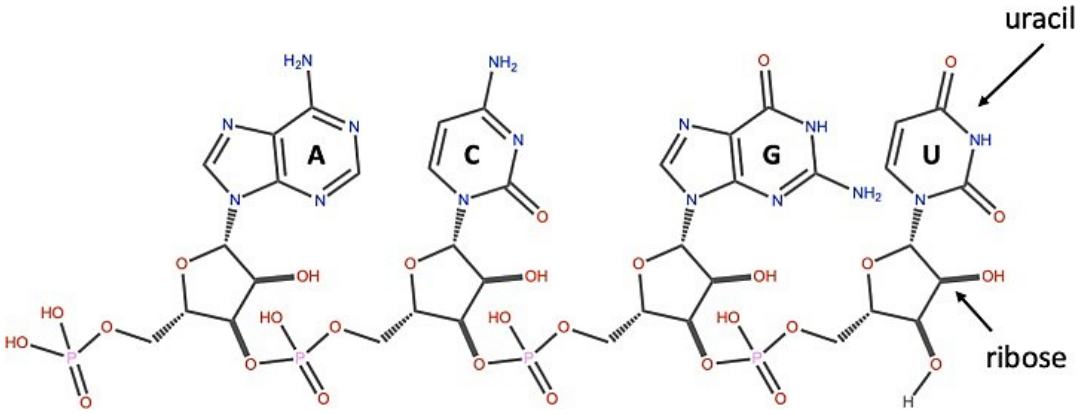

Figure 20. An RNA strand consists of the four nucleotides with the nitrogenous bases adenine (A), cytosine (C), guanine (G), and uracil (U). The 3′ carbon of the ribose in one nucleotide is connected to the 5′ carbon of the next nucleotide through a phosphodiester bond. The 5′ end is on the left, and the 3′ end is on the right. Image from [115].

G-quadruplexes (G4s)

Although canonical nucleic acids have specific secondary structures reported as “canonical”, several studies reported the existence of alternative conformations involved in the regulation of several cellular processes.

In this context, four-stranded G-quadruplexes (G4s) form through the self-recognition of guanines in specific regions of the guanine-rich regions in the genome, resulting in regulatory effects on nucleic acid-related processes [118]. G4s can form within a DNA and RNA or between multiple strands and can adopt various topologies, depending on strand orientation and loop composition [119–122].

From the structural point of view, G4s are formed by the stacking of two or more G-tetrads (or tetrads), where four guanine bases interact through Hoogsteen hydrogen bonds. These stacking G-tetrads are further stabilized by the presence of cations (such as K^+ and Na^+), which are coordinated by the electron-rich O6 of eight guanines belonging to two stacking G-tetrads, leading to a stoichiometry for monovalent cations of *n-1* where *n* is the number of the present tetrads (**Figure 21**) [123].

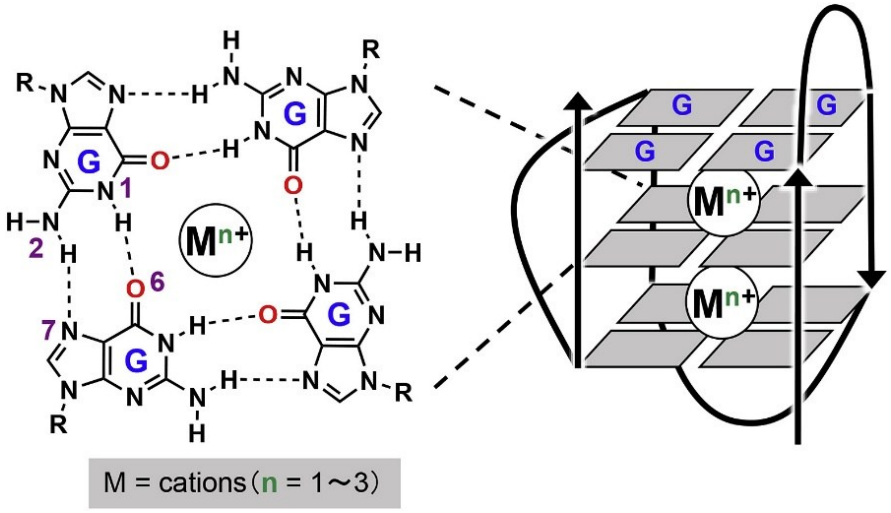

Figure 21. Structures of tetrad (left) and G-quadruplex (right). Image from [124].

In G4 terminology, residues before or after G-tetrads are called flanking regions, and residues that connect G-tetrads and flanking regions are known as loops. The loops can adopt several geometries, such as the propeller (connecting guanines from adjacent G-tracts but opposite quartets), lateral (connecting adjacent G-tracts and the same quartets), and diagonal (connecting diagonally opposed G-tracts and the same quartets) (**Figure 22A**) [125]. Furthermore, G4s can adopt different topologies according to the relative orientation of G-tracts. When all tracts are running in the same direction, this configuration is referred to as a parallel topology. When two strands are oriented in the opposite direction to the other two, these are known to be antiparallel. Lastly, when one strand lies in the opposite direction to the three others, these are hybrid-1 or hybrid-2 (**Figure 22B**) [124,125].

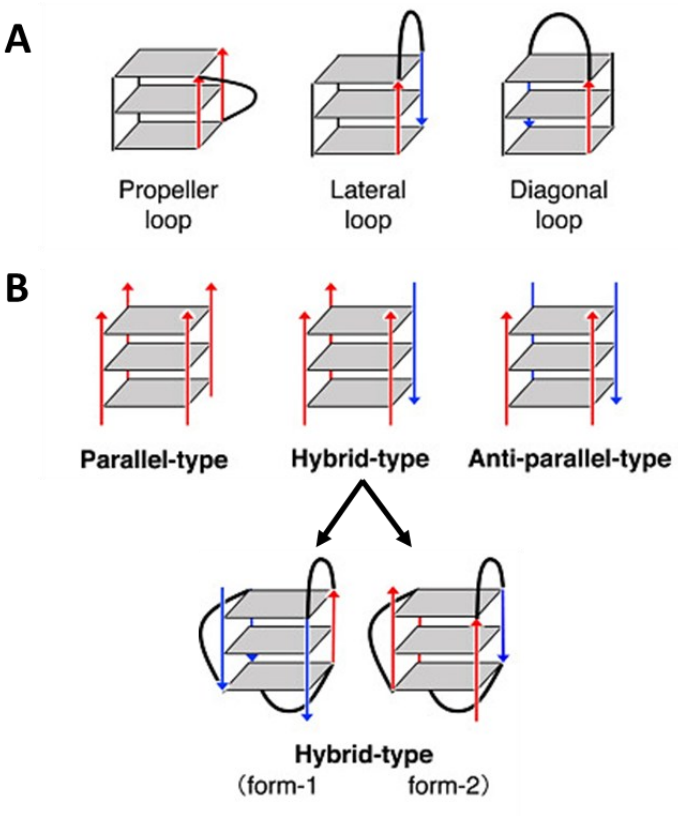

Figure 22. Depiction of loops and of the G4 typical topologies. Adapted from [124].

Identification of G4s

To identify and address the presence and function of G4s, computational, biophysical, and *in vitro* studies have been conducted over the years. Biophysical studies have supported the definition of the diversity and stability of G4s, leading to rules for predicting G4-forming sequences and paving the way for bioinformatic prediction. The first predictive model used for G4 prediction assumed that intramolecular G4s required four short stretches of at least three consecutive guanines separated by short spacers that would become the loops of the assembly [126,127]. Nowadays, the G4-forming sequence is defined by the following template: $G_{3–5}L1_{1–7}G_{3–5}L2_{1–7}G_{3–5}L3_{1–7}G_{3–5}$ where L1, L2, and L3 represent the three loops connecting the guanines that assemble into tetrads [128].

Early predictive models, such as the one used by the Quadparser algorithm, predicted around 375,000 potential G4 sites (putative G4 sequences, PQS) in the human genome; however, newer tools have since expanded this number and improved G4 detection [129].

Modern algorithms, such as pqsfinder (https://pqsfinder.fi.muni.cz/) and G4Hunter (http://bioinformatics.ibp.cz), allow for imperfections like bulges and long loops, and some

now utilize ML trained on experimentally confirmed G4 sequences [130,131]. Moreover, tools like 3D-NuS (https://iith.ac.in/3dnus/) can predict the inter- and intramolecular 3D structures of G4 and analyze the dynamics of different G4s, as well as facilitate the docking of proteins and ligands. This leads to a deeper understanding of G4-related events [132].

Then, the efficacy of computational PQS-identifier tools was assessed *in vitro* using high-throughput methods, such as G4-seq and rG4-seq, which detected G4 formation by observing polymerase or reverse transcriptase stalling during sequencing [133,134]. G4-seq employs a modified Illumina sequencing protocol where a decrease in sequencing quality scores identifies polymerase arrest caused by a folded G4 in the template. The reduction in G4-specific Q-scores was determined by comparing a standard sequencing run with one in which G4-stabilizing agents, like K^+ or small-molecule ligands such as pyridostatin (PDS), were added to the sequencing buffer [128]. G4-seq of the human genome revealed more than 700000 G4-forming sites, many of which were missed by traditional predictive motif-based algorithms [128,134]. However, G4-seq also failed to detect 27% of canonical G-forming motifs in PDS due to technical limitations, such as poor coverage in GC-rich regions and ligand-specific biases [135]. To identify and confirm the presence of RNA-based G4s, the G4-seq method was adapted for transcriptomic analyses, resulting in rG4-seq. In rG4-seq, reverse transcriptase stalls occur when G4s form *in vitro* on template mRNA upon addition of K^+ or K^+/PDS. After reverse transcription and Illumina sequencing, sequences that form G4s are identified by a decrease in coverage. This approach, applied in the evaluation of HeLa cells, revealed that 88% of detected reverse transcriptase arrests match with G4s. Although these advances are significant, both bioinformatic and sequencing methods have limitations and need *in vivo* validation to verify G4 formation. In this context, emerging technologies such as nanopore sequencing are reported to offer promising results for direct G4 detection in living cells by analyzing DNA translocation timing of canonical and non-canonical DNA, potentially revolutionizing G4 research [136]. Furthermore, a more sensitive and physiologically relevant method, called G4 CUT&Tag, was developed [137]. This technique utilizes permeabilized cells and a G4-specific antibody conjugated to a transposase fusion protein (pA-Tn5), which targets G4 sites for sequencing. G4 CUT&Tag significantly improved resolution and doubled the number of detected G4s compared to previous conceptualized methods [138]. Interestingly, in cancer cells, this method detected approximately 700 G4 peaks per cell. When aggregated, the data summarized G4 profiles obtained from bulk

mapping results [139,140]. Currently, this technique has been adapted for single-nucleus analysis, allowing G4 mapping at single-cell resolution. Similar numbers found *in vitro* were confirmed, revealing high variability in G4 positions across cells, and demonstrating that only a small fraction of PQS fold into G4s *in vivo* [139].

Retrieving 3D structural information becomes crucial when performing G4-oriented drug discovery. In this context, *in vitro* studies are critical for understanding the structure, stability, and dynamics of G4s. Biophysical techniques, such as NMR spectroscopy, X-ray crystallography, and Cryo-EM, have played a crucial role in revealing G4s polymorphism and their response to environmental conditions, including pH, cations, and molecular crowding. X-ray crystallography provides high-resolution 3D structural data but requires well-ordered crystals, which are difficult to obtain for G4 molecules [141]. In contrast, NMR does not require crystallization, enabling the study of G4 structure and dynamics in solution under near-physiological conditions. This allows for the detection and monitoring of multiple G4 topologies over time or during ligand binding, making it a key tool in G4-drug discovery. Some NMR protocols can even be applied in living cells, as demonstrated by a ^{19}F-based NMR study conducted with human telomeric RNA G4s, which were identified as a key component in telomere machinery. By this, the formation of a stable telomeric RNA G4s in a cellular environment was proved [128,142].

In addition to X-ray crystallography and NMR spectroscopy, Circular dichroism (CD) spectroscopy is a more straightforward, less detailed method that distinguishes between the main G4 topologies [143]. CD is used to study the structure of nucleic acids by measuring their ultraviolet light absorption (200-330 nm). Although single nucleosides produce CD signals on their own, the main source of chirality comes from the secondary structure of nucleic acids, such as asymmetrical helical folding. CD is highly sensitive to changes in structural conformation, playing a crucial role in characterizing G4 topologies nowadays. CD spectroscopy interpretation mainly clearly distinguishes between parallel, antiparallel, and hybrid G4s, based on strand orientation and guanine conformations. The stacking orientation of guanine tetrads (head-to-tail vs. head-to-head/tail-to-tail) determines the CD spectral features (**Figure 23**). Advancements gained thanks to CD were a lot, as in the case of identifying intramolecular parallel quadruplexes in c-Myc gene promoter regions before other methods did [128,143–145]. In this context, Cryo-EM is a structural, molecular, and cellular biology technique that has experienced major advances in recent years. Technological advancements in image recording, as well as in processing

software, enable the creation of 3D reconstructions of macromolecular assemblies at near-atomic resolution, a feat previously achievable only through X-ray crystallography or NMR spectroscopy, thereby accelerating the structural resolution of G4 structures. Furthermore, additional techniques such as UV melting, Raman spectroscopy, and differential scanning calorimetry were employed to provide further insights into the G4 structure and stability [146–149]. Alternatively, when no experimental evidence can be obtained, predictive systems are used to gain information on the putative folding that sequences can achieve at specific conditions and programs, such as RNAFold (http://www.tbi.univie.ac.at/RNA), and AlphaFold4 is the case.

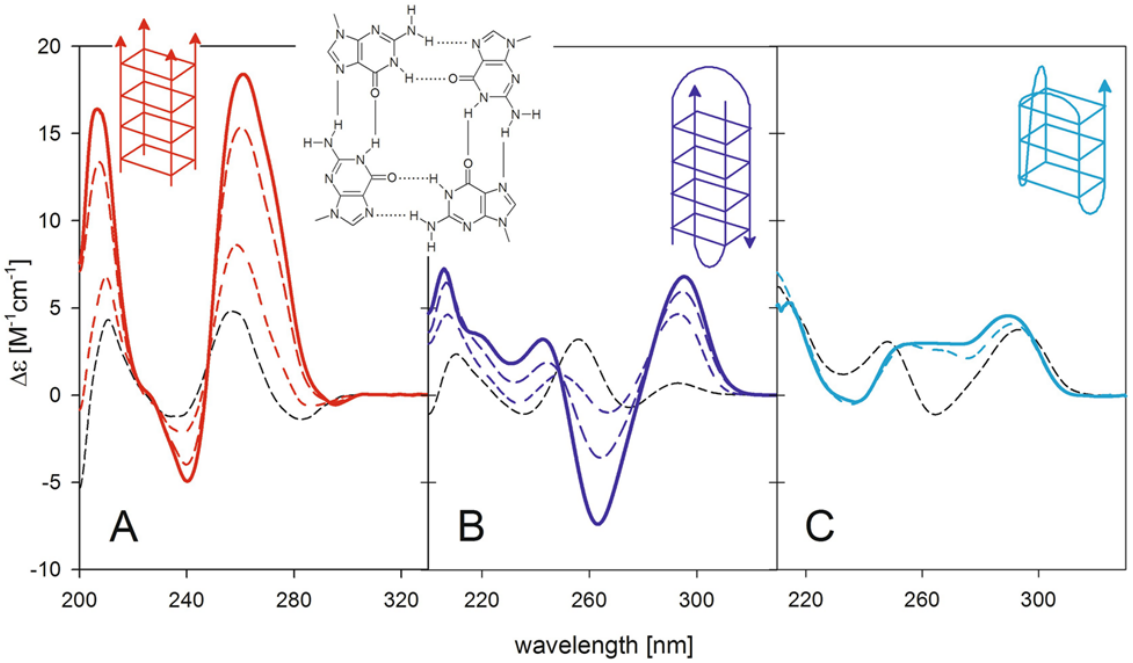

Figure 23. CD spectra of G4s with different topologies. Black dashed spectra were taken in 1 mM sodium phosphate buffer, pH 7. (a) Time-dependent formation of a parallel-stranded G4 in the presence of 16 mM K^+. (b) Na^+-induced formation of an antiparallel bimolecular G4 of d(G4T4G4). (c) K^+-induced formation of a (3 + 1) hybrid G4 structure of d($G_3(TTAG_3)_4$). The chemical structure of a G-tetrad and the schematic sketches of the respective quadruplex structures are inserted. Image from [150].

While *in vitro* and *in silico* studies supported discoveries about G4 structures and their localization at the genome level, understanding their biological relevance *in vivo* was challenging due to the lack of tools to detect them in living cells. In living cells, G4-related biological events, including the interplay with native chromatin context, maintenance of RNA and G4 binding proteins, result in the modulation of *in vivo* homeostasis. Over the years, a small number of antibodies and single-chain variable fragments (scFv), which combine antibody recognition regions into a single chain, have been developed to directly detect G4 in cells. Among these, the probes Sty3 and Sty49 were initially selected for high-

affinity binding to telomeric G4s in *Stylonychia lemnae* d($G_4(T_4G_4)_4$) [151]. Sty3 was found to bind specifically to parallel G4s with picomolar affinity. In contrast, Sty49 was found to bind to both parallel and antiparallel topologies, demonstrating that G4s are absent during telomere replication, likely to avoid polymerase stalling [152]. Subsequently, in human cancer and non-cancer cells, BG4 was used, allowing it to bind to various G4 conformations *in vitro* but preferring the parallel topology [153]. Several experiments reported that upon G4 stabilization induced by PDS treatment, an increase in the fluorescent signal was detected in nuclear *foci* but did not colocalize with telomeres. Furthermore, BG4 allowed the identification of RNA G4s in the cytoplasm [154]. Then, D1 is a less commonly used ScFv that, like BG4, primarily binds to parallel G4s and shows similar staining patterns in cells. To support this, Liu et al. demonstrated that co-staining with the telomere-binding protein (TRF2) confirmed that telomeric repeats in human SiHa cells mostly fold into parallel G4 structures [155]. Furthermore, other monoclonal antibodies, such as 1H6, were designed to recognize various G4 topologies; however, in this case, 1H6 displayed cross-reactivity with adjacent thymine residues, complicating its reliability in G4 Detection [156]. Despite some limitations compared to other probes, BG4 remains the most widely used probe due to its ability to bind multiple conformations, though it may favor specific folds. For this, BG4 has been adapted for advanced techniques such as ChIP-seq and CUT&Tag, revealing that only a subset of G4s observed *in vitro* are present *in vivo*, and that their distribution varies by cell type and state [157–159]. However, BG4's specificity is still under scrutiny, and its use in live cells is limited due to structural constraints [139,151].

G4 in transcriptional, post-transcriptional, epigenetic regulation, and in telomeres

The biological relevance of G4s led to an extensive study of their role at the transcriptional level since both *in silico* and *in vitro* evidence (as by BG4 ChIP-seq experiments) demonstrated the presence of PQS at the level of gene promoters of cancer and non-cancer cells [126,160,161].

Models initially used to explain G4s' role at the transcription level viewed G4s as physical barriers to RNA polymerase, thereby reducing transcription rates. This idea was supported by *in vitro* experiments and by observations done in HaCaT cells, which revealed that stabilization of G4s with small molecules induced gene downregulation [128,161–163].

Over time, research has demonstrated that G4s in transcription play a complex role as either inhibitors or promoters, depending on the biological context, such as when specific transcription factors bind to folded G4s [164]. BG4 ChIP-seq data further revealed that G4s are mainly found in nucleosome-free regions, which are accessible for initiating transcription and thereby suggesting that G4 can influence gene expression by altering chromatin structure [165]. Overall, G4s participate in different stages of transcription, and although several models have been suggested, more research is necessary to fully understand their impacts.

G4 functions are not related just to transcription since they are involved in RNA biology and translation of cells [122,166]. G4s were detected at the level of many different non-coding RNAs [167–169]. Furthermore, G4s are reported to affect mRNA maturation in alternative splicing, as shown in the case of p53 and hTERT transcripts due to the ability of G4s in recruiting several splicing factors, such as hnRNPH and hnRNPF [170,171]. Furthermore, in translation, RNA G4s are reported to block 43S ribosome recruitment and reduce translation efficiency unless unwound by factors like translation initiation factor eIF4A [172]. G4s were also reported to repress translation by causing ribosomes to stall at upstream open reading frames, as in the case of the G4 in the 5'-UTR of NRAS, which was shown to inhibit translation of the gene *in vitro* [173,174].

Then, other biological events related to G4 presence include transcription and replication, which occur while dsDNA is in its unwound state, favoring G4 folding and hindering DNA polymerase progression (as demonstrated by *in vitro* and *in vivo* studies) [175]. Several research groups have attempted to demonstrate that G4s can stall replication, thereby negatively impacting DNA replication. In this context, evidence has been found in various biological systems, including *Xenopus laevis, Saccharomyces cerevisiae*, human patient-derived cell lines, and *Caenorhabditis elegans* [176–178]. In all these systems, it has been proven that when cells fail to resolve these G4 structures, DNA deletions of varying sizes (from 60–300 nucleotides to large deletions of up to 80 kilobases) are present [176,178]. One of the compensation mechanisms adopted from cells is the use of helicases to unwind G4s and specialized DNA polymerases. For instance, REV1 and PrimPol, respectively, were shown to be recruited to avoid replication fork stalling and resume elongation downstream of the folded G4 [128,179]. Other pivotal roles of G4s in cell homeostasis involve the DNA damage response (DDR). DNA lesions threaten genome stability, and in this context, DDR is involved to mitigate these adverse effects and address

the potential issue [180]. DDR begins when sensor proteins recognize damage and activate complex signaling pathways involving key kinases like Ataxia-Telangiectasia Mutated protein (ATM), Rad3-related protein (ATR), and DNA-dependent protein kinase (DNA-PK), which are recruited to damage sites and trigger a cascade of phosphorylation events that activate repair proteins or halt the cell cycle [128]. One early marker of DNA damage is the phosphorylation of the histone variant H2A.X at Ser139, known as γH2A.X. This modification helps recruit repair proteins such as Breast Cancer Gene 1 (BRCA1), Tumor Suppressor p53-binding protein 1 (TP53BP1), and Mediator of DNA Damage Checkpoint 1 (MDC1), concentrating them at the damage site and promoting efficient repair. DDR also activates cell cycle checkpoints through Checkpoint Kinase 1 and 2 (Chk1 and Chk2, respectively), which prevent progression by targeting Cdc25A phosphatase. Additionally, ATM and ATR stabilize the tumor suppressor p53, which promotes cell cycle arrest or apoptosis if the damage is too severe [181,182].

This system is robust and includes overlapping pathways, so even if one fails, others can compensate for it. However, persistent G4 structures that block polymerases can increase the burden on DDR, leading to chromosome fragility [136]. Furthermore, G4s are reported to interfere with repair pathway choice by blocking DNA end processing, affecting the balance between homologous recombination and non-homologous end (NHE) joining [183].

Eukaryotic chromosomes are linear and have a 3’ single-stranded overhang, which creates challenges for end replication and protection. These problems are managed by specific DNA sequences and structures at the ends of chromosomes, along with nucleoprotein complexes called telomeres. Telomeres are crucial for preventing genomic instability and supporting the complex processes that maintain the eukaryotic genome [184]. Human telomeric DNA is composed of repeated TTAGGG repeats and terminates with a single-stranded guanine-rich overhang consisting of 100-200 nucleotides. These shorten with each cell division and play a crucial role in aging and cancer-related events, as, depending on their "capped" or "uncapped" state, they are responsible for regulating cell viability [185–187]. Telomeric DNA was demonstrated to form G4s, which, due to their relevant role, are potential targets for drug discovery [188]. Although telomeric DNA was previously thought to be non-transcribed into RNA, it is now known to produce telomeric RNA in cells, which varies in length and may help protect chromosome ends, thereby adding new insight into how telomeres influence aging and cancer [189,190]. Recent

studies performed with chemical probes demonstrated the presence of G4 structures formed by DNA:RNA hybrids, both *in vitro* and in human cells, which are believed to protect the ends of chromosomes (**Figure 24**) [191–193].

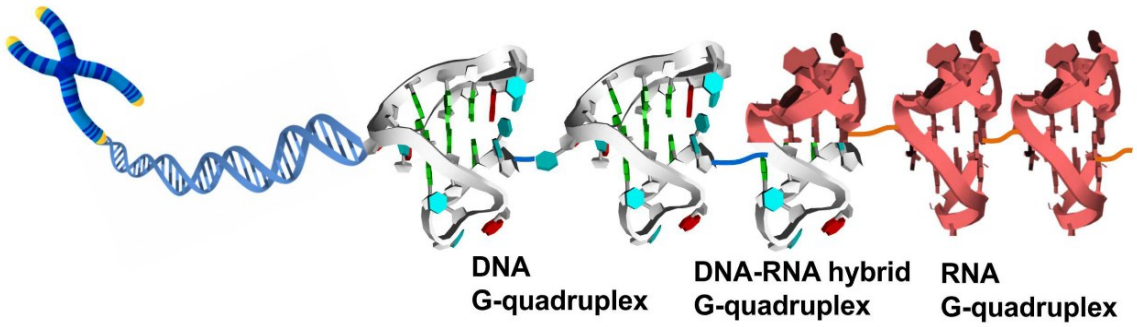

Figure 24. Superhelix structure formed at the ends of chromosomes from telomeric DNA G4s, DNA:RNA G4s, and RNA G4s. Adapted from [186].

In addition to these basic structural features, modern eukaryotic cells utilize complex mechanisms to safeguard, maintain, and replicate telomeres. Key components in this process include telomerase, the shelterin complex (including also the Telomeric repeat-binding factor 2, TRF2), the CST (CTC1-STN1-TEN1) complex, and telomeric repeat-containing RNA (TERRA) [194].

Telomerase helps solve the end-replication problem in chromosomes by extending the 3'-end of a chromosome lagging strand, thus preventing the loss of genetic information [195]. Then, telomere protection is also supported by protein complexes, such as Shelterin and CST complex, which bind to telomeric DNA and prevent it from being mistaken for DNA damage [196,197]. If unprotected, chromosome ends could go into misleading recombination, repair, or fusion events in which proteins such as TRF2, which promotes t-loop formation, and the protection of telomerase 1 (POT1), protect the single-stranded overhang [198].

The first direct evidence of G4 formation at telomeres in living cells came from studies on ciliated protozoa, which have two nuclei: a macronucleus and a micronucleus. In hypotrichous ciliates, the macronuclear genome is fragmented into numerous small pieces, each ending in a telomere, making them ideal for telomere research. A single-chain antibody created against a G4 structure from the telomeric sequence of *Stylonychia lemnae* specifically recognized the macronucleus, but not the replication band, suggesting that G4s were resolved during DNA replication and telomere extension to allow telomerase access.

In related ciliates, the β subunit of the telomere-binding protein TEBP was shown to promote G4 formation *in vitro,* and by removing this subunit in *Stylonychia* cells, the antibody signal for G4s was absent, confirming its role in G4 formation *in vivo*. During the S phase, the β subunit appeared phosphorylated, recruiting telomerase and a G4-unwinding helicase to resolve G4s at telomeres, leading to one of the most detailed descriptions of telomeric G4 dynamics in living cells [199,200].

DNA G4s in human telomeres

Human telomeres are composed of repeated 5'-TTAGGG-3' sequences, and they can fold in several G4 structures, which differ based on the DNA sequence, loop types, the nature of present cations, the conformation of guanine residues (syn/anti), and the orientation of the G-tetrads [201]. All the previously mentioned differences result in the presence of various G4 topologies, including antiparallel, hybrid, and parallel, making it necessary to thoroughly understand these structures to target them with novel drugs. For instance, Tel22 d[AGGG(TTAGGG)$_3$] forms an antiparallel G4 in the presence of NaCl, but in KCl this topology shifts to parallel [202].

The exact topology of telomeric DNA G4s in living human cells remains unclear. To address this issue, Bao et al. used in-cell ^{19}F NMR spectroscopy, which is ideal due to its clear signals and sensitivity [203]. Furthermore, by tagging the 5'-end of telomeric DNA with a 3,5-bis(trifluoromethyl)phenyl moiety and by injecting the mixture into HeLa cells, hybrid-1 and hybrid-2 G4s were found [204]. To confirm the evidence, similar studies were conducted in *Xenopus laevis* oocytes, highlighting the formation of hybrid-2 G4s [205]. To support research on telomeric DNA G4s, fluorescent probes such as epiberberine have been developed to detect G4s in living cells by emitting light upon G4 binding [206].

Considering this, numerous small molecules targeting G4s are under investigation as potential treatments for cancer and other G4-related conditions. For instance, phenyl-ethenyl-quinoline (PEQ) was developed and was found to selectively bind in a 2:1 stoichiometry to the G4 structure in the guanine-rich NHE III1 of the Myc oncogene, thereby proposing itself as a possible drug for cancer therapy (**Figure 25**) [207–209].

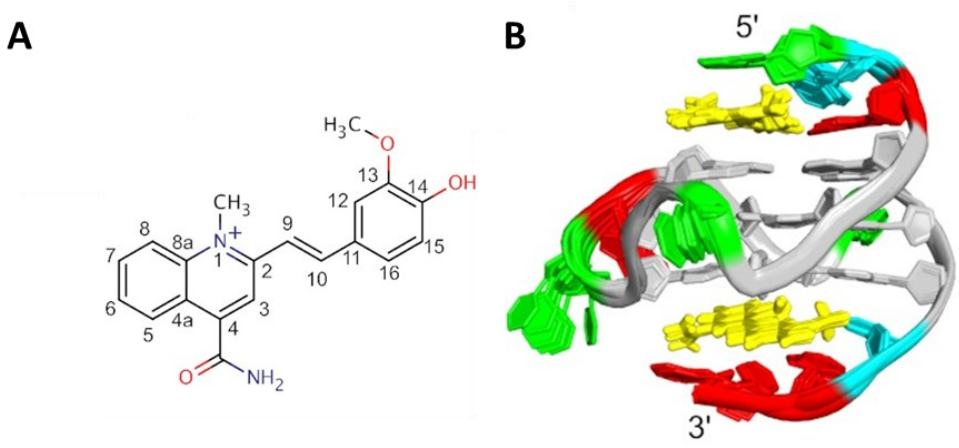

Figure 25. A) Structure of the quinoline derivative PEQ. B) Superposition of the 10 lowest energy structures. Adapted from [209].

RNA G4s in human telomeres

Telomeric DNA is transcribed into telomeric RNA, which can form G4 structures with critical biological functions [210]. Unlike DNA G4s, RNA counterparts typically adopt a stable parallel topology due to the 2'-OH in RNA. This evidence was further demonstrated by Xu et al., who, using ^{1}H-NMR, reported a Tel12 r(UAGGGUUAGGGU) sequence that folded into the same parallel topology in both K^+ and Na^+ solutions [211–214]. Furthermore, recently, other topologies have been discovered, such as the RNA Tel22 G4, which, in Na^+ solution, was found to adopt an antiparallel topology [215].

The formation of telomeric RNA G4s has been shown to play a vital role in regulating mRNA translation, maintaining telomere homeostasis, influencing mRNA splicing, and various other processes, thereby also impacting pathological cellular states [216,217]. For instance, in viruses with RNA-based genomes, evidence supported RNA G4's role in the control of viral replication and transcription, as in the case of SARS-CoV-2, which possesses G4s able to regulate open reading frame regions [218]. The investigation of telomeric RNA G4s in cells was conducted by developing pyrene fluorescent probes incorporated into both the 5′- and 3′-ends of r(GGGUUAGGG), which lighted up when bound to these structures that fold into G4s, thus enabling real-time imaging (**Figure 26**) [219]. Furthermore, ^{19}F NMR and specialized probes (e.g., QUMA-1 and PyroTASQ) are also applied to detect and analyze these structures in living cells of telomeric RNA G4s [220–222].

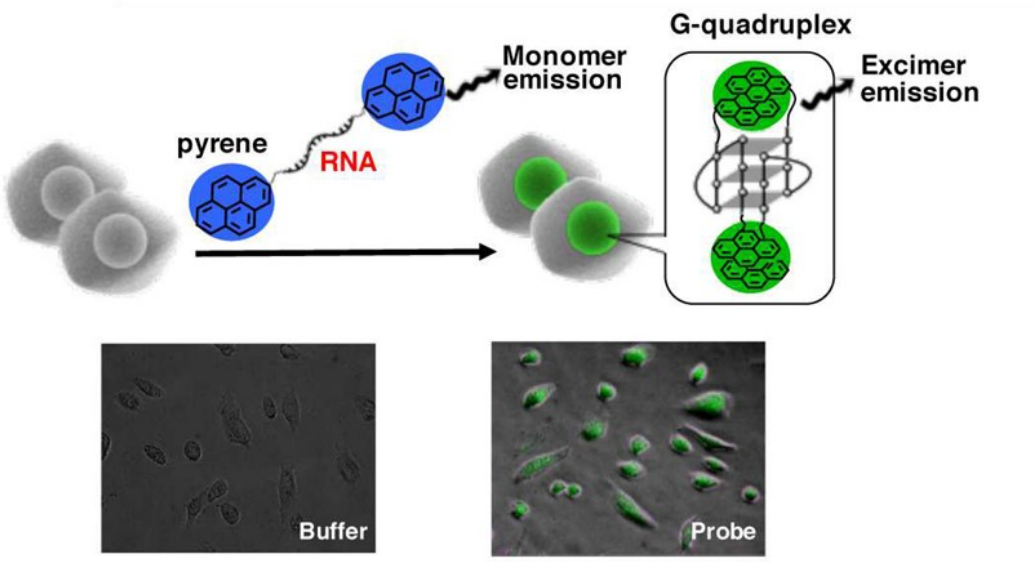

Figure 26. A pyrene probe used to detect in-cell formation of G4s from telomeric RNA r(GGGUUAGGG). Fluorescence microscopy images of living cells with or without the probe are shown below. Adapted from [186].

In human cells, TERRA is rich in UUAGGG repeats and forms stable, parallel G4s that are reported to interact strongly with telomere-associated proteins, such as TRF2 and POT1, which are essential for telomere integrity [223,224]. Although TERRA's specific molecular roles are still not fully understood, ongoing research is uncovering its increasing importance in maintaining genome stability, leading to the development of G4-stabilizing compounds as potential cancer treatments.

2.2 Therapeutic relevance in targeting G4s

As demonstrated in earlier chapters, G4 plays a significant but still incompletely understood role in cell biology. Since G4s are mainly formed in regions of the genome rich in guanines, the case of the expansion of GGGGCC repeats in the C9ORF72 gene, which is the most common genetic cause of Amyotrophic Lateral Sclerosis (ALS) and Frontotemporal Dementia, is particularly notable [225]. While healthy individuals have fewer than 23 repeats, affected patients can have hundreds or even thousands, which form stable G4 structures in RNA. In this context, it has been shown that G4 levels linked to ALS in C9ORF72 mRNA can cause the formation of cytosolic membrane-less organelles, both *in vitro* and inside cells. The increased buildup of RNA granules was proposed to trap essential proteins and disrupt RNA metabolism, leading to neurodegeneration. This idea is supported by observations of hnRNP H, which was found to colocalize with G4 structures

and form insoluble aggregates in C9-ALS patient cells and brain tissues, thereby causing cell dysfunction and death, and indicating another pathway for disease development [171,226].

Another relevant role in pathogenesis from G4 is observed in the case of Bloom syndrome, a rare genetic disorder caused by mutations in the BLM gene, which encodes a helicase that unwinds G4 Structures. Symptoms include growth defects, an increased risk of cancer, and immune system problems. Although BLM is involved in various DNA repair functions, its absence makes G4-rich regions more difficult to replicate, leading to genome instability. Overall, G4s play a key role in diseases such as ALS and Bloom syndrome, as they interfere with RNA processing and DNA replication. Proper regulation of these structures is vital for preserving cellular and genomic integrity, and they are being studied more extensively as potential therapeutic targets [227]. Most research on G4s as drug targets has concentrated on cancer, as genomic instability is a key characteristic of this disease, allowing tumors to evolve and acquire traits such as uncontrolled growth, resistance to cell death, and the ability to invade tissues [228]. Cancer cells often exhibit defective DNA repair and disrupted cell cycle control, and several studies indicated that G4 levels tend to be higher in cancer cells than in normal cells. It is still uncertain whether G4s are a cause of cancer or a consequence. Still, they are viewed as promising targets for therapy because G4s can inhibit telomerase, an enzyme that cancer cells use to maintain telomeres and achieve immortality. Moreover, G4s can induce replication stress and DNA damage, especially when the cell's ability to resolve G4 structures is impaired.

Furthermore, G4s gain a therapeutic relevance since they are also found in the promoter regions of several genes (i.e., innate immune adaptor MYD88 [229], insulin [230], vascular endothelial growth factor [231], hypoxia inducible factor 1a [232], and oncogenes (i.e., c-myc [233], c-kit [234], KRAS [235], bcl-2 [236]) where they play a role in regulating gene expression. As a result, numerous small molecules have been developed to bind and stabilize or destabilize G4s. Some of these compounds have shown success in reducing telomerase activity, lowering oncogene expression, inducing DNA damage, and inducing apoptosis in *in vitro* cancer cell lines. However, only a few of these drugs have advanced to clinical trials, mostly stopping at Phase II due to issues such as poor solubility, limited potency, and side effects. In this context, ligands such as BRACO-19, RHPS4, quarfloxin, and APTO-253 were withdrawn from clinical evaluations due to safety concerns, tolerability issues, lack of efficacy, and toxicity [237].

One of the ligands that reached Phase II was quarfloxin (CX-3543), which targets G4s in ribosomal DNA and disrupts nucleolin [238]. Another compound, CX-5461, is in advanced Phase I trials for BRCA1/2-deficient tumors and has shown promise when combined with UBE2N inhibition, increasing cancer cell toxicity (NCT04890613).

Then, the compound SOP1812 (QN-302) entered clinical trials for the treatment of patients with advanced or metastatic solid tumors, including pancreatic ductal adenocarcinoma, sarcomas, prostate cancer, and gastrointestinal stromal tumors (NCT06086522) [239]. Due to the unique properties and essential locations of RNA G4s, selective RNA G4 Ligands are under development, often starting with DNA G4 ligands to improve their effectiveness.

Targeting G-quadruplex with small molecules

Growing evidence suggests that DNA and RNA G4s play crucial roles in the pathogenesis of cancer and neurological disorders, prompting exploration of G4-targeting ligands as potential therapeutic agents. Beyond therapy, these ligands are also being explored for diagnostic applications in biosensing and bioimaging [240,241].

Due to the structural features of G4s, their binders typically include a large heteroaromatic group able to establish π-π interactions with the tetrads, along with charged side-chain substituents designed to bind with negatively charged phosphate groups present in the loops and grooves through hydrogen bonds or electrostatic interactions [242]. Then, another important requirement for G4-ligands is to prevent binding to the canonical counterpart. To overcome this issue, often, the modification of chemical groups is followed by a worsening of drug-like properties, leading to problems with solubility, aggregation, and poor *in vivo* performance. Most of G4-ligands do not meet Lipinski's Rule of Five, which guides drug-likeness, although it is not an absolute requirement [243]. Then, the binding constant of the G4/ligand complex can be used to define a possible G4-ligand, and in this context, values in the order of 10^6 M^{-1} are preferred when evaluating putative G4-binders. Examples of G4 binders include telomestatin, naphthalene diimides (NDIs), berberine, and TMPyP4. These binders exhibit selectivity for G4 over duplex DNA and can influence the topology of G4, leading to conformational switches.

Despite many of the designed G4-ligands performing well in the initial phases of the drug discovery process, thereby achieving *in vitro* G4 stabilization, *in vivo* efficacy is often limited due to several factors related to the complexity of the cellular environment,

including protein interactions, epigenetic modifications in gene promoters, and cellular context [244]. Since CADD is involved in identifying G4 Ligands, considerable effort has been made to create repositories of G4 Ligands. In this context, the G4 Ligands Database (G4LDB 3.0, http://www.g4ldb.com/) has been implemented and became a valid starting point [245,246].

DNA G4s Ligands

Because telomeric ends and oncogene promoters contain G-rich sequences that form G4s, they have become attractive targets for cancer therapy. As a result, many DNA G4-targeting ligands have been developed to interfere with telomerase activity and disrupt the growth of cancer cells [247].

In this context, the 3,6,9-trisubstituted acridine derivative BRACO-19, which is one of the earliest investigated G4 ligands, was designed to inhibit telomerase in the elongation of single-stranded telomere overhang. BRACO-19 demonstrated the ability to induce selective cell death by inhibiting telomerase in A2780 human ovarian carcinoma cells (IC_{50} of 0.06 μM) and in human uterine carcinoma UXF1138L cells (IC_{50} of 2.5 μM).

Although BRACO-19 is one of the most potent cell-free inhibitors of human telomerase, with high affinity for G4s, druglikeness-related challenges have become evident. Its pharmacological profile is suboptimal, with a half-life of 1.1 hours, limited bioavailability after 1 hour, poor membrane permeability, and a narrow therapeutic window, all of which hinder further development. In support of *in vitro* evidence, molecular simulations examining the BRACO-19 binding mode showed that the ligand interacts differently based on the G4 topology: end-stacking occurs in parallel G4s, bottom-stacking in antiparallel G4s, and top-stacking in hybrid structures. Its limited selectivity might stem from comparable groove-binding interactions with both G4 and dsDNA [248–251]. Then, AS1410, a modified version of BRACO-19, was designed to enhance its properties by adding a difluorobenzylamino group. Compared to BRACO-19, AS1410 has a higher hydrophobicity, enhanced binding affinity, and a longer plasma half-life of 2 hours, and showed promising results when combined with cisplatin, significantly reducing tumor size in the A549 lung cancer (LC) xenograft model [252]. Nonetheless, BRACO-19 and AS1410 were bioactive and efficacious; however, due to their low maximum tolerated doses (2 mg/kg), the development of AS1410 was discontinued (**Figure 27**).

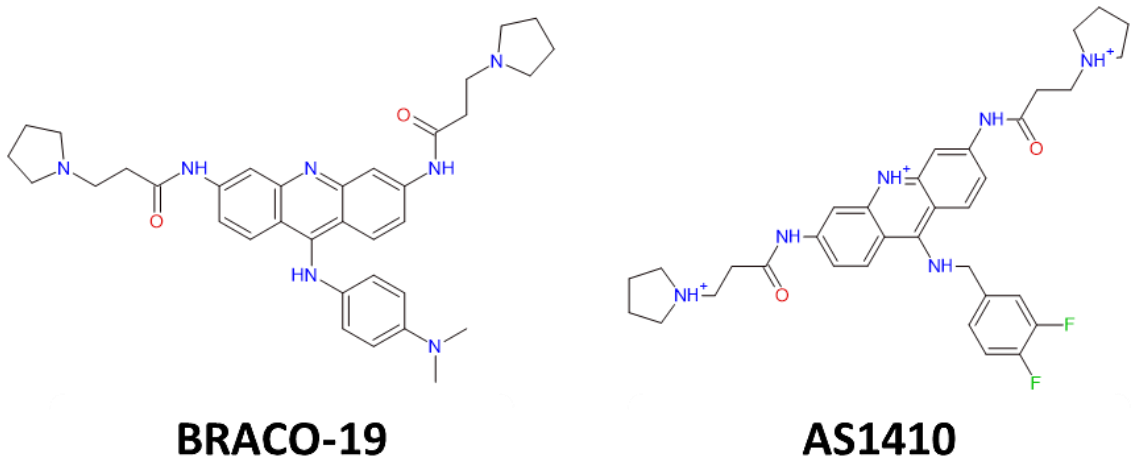

Figure 27. Chemical structure of BRACO-19 and AS1410 compounds.

To improve π-π stacking interactions, acridine compounds were modified into tetracyclic or pentacyclic structures. In this context, RHPS4, which is a pentacyclic acridinium derivative, was reported to inhibit telomerase and induce DNA damage (IC_{50} of 0.33 μM) (**Figure 28**). This compound caused growth arrest and telomere shortening in MCF-7 breast cancer cells at non-toxic doses, showing strong antitumor effects in xenograft models, especially in CG5 breast tumors, where it achieved up to 80% inhibition and 40% cure rates. Furthermore, RHPS4's anticancer activity is linked to telomere dysfunction and DNA damage; however, despite its promising profile, it exhibits severe off-target cardiotoxicity due to hERG channel inhibition and interactions with β2-adrenergic and muscarinic receptors. Modified derivatives reduced hERG activity but still showed strong off-target effects, preventing clinical development [253,254].

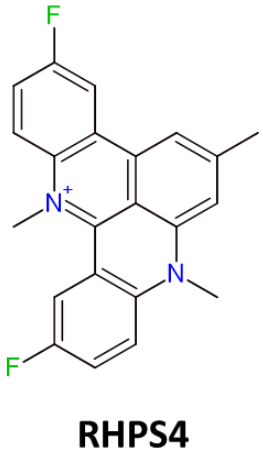

Figure 28. Chemical structure of compound RHPS4.

Then, the class of quinazolone and quinolone compounds has been exploited for identifying new G4-binders. Several indenoisoquinoline derivatives, such as indotecan, indimitecan, and LMP744, have entered Phase I clinical trials for the treatment of solid tumors and lymphomas (**Figure 29**) [255]. These compounds inhibit topoisomerase I and induce DNA damage by binding to the c-MYC G4, showing moderate stabilization.

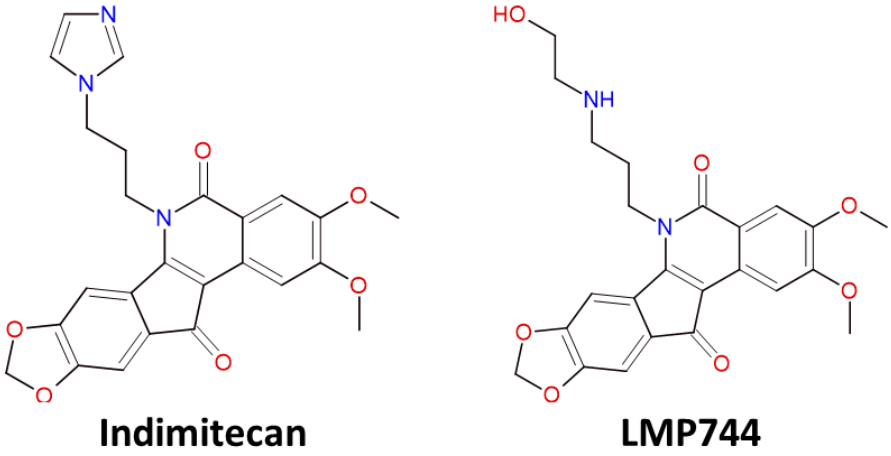

Figure 29. Chemical structure of indimitecan and LMP744.

Quarfloxin, a derivative of fluoroquinolone QQ58, was the first G4 stabilizer to enter clinical trials (NCT00955786). Its design was aimed at selectively binding G4 structures and avoiding topoisomerase II toxicity. Here, the compound showed antitumor activity *in vivo* against mouse breast xenograft models and was well-tolerated. Following investigations, quarfloxin (CX-3543) was shown to disrupt nucleolin binding to ribosomal DNA G4s, thereby inhibiting RNA polymerase I and inducing apoptosis in cancer cells (**Figure 30, left**). After entering Phase II (NCT00485966), where it displayed promising results, the compound was discontinued due to poor bioavailability and unusual accumulation in plasma.

To improve drug-like properties, a quarfloxin derivative, CX-5461 (Pidnarulex), was developed (**Figure 30, right**). It was reported to effectively stabilize multiple G4s (present in c-Myc, c-Kit1) and to induce G4-mediated DNA damage *in vivo* [256]. Then, CX-5461 showed potent antitumor activity *in vivo* in pancreatic xenograft models and melanoma A375 cellular lines, through the inhibition of RNA polymerase I [257].

Once entered in Phase I (NCT02719977) clinical trials, the compound demonstrated synthetic lethality in HR-deficient tumors, but it also caused extensive mutagenesis, raising concerns about long-term effects. Currently, CX-5461 is undergoing Phase Ib trials

(NCT04890613) to determine a safe dosing regimen for future studies in patients with solid tumors and BRCA1/2, PALB2, or HRD mutations, paving the way for Phase II trials.

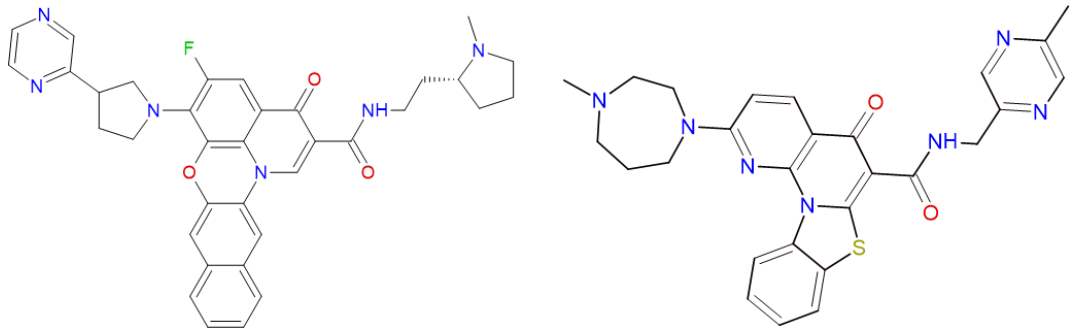

Figure 30. Chemical structure of Quarfloxin and Pidnarulex compounds.

To achieve binding and selectivity, NDIs are currently used because their structures enable selective, potent G4 binding by modifying side chains and aromatic cores. BMSG-SH-3, a derivative of a tetra-substituted NDI, demonstrated strong G4 stabilization in the G4 formed in the human telomere and in the promoter of HSP90, resulting in reduced tumor volume of the murine MIA-Pa-Ca2 xenograft model and a 50% decrease in telomerase activity in pancreatic cancer models (**Figure 31**). However, its study was discontinued due to poor pharmacological properties stemming from its high molecular weight and four positive charges, which led to violations of Lipinski's Rule of Five [258,259]. To enhance its properties, BMSG-SH-3 was modified by adding two side chains with N-methyl-piperazine end groups and two side chains with morpholine end groups. This modification resulted in a lead compound in this series. MM41 was found to strongly bind to G4 structures in both telomeric ends and oncogene promoters of HSP90, BCL2, and KRAS (IC_{50} = 10 nM), demonstrating potent anticancer effects in pancreatic ductal adenocarcinoma cells (**Figure 31**). It demonstrated strong anticancer activity, including an 80% reduction in tumor size and long-term suppression in pancreatic models. Its structure enabled better interactions with G4 grooves and improved drug-like properties. These findings were also supported by structural studies, which led to the generation of the crystal structure within the intramolecular human telomeric parallel (PDB ID: 3UYH). From this, computational studies were done and revealed that the morpholine ring favored the interactions with G4 grooves and water-mediated G4 side-chain hydrogen-bonding, which showed a groove-binding mode with G4s [260,261].

Due to the relevance that substitutions with morpholino moieties demonstrated, CM03, which had two side chains ending in morpholino groups, and a third side chain terminating in a protonated pyrrolidine group, was synthesized (**Figure 31**). CM03 showed lower strength in G4 stabilization compared to MM41. Still, it downregulated more G4-related genes (i.e., *KRAS*, *TP53*, *SMAD4*, and *CDKN2A*). Furthermore, it was proven to cause DNA damage, leading to strong antiproliferative effects in the MIA PaCa-2 xenograft model and improved survival in the KPC mouse model, outperforming standard treatments such as gemcitabine [261,262].

Unlike earlier reported NDIs, QN-302, an even more optimized tetra-substituted NDI, showed the strongest binding affinity for hTERT G4 and HuTel21 G4 (K_d of 4.9 and 28.4 nM, respectively). It also demonstrated greater anticancer potency in pancreatic cancer cell lines, with a half-growth inhibitory concentration of 1.5 nM, particularly against pancreatic cancer cells. QN-302 has progressed to Phase Ia clinical trials (NCT06086522) for patients with advanced and metastatic solid tumors, demonstrating good bioavailability and broad pathway suppression [263]. Structures of the previously mentioned NDIs are reported below in **Figure 31**.

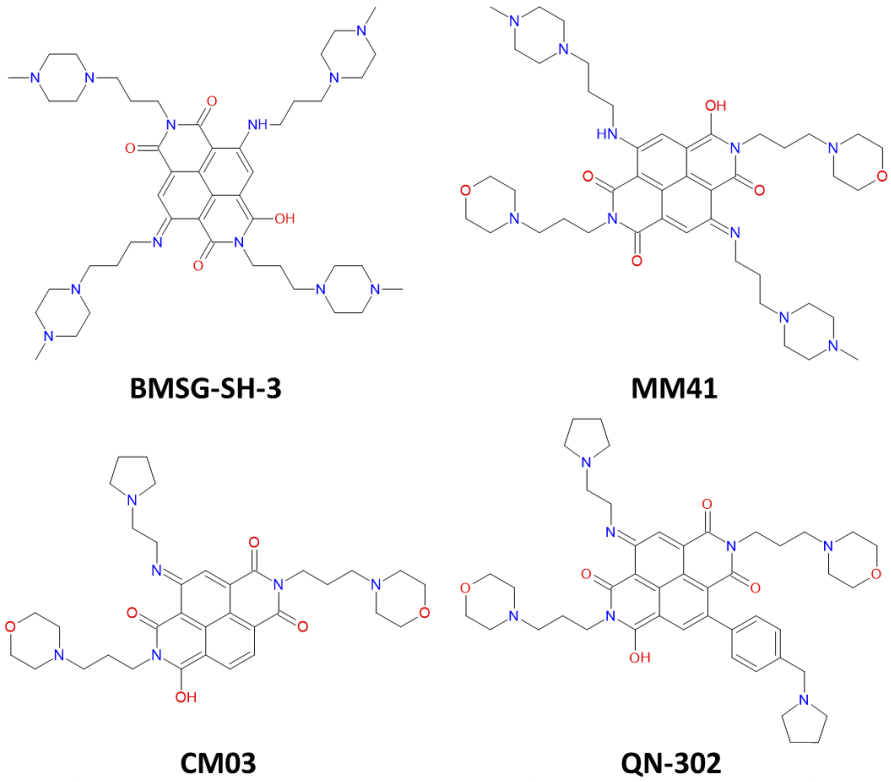

Figure 31. Chemical structures of BMSG-SH-3, MM41, CM03, and QN-302 compounds.

RNA G4 ligands

While DNA G4s have been widely studied, interest in RNA G4s has increased more recently. The first RNA G4 was discovered at the 3′ end of 5S rRNA in *E. coli*, followed by findings in the 3′-UTR of insulin-like growth factor II (IGF II) mRNA and other mRNAs such as NRAS, Bcl2, VEGF, and ADAM10, as well as in non-coding RNAs like telomeric RNA [264–267].

Although many RNA G4s have been identified and studied, their interactions with G4 binders remain largely unexplored, despite their presence in key genes and regulatory regions [268]. Interestingly, while most research focuses on stabilizing G4s, some recent studies show that certain ligands, such as TMPyP4, are reported to destabilize RNA G4s [269,270]. However, the exact mechanism by which TMPyP4 causes this unfolding remains unknown. Furthermore, designing ligands that specifically recognize and bind RNA G4s has proven challenging over the years, and most ligands initially developed for DNA G4s have been tested on RNA G4s (**Figure 32**).

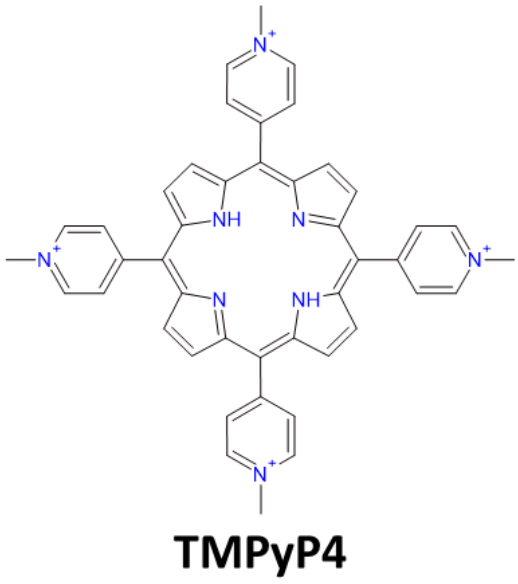

Figure 32. Chemical structure of the TMPyP4 compound.

Development of RNA G4-ligands started with the class of Benzothiazole and benzopyridine, in which thioflavin T (ThT), which was initially used as a fluorescent probe to detect amyloid fibrils, was later found to emit stronger fluorescence when bound to RNA G4s, mainly due to stacking interactions with the top tetrad of the structure. To enable real-time monitoring of RNA G4 folding during transcription in cells, researchers developed ThT-HE, a modified version of ThT with a hydroxyethyl group instead of the methyl group

on the benzothiazole ring [271]. Building on this, a new probe called ThT-NE was developed with improved structural selectivity and cell permeability. ThT-NE successfully targeted and visualized RNA G4s in the hepatitis C virus genome within live cells, enabling real-time tracking of HCV RNA localization and viral spread. This demonstrates its potential for studying RNA G4s in infectious diseases. The Chemical structures of the mentioned compounds are reported in **Figure 33**.

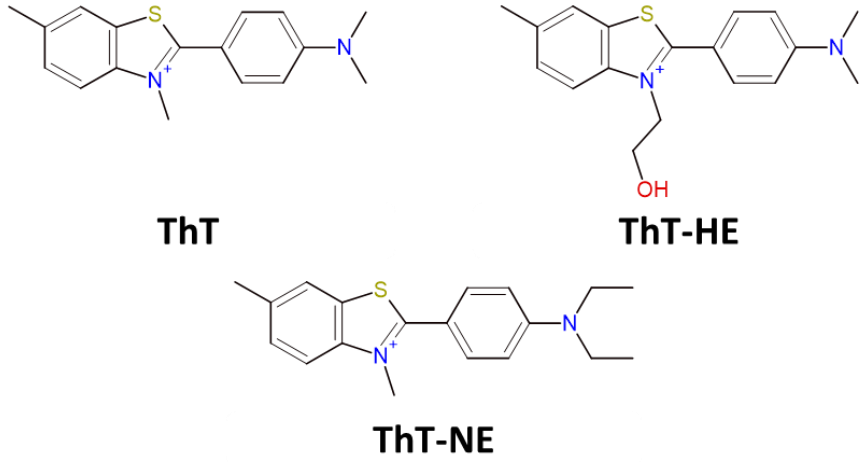

Figure 33. Chemical structure of ThT, ThT-HE, and ThT-NE compounds.

Isaindigotone, a natural alkaloid found in the root of *Isatis indigotica*, and its chemical structure make it suitable for designing ligands that recognize RNA G4s. Researchers developed a fluorescent probe called ISCH-oa1 based on isaindigotone. By attaching a DNA sequence to it, they created ISCH-nras1, which specifically binds to the G4 in the mRNA of NRAS [272].

Another natural alkaloid, Sanguinarine, extracted from *Sanguinaria canadensis*, is known for its RNA intercalating ability and anticancer properties [273,274]. Chemical structures of isaindigotone and sanguinarine are shown in **Figure 34**.

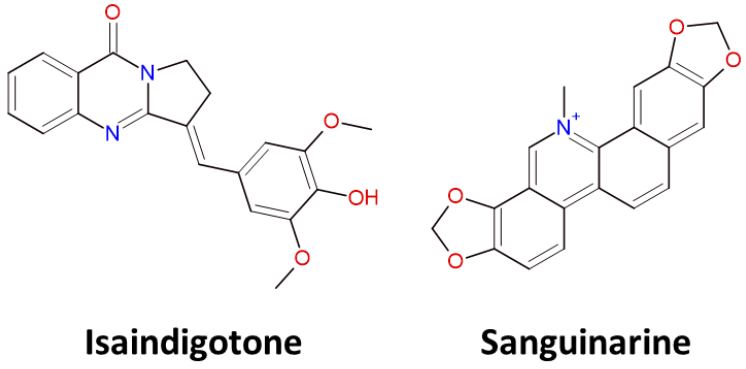

Figure 34. Chemical structure of isaindigotone and sanguinarine compounds.

Recent studies suggest that RNA G4s in the 5′-UTRs of mRNAs may regulate gene expression similarly to DNA G4s in promoters [275]. In recent years, bisquinolinium compounds such as Phen-DC3, Phen-DC6, and 360A have been developed that bind to G4s present in the mRNA of TRF2 through π–π stacking with external tetrads (**Figure 35**) [276].

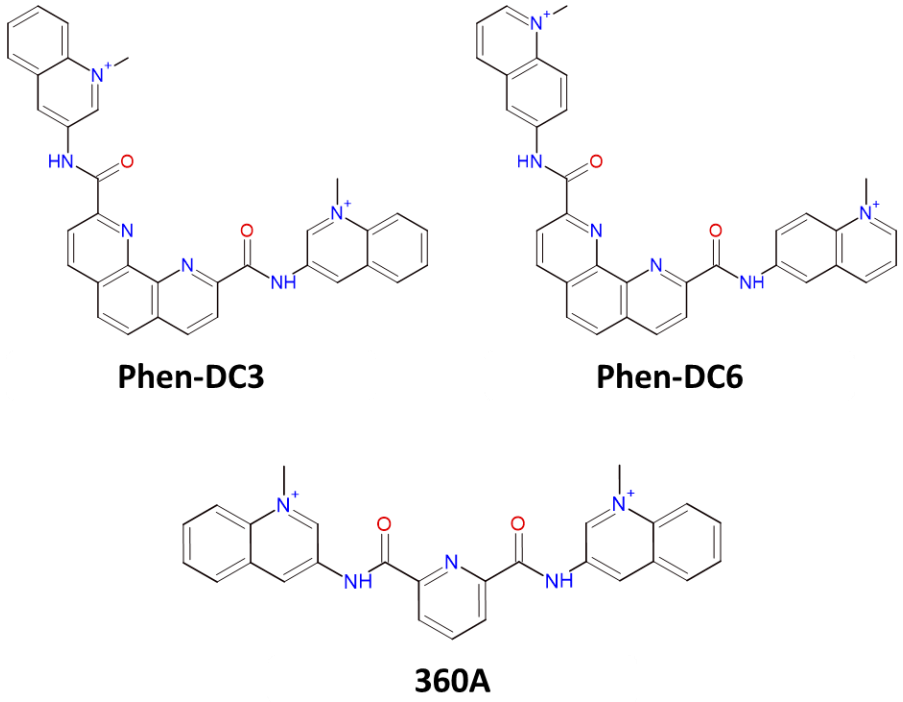

Figure 35. Chemical structure of Phen-DC3, Phen-DC6, and 360A compounds.

Furthermore, TERRA is reported to actively participate in the mechanisms regulating telomere maintenance and chromosome end protection. In this context, the RGB-1 ligand was demonstrated to interact with TERRA and G4s in the NRAS mRNA, possibly through hydrogen bonding with the RNA's 2′-OH group [277]. Then, Carboxy-PDS, characterized by Rocca et al., was shown to possess strong specificity for TERRA G4s and significantly stabilizes them via hydrogen bonds, even in the presence of competing DNA G4s; thus highlighting a possible way to develop RNA G4-selective compounds (**Figure 36**) [278].

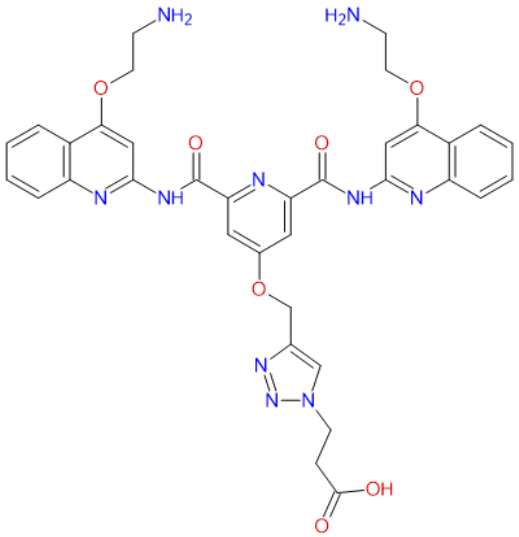

Carboxy-PDS

Figure 36. Chemical structure of the carboxy-PDS compound.

Furthermore, quindoline derivatives have also shown effective interaction with G4s, and a series of novel p-(methylthio)styryl substituted quindoline (MSQ) derivatives by incorporating the p-(methylthio)styryl group as a side chain were developed [279,280]. The MSQ derivative, MSQ-10, stabilized the G4 in the NRAS RNA, thereby suppressing its translation and reducing cancer cell growth.

2.3 Methods to study G-quadruplexes and their interaction with ligands

Recently, advances in G4 ligand design have coincided with the development of methods to detect G4-ligand complexes. Biophysical techniques are usually the top choice for examining physical interactions. These methods vary from simple to complex, but all deliver essential insights into how G4s and their ligands interact. Many approaches developed initially for dsDNA interactions have been adapted to examine the contact points between G4s and their binders. Biophysical techniques are the primary tools for studying physical interactions and are generally classified into three categories: structure-based methods, affinity and apparent affinity methods, and high-throughput techniques. Methods like CD, NMR, X-ray crystallography, surface plasmon resonance, and MS are used in different ways, each offering unique benefits and limitations. Often, multiple techniques are needed to fully understand G4/ligand interactions [281].

ESI-MS for the study of G-quadruplex/ligand interaction

Native MS is an analytical mass spectrometry technique in which both the sample solution and the spectrometer conditions are non-denaturing during the ionization and vaporization phases. This soft method ensures that the integrity of the investigated macromolecule is not compromised. ESI-MS has become widely used for analyzing various biomolecules, including peptides, proteins, and nucleic acids. In this context, the earliest reports on detecting intact dsDNA by ESI-MS date back to the early days of native mass spectrometry [282].

Native ESI-MS is a technique used to study G4 structures while maintaining their native conformation, which is stabilized by monovalent cations such as K^+ and NH_4^+. To achieve this, the solutions' samples must be prepared with an appropriate ionic strength, typically ranging between 100 and 150 mM [283]. However, ESI-MS has limited tolerance for salts due to the counterion effect on nucleic acid molecules, especially Na^+, which leads to the formation of multiple adduct species that are overcome by using ammonium acetate (NH_4OAc) since it reduces adduct formation and supports G4 folding similarly to K^+ [284].

Usually, nucleic acids in MS are analyzed under negative ion mode, where the proton transfer from NH_4^+ to phosphate groups neutralizes many phosphates, leaving only a fraction of negatively charged residues. This process explains the typical charge states observed for the G4 structure, which is typically for a 23-mer between -4 and -7. Additionally, pH plays a crucial role in the formation and stability of G4, as acidic

conditions (pH 4) favor G4 formation while alkaline conditions promote the presence of random-coil DNA structures [285].

In analytical chemistry, instrumental setup and conditions significantly affect experimental outcomes. For G4-ligand interaction analysis using ESI-MS, the key factor is achieving efficient droplet formation and desolvation without applying excessive energy, which could disrupt noncovalent interactions or cause fragmentation. To preserve G4 structures, the temperature of the source and capillaries, as well as the acceleration voltages, should be kept as low as possible. Compared to traditional spectroscopic methods for studying ligand–G4 interactions, ESI-MS is a highly sensitive technique and requires low sample volumes. Typically, a 20-100 μL sample with a nucleic acid concentration of 1–10 μM is sufficient for routine experiments; however, this may vary depending on the injection system. Information about the binding affinity of a ligand and equilibrium binding constants can be directly obtained from the relative intensities of peaks corresponding to different species in the m/z spectrum. The results are generally semiquantitative and can be expressed as the amount of complexed G4, based on the ratio of complexed to free G4, or by monitoring the decrease in the free nucleic acid signal compared to an internal standard [286,287].

The concentration of bound ligand can also be calculated from the relative peak intensities that are used to calculate macroscopic equilibrium binding constants, where K_d is defined as [DNA][ligand]/[1:1 complex], considering the total amount of the 1:1 complex without regard to the specific binding site. It is assumed that both free and bound nucleic acid have the same response upon ionization, so peak intensities reflect their relative concentrations in solution. However, this depends on ionization efficiency and instrumental parameters. Generally, complexed, and non-complexed G4 species respond similarly in ESI, but the contributions of ion adduct peaks for each stoichiometry must be summed. Species with similar m/z values and the same charge state are detected with comparable efficiency, so quantitative analysis should ideally compare the same charge state and avoid comparing assemblies of very different sizes [288]. ESI-MS provides the total mass of the complex, reflecting the macroscopic equilibrium binding constant, but does not directly reveal the nature of the binding site or mechanism. However, information on microscopic binding constants can be inferred, especially when there is a limited number of binding sites. For example, compounds that interact with G4 via π-stacking typically have two binding sites on the nucleic acid, corresponding to the external tetrads. The measured

amount of the 1:1 complex includes all complexes with one ligand, regardless of binding site position. Then, the amount of the 2:1 complex provides insight into possible cooperativity or independence between the two binding sites. Since relative intensities in a mass spectrum are assumed to be proportional to the concentrations of the species in solution, the tendency of a compound to form a complex with the nucleic acid is also expressed as binding affinity (BA) [289,290], which can be calculated from the m/z spectrum as:

$$BA = \frac{(\sum I_{G4\ bound})}{(\sum I_{G4\ bound} + \sum I_{G4\ unbound})} \times 100$$

The concentration of bound ligand per nucleic acid molecule can also be calculated, considering the initial nucleic acid concentration and the formation of complexes with different stoichiometries. ESI-MS is also helpful for visually determining the relative affinity of a ligand for different nucleic acid sequences in selectivity screening experiments, where a compound is incubated simultaneously with G4, dsDNA, and single-stranded DNA. The graphical comparison of bound ligand amounts provides information on selectivity, provided that sufficient resolution and no peak overlap are achieved.

Since ESI-MS provides a single signal for each species that differs by mass, it allows the direct determination of the stoichiometry of complexes by unraveling how many nucleic acid strands, cations, or ligand molecules are present in each complex [291].

From a structural perspective, the number of cations in G4 is significant. By using ESI-MS, additional information about ligand interactions with G4 structures can be retrieved. For instance, ligand intercalation into the G4 may lead to the displacement of one of the cations that stabilize the assembly, a detectable feature of ESI-MS. In some cases, depending on the structure, ligand binding may instead promote the entrapment of an extra cation [292].

In tandem mass spectrometry (MS/MS), a specific ion is isolated and fragmented by colliding it with a gas (usually nitrogen), which increases its internal energy until it breaks apart. Studies have shown that different CID patterns are associated with distinct binding motifs. For instance, if the complex fragments by losing the small molecule ligand, this is typically associated with stacking interactions [291].

Further application of ESI-MS in G4-ligand evaluation focuses on the stability of the complex, primarily achieved through dissociation studies. These are done in a vacuum environment, leading to a not straightforward association between activation energy and dissociation kinetics. To evaluate the energetic contribution in the G4-ligand complex, the only way to obtain energetic information is through the promotion of the loss of a neutral ligand from a negatively charged nucleic acid. With these assumptions in place, Collision-Induced Dissociation (CID) experiments can be used to evaluate the relative gas-phase stability of the complexes. By analyzing the intensities of the intact complex and its dissociation products at increasing collision energies, the $E_{COM}^{50\%}$ can be calculated, thereby gaining the energy required to dissociate half of the complex, and is crucial for evaluating how effectively small molecules stabilize G4 structures [293,294]. The subsequent reaction, measured via MS/MS, involves the ligand dissociating from the complex as follows: [ligand + GQ]$^{z-}$·[GQ]$^{z-}$ + ligand (**Figure 37**). The $E_{COM}^{50\%}$ value can be directly determined by comparing the relative intensities of these complexes and fragmentation products, plotting dissociation curves (see the following equation).

$$E_{COM} = \frac{I_{complex}}{(I_{complex} + I_{dissociation\ products})}$$

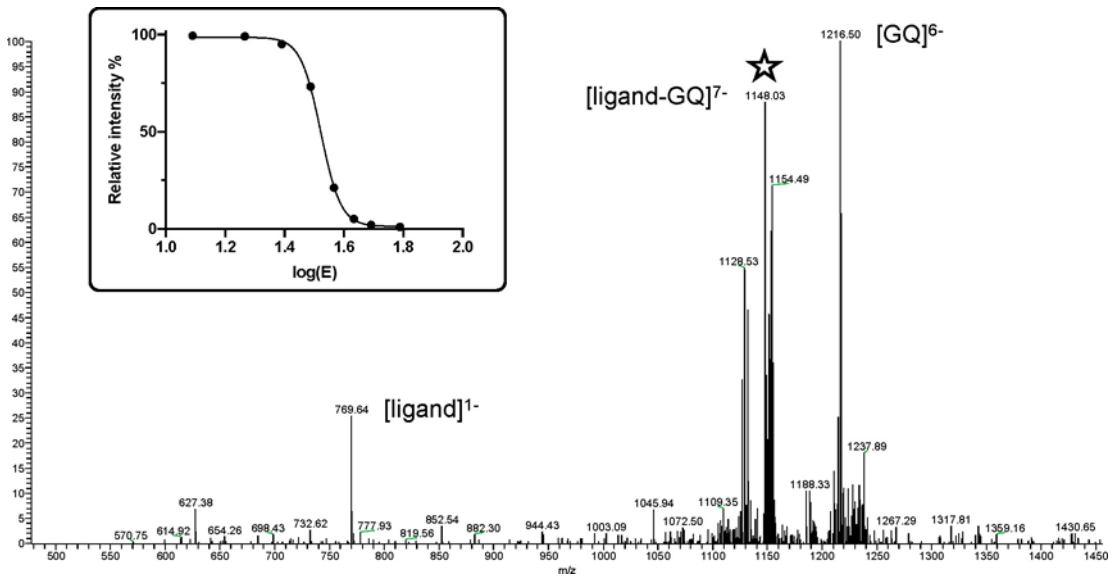

Figure 37. This is an example of the dissociation study carried out by our group. A ligand–GQ complex (5'-AGGGTTAGGGTTAGGGTTAGGGT-3' human telomeric sequence), marked with a star in the spectrum, undergoes fragmentation by loss of the ligand. In the inset, the plot of the relative intensity of the complex against the collision energy (eV) is depicted. Image from [291].

NMR for G4s

NMR spectroscopy is essential for exploring the structure, kinetics, and dynamics of G4/ligand complexes [281]. Selecting appropriate NMR techniques depends mainly on the exchange regime of the molecules and the complex, as well as the ligand's properties, such as hydrophobicity and water immiscibility. Since many G4-targeting ligands are polyaromatic, they are typically prepared in solvents such as DMSO, which are suitable for hydrophobic substances. Typically, NMR studies analyze ligand interactions by monitoring chemical shifts, peak intensities, and linewidths of the signals. Methods such as STD and Water-LOGSY require more time and involve more complex controls [295]. Additionally, these methods often pair with indirect NMR studies, such as measuring H_2O/D_2O exchange rates or using paramagnetic spin labels attached to different parts of the G4. Initially, most studies focus on the G4 imino (Hoogsteen base pairing) region, located near 10-12.5 ppm, and on the aromatic (7–8.5 ppm). Still, the imino regions of G4 guanines provide a straightforward and clear way to monitor G4 structure formation and ligand binding interactions [296].

Researchers led by Kerkour showed that the G4 ligand 2,4,6-triarylpyridine (TAP) binds to the 22AG G4 structure. However, the ligand displayed some signal dispersion, indicating loose binding in multiple conformations. The aromatic protons weren't well-resolved, and the structural studies relied on unambiguous restraints from the aliphatic protons. To determine the 3D model of the TAP-22AG G4 complex, the researchers supplemented their NMR data with restrained-docking studies. The results from NMR spectroscopy matched those from molecular docking experiments, which revealed two binding sites in the 22AG structure, with the most favored site being the lateral loop formed by T17, T18, and A19. Additionally, the results showed that TAP had a low tendency to bind through π–π stacking, instead preferring the grooves and loops interface [297].

Computational studies for the study of G4/ligand complex interaction

Over the last twenty years, CADD has revolutionized the discovery of small molecules targeting large biological structures. Virtual screening allowed researchers to evaluate thousands of compounds using either SBDD or LBDD [56]. However, modeling of nucleic acids, especially alternative conformations such as G4s, remains challenging due to their structural diversity, the presence of metal ions, and the flexibility of flanking

sequences. Despite these challenges, new methods and prediction algorithms have been developed and improved.

The study of interactions between G4 structures and potential ligands has greatly benefited from the use of computational methods. In SBDD research, molecular docking and MD are widely used to explore how ligands bind to G4s.

In the context of molecular docking in the G4 field, significant strides have been made using AutoDock. This widely used molecular docking software is available in two main free versions: AutoDock4 and AutoDock Vina, which differ in the type of scoring functions employed. AD4 uses a semiempirical AMBER force field-based scoring function, while Vina uses an entirely empirical one. Within this context, Alcaro et al. screened 2.7 million compounds from the ZINC database to identify a possible binder for G4. The work was conducted on several topologies, including parallel, antiparallel, and hybrids, leading to the identification of the psoralene scaffold, which was further confirmed by CD, fluorescence spectroscopy, and photodynamic techniques [298]. Then, Ranjan et al. studied aminosugar-intercalator conjugates deriving from *Oxytricha nova* binding to an antiparallel G4. In this work, among four neomycin-intercalator conjugates, the BQQ–neomycin showed the strongest binding, with an association constant nearly 100 times higher than neomycin alone to the same G4. Support from computational studies, conducted using Vina, allowed for the observation of neomycin docked in the wide groove with a linker extending the intercalating moieties toward the thymine loops [291,299].

One of the commercial tools for performing molecular docking is Glide, the docking engine of the Schrödinger suite, which uses a grid-based algorithm that begins with rough positioning and scoring, followed by flexible energy optimization using the OPLS force field. The identified best candidates are further refined through Monte Carlo sampling and selected using a combined empirical and force field-based energy model [300,301]. In this context, Artese et al. used Glide to screen a dataset of 31000 natural compounds for finding interactors with telomeric DNA G4. A pharmacophore model based on crystal structures of ligand-telomeric G4 complexes was generated and validated, leading to the identification of 12 hits with known G4 binding and antiproliferative properties [302].

Further, other studies employing Glide for the identification of G4-binders are present in the literature, underlying the importance of molecular docking to increase the rate of G4-ligand discovery [303,304].

Another relevant computational technique in the field of G4-ligand drug discovery is MD simulations. These simulations enable G4 systems to evolve over time in a solvated environment by applying force fields, allowing researchers to observe molecular behaviors such as side chain movements or folding/unfolding events. Choosing the right force field is especially important for simulating DNA and G4 structures, though many force fields can be used across different MD software like GROMACS, AMBER, and Desmond [305,306].

AMBER's parmbsc0, modified parm99 force field, improved the modeling of α- or γ-concerted nucleic acid rotations and was validated through quantum mechanical comparisons, long simulations, and experimental data [307]. Other relevant and widely used force fields are OL15 and OL3, which are used for DNA and RNA, respectively [308]. Instead, the parametrization of ligands is more straightforward by being done with GAFF and GAFF2. In this context, Macchireddy et al. used OL15 and GAFF2 to simulate BRACO-19 binding to G4, identifying end-stacking as the most stable mode of binding. Different topologies were tested, and among parallel, antiparallel, and hybrid G4 topologies, the parallel topology showed the most favorable binding mode, which was confirmed by the X-ray structure of the G4/BRACO-19 complex (PDB ID: 3CE5) [309].

2.4 Development of G-quadruplex ligands

2.4.1 Flavonoids

Recently, researchers have explored small molecules able to interact with G4 structures, which could be a potent agent in cancer therapy and could act as regulators at the level of oncogene promoters such as c-MYC, c-KIT, k-RAS, B-RAF, BCL2, RET, VEGF, HIF, hTERT, and HSP90 [310,311]. Nature provides an abundant source of chemically diverse molecular scaffolds, which are known to be, to some extent, less toxic and to have better bioavailability profiles than synthetic counterparts [312].

In this context, polyphenols are complex organic compounds found in many plant species, which can be divided into two main groups that together comprise more than 8000 different chemicals: non-flavonoids (e.g., lignans, stilbenes, and phenolic acids) and flavonoids [313]. From the structural point of view, the flavonoid core is constituted by the flavan nucleus, which contains 15 carbons arranged in two aromatic rings connected by a three-carbon bridge, forming a diphenyl propane structure (C6-C3-C6) that may or may not be part of a third ring. In turn, flavonoids can be categorized into various families, including flavones (such as apigenin and luteolin), flavanones (such as naringenin and hesperidin), flavonols (such as quercetin and myricetin), catechins or flavanols (such as epicatechin and gallocatechin), anthocyanidins (such as cyanidin and pelargonidin), and isoflavones (such as genistein and daidzein) (**Figure 38**). Additionally, some of these compounds have been found to serve multiple roles from a biological perspective, including acting as antioxidants, anti-inflammatory agents, antivirals, antibacterials, cytotoxins, and antiproliferative agents. They can also inhibit a broad range of enzymes, including phosphodiesterases, lipases, and hydrolases [313–315].

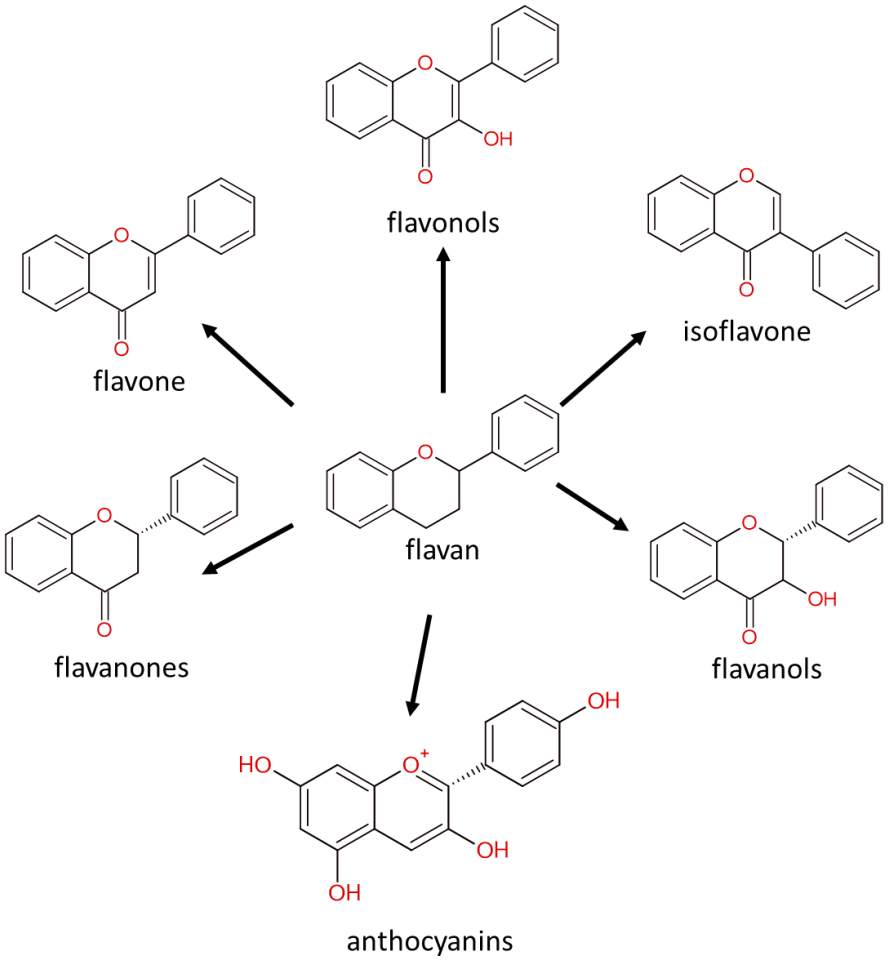

Figure 38. Chemical structures of the principal-mentioned scaffolds.

Several studies reported the use of flavonoids to target G4s to gain antiproliferative activity. In this context, Tawani et al. also explored how flavonoids such as luteolin, quercetin, rutin, and genistein interact with the human telomeric DNA G4 motif, specifically d(TTAGGGT, Tel7). Through biophysical methods, they identified a parallel topology in K^+ solution (PDB ID: 2MS6). Techniques like NMR spectroscopy, CD, UV-Vis, and fluorescence titration identify quercetin as the most effective stabilizer among these flavonoids. This was achieved by intercalation at the T1pT2 and G6pT7 sites of Tel7 [316]. Quercetin was then confirmed as a selective binder for the Pu24T G4 DNA structure present in the promoter regions of the human c-myc gene, over dsDNA, by intercalating via a π-π stacking interaction in this case, the biological activity of quercetin was subsequently evaluated by the authors in HeLa cells, confirming its nuclear localization, leading then inhibition of cellular growth, and promotion of apoptosis by reducing c-myc

gene expression in cancer cells. Furthermore, this study highlighted that myricetin also suppressed telomerase activity and significantly reduced hTERT expression [310].

Due to the relevance of using flavonoids as scaffolds for G4 Ligands, Ribaudo et al. studied rutin and quercetin using ESI-MS and computational methods, finding that both molecules interacted with the human telomeric G4 23-mer (Tel23) with a similar binding mode. However, a difference in stability was present with rutin being more effective at stabilizing the G4 topology due to a higher number of π-π stacking interactions [317].

Furthermore, other flavonoids were investigated, and kaempferol and morin were reported to interact with various DNA structures. For instance, kaempferol binds strongly and selectively to the DNA G4 present in VEGF, thereby enhancing its stability; in contrast, morin shows weak and non-specific binding. This difference was attributed to their molecular shapes (kaempferol is planar, while morin is not), suggesting the use of kaempferol as a gene expression regulator in cancer cells [318,319].

Maclura pomifera is the only species of the genus Maclura, belonging to the family Moraceae, and is known to be one of the convenient sources of isoflavones such as osajin, pomiferin, scandenone, and auriculasin [315].

In G4-ligand drug discovery, our team studied osajin, pomiferin, scandenone, and auriculasin against telomeric G4 and dsDNA through computational analysis and ESI-MS. Osajin and scandenone showed greater selectivity for telomeric G4. Further, modifications of osajin's B-ring by adding various aryl sulfonate groups enhanced G4 selectivity over dsDNA [317,320].

Given the importance of G4 over dsDNA in designing G4-ligands, during my PhD, semi-synthetic flavonoids were investigated as possible G4-binders using ESI-MS and NMR spectroscopy. This method served as a screening tool to evaluate sequence selectivity by comparing it to a dsDNA sequence. Additionally, I employed computational tools to examine the ligand binding modes, correlating the results with MS-based fragmentation studies [321].

Results and Discussion

In the current work, isoosajin (5), isopomiferin (6), and their tosylated derivatives (11, 12), together with di-p-toluensulfonyl pomiferin, di-p-toluensulfonyl auriculasin- and p-toluensulfonyl scadenone (8-10), which were extracted and synthesized by our research group, were tested against the Tel23 G4 sequence and a dsDNA oligonucleotide using ESI-MS, comparing the results with our previous data on the binding of natural flavonoids (**Figure 39**).

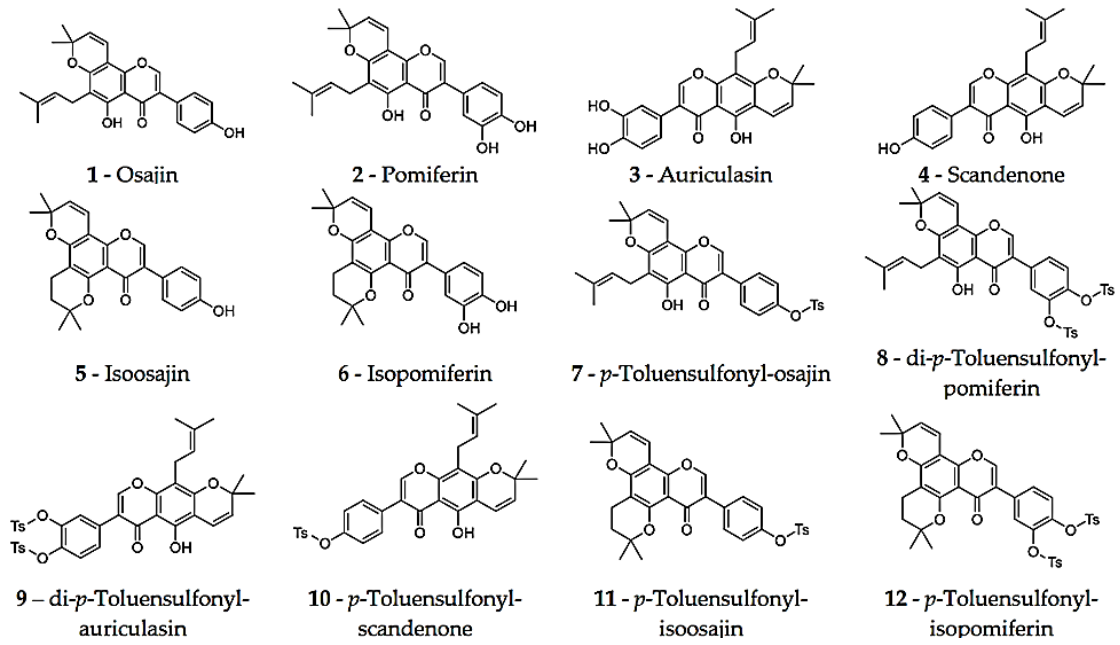

Figure 39. Chemical structures of the studied compounds.

In the 1990s, ESI-MS emerged as a valuable tool for the discovery of DNA binders, given the "softness" of the ionization technique, which minimizes fragmentation and preserves non-covalent interactions during the ESI process [322]. The experiment is conducted in a negative ionization mode, as the analyte is dissolved in an aqueous environment and infused at atmospheric pressure, conditions under which the phosphodiester backbone of the DNA sequence is fully deprotonated (pKa < 1) [282]. Due to the similar topologies adopted by G4s that fold in the presence of ammonium and potassium ions, the ESI-MS experiment is performed in NH4OAc (150 mM) [284,323]. Indeed, more specifically, we also observed in a previous study, using CD, that the same Tel23 G4 telomeric sequence used in the current work behaves comparably in buffer solutions containing either K^+ or NH_4^+ [324]. In the MS spectra, the intensities of the peaks corresponding to the different species are assumed to be proportional to the concentrations

of the species in the analyzed solution. While accurate K_d determination would require titration experiments at an increasing concentration of the species, BA is a semiquantitative property that efficiently describes the tendency of a molecule to interact with its target and is used to rank the binding of small molecules to G4s in ESI-MS screenings [289,325]. This is because the relative intensities of the ion peaks of comparable species within a mass spectrum are assumed to be proportional to their abundance. Since this value is calculated as the ratio of the bound over the total nucleic acid, as detailed in the Materials and Methods section, BA is generally expressed as a percentage without units of measurement [289–291]. The results of the ESI-MS study are summarized in **Table 1**, and a representative mass spectrum is shown in **Figure 40**. Most of the studied molecules, except for compound 8, which does not bind the nucleic acid, interact with both G4 and dsDNA. Notably, the selectivity of the molecules for G4 increased upon derivatization with the tosyl moiety for most of the ligands compared to natural isoflavones, even though lower BA values were recorded [326]. Only in the case of compound 7, the interaction occurred exclusively with G4. Nevertheless, it must be considered that, in the context of G4-ligand screenings based on ESI-MS, a selectivity ratio above 2 is considered promising [327] and that, more in general, very popular and biologically active G4 ligands such as BRACO-19 and PIPER show limited selectivity over dsDNA [309,327].

Compound	BA G4	BA dsDNA	Selectivity Ratio	$E_{COM}^{50\%}$ G4 (eV)	$E_{COM}^{50\%}$ dsDNA (eV)
1—osajin *	67	21	3.19	56.61	36.98
2—pomiferin *	94	90	1.04	41.10	31.29
3—auriculasin	97	99	0.98	41.09	30.33
4—scandenone *	76	38	2.00	51.97	48.96
5—isooasajin	27	16	1.69	44.98	33.82
6—isopomiferin	26	15	1.73	40.91	50.72
7—p-toluensulfonyl-osajin*	34	-	-	54.09	-
8—di-p-toluensulfonyl-pomiferin	-	-	-	-	-
9—di-p-toluensulfonyl-auriculasin	34	21	1.62	45.27	40.26
10—p-toluensulfonyl-scandenone	19	8	2.38	45.27	48.32
11—di-p-toluensulfonyl-isooasajin	18	10	1.80	43.81	39.87
12—di-p-toluensulfonyl-isopomiferin	35	31	1.13	51.69	61.46

Table 1. BA and $E_{COM}^{50\%}$ values determined by ESI-MS interaction assays between compounds 1–12 and the 23-mer G4 telomeric or dsDNA sequences. Selectivity ratio is calculated according to the following equation: BA G4/BA dsDNA (indicates data from references) [320,328].*

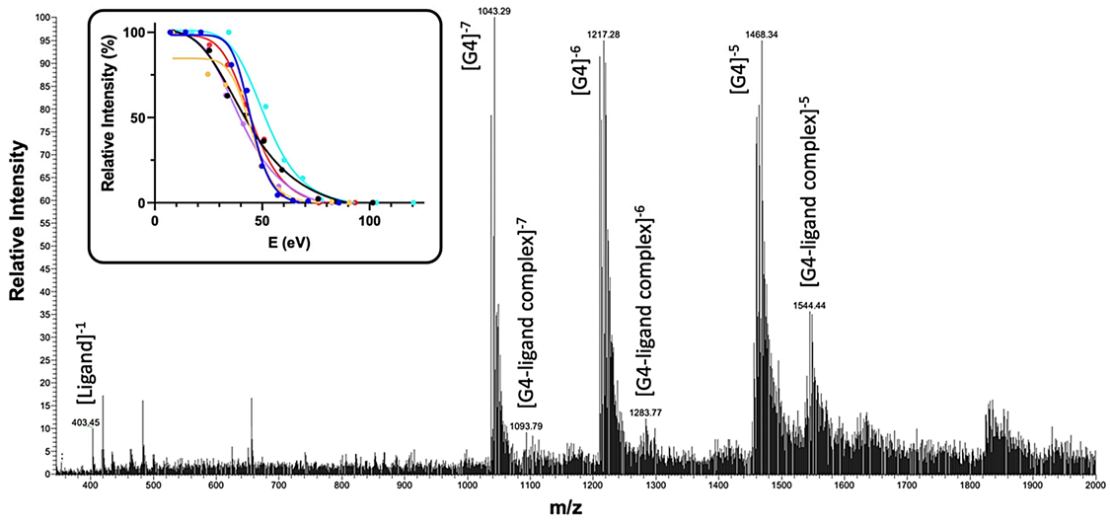

Figure 40. Representative mass spectrum showing the interaction of a ligand (isoosajin 5) with G4 DNA. In the inset, CID curves of G4–ligand complexes for compounds 5 (yellow), 6 (pink), 9 (blue), 10 (red), 11 (black), and 12 (cyan) are reported.

The efficiency in stabilizing the macromolecular arrangement, a pivotal aspect for ligands targeting G4s, can be determined using ESI-MS through CID experiments. In these experiments, the molecular ion of the G4-ligand complex is isolated and accelerated by applying an increasing potential, causing a collision with a gas that promotes its fragmentation. Based on the relative intensities of the adduct and of the dissociation products (i.e., the unbound nucleic acid, the ligand, or fragments) in m/z spectra recorded at increasing collision energy values, it is possible to calculate the gas-phase stability in terms of $E_{COM}^{50\%}$, which is expressed in electron-volts (eV). This value, also referred to as CE_{50}, represents the collision energy required to cause the dissociation of the complex to its relative half-intensity (**Figure 40**). Thus, a higher $E_{COM}^{50\%}$ value indicates a more stable ligand-G4 complex [282,291,294,329], and this could be directly related to biological effects, as it has been shown that compounds promoting a higher stabilization of G4s also induce more efficient telomerase inhibition [330]. When considering this parameter, tosylated derivatives (7–12) retained the $E_{COM}^{50\%}$ values measured for natural isoflavones; thus, it can be deduced that their ability to stabilize the G4 arrangement is maintained upon tosylation. In most of the recorded fragmentation spectra, the first and main observed event upon CID fragmentation consists of the loss of the ligand and the appearance of the peaks corresponding to the unbound G4. This behavior suggests that interaction may occur via stacking, as observed for isopomiferin 6 [331]. Nevertheless, it is also worth pointing out that some tosylated isoflavones, such as p-toluenesulfonyl-scandenone 10, show the ability

to alkylate the G4 sequence. Notably, the same effect was not observed for dsDNA, thereby paving the way for the development of small molecules that selectively deliver DNA damage to G4s. On the other hand, in the case of the complex generated by di-p-toluensulfonyl-isopomiferin 12, base loss upon fragmentation was noted.

The investigation of the ligand–G4 interaction motif can be carried out by combining information from ESI-MS screening and molecular modeling [291]. Thus, a computational study was performed on the most promising compounds, i.e., those showing the highest experimental selectivity ratio values for G4 over dsDNA. Osajin, p-toluenesulfonyl-osajin, scandenone, and p-toluenesulfonyl-scandenone (1, 4, 7, and 10) were considered as models for this step of the investigation. In particular, the interaction pattern toward a telomeric parallel G4 structure was studied, which is reported as the prevalent topology in the cellular overcrowded solution conditions [332]. The study was composed of two parts, consisting of molecular docking and MD. In the first part, we generated the initial structures of the complexes for the following MD runs through a multiparametric docking process. Precisely, the four compounds were docked to the telomeric parallel G4 structure (PDB ID: 7KLP) [333] using Glide [Schrödinger Release 2020-1: Glide; Schrödinger, LLC.: New York, NY, USA, 2020]. To obtain a complete ensemble of interaction modes for each complex, key parameters were varied in every computation, namely grid dimension (15 to 32 Å), docking precision (SP or XP), presence of ions (two or three), and exhaustiveness of conformer generation and pose selection sampling. This workflow produced a multitude of possible poses for each docked compound, allowing us to form clusters of poses in stacking and groove binding modes for the studied molecules. Within these clusters, we observed an overall similarity among poses, as shown in **Figure 41**. Thus, we then selected for each compound the stacking and groove binding poses showing the best energetic score for performing the subsequent MD simulations.

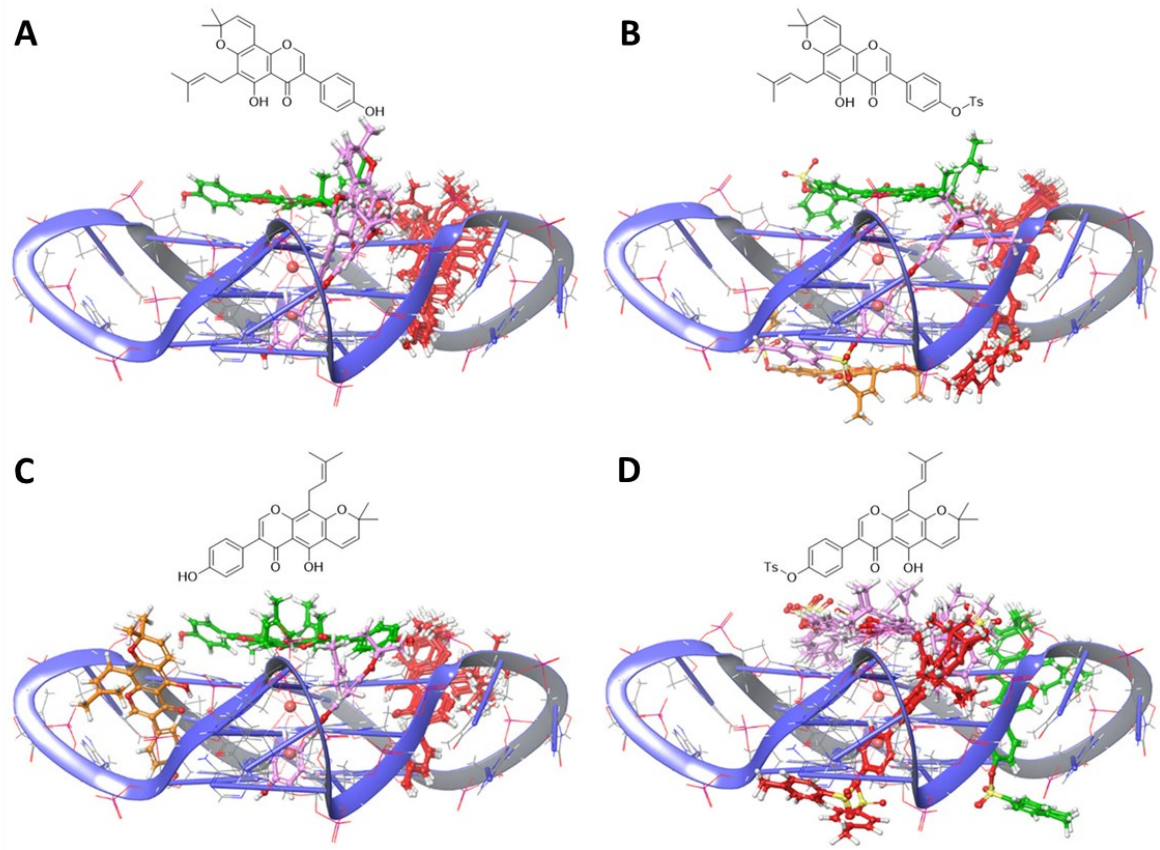

Figure 41. Poses overlap of the multiparametric molecular docking: osajin 1 (a), p-toluensulfonyl osajin 7 (b), scandenone 4 (c), p-toluensulfonyl scandenone 10 (d). The chemical structures of the compounds are reported in the upper part of every panel.

After parameterization of the ligands (Antechamber: GAFF2, AM1-BCC), the ligand–G4 complexes were enclosed in a cubic water box (TIP4Pew) with 0.20 M of KCl ions and subjected to a 100 ns simulation with Desmond [334] under a specific AMBER force field for nucleic acids (OL15) [335–337]. The eight trajectories obtained were then analyzed (Schrodinger embedded app - Simulation Event Analysis), and the over-time RMSD values were calculated for the ligands and for the guanines of the G4 structures. The MD study showed a preference for a stacking mode of interaction for osajin and scandenone (1 and 4). In contrast, their tosylated derivatives (7 and 10) demonstrated a preference to interact with the G4 by groove binding. More specifically, the stacking pose of scandenone 4 produced a stable trajectory throughout the entire simulation timeframe, with only minor RMSD fluctuations, likely due to the flexibility of the isoprene moiety. A different behavior was observed for the same compound in terms of the groove binding pose. Indeed, throughout the MD simulation, a transition was detected, and the ligand changed its interaction mode to stacking after about 85 ns (**Figure 42**). Similarly, the

simulation initiated from the groove binding mode of osajin 1 resulted in a transition to a stacking position after 10 ns, which was maintained throughout the simulation time (**Figure 42**). To further confirm this observation, we measured the distance from the center of mass of the ligands and the upper tetrad targeted through stacking in the frames across the binding pose transition event. In the case of osajin 1, a change was measured between 12.25 Å (groove binding, 6 ns) and 5.04 Å (stacking, 15 ns). For scandenone 4, a transition from 8.32 (groove binding, 85 ns) to 6.59 Å (stacking, 95 ns) was observed. Interestingly, in the case of the tosylated derivatives (7 and 10), an opposite behavior was observed. In fact, the stacking mode produced high RMSD fluctuations, whereas the groove binding produced stable trajectories after an initial stabilization period. This could be explained by the steric effects of the tosylate moiety that may direct the molecules toward the grooves. Additionally, this substituent could hinder intercalation in dsDNA, thus leading to improved selectivity.

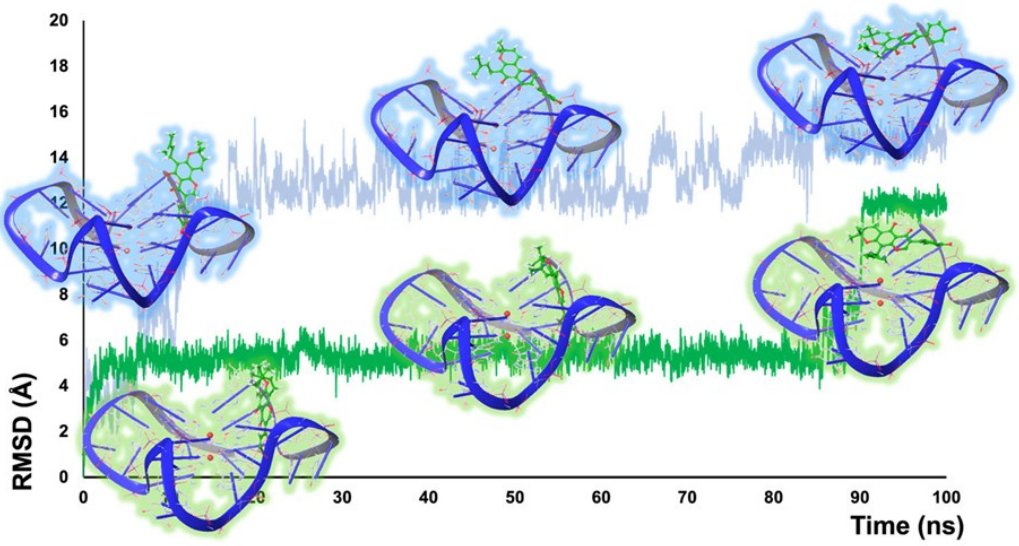

Figure 42. MD trajectories and snapshots showing the pose transition from groove to stacking binding mode for osajin 1 (blue) and scandenone 4 (green).

To provide further insights into the interaction motif, another analytical technique was eventually employed. NOE-based NMR experiments, such as STD, are used to study the binding of small molecules to macromolecular targets in solution. NOE causes the transfer of nuclear spin polarization from one population of spin-active nuclei to another in proximity, thus providing interaction information under conditions that closely resemble

the physiological environment. STD is an established technique used for compounds targeting peculiar arrangements of nucleic acids [338].

In this experiment, p-toluensulfonyl osajin 7 was used as a model compound. STD spectra showed that, in agreement with observations from docking studies (**Figure 41**), the different portions of the molecule do not interact identically with the macromolecular target. In fact, while the experiment confirmed the interaction of the compound with G4 in solution, STD signals were only observed for the protons of the double bonds inserted in the cycles of the scaffold and for the Ph-CH3. On the other hand, the isoprenyl chain and the aromatic rings showed weaker interactions. Importantly, this behavior was observed when irradiating in the deoxyribose/backbone spectral region ($\delta = 5.8$ ppm). In comparison, no STD effect was observed when considering the imino and aromatic portions ($\delta = 11.0$ ppm and $\delta = 9.5$ ppm, respectively). This observation further suggests that the binding would preferentially occur with the loops of the G4 rather than with the tetrads.

Materials and Methods

All the current data are published; readers can access the Supporting Information on the publication site [339].

ESI-MS Binding Studies

DNA sequences were obtained from Sigma-Aldrich (Milan, Italy). Samples were heat-denatured and folded in 150 mM ammonium acetate before incubation with the ligands. Stock solutions of the compounds were prepared in methanol. The final concentration of the oligonucleotide was 5 μM in 150 mM ammonium acetate, with a 10:1 compound/oligo ratio. Samples were acquired after an equilibration time of 30 min and methanol was added to the samples to obtain a stable ESI signal. Mass spectra were recorded by direct infusion ESI on a Thermo Fisher Scientific (Waltham, MA, USA) LCQ Fleet ion trap mass spectrometer. The instrument was set in negative ionization mode with a 3.4 kV capillary voltage, 120 ◦C capillary temperature and a flow rate of 5 μL/min. Binding affinity (BA) was calculated based on signal intensities (I) as follows: $BA = I_{G4bound}/(I_{G4bound} + I_{G4unbound})$. CID experiments were performed on the complexes by isolating the precursor ion in the trap. The fragmentation was promoted, increasing the "normalized collision energy" parameter. Exact mass for the G4 sequence (5′-AGGGTTAGGGTTAGGGTTAGGGT3′): 7270.774 Da. Exact mass for dsDNA (5′-ACTATTTACGTATAATGA-3′, 5′-TCATTATACGTAAATAGT-3′): 10987.922 Da. For data processing, Qual Browser Thermo Xcalibur 4.0.27.13 software was used.

Molecular Docking

G4 structure file was retrieved from the RCSB Protein Data Bank (PDB, www.rcsb.org, accessed on 24 May 2024) (PDB ID: 7KLP) and was prepared with the Protein Preparation Wizard included in the Schrodinger suite [19], using default settings, i.e., adding hydrogens, removing waters further than 5 Å from the ligand, adjusting charges, capping termini, optimizing hydrogen bond clusters, and performing a final minimization under the OPLS3e force field [20]. The ligands were prepared for docking with Ligprep tool under OPLS3e force field using Epik ionizer, and all possible states in the 7 ± 2 pH range were generated, including the possible metal binding states, therefore allowing for the interaction with the potassium ions. The docking protocol consisted of rigid receptor/flexible ligand docking, which was performed with Glide under the OPLS3e force

field, using default settings. Specifically, this involved a 0.80 scaling factor for the ligand atom van der Waals radius and a 0.15 partial charge cut-off, with the generation of one pose per ligand. Different parameters, such as grid dimension, docking precision (standard precision is labelled as SP, whereas higher precision docking is marked as XP), and sampling mode, were changed throughout the study to investigate their influence on the computation. Five cubic grids were prepared with the Receptor Grid Generation tool included in the Schrodinger suite and generated by manually selecting the two potassium ions in the inner channel of the G4 quartets as the center. The dimensions of the grids were varied as mentioned earlier, and the third potassium ion included in the 3D structure was either left unmodified or removed. The settings used for each calculation are summarized in Table S1.

Molecular Dynamics

The structures of the G4–ligand complexes, obtained by the molecular docking study, were prepared for the simulations with Schrodinger application System Builder as follows: the structures were solvated in a triclinic water box (10 Å buffer) composed by 4-site model TIP4Pew water molecules, the total charge was neutralized by the addition of an adequate number of K^+ ions and a 0.20 M KCl concentration was set. The system initially prepared for Schrodinger default force field OPLS3e was converted through Viparr application to the AMBER OL15 force field specific for nucleic acids [21–23], and the parameters set used for the ions was the one developed by Joung et al. [24]. The ligands were parameterized with Antechamber application of AmberTools20 using GAFF2 parameters and AM1-BCC atomic charges, and missing parameters were generated with Parmchk2. The simulations were conducted with Schrodinger Desmond for 100 ns each, recording 1 frame every 10 ps using the NPT ensemble at a temperature and pressure of 300 K and 1.01 bar. Default settings were used for the RESPA integrator (2.0 fs for bonded interactions, 2.0 fs for near and 6.0 fs for far interactions), and the system was relaxed prior to the simulation using the default Desmond protocol. The trajectories were analyzed after the simulations with Simulation Event Analysis Schrodinger application, and, for the over-time ligand RMSD calculations, the ligand atoms positions were fitted to the guanine planes.

Nuclear Magnetic Resonance

Saturation transfer difference (STD) NMR experiments were performed on a Bruker Ascend spectrometer (frequency: 400.13 MHz for 1H) (Bruker, Billerica, MA, USA) using the pulse program stddiffesgp.3. For data processing, TopSpin 4.3.0 was used. In these experiments, the same G4 sequence used in ESI-MS binding studies was adopted (5′-AGGGTTAGGGTTAGGGTTAGGGT-3′), and a ligand/target ratio of 400:1 was used. NMR samples were prepared in a 5 mm NMR tube with a final volume of 465 µL using a 2/1 mixture of deuterated phosphate buffered saline (6.218 mM K2HPO4, 3.782 mM KH2PO4 dissolved in D2O, pH 7.1) and DMSO-d6. The final concentration of the DNA sequence and of the ligand was 10 µM and 4 mM, respectively. In all the experiments, 4096 scans were recorded, and a saturation time (d20) and relaxation delay (d1) of, respectively, 2 and 2.5 s were applied. The water ^{1}H signal was suppressed by using an excitation sculpting with perfect echo (Bruker library: zgesgppe) pulse sequence. The STD effects of the individual protons were calculated in each sample in relation to a reference spectrum recorded with off-resonance saturation at $\delta = -40$ ppm. The on-resonance spectra were acquired by saturating the DNA sequence in three different spectral regions, thus performing three experiments. In particular, the portions that have been irradiated are the imino, aromatic, and deoxyribose/backbone spectral regions at $\delta = 11.0$ ppm, $\delta = 9.5$ ppm, and $\delta = 5.8$ ppm, respectively. The three sets of STD spectra were recorded with target saturation achieved using a series of 90° Gaussian-shaped 50 ms pulses, repeated to reach the desired d20 time.

Conclusions

The experimental and computational results of this study supported the potential of isoflavones as promising scaffolds for developing selective G4 binders and stabilizers. Within the set of investigated compounds, we observed that derivatizing the B-ring with the tosyl moiety affected BA, leading to an increase in selectivity for G4 over dsDNA.

Concerning the structural details of the ligand–target interaction motif, combined docking and MD simulations studies demonstrate that tosylated derivatives interact with G4 differently when compared to their natural precursors. In fact, π-π stacking is not predicted as the favored binding motif for these molecules since MD trajectories for groove binding interactions showed lower RMSD fluctuations. This observation was also confirmed by NMR analysis. On the other hand, the preferred binding motif of unmodified

isoflavones is π-π stacking, as demonstrated by docking and MD simulations. These results partially parallel experimental observations from CID fragmentation studies, from which a conventional dissociation mode was observed for non-tosylated flavonoids, while more complex phenomena were observed in the case of tosylated derivatives.

2.4.2 Anthracenes

Achieving specific π-π stacking interactions within G4s and ligands is usually pursued with ligands that have aromatic systems in their scaffolds. In this context, anthracenes are relevant aromatic hydrocarbon systems consisting of three linearly fused benzene rings, which, thanks to their complete planarity, can fulfill the requirement to establish stabilizing interactions with G4s.

One compound studied for G4 stabilization is anthracenyl bishydrazone, also known as bisantrene. This compound exhibits strong binding to dsDNA through intercalation, thereby inhibiting topoisomerase II. Research by Kumar and Asuncion found that 9-aminomethylanthracene binds to DNA with high affinity [340]. Furthermore, Van Arman and Czamik reported that a derivative of this compound with an additional side chain that increases the amine count to four enhances intercalation into dsDNA. All studies presented so far suggest significant potential for interaction with dsDNA. A 2010 study by Folini and colleagues examined anthracene derivatives substituted with one or two 4,5-dihydro-1H-imidazol-2-yl-hydrazonic groups (the bisantrene side chain) at various positions on the aromatic system. Here, Derivatives substituted at positions 1 and 1,5 showed a strong ability to stabilize G4 already with a concentration of the ligand 5 μM [341].

Based on these findings, Ribaudo and colleagues developed a series of constrained bisantrene derivatives as G4 binders, which were evaluated through fluorometric and ESI-MS binding assays. These studies revealed the ligands' propensity to interact with G4 [323]. Another study performed by Gama et al. synthesized anthracene-terpyridine metal complexes and investigated their role as G4 ligands, achieving high selectivity for G4 over dsDNA [342]. In 2021, Coban and colleagues synthesized 9,10-dihydro-substituted anthracene derivatives and examined their capacity to bind G4 using NMR spectroscopy, which revealed that the ligands exhibited notable inhibitory activity against the telomerase enzyme, with IC_{50} values ranging from 0.1 to 18 μM in HeLa cell assays [343].

My research group has studied the anthracene scaffold over the years, synthesizing a series of anthracene-propargylamine derivatives designed to bind G4s and dsDNA structures. Additionally, an alkyne group was added to the aromatic ring to increase the overall π-conjugation of the anthracene scaffold and enhance the binding of sidechains to the G4 backbone. A hybrid approach combining *in silico* and *in vitro* analyses revealed that these compounds exhibited a preferred interaction with dsDNA over the G4 arrangement,

as indicated by a higher docking score, confirmed by $E_{COM}^{50\%}$ values, but not by ESI-MS and fluorescence. Therefore, optimizing the compounds was necessary, and a new anthracene derivative, OAF89, was synthesized and tested on telomeric G4 and dsDNA as a control.

In 2019, Ongaro et al. aimed to develop new anthracene-based compounds capable of interacting with dsDNA and G4 structures, to identify new putative anticancer compounds [344]. In this work, a series of anthracene-propargylamine derivatives was synthesized through a final A3 coupling with formaldehyde and various secondary amines, resulting in target compounds designed to be fluorescent and G4-binders (**Figure 43, 4a-4f**). To target the negatively charged backbone by electrostatic interactions, a long linear alkyne arm ending with a tertiary amine was included.

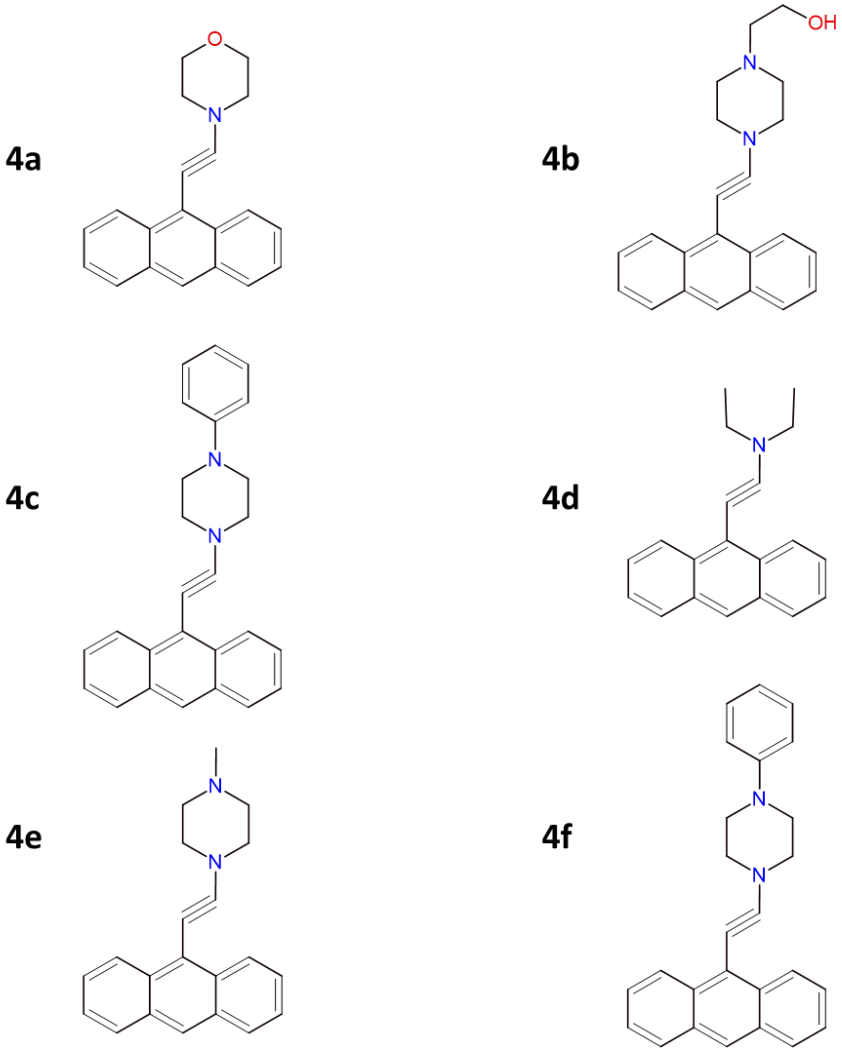

Figure 43. Chemical structures of compounds 4a–4f.

To unravel the putative binding mode of 4a-4f ligands, molecular docking of the ligands was performed on the dsDNA crystallized model (PDB ID: 2DES, CGTACG) and with the G4 crystallized human telomeric model (PDB ID: 3UHY), thus revealing a general preference for dsDNA binding over G4 (**Figure 44A**). Since the goal of this work was to find the best binder for dsDNA and G4, the compound 4b, which showed the strongest binding affinity to both DNA types, was considered the best (**Figure 44B**).

A

Compound	Glide score dsDNA	Glide score G4
4a	-8.182	-5.809
4b	-9.169	-7.662
4c	-7.826	-4.748
4d	-7.964	-6.555
4e	-8.626	-6.164
4f	-7.223	-6.365

B

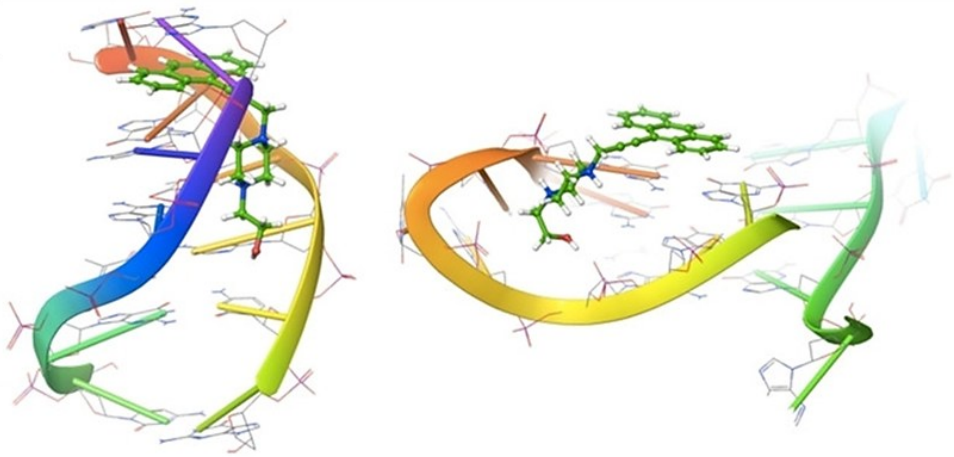

Figure 44. A) Glide score calculated for compounds 4a–4f interaction with ds and G4 DNA (kcal/mol). B) Best binding pose for 4 b in complex with dsDNA (left) and G4 (right).

Then, to confirm the computational findings, the authors performed ESI-MS studies that confirmed non-covalent interactions and supported the docking results via BA values, which generally suggested an overall preference of the compounds for dsDNA sequences, with 4b showing similar and relatively high BA values towards both the dsDNA and G4 (**Table 2**). Furthermore, the selectivity ratio was calculated by performing a ratio between BA achieved within the G4 and the dsDNA; thereby highlighting compound 4b as the most performing in this sense. In these experiments, the overall experimental approach was validated by directly using mitoxantrone, a known agent that interacts with DNA, as a positive control.

Compound	BA G4	BA dsDNA	selectivity ratio (G4/dsDNA)
4a	41.7	65.5	0.64
4b	68.4	79.8	0.86
4c	33.6	49.3	0.68
4d	47.3	61.5	0.77
4e	48.4	85.9	0.56
4f	28.3	45.8	0.62
mitoxantrone	27.2	45.5	0.60

Table 2. BA values for the compounds 4a–4f and for mitoxantrone towards G4 and dsDNA, as calculated from the ESI-MS binding experiment. The selectivity ratio was calculated by dividing the G4 BA value by the dsDNA BA value.

Furthermore, CID experiments were used to assess the gas-phase kinetic stability of DNA-ligand complexes, and some of the tested compounds demonstrated the ability to stabilize the complex in 1:1 and 1:2 stoichiometry of ligand/G4 complex (**Table 3**).

Compound	$E_{COM}^{50\%}$ 2:1 ligand/G4 (eV)	$E_{COM}^{50\%}$ 1:1 ligand/G4 (eV)	$E_{COM}^{50\%}$ 2:1 ligand/dsDNA (eV)
4a	60.67	36.29	47.39
4b	34.57	40.07	39.43
4c	-	39.98	76.01
4d	67.02	25.79	59.08
4e	19.59	22.37	32.46
4f	-	29.54	58.4
Mitoxantrone	-	44.40	44.64

Table 3. Relative gas-phase kinetic stability ($E_{COM}^{50\%}$) investigated by CID.

Then, fluorescence titration experiments were conducted to confirm the effective interaction between compound 4b and G4, demonstrating its preferential binding to dsDNA in solution (**Table 4**).

DNA sequence	K_b (mol/L)
G4	$(3.8 \pm 0.5) \times 10^5$
dsDNA	$(1.3 \pm 0.3) \times 10^6$

Table 4. DNA-binding constants (K_b) for compound 4b towards G4 and dsDNA.

In conclusion, this study successfully introduced a new class of anthracene-based DNA ligands with promising properties for further development as anticancer agents or molecular probes. This work paved the way for increasing the selectivity for the DNA G4 of compound 4b. Within this context, the synthesis of the compound 9,10-bis[(4-(2-

hydroxyethyl)piperazine-1-yl)prop-2-yne-1-yl]anthracene (OAF89) was designed and performed (**Figure 45**).

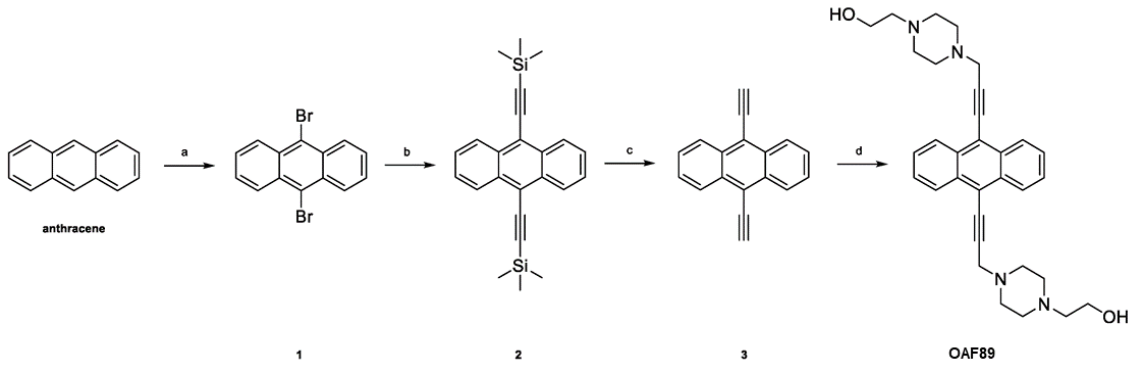

Figure 45. Synthetic scheme for the preparation of compound OAF89. (a) Br_2, $CHCl_3$; (b) TMS, $Pd(PPh_3)_4$, CuI, TEA, toluene; (c) KOH, MeOH, THF; (d) HCOH, CuI, 1-(2-hydroxyethyl)piperazine, DMSO.

Furthermore, DNA-binding studies were performed using ESI-MS, in which the selectivity of OAF89 for Tel23 and dsDNA was assessed. OAF89 showed a higher affinity for Tel23 (BA of 80.3) than for dsDNA (BA of 41.8), with a selectivity ratio of 1.92, indicating that the presence of two side chains in the scaffold favors selectivity towards the first structure. Compared to the previously studied monosubstituted analogue 4b, which favored dsDNA, OAF89 demonstrated enhanced selectivity due to its disubstituted structure. Furthermore, CID experiments revealed that OAF89 formed a stable 2:1 complex with Tel23 G4. In this context, the equilibrium K_d for the OAF89/Tel23 complex was calculated to be 0.69 μM, indicating strong binding, which supports considering this compound as a promising lead (**Table 5**).

Compound	BA G4	BA dsDNA	Selectivity ration (G4/dsDNA)	$E_{COM}^{50\%}$ 2:1 ligand/G4 (eV)	$E_{COM}^{50\%}$ 1:1 ligand/G4 (eV)	$E_{COM}^{50\%}$ 2:1 ligand/dsDNA (eV)
OAF89	80.3	41.8	1.92	43.58	34.39	33.42
4b	68.4	79.8	0.86	40.07	34.57	39.43

Table 5. Results of the ESI-MS binding and CID studies of compounds 4b and OAF89 in complex with Tel23 G4 and dsDNA as a control.

To predict the binding mode of OAF89 within Tel23, molecular docking was done, predicting a π-π stacking interaction as the preferred binding mode, consistent with the planar nature of the anthracene scaffold (**Figure 46**). This work highlighted and revealed that OAF89 is a first-in-class disubstituted anthracene derivative with promising selectivity for G4 Tel23 over dsDNA since its structure allows for enhanced non-covalent interactions

and reduced intercalation with dsDNA, making it a potential lead for developing selective G4-targeting agents.

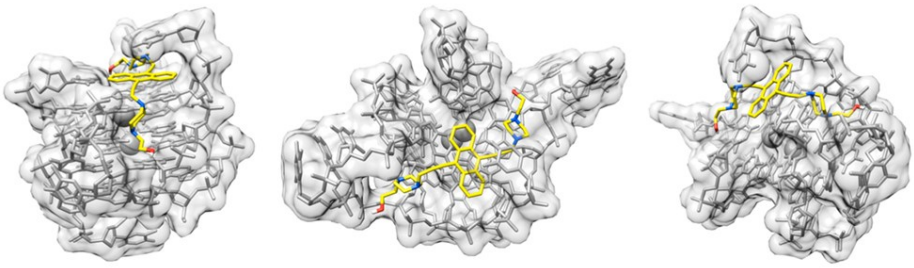

Figure 46. Predicted interaction pattern for OAF89 with G4 DNA (PDB ID: 3CE5), in three different views. Calculated binding energy: -8.5 kcal/mol.

Within this context, my PhD thesis work enabled a more detailed characterization of OAF89, specifically regarding its interactions with G4s and dsDNA. In this context, two human telomeric sequences, namely Tel23 and Tel26, were used. Both sequences are characterized by the presence of the d(TTAGGG) telomeric base repeat and are accepted as telomeric models, with experimental 3D structures deposited, thereby enabling computational studies. Furthermore, to characterize the biological activity of OAF89, it was tested against several LC cell lines.

Results and Discussion

OAF89 was tested to gain insight into the selectivity of G4 (Tel23) and dsDNA. Results showed that OAF89 interacted with both Tel23 (BA of 80.3) and dsDNA (BA of 41.8), supporting the relevance of the added sidechain. Furthermore, molecular docking was performed on both a parallel telomeric G4 and dsDNA, revealing a good interaction of the compound with the G4 structure. Moreover, this analysis confirmed that the complex with the G4 receptor forms through external stacking, with the two side chains pointing towards the G4 grooves. The calculated energy of interaction, represented by the Glide Score values, was -13.012 kcal/mol, whereas its mono-substituted analogue showed a binding energy of -10.307 kcal/mol [345]. The study was conducted using ESI-MS, NMR experiments, and *in silico* techniques. Furthermore, *in vitro* experiments were conducted to evaluate the effects on LC cells, given the involvement of G4s in this disease [346,347]. First, ESI-MS was used to study the binding of the compound with nucleic acid sequences, and the interaction efficiency was expressed in terms of BA by measuring signal intensities

of species in the gas phase in the mass spectra [291]. Additionally, CID experiments were used to investigate the stability of small molecule-DNA complexes ($E_{COM}^{50\%}$) [331]. This parameter is biologically relevant because G4 stabilization is a primary goal of ligands targeting such arrangements to influence downstream biological processes. In a previous study, we demonstrated that the molecule interacts preferentially with Tel23 compared to dsDNA (BA = 80.3 and 41.8, respectively). Accordingly, higher $E_{COM}^{50\%}$ values were calculated for Tel23 (43.58 and 34.39 eV for 2:1 and 1:1 complexes, respectively) than for dsDNA (33.42 eV) [348]. Then, new experiments carried out using Tel26 in the ESI-MS screening under the same conditions showed that the compound binds this G4 structure with a BA of 48.1 (Figure S1), sensitively lower than that measured for Tel23. Despite both sequences being reported to fold in the hybrid-2 topology, it must be considered that the two 3D arrangements are structurally different. The lack of accessibility to the tetrad in wtTel26 could justify this behavior [324,349]. Accordingly, an $E_{COM}^{50\%}$ value of 31.62 eV, even lower than that previously calculated for dsDNA, was measured for the complex formed by the ligand with wtTel26 (Figures S2− S3). Thus, ESI-MS highlighted Tel23 as the preferential target for the oxidation of OAF89. Then, Saturation Transfer Difference (STD) experiments were performed to better define the interaction pattern of OAF89 with Tel23, wtTel26, and dsDNA from a structural perspective. NOE-based experiments are one of the most attractive NMR techniques when it comes to performing ligand library screening against targets of interest and to characterize ligand-target interactions from a structural point of view. In this context, STD experiments have recently found successful applications in the study of nucleic acids [338,350,351]. In these experiments, macromolecules become saturated through the selective irradiation of a narrow spectral region of their signals. As a result, ligands that can interact significantly with the target of interest will be saturated as well due to the NOE effect; in contrast, ligands that do not interact will not be magnetized. Indeed, STD experiments can be used to determine which portions of ligands interact most closely with the surface of the macromolecule, thereby providing epitope mapping of the ligand itself and structural information about the key features of the pharmacophore. In our study, DNA sequences were irradiated in the imino (δ = 11.0 ppm), aromatic (δ = 9.5 ppm), and deoxyribose/backbone (δ = 5.8 ppm) regions, with the aim of highlighting which moieties were more important in ligand-target complex formation and stabilization (Figures S4−S6). In the case of the binding study with Tel23, relevant STD effects were observed only for the protons of the polycyclic aromatic core of

OAF89, suggesting a possible interaction via π–π stacking with nucleobases. The involvement of the aromatic region was also confirmed with T1ρ NMR, an experiment that distinguishes bound and unbound ligands thanks to differences in relaxation time (Figure S7A) [207,352]. As further confirmation, a water-ligand observed via gradient spectroscopy (wLOGSY) study was also performed. This experiment, based on the transfer of magnetization from water to the macromolecule and then to the ligand, confirmed that OAF89 interacts with Tel23 (Figure S7B) [353]. The results of such studies are depicted in **Figure 47**, and the full results of the STD experiments are reported in the Supporting Information, showing that OAF89 also interacts with the other tested sequences. More specifically, a negligible STD effect was observed for Tel26, whereas STD signals were observed for the complex with dsDNA under the same experimental conditions (Figures S5-S6). Control experiments were carried out to support the observations: fructose was used as a non-binder in an STD experiment with Tel23 under the same conditions, and no interaction was observed. At the same time, the STD effect was also measured in a sample lacking the nucleic acid for reference (Figures S8−S9).

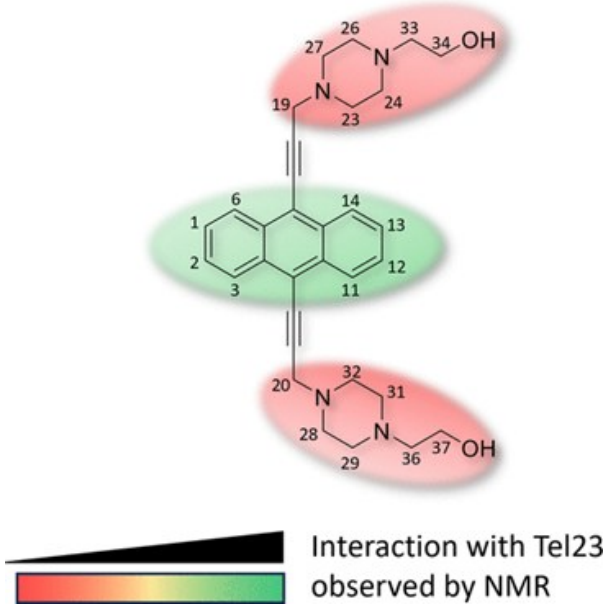

Figure 47. Graphical representation summarizing the results of the NMR experiments for OAF89 with Tel23.

Following the previously reported results, the binding mode of OAF89 to Tel23 was also investigated using *in silico* techniques, as the compound demonstrated a preference for this sequence in both ESI-MS and NMR experiments. A 3D model of human telomeric DNA folded into a G4 arrangement was selected from the Protein Data Bank (PDB ID 7PNL). Importantly, this structure is based on the same sequence that was used for ESI-

MS and NMR studies (Tel23). Molecular docking showed that OAF89 interacted by stacking with the upper tetrad composed of residues G4, 10, 16, 22 (−8.3 kcal/mol). The complex is characterized by three hydrogen bonds established by the -NH group of OAF89, which interact with T11 (2.06 and 2.72 Å, respectively) and with G22 (2.13 Å). Further, two π–π interactions occurred between G4 and the anthracene scaffold (respectively, 4.22 and 3.53 Å), and another π–π interaction between the anthracene scaffold and the pyrimidine component in G22 (4.00 Å) was detected (**Figure 48A**; in Figure S10, a comparison of the pose with the cognate ligand is reported). Moreover, to evaluate the stability of the interactions, an MD simulation was performed over a 250 ns time span, and the structural stability of the complex was observed. The RMSD trajectory confirmed that OAF89 was able to maintain Tel23 stability during the simulation time (**Figure 48B**, Figure S11). Additionally, the prediction of physicochemical descriptors relevant for ADME properties of OAF89 was carried out. The molecule can be defined as "drug-like" in terms of size, polarity, lipophilicity, and degree of insaturation, except for one violation of Lipinski's rule since the ideal molecular weight should be <500 g/mol (MW OAF89 = 510.64 g/mol). Nevertheless, according to computed physicochemical descriptors, absorption through the gastrointestinal tract is presumed to be high, while the compound was not predicted to cross the blood-brain barrier by passive diffusion.

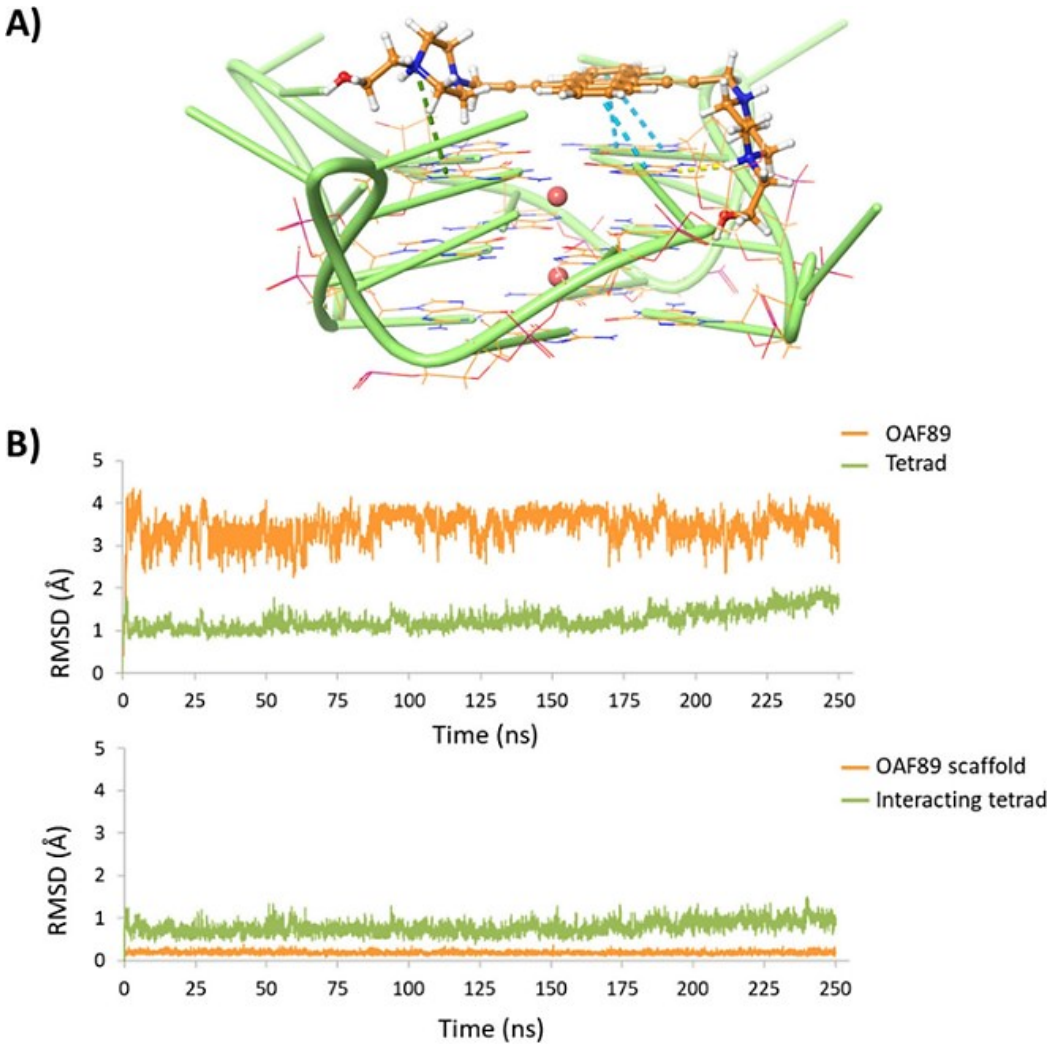

Figure 48. Predicted interaction motif for OAF89 (orange) with Tel23 (A) and trajectories retrieved from MD simulation showing the RMSD of the OAF89/Tel23 complex over the simulation time (B). The plot for the heavy atoms of the ligand is depicted in orange (aligned with Tel23), while the plot for tetrads in Tel23 is depicted in green (upper panel). The trajectories for the anthracene scaffold of OAF89 and for the interacting tetrad are depicted in orange and green, respectively, in the bottom panel (B).

Given the interest recently dedicated to the involvement of G4s as targets for innovative therapeutic strategies in LC, the compound was tested against a panel of LC cell lines consisting of adenocarcinoma human alveolar basal epithelial cells (A549), non-small cell lung carcinoma cells (PC-9), bronchioalveolar carcinoma epithelial like cells (H358), large cell LC cells (H460), nonsmoker non-small cell LC cells (H1975), and smokers with stage 3B bronchoalveolar carcinoma cells (H1650) [346,347]. Normal human bronchial epithelial cells (BEAS2B) were also included in the study as a control. The MTT assay demonstrated that the compound reduces the viability of cancer cells in the tested cell lines in the low micromolar range, except for the case of H1650, for which an IC_{50} value > 10 μM was detected. Nevertheless, the molecule lacks selectivity, as it was observed to be

toxic in the same concentration range in BEAS-2B cells (**Figure 49**). The *in vitro* data are indeed partially in line with the information obtained from mechanistic binding studies, as the compound was shown not to interact exclusively with G4 in the ESI-MS and NMR studies.

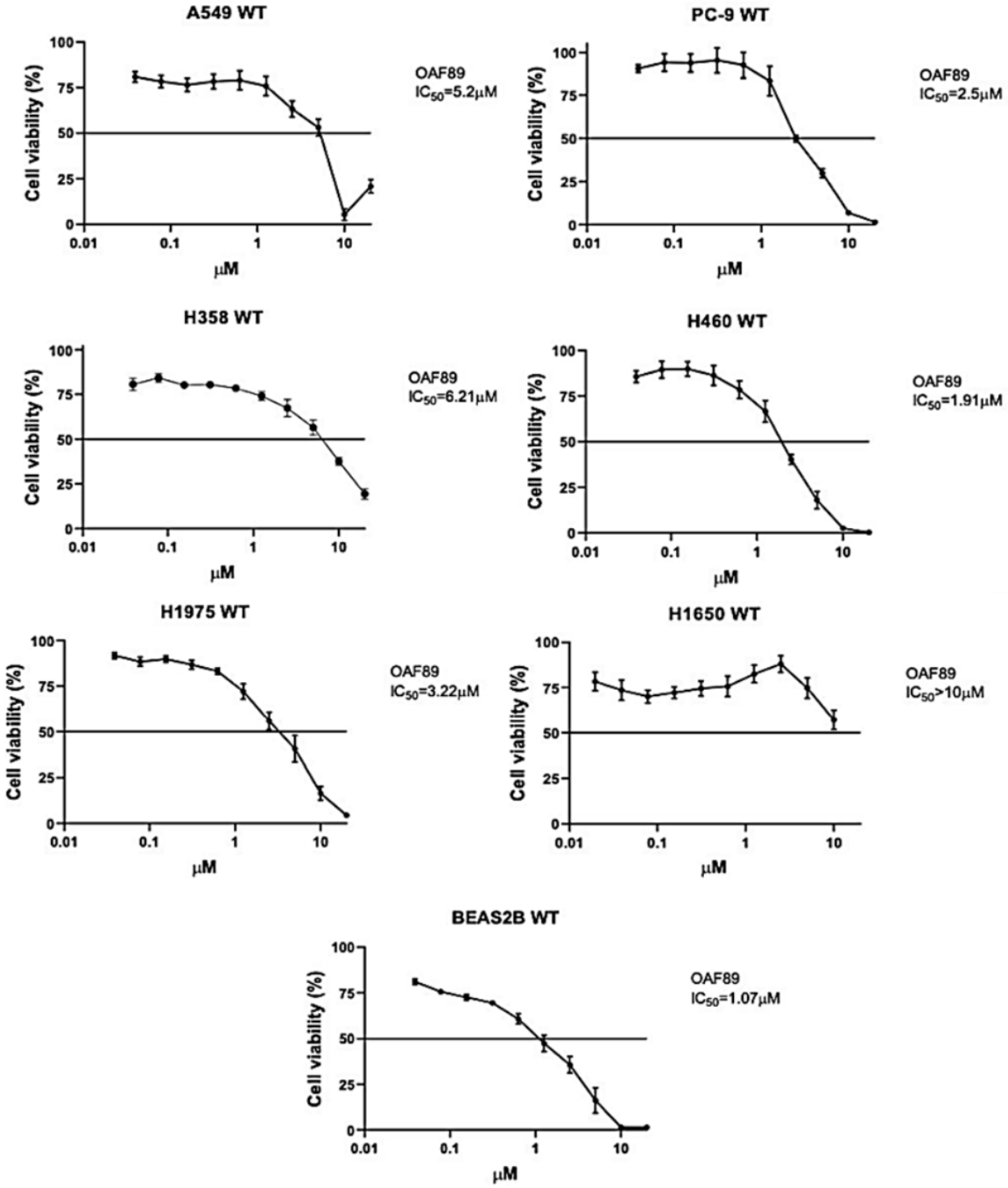

Figure 49. MTT cell viability assay carried out on LC cell lines (A549, PC-9, H358, H460, H1975, and H1650) and lung normal epithelial cells BEAS-2B.

Materials and Methods

All the current data are published; readers can access the Supporting Information on the publication site [354].

ESI-MS binding studies

DNA sequences were obtained from Sigma-Aldrich (Saint Louis, MO, USA). Samples were heat-denatured and folded in 150 mM ammonium acetate before incubation with the ligand; ligand stock solution was prepared in methanol. The final concentration of the oligonucleotide was 5-10 μM in 150 mM ammonium acetate, with a 10:1 compound-to-oligo ratio. Samples were acquired after an equilibration period of 30 min, and methanol was added to stabilize the ESI signal. Mass spectra were recorded by direct infusion using a Thermo Fisher Scientific (Waltham, MA) LCQ Fleet ion trap spectrometer and processed with Thermo Xcalibur 4.0.27.13 Qual Browser. The instrument was set in negative ionization mode with a 3.4 kV capillary voltage, a 120 °C capillary temperature, and a flow rate of 5 μL/min. CID experiments were performed on the complexes by isolating the precursor ion and increasing the "normalized collision energy" parameter. Exact mass for Tel23 (5'-AGGGTTAGGGTTAGGGTTAGGGT-3'): 7270.774 Da. Exact mass for wtTel26 (5'-TTAGGGTTAGGGTTAGGGTTAGGGTT-3'): 8179.356 Da. Exact mass for dsDNA (5'-ACTATTTACGTATAATGA-3', 5'-TCATTATACGTAAATAGT-3'): 10987.922 Da. Exact mass for 9,10-bis[(4-(2-hydroxyethyl)piperazine-1-yl)prop-2-yne-1-yl]anthracene: 510.299 Da. Binding affinity (BA) was calculated using the formula: BA= (ΣDNAbound/(ΣDNAfree + ΣDNAbound)) × 100. In CID studies, the relative intensity (%) of the DNA/ligand signal was plotted against the applied energy in eV (logarithmic scale) to calculate $E_{COM}^{50\%}$. Relative I (%) = (Icomplex/(Icomplex + Idissociation products)) × 100.

NMR binding experiments

NMR experiments were conducted on a Bruker Ascend spectrometer (frequency: 400.13 MHz for ^{1}H) (Bruker, Billerica, MA). Data processing was performed using TopSpin 4.3.0. All reactants were purchased from Sigma-Aldrich and used without further purification. A ligand:target ratio of 100:1 was employed for these analyses. The dsDNA, Tel23, and wtTel26 sequences were the same as those used in ESI-MS experiments. For Saturation Transfer Difference (STD) experiments, NMR samples were prepared in 200 μL

volumes (3 mm NMR tube), composed of 193 µL of deuterated phosphate-buffered saline (PBS; 6.218 mM K2HPO4, 3.782 mM KH2PO4 dissolved in D2O, pH 7.1), 5 µL of DNA sequences (final concentration 10 µM), and 2 µL of OAF89 (final concentration 1 mM). In all experiments, 3072 scans were recorded, with a saturation time (d20) of 2 seconds and a relaxation delay (d1) of 2.5 seconds, using the pulse program stddiffesgp.3 from the Bruker library. Water ^{1}H signal suppression was achieved via excitation sculpting with a perfect echo (Bruker library: zgesgppe) pulse sequence. STD effects of individual protons were calculated relative to a reference spectrum (REF) recorded with off-resonance saturation at δ = -40 ppm. The STD amplification factors (STD_{amp}) were calculated as: STD_{amp} = (ISTD / IREF) * ([L]tot / [T]tot), where ISTD and IREF are the signal intensities in STD and REF spectra, respectively, and [L]tot and [T]tot are the concentrations of ligand and target in molar equivalents. Results were normalized to a percentage based on the highest ratio for each spectrum. On-resonance spectra were recorded by saturating the DNA in three different spectral regions, performing three experiments per tube: the imino, aromatic, and deoxyribose/backbone regions, irradiated at δ=11.0 ppm, δ=9.5 ppm, and δ=5.8 ppm, respectively. These STD spectra were obtained with target saturation achieved through a series of 90° Gaussian-shaped pulses, each 50 ms long, repeated to reach the desired d20 time. For water-Ligand Observed via Gradient SpectroscopY (wLOGSY) and T1ρ relaxation experiments, the NMR sample was prepared in 200 µL (3 mm NMR tube), containing 172 µL of phosphate-buffered saline (PBS; 6.218 mM K2HPO4, 3.782 mM KH2PO4 in H2O, pH 7.1), 20 µL of D2O, 5 µL of DNA sequence (final concentration 10 µM), and 3 µL of OAF89 (final concentration 1.5 mM). The wLOGSY experiment involved 1024 scans, with a relaxation delay (d1) of 2 seconds, using the ephogsygpno.2 pulse program from the Bruker library. T1ρ experiments used the t1rho_esgp2d pulse program, also from the Bruker library, with 48 scans and a d1 of 5 seconds. Water ^{1}H signal suppression was achieved via excitation sculpting with a perfect echo (Bruker library: zgesgppe) pulse sequence.

Computational studies

The structure files for the G4 Tel23 in complex with a berberine derivative (PDB ID 7PNL) was downloaded from the RCSB Protein Data Bank (www.rcsb.org, accessed on 18 January 2024, resolution 1.83 Å). Ligands were built and optimized using Avogadro2 (Version 1.96.0) 4. Prior to site-specific molecular docking investigation, the receptor was

prepared, and only selected atoms were considered. The site-specific molecular docking study was performed using AutoDock Vina 5,6. The search grid was set according to the following parameters: x = -2.22, y = 0.34, z = 4.12; size: 26.55 × 31.62 × 14.41 Å. Docking simulation was carried out with default Vina parameters, the number of generated docking poses was set to 8, and the docking energy conformation value was expressed in kcal/mol. Total system energy for the obtained complex was computed with UCSF Chimera 1.15, resulting in -4937.762748 kJ/mol (AMBER ff14SB; total system energy for the complex with the cognate ligand = -4783.515409 kJ/mol).6 The best-scoring pose was considered for further analysis. Schrödinger Maestro was used to produce the artworks (Schrödinger Release 2023-1: Desmond Molecular Dynamics System, D.E. Shaw Research, New York, NY, USA, 2021. Maestro-Desmond Interoperability Tools, Schrödinger, New York, NY, USA 2021). Molecular dynamics (MD) simulations were performed using the GPU-accelerated Desmond tool of Schrödinger LLC (Schrödinger Release 2023-1: Desmond Molecular Dynamics System, D.E. Shaw Research, New York, NY, USA, 2021; Maestro-Desmond Interoperability Tools, Schrödinger, New York, NY, USA, 2021). The best G4-ligand complex obtained in the molecular docking phase was used to prepare a solvated system to perform MD, and was prepared according to 7. By using System Builder 8, the complex was solvated using the explicit TIP4Pew water model. Periodic boundary conditions were set with a triclinic box shape of 10 × 10 × 10Å. During ion placement, K^+ ions were used to neutralize the system; a concentration of 0.20 M of KCl was set. A run of 250 ns was performed under the OL15 force field with the temperature set at 300K and pressure at 1.0 bar. Further, the MTK chain coupling scheme with anisotropic coupling constant of 2.0 ps for the pressure control and the Nosé−Hoover chain coupling scheme for the temperature control (NPT ensemble) were used. The cutoff radius in the Coulomb interactions was 9.0 Å. A RESPA integrator was set with a time step of 2.0, 2.0, and 6.0 fs, respectively, for bonded interactions and near and far interactions. Trajectories were saved at 50 ps intervals for analysis 8. Then, interactions, RMSD, and RMSF of OAF89/Tel23 complex were checked. Artworks were made with Schrodinger Maestro. Physicochemical descriptors relevant for ADME properties of OAF89 were calculated using the SwissADME tool.

***In vitro* studies**

LC cell lines (A549, PC-9, H358, H460, H1975, and H1650) were purchased from ATCC and cultured in RPMI-1640 medium with 10% FBS, 100 U/ml penicillin, and 100 μg/ml streptomycin. The lung normal epithelial cells, BEAS-2B, were cultured in BEBM medium. All the cells were cultivated at 37 °C in 5% CO2 incubator. In the MTT cell viability assay, LC or normal cells were seeded one night in 96-well plates (n = 65000 cells/well) before treatment. After treatment with various concentrations of the compound for 24 h, cell viability was calculated by MTT assay. The 24 h timeframe was selected based on the duration of the cell cycle, allowing us to assess the compound's effects on cell proliferation throughout the entire cycle. The viability (%) was expressed as = [OD of treated group/OD of control group] × 100. The viability of the control group was considered as 100%.

Conclusions

The results obtained from computational and experimental interaction studies prompted us to evaluate the compound's activity *in vitro*. Thus, at this stage, the candidate is not ideal in terms of sequence selectivity or biological activity, suggesting that the preference observed for Tel23 is not sufficient to avoid toxicity. Interestingly, experimental data showed that the compound has the lowest affinity toward wtTel26, likely due to the hindrance of the tetrads in this arrangement. Most importantly, thanks to NMR experiments, we were able to determine which parts of the molecule are more involved in interacting with the nucleic acid structures. In particular, the findings regarding the interaction of OAF89 and Tel23 are supported and confirmed by the MD simulation experiment, which highlighted the anthracene scaffold as pivotal in the stabilization of the complex. Experimental observation, combined with computational data, could guide the synthesis of novel derivatives, and pave the way for developing sequence- or topology-selective molecules based on the anthracene scaffold that exhibit improved G4 over dsDNA recognition and lower toxicity.

2.5 Current and future directions of the main project

Beyond anthracenes and flavonoid-derived compounds, other chemical classes, such as anthraquinones, are recognized as scaffolds for designing G4-targeting molecules. Additionally, emerging evidence has shown that the dimeric scaffold has the potential to enhance BA, stability, and selectivity of complexes with G4s due to cooperative binding in a tweezer-like fashion. In this context, Maji et al. proposed the synthesis of six novel carbazole-based benzimidazole derivatives and four compounds in which different linkers connected these derivatives to form dimeric molecules. The ability of the ligand to bind with G4 was then examined using several studies of different nature (i.e., spectroscopic and enzymatic). In support of this, all the dimeric compounds demonstrated high G4 DNA binding affinity and selectivity over the canonical structure, as well as potential to inhibit telomerase and exhibit selective toxicity in cancer cells [355].

Over the years, our research group, in collaboration with Prof. Sissi's team at the University of Padua, developed a range of dimeric compounds designed to function as molecular tweezers, allowing both aromatic moieties to stack onto the final quartets, separated by a flexible spacer that extends into the groove. Studies on spacer length were conducted to determine the optimal size for interaction with a specific G4 topology, allowing for selective binding. The spacer was composed of two parts: a polyethylene glycol (PEG) chain to confer hydrophilicity and facilitate interactions with the backbone, and two piperazines that, through protonation, could better interact with the negatively charged phosphate groups of the backbone.

Based on their aromatic moieties, anthracene and anthraquinone were chosen for their ability to interact well with the tetrads, thanks to their planarity, which enables them to form π-π stacking interactions, in addition to hydrophobic interactions, as demonstrated in the previous chapters.

Compounds including monomers and piperazine derivatives (**Figure 50**) have been synthesized and characterized, and they were further processed by ESI-MS binding assays with dsDNA and a Tel23, to calculate their BA and selectivity for G4 over dsDNA. Subsequent CID experiments were performed to investigate the stability of the formed complexes. The most promising compound was AQA3, exhibiting strong BA with Tel23 (BA=30.0) and, interestingly, no interaction with dsDNA (BA not calculable), thereby indicating AQA3 as a selective binder for the telomeric G4.

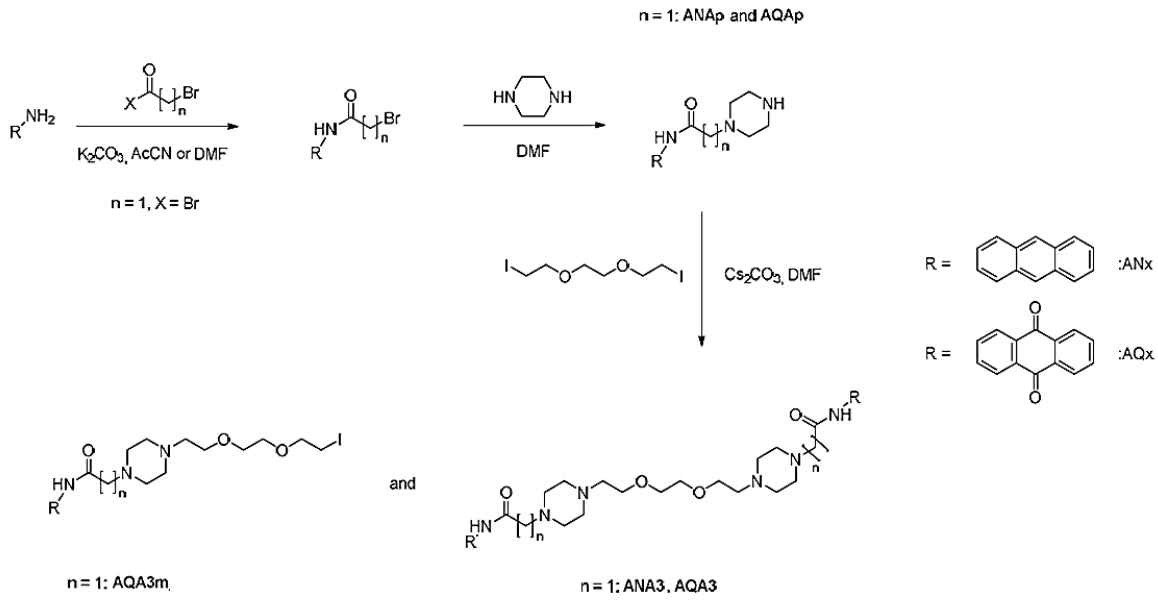

Figure 50. General scheme for the synthesis of the set of anthracene and anthraquinone dimers and monomers. The intermediates ANAp and AQAp were dissolved in 1 mL of DMF, Cs2CO3 (1.5 eq), and PEG3-I (0.4 eq) were added to the solution, which was stirred at 100 °C. The reaction was monitored with TLC with the proper eluent (DCM:MeOH:TEA, 92:7.5:0.5). After 2 hours, 10 mL of H2O were added to quench the reaction. Subsequently, the reaction mixture was centrifuged at 4000 g for 5 minutes, the supernatant was discarded, and the procedure was repeated 3 times. The solid was then washed with a solution of MeOH:H2O (3:7) and centrifuged with the same parameters applied before (3 times). The solid fraction was collected after removal of the liquid. The crude products were purified by column chromatography (silica gel, DCM:MeOH 9:1), the fractions corresponding to the monomer and the dimers for each compound were collected, and the products were characterized with ESI-MS and ^{1}H and ^{13}C NMR.

Regarding the anthracene-based derivatives, this approach identified ANAp as a weaker and less selective G4 binder, while confirming that ANA3 is unable to interact with either of the two tested DNA sequences. Then, the promising results obtained with AQA3 led to the use of CID to further investigate its interaction with the nucleic acid, which resulted in an $E_{COM}^{50\%}$ value of 52.4 eV, which indicated a stable interacting complex.

Furthermore, the compounds were screened through a fluorescence thermal shift assay (FTSA) and CD [356,357]. Unexpectedly, the obtained results did not fully align with the ESI-MS output. While both experimental approaches confirmed that no compounds of this dataset stabilized dsDNA, under FTSA experimental conditions, only anthraquinone-based derivatives stabilized Tel23. Additionally, AQAm and AQA3 were less effective in comparison to AQAp.

To further provide insights into the interpretation of experimental results, molecular docking was employed to elucidate the putative binding modes of AQA3 and its monomeric counterpart, AQAp, the most efficient in aqueous solution. To comprehensively investigate the ligand-G4 interaction at a molecular level, docking was conducted against the

1KF1,[358] 2JPZ [359], and 143D [360] PDB structures, corresponding to parallel, hybrid-2, and antiparallel topologies, respectively. Since AQA3 was designed to bind G4 structures with a molecular tweezer-like interaction, binding the guanines that form tetrads *via* aromatic stacking interactions and with piperazines interacting with the grooves was expected. In agreement to this, AQA3 behaved as predicted by the rationale design with the 1KF1 model (docking score computed for this pose: -10.286 kcal/mol) but not for 2JPZ (-10.795 kcal/mol) and 143D (-8.288 kcal/mol), suggesting that a longer spacer may be required by the ligand to properly adopt the tweezer binding mode on these structures and highlighting a less efficient binding to 143D. Furthermore, it is worth noting that an additional binding mode for AQA3 in complex with 1KF1 was identified (designated as hugger-like, AQA3h). To compare this binding mode with the tweezer one (AQA3t), we mapped their interaction networks using parallel G4. Specifically, within the AQA3t-1KF1 complex, each anthraquinone unit interacted through two π-π stacking interactions with guanines of the two outer tetrads, namely DG8 (3.66 and 3.76 Å, respectively) and DG16 (3.79 and 4.21 Å, respectively). Other stabilizing interactions involved the piperazine group, which formed one hydrogen bond (2.31 Å) and one salt bridge (3.03 Å) with DG21, located in the central tetrad. Additionally, another hydrogen bond was seen between DG14 and the secondary amide in the linker (2.57 Å). In contrast, in AQA3h, only one anthraquinone moiety formed π-π stacking interactions with DG16 present on the external tetrad in 1KF1 (3.97, 4.28, and 4.39 Å, respectively). In this case, the piperazine moieties in AQA3h were able to establish, in one instance, one hydrogen bond and one salt bridge with DG9 (1.80 and 2.73 Å, respectively). In contrast, in another pose, there was one π-cation interaction with DG4 (4.19 Å). Concerning AQAp, the anthraquinone moiety established three π-π stacking interactions with DG16 (3.59 and 3.98 Å) and DG22 (3.79 Å). In the case of the piperazine ring of AQAp, one of the nitrogen atoms interacted with DG21 via a salt bridge and a hydrogen bond (1.62 and 2.54 Å), while the other interacted with DG16 through another hydrogen bond (2.65 Å).

To better clarify the stability of the different binding modes of AQA3, MD simulations were performed using two starting points: 1KF1-AQA3h and 1KF1-AQA3t. Trajectories were analyzed using the RMSD parameter to gain insights into the stability of 1KF1, AQA3h, and AQA3t. This revealed that parallel 1KF1 was more stabilized by hydrogen bonds and π-π interactions with AQA3t, thereby supporting the rationale of the work. On the contrary, AQA3h lost partial interactions with the G4 after 72 ns of

simulation, leading to a lower stability of the structure (**Figure 51**). Furthermore, MD simulation studies managed to explain the apparently contradictory evidence retrieved from ESI-MS and FTSA.

To preliminarily investigate whether the different behavior of AQAp and AQA3 in solution might drive variable cellular effects, their cytotoxicity was examined in a human gastric carcinoma cell line (HGC-27). To properly observe both short- and long-term effects, ligand treatments were performed for 24 hours and 72 hours. At both treatment times, AQAp (9.9 ± 0.6 μM and 3.3 ± 0.1 μM, respectively, for 24 and 72 hours) exhibited IC_{50} values almost 2-fold lower compared to AQA3 (23.1 ± 1.6 μM and 7.2 ± 0.6 μM, respectively, for 24 and 72 hours) in the tested HCG-27 cell line. It may be tempting to relate this difference to the above-reported preferential G4 binding of AQAp versus AQA3 in aqueous solution. Whether this holds, it would suggest that also in the cellular environment, the dimeric compound is not fully available to interact with G4s. However, it is essential to note that the chemical-physical properties of this compound can affect several physiologically relevant steps beyond G4 recognition. Indeed, this work showed that the self-stacked form of AQA3 is highly stable, and it was predicted to be more lipophilic than the monomeric derivative (LogP 2.87 and 0.81 for AQA3 and AQAp, respectively). Thus, it is not possible to rule out that these features, along with the high molecular weight, can modulate AQA3 cellular uptake and/or intracellular distribution, ultimately resulting in a reduced effective drug concentration at functional target sites, including G4. Please note that the reader could find the experimental and supporting information on the publication page [361].

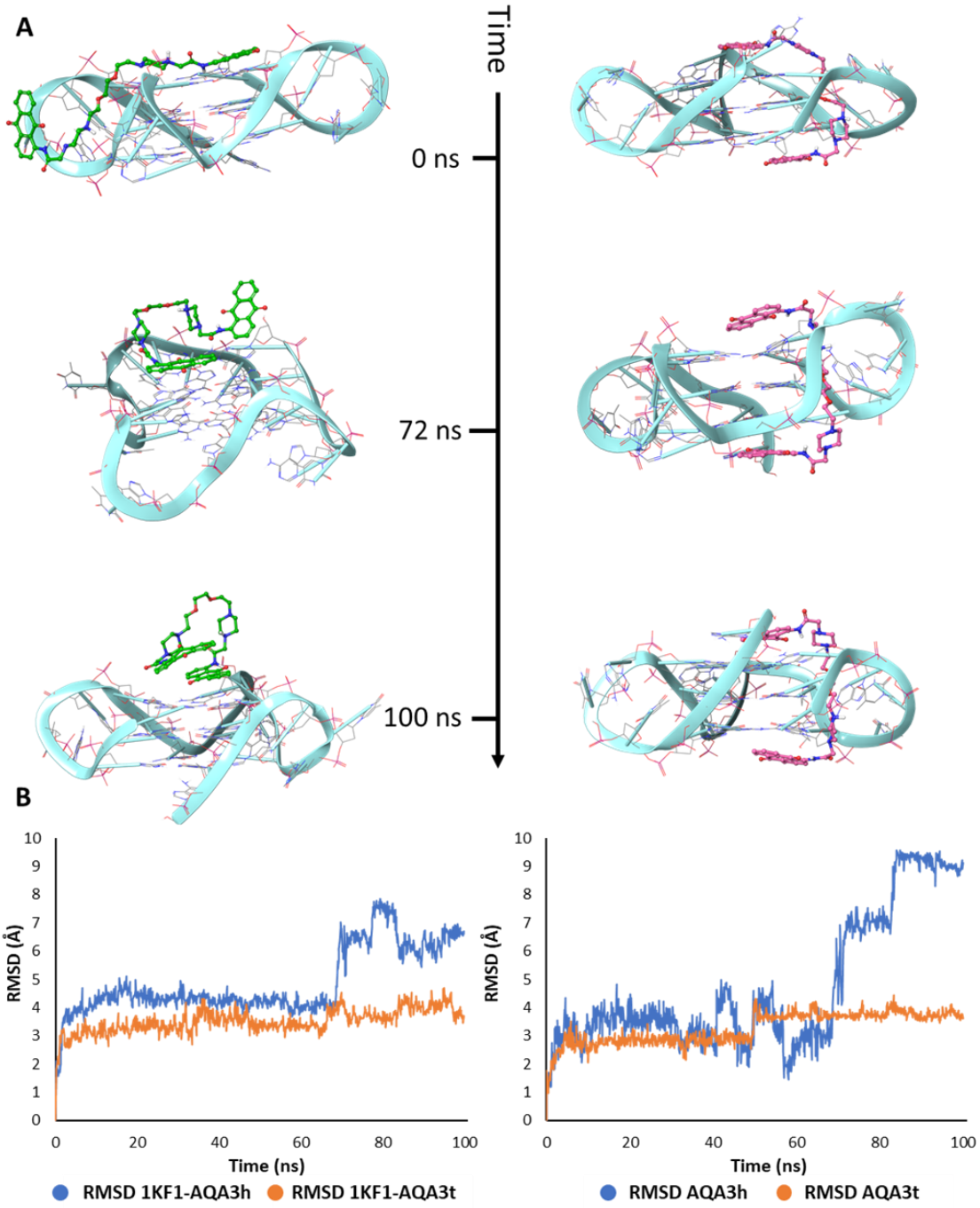

Figure 51. ***A****) Snapshots of the 1KF1-AQA3h complex in the "hugger" binding mode (on the left) and of 1KF1-AQA3t complex in the tweezer-like binding mode (on the right) are presented relative to frame 1 (0 ns), frame 735 (72ns), and frame 1000 (100 ns);* ***B****) Depiction of trajectories of 1KF1-AQA3h and 1KF1-AQA3t over 100 ns of MD simulation, RMSD of 1KF1 bound to AQA3h (blue) and to AQA3t (orange), and RMSD of ligands for AQA3h and AQA3t.*

3. Side projects 1: Phosphodiesterase 9 as a target for CNS–related diseases

3.1 Introduction

Neurons are essential for brain communication and are found throughout the body, although most originate in the central nervous system (CNS), specifically in the brain. During childhood, neural stem cells produce most neurons, but this production declines significantly in adulthood. Neurodegeneration, the gradual loss of neurons, their structure, or function, is a key factor in many brain disorders and a major health concern. It is associated with synaptic dysfunction, disrupted neural networks, and the accumulation of altered proteins in the brain. Diseases marked by neurodegeneration are known as neurodegenerative disorders and include Alzheimer's disease (AD), Parkinson's disease (PD), prion diseases, amyotrophic lateral sclerosis, motor neuron disease, Huntington's disease, spinal muscular atrophy, and spinocerebellar ataxia [362]. Patients affected by neurodegenerative diseases (NDDs) often experience severe and untreatable physical and cognitive decline, including impairment of mental and motor systems, leading to common symptoms. While the exact causes remain unclear, these diseases share standard molecular features, including neurotransmitter imbalance, abnormal protein aggregation, neuroinflammation, oxidative stress, and disrupted metal homeostasis [362–364].

Phosphodiesterases (PDEs) are enzymes that hydrolyze cyclic adenosine monophosphate (cAMP) and cyclic guanosine monophosphate (cGMP), which are crucial for intracellular signaling in neurons [365]. These messengers are synthesized by adenylate and guanylate cyclases starting from ATP and GTP, respectively. Then, the increase of cAMP and cGMP activates protein kinases (PKA and PKG, respectively), which regulate various intracellular processes [366]. In this context, cAMP/PKA and cGMP/PKG pathways are essential for neurotransmitter release, synaptic transmission, and plasticity [367,368]. Notably, several studies have reported that disrupting these pathways can impair synaptic vesicle recycling and long-term synaptic plasticity. For this reason, PDE inhibitors, which are reported to increase cAMP and/or cGMP levels, were demonstrated to enhance signaling pathways that activate cAMP response element-binding protein (CREB), a key transcription factor that, upon phosphorylation, promotes the expression of genes like Brain-derived neurotrophic factor (BDNF), thus supporting synaptogenesis, neurogenesis, and neuronal survival [369]. Then, BDNF binds to the tropomyosin-related kinase B (TrkB) receptor, triggering pathways such as MAPK and PI3K/Akt that promote cell survival and inhibit apoptosis, as well as neurogenesis, memory, and learning [370].

By modulating these signaling pathways, PDE inhibitors can improve cognitive function, restore neuronal plasticity, reduce cell death, and offer neuroprotection. They also help reduce inflammation by lowering the levels of cytokines such as TNF-α and NF-κB. Overall, PDE inhibitors show promise in treating NDDs by enhancing neuronal communication, survival, and regeneration [371–373].

Cyclic nucleotide PDEs are encoded by 11 gene families (PDE1 to PDE11), which together produce over 100 different proteins or isoenzymes from 21 distinct genes in mammals (**Table 6**). PDEs belong to the metalophosphohydrolase superfamily (EC 3.1.4.17), and each monomer is composed of three main domains: a regulatory N-terminal domain unique to each family, a conserved catalytic domain (~340 amino acids), and a C-terminal domain that may be modified by phosphorylation or prenylation [374]. This high degree of similarity (60% on the homologous amino acid sequence) leads to issues in identifying selective PDE inhibitors.

Based on structural differences that also affect their tissue, cellular, and subcellular distribution in the brain, the PDE superfamily is classified into three groups according to their substrate specificity. Among the 11 subtypes, PDEs 4, 7, and 8 specifically hydrolyze cAMP, while PDEs 5, 6, and 9 hydrolyze cGMP; the others are capable of degrading dual second messengers.

Type	Isoforms	Substrate	Localization (in brain)
PDE1	A, B, C	cAMP/cGMP	Hippocampus, cortex, olfactory bulb, striatum (highest expression levels), thalamus, amygdala, cerebellum
PDE2	A	cAMP/cGMP	Hippocampus, cortex, striatum, hypothalamus, amygdala, midbrain
PDE3	A, B	cAMP/cGMP	Throughout the brain
PDE4	A, B, C, D	cAMP	Hippocampus, cortex, olfactory bulb, striatum, thalamus, hypothalamus, amygdala, midbrain, cerebellum
PDE5	A	cGMP	Hippocampus, cortex, cerebellum
PDE7	A, B	cAMP	Hippocampus, cortex, olfactory bulb, striatum, thalamus, hypothalamus, midbrain
PDE8	B	cAMP	Hippocampus, cortex, olfactory bulb, striatum, thalamus, hypothalamus, amygdala, midbrain, cerebellum
PDE9	A	cGMP	Hippocampus, cortex, olfactory bulb, striatum, thalamus, hypothalamus, amygdala, midbrain, cerebellum
PDE10	A	cAMP/cGMP	Hippocampus, cortex, striatum, midbrain, cerebellum
PDE11	A	cAMP/cGMP	Throughout the brain

Table 6. Isoforms and localization of the different PDE families for neurodegenerative diseases. Reference [364].

Developing PDE inhibitors offers a practical approach to treating age-related cognitive decline in NDDs. In this context, multiple PDE inhibitors are either on the market or in clinical trials [364]. During my PhD, leveraging the lab's expertise, I primarily focused

on identifying PDE9A ligands through computational studies, leading to the discovery of compounds that inhibit PDE9A, as documented in the literature.

Overview of PDE9A

PDE9A, discovered in 1998 [375,376], specifically hydrolyzes cGMP with very high affinity (70-170 nM) over cAMP (230 mM), making it one of the most sensitive PDEs to low cGMP concentrations [377].

PDE9A plays a regulatory role in brain function, memory, platelet aggregation, vascular tone, cell growth and death, and heart contractility [378,379]. PDE9A's role was linked to several conditions, including AD, schizophrenia, Huntington's disease, stroke, vascular dementia, diabetes, obesity, heart failure, benign prostate hyperplasia, erectile dysfunction, sickle cell disease, and certain breast cancers [380–382] (**Figure 52**).

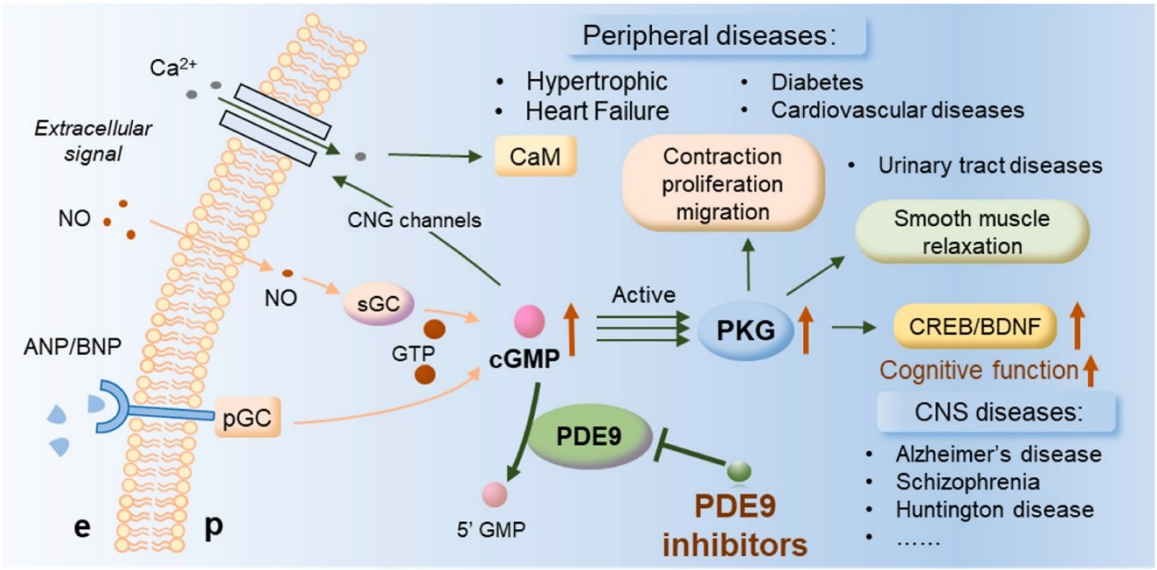

Figure 52. Schematic presentation of PDE9A and cGMP signaling pathway: ANP, atrial natriuretic peptide; BDNF, brain-derived neurotrophic factor; BNP, B-type natriuretic peptide; CaM: calmodulin; CNG channels, cyclic nucleotide-gated ion channels; CREB, cAMP-response element-binding protein; pGC, particular guanylyl cyclase activated by ANP/BNP; sGC, soluble guanylyl cyclase; NO, nitric oxide; GTP, guanosine triphosphate; PKG, protein kinase G. Adapted from [377].

The only known subtype of PDE9 is PDE9A, encoded by a single gene located on chromosome 21q22.3. This gene produces over 20 splice variants with distinct subcellular localizations, allowing for precise control of cGMP signaling through the formation of cGMP microdomains [383]. For instance, Rentero et al. in 2003 reported distinct subcellular localizations for PDE9A6 (cytoplasmic) and PDE9A1 (nuclear), with PDE9A1

exhibiting exclusive nuclear localization due to the presence of a Pat7 motif, a nuclear localization signal. In contrast, other PDEs are cytosolic (**Figure 53**) [384].

Furthermore, PDE9A mRNA was widely expressed in various tissues, including the brain, prostate, colon, kidney, and spleen [385].

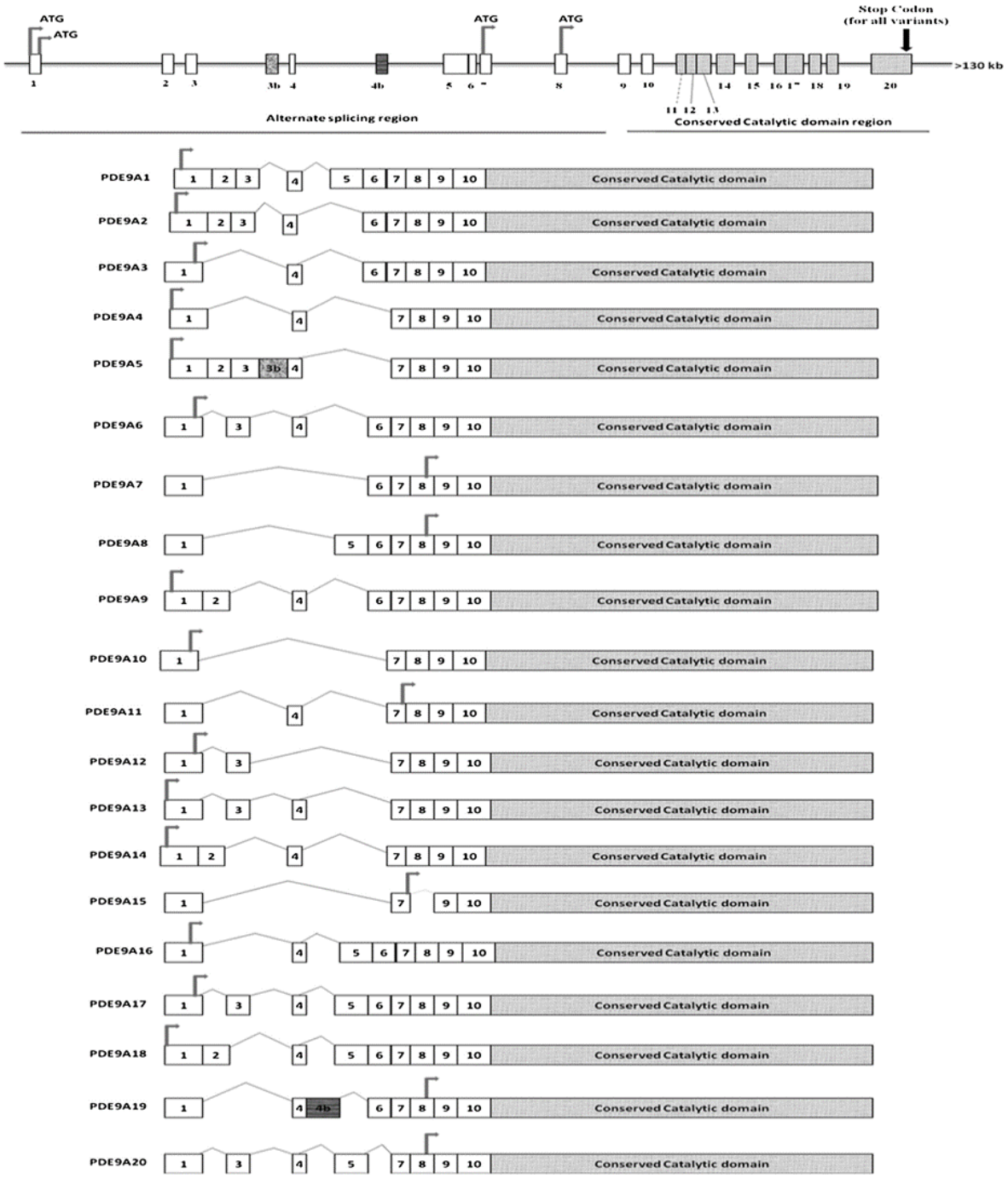

Figure 53. Schematic diagram of the human PDE9A gene and its mRNA transcripts. Image from [378].

Furthermore, from a structural perspective, the N-terminal portion was investigated functionally, revealing that different N-terminal regions do not alter the catalytic activity of PDE9A.

Then, the catalytic site of PDE9A was extensively investigated, and 16 α-helices able to dimerize through the establishment of hydrogen bonds within the two subunits through Tyr315, Asn316, Asp317, Asn323, and Arg353 residues were found.

Then, three key sub-pockets pivotal for enzymatic activity were identified in the catalytic site: the Q pocket, which binds the purine ring of cGMP; the M pocket, which contains Zn^{2+} and Mg^{2+} ions essential for catalysis; and the H pocket, which is rich in hydrophobic residues.

Several mutagenesis studies in the Q pocket have highlighted the significance of key residues, such as Glu406 and Gln453, which were reported to establish a 2.8 Å hydrogen bond between the Nε side chain of Gln453 and the Oε of Glu406, thereby stabilizing the orientation of Gln453 and influencing the substrate selectivity of PDE9A [386]. Then, Phe456 was found to possess a relevant role at the level of the Q pocket, within which π-stacking interactions were found with the purine core of cGMP and became an exploitable feature for structure-based drug discovery [377].

The M pocket contains two divalent cations, Zn^{2+} and Mg^{2+}, a network of water molecules, and seven residues, His252, His296, His325, His292, His256, Asp293, and Asp402, which, through the octahedral coordination geometry of the cations, play a role in stabilizing the structure and activating hydroxide for mediating catalysis.

Lastly, the H pocket is mainly composed of Phe251, Trp416, Val417, Leu420, Leu421, Tyr424, Phe441, Ala452, and Val447. In this pocket, Tyr424, found only in PDE9A and PDE8, is defined as a critical target residue for designing selective PDE9A inhibitors, thus contributing to PDE9A's high specificity for cGMP and its potential as a therapeutic target (**Figure 54**) [387].

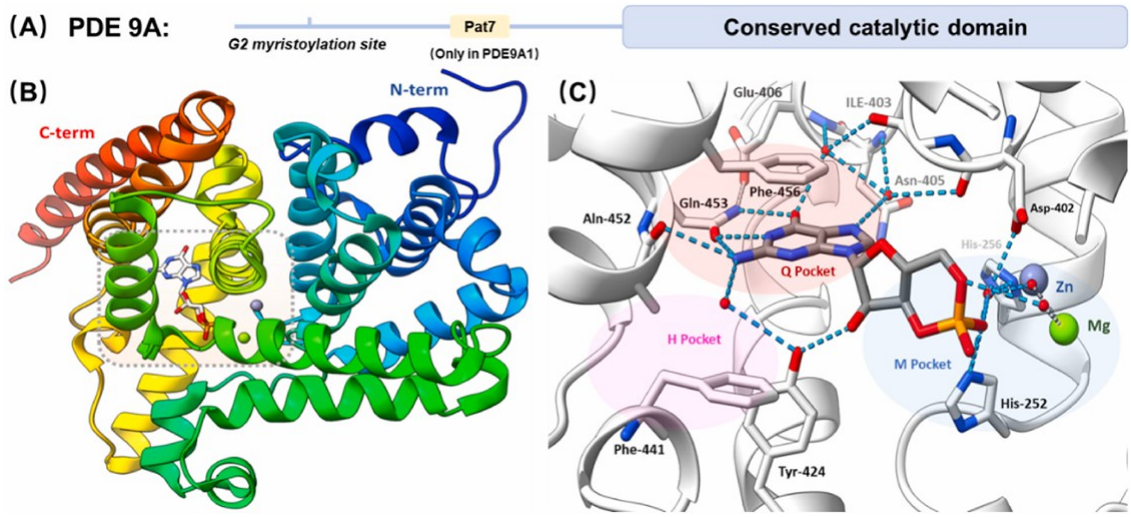

Figure 54. (A) The currently known domain organization of PDE9A includes Pat7 in the N-terminal, which determines the nuclear localization of PDE9A1. (B) PDE9A crystal structure complexed with cGMP (PDB code 3DYL). (C) Main amino acids interactions of cGMP with PDE9A and three major subpockets: Q pocket (red), M pocket (blue), and H pocket (pink). Image from [377].

As PDE9A is the most cGMP-specific phosphodiesterase involved in the nitric oxide/cGMP signaling pathway, its inhibition has been reported to increase cGMP levels, thereby enhancing synaptic plasticity and improving cognitive functions [388]. In this context, the pyrazolopyrimidinone scaffold has been widely utilized in the design of PDE9A inhibitors, and compounds like BAY73-6691, PF-04447943, and BI-409306 demonstrated improvements in memory and synaptic function [364,389–391].

The evaluation of the designed compounds was conducted using computational methods, including molecular docking and MD simulations, to identify the most effective PDE9A binder. *In silico* studies revealed that all designed compounds established interactions with residues Gln453 and Phe456, thus supporting the synthesis. Furthermore, *in vitro* studies allowed the identification of 1k as the compound with the best inhibitory profile against PDE9A (IC_{50} of 2.0 nM), good metabolic stability ($t_{1/2}$ of 57 min), and good solubility (195 mg/L) (**Figure 55**) [392]. Some compounds also exhibit dual activity, targeting both PDE9A and other enzymes, such as histone deacetylase or butyrylcholinesterase, which may be beneficial for treating advanced AD.

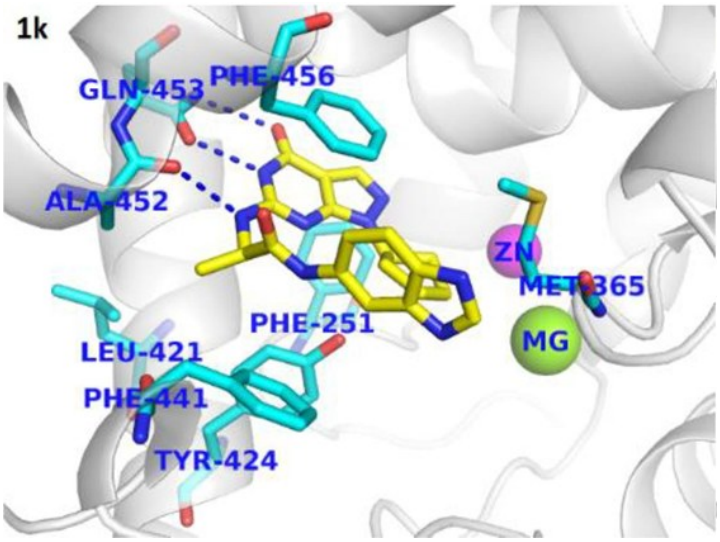

Figure 55. The binding mode of compounds 1k and 1m with PDE9A by molecular docking. Image from [392].

Furthermore, natural-derived compounds, such as flavonoid- and cannabinoid-derived PDE9A inhibitors, have been explored, with some showing nanomolar potency and neuroprotective effects [393,394].

The study by Ribaudo et al. investigated the potential of cannabidiol (CBD), a non-psychoactive compound derived from *Cannabis sativa*, as a selective inhibitor of PDE9A using both computational and *in vitro* methods. Seven phytocannabinoids and four terpenes for drug-like properties and ability to target the CNS were screened, and CBD, along with Δ9-tetrahydrocannabinol (THC), cannabinol (CBN), and cannabitriol (CBT), showed favorable characteristics. Still, CBD was selected for further study due to its non-psychotropic nature and promising computational results.

Molecular docking and MD simulations revealed that CBD binds stably and selectively to PDE9A, with a calculated binding energy comparable to that of a known PDE9A inhibitor (docking score of -9.1 kcal/mol). Then, *in vitro* experiments confirmed that CBD can inhibit PDE9A with an IC_{50} of 110 nM, supporting its potential as a therapeutic agent [393].

The data presented in this section on PDE9A-related drug discovery were obtained to identify novel inhibitors derived from both natural and synthetic sources. This research was made possible through collaborations established within the University of Florence, whose contributions were pivotal in advancing the molecular investigation and experimental validation of potential therapeutic candidates targeting PDE9A.

3.2 Virtual screening-accelerated discovery of a phosphodiesterase 9 inhibitor *with neuroprotective effects in the kainate toxicity in vitro model*

In the CNS, some specific PDE isoforms modulate pathways involved in neuronal plasticity. Accumulating evidence suggests that PDE9A may be a promising therapeutic target for neurodegenerative diseases. In the current study, computational techniques were employed to identify a nature-inspired PDE9A inhibitor with an isoflavone scaffold, starting from a database of synthetic small molecules using a ligand-based approach. Furthermore, docking studies supported by MD simulations allowed us to evaluate the features of the ligand–target complex. *In vitro* assays confirmed the computational results, showing that the selected compound inhibits the enzyme in the nanomolar range. Additionally, the expression of the PDE9A mRNA and protein levels in organotypic hippocampal slices was evaluated, observing an increase following exposure to kainate (KA). Significantly, the PDE9A inhibitor reduced CA3 damage induced by KA in a dose-dependent manner in organotypic hippocampal slices.

Results and Discussion

In the search for potential PDE9A binders, we exploited our in-house database, which comprises hundreds of small molecules synthesized and characterized by our research group over the years. The first step in preparing the virtual library involved evaluating the druglikeness of the molecules and their predicted pharmacokinetic properties. The database was therefore imported into Schrödinger Maestro and analyzed using the QikProp tool embedded in the software, after the compounds were prepared with LigPrep. Only the molecules bearing a maximum of one violation to the "Lipinski's rule of five" was admitted to the following step of investigation, and in particular, the criteria that were adopted are reported as follows: molecular weight < 500 g/mol, logP < 5, number of hydrogen bond donors ≤5, and number of hydrogen bond acceptors ≤10 [395].

Natural or nature-inspired compounds have been widely demonstrated to possess neuroprotective action, and it is well accepted that this behavior is associated with the inhibition of one or more PDE isoforms [396–399]. In the past, attention has been dedicated to caffeine, theophylline, papaverine, and other nonspecific alkaloids. However, over the years, the focus has been moved to flavonoids, although they were mostly associated with their role in inhibiting PDE5 [400–402]. In this context, our group recently proposed a set of *in silico* tools to evaluate the effects of flavonoids and other natural compounds in the

inhibition of various PDEs involved in neurodegenerative disorders [403]. This first study indeed showed that flavonoids represent a promising class of compounds targeting PDE9A. The results laid the basis for a subsequent *in silico* analysis, in which a small library of compounds was screened for PDEs, demonstrating improved affinity toward PDE9A [404].

Based on these results and other data from the literature, our in-house database was filtered using a structural query to highlight compounds bearing a chromone scaffold, the core of flavonoids, using a ligand-based approach [405]. Additionally, the oxygen in position 1 of the pyran ring was allowed to be substituted to also include other natural or nature-inspired compounds such as naphthoquinones and anthraquinones (**Figure 56A**). As a result, we obtained a subset of 441 compounds that were processed using the Schrödinger suite and docked to the 3D structure of PDE9A using Glide. The 20 most promising compounds, based on docking score, were subjected to a subsequent experimental solubility test, which was performed in both water and PBS buffer. Compound solubility is a crucial aspect that should be considered in drug discovery studies. We introduced this fast and cost-effective step in the screening protocol to further refine computational data, thereby building a bridge toward *in vitro* experiments.

Considering the results of the virtual screening and solubility test, we decided to analyze the isoflavone DB987 in more detail (**Figure 56B**). Interestingly, the identified compound can be defined as a semisynthetic molecule. Indeed, the isoflavone DB987 can be obtained through the modification of pomiferin, a natural flavonoid extracted from *Maclura pomifera* [406].

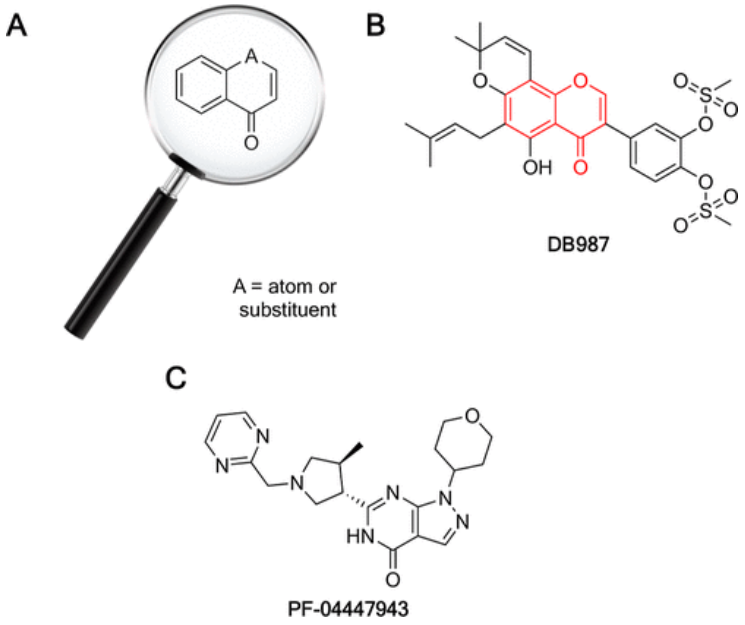

Figure 56. Chemical structure of the chromone scaffold used for the virtual screening procedure (A). Chemical structure of DB987, the compound highlighted by the screening, in which the red structure represents the part of the molecule matching query (B). Chemical structure of the reference compound, PDE9A inhibitor PF-04447943 (C).

Structure of PDE9A and Molecular Docking

The 3D structure consisting of a crystallized PDE9A enzyme and a co-crystallized PF-04447943 ligand was retrieved from the RCSB Protein Data Bank (PDB ID: 4E90) (**Figure 56C**) [407]. In the context of this structure, it is notable that PF-04447943 establishes hydrophobic interactions with some residues in the hydrophobic clamp of PDE9A. The aromatic ring present in Phe456 established three π–π stacking interactions with pyrazole, the hydroxy-substituted pyrimidine ring, and the pyrimidine moiety (4.29, 3.70, and 5.08 Å, respectively). Two hydrogen bonds were identified between Gln453 and the hydroxy-substituted pyrimidine of the ligand. The first (1.75 Å) occurs between N7 and the carbonylic oxygen in Gln453, and the other (2.12 Å) between O6 present in the pyrimidine of the ligand and $–NH_2$ in the amino acid.

The complexes obtained from molecular docking analysis were evaluated from the perspective of the ligand–PDE9A interactions. Redocking of the ligand (-9.8 kcal/mol, **Figure 57A**) reproduced the original pose, and the RMSD value with respect to the cognate ligand, which should be at most 2.50 Å [408], was 1.18 Å, thus indicating that the method is accurate. For comparison, the docking pose of DB987 is reported in **Figure 57B**.

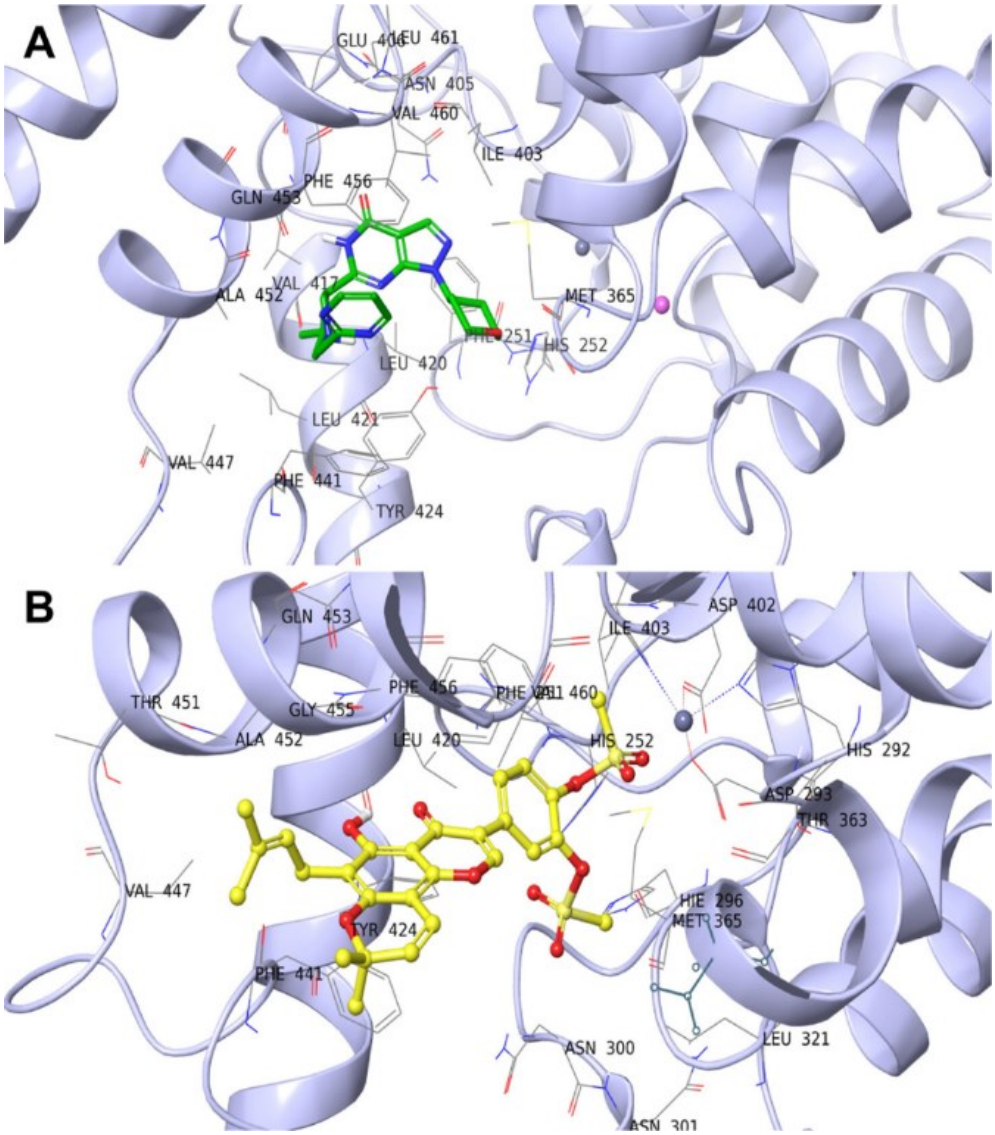

Figure 57. Binding poses for PF-04447943 (A) and DB987 (B) in the predicted interaction pattern with PDE9A. Residues within the binding pocket at interaction distances (<5 Å) have been labeled.

Since Gln453 and Phe456 are considered essential residues in the literature for achieving the inhibitory effects of the ligand against the enzyme, their interaction with the identified compound was studied [409–411]. More specifically, interaction analysis revealed the presence of hydrogen bonds, π–π stacking interactions, salt bridges, and metal coordination in the evaluated complex.

More specifically, isoflavone DB987 (−11.7 kcal/mol, **Figure 57B**) established two hydrogen bonds and one metal coordination bond. These were generated, respectively, with O38 and –OH in Tyr424 (2.06 Å) and between O37 and $–NH_2$ concentrations in Asn300 (2.67 Å). One metal coordination bond (2.13 Å) with Zn^{2+} and O32 was also detected.

MD Simulations

To more accurately assess the stability of the interaction predicted by molecular docking, MD simulations were performed. The starting point for these simulations was, in both cases, the best-docked poses from molecular docking. The dynamics simulation demonstrated that most of the interactions present in the best-docked poses were confirmed and maintained over time, despite varying contributions from different components. The studied PDE9A/ligand complexes yielded stable MD trajectories over the simulation time frame (500 ns; **Figure 58**).

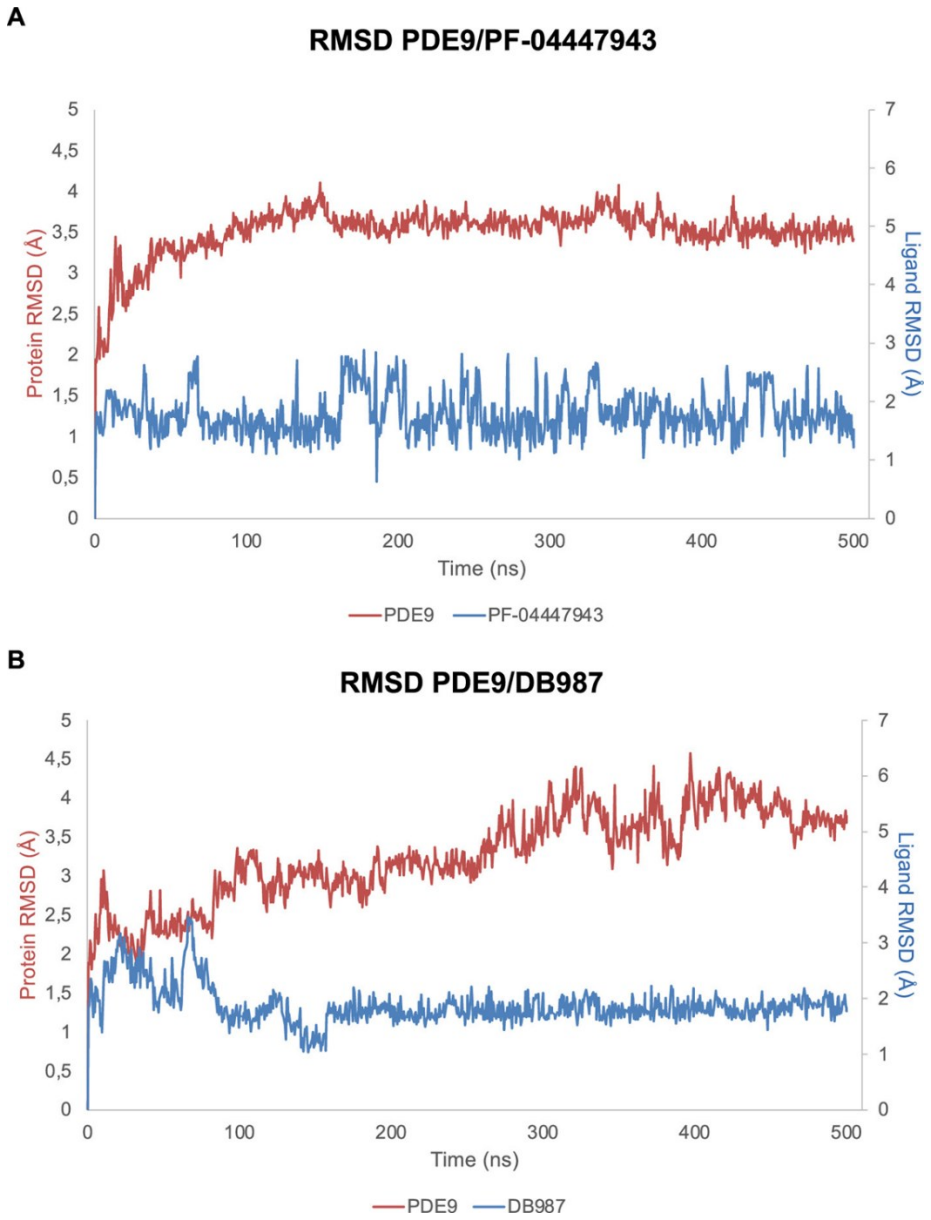

Figure 58. Trajectories retrieved from MD simulations showing the RMSD of the PDE9A/ligand systems over the simulation time (A: PF-04447943, B: DB987). The plots for the heavy atoms of the ligand are depicted in blue (aligned with the protein), while the plots for protein C-alphas are depicted in red.

First, the binding mode of PF-04447943 was analyzed. The stability of the receptor was achieved after 150 ns (**Figure 58A**). Even in the case of the ligand, the RMSD trajectory was observed to be stable, except for a few sections of the simulation where it showed some fluctuations. This could be explained by the measurement of the RMSF value (Figure S1A), which shows that the pyrimidine ring and tetrahydropyran portions of the ligand, being bound to the scaffold by a single bond, have a larger degree of freedom. This is also confirmed by Figure S2, which shows the RMSD plot related only to the ligand scaffold. As it is more rigid, it exhibits minimal fluctuation and remains in place throughout the simulation. The behavior of the protein was also taken into consideration. As expected, the most flexible components of the structure proved to be the C- and N-terminal regions, as well as the side chains that contain most of the residues that establish bonds with the ligand.

In addition to the system's stability and flexibility, the predominant interactions established between the ligand and PDE9A during the simulation were also evaluated. The hydrogen bond between the carbonyl oxygen atoms of Gln453 and N7, observed in the docked model, is maintained over time. Subsequently, Asn405 also established one hydrogen bond with O6 of the previous moiety. Then, Phe456 establishes a π–π stacking interaction with the hydroxy-substituted pyrimidine ring of allopurinol and creates a π-cation interaction with –N13. Other less prevalent hydrophobic interactions, such as π–π stacking, π-cation, and van der Waals forces, have been identified among residues including Phe251, Met365, Ile403, Leu420, Leu421, Tyr424, Phe441, and Phe456. An overview of the established interactions is reported in Figures S3–S5.

The MD profile of the PDE9A/DB987 complex was then studied (**Figure 58B**). Unlike in the case of the PDE9A/PF-04447943 complexes, system stability is achieved after approximately 100 ns, as indicated by RMSD plots. Looking at the stability of the ligand, some spikes were again observed in the RMSD curve. This may be due to the presence of the single bond between C6 and C7, which introduces more freedom to C7–C11 groups (Figure S1B)—concerning the flexibility of PDE9A verified by RMSF, as in the two previous cases, the C- and N-terminal parts and the areas of the side chains interacting with the ligand are the most flexible.

To assess this, in addition to being stable, the ligand was also capable of establishing interactions with the receptor, which was evaluated using the same threshold value adopted for PF-04447943 (*see Materials and Methods*). One hydrogen bond exists between Met365

and O38. The other hydrogen bonds detected below the threshold value are those established with residues His296, Asn300, Asn301, and Met365.

In the case of DB987, hydrophobic interactions, including π–π stacking, π–cation interactions, and van der Waals forces, were observed during the simulation. For instance, Phe456 established one π–π stacking interaction with one of the aromatic rings of the ligand. Less predominant hydrophobic interactions such as those with Leu321, Met365, Ile403, Val417, Leu420, Leu421, Tyr424, Phe441, Ala452, and Phe459 were present. The analysis also reported ionic interactions due to the presence of metal coordination centers. Zn^{2+} formed metal coordination bonds with His296, His292, Asp402, Asp403, and O32 of DB987 during the simulation. Mg^{2+}, on the other hand, established bonds of the same nature with residues His292, Asp293, Glu322, His325, and Thr363 and with the O31 of the ligand. An overview of the established interactions is reported in Figures S3–S5.

Assessment of PDE9A Expression in Organotypic Hippocampal Slices

The expression of PDE9A was detected in organotypic hippocampal slices with or without exposure to KA. The gene and protein expression of PDE9A was elevated as determined by PCR, real-time PCR, and western blot, as shown in **Figure 59**. A significant increase in the level of PDE9A in slices exposed to 5 μM KA for 24 h was observed (**Figure 59C, D**). Previous studies showed that PDE9A mRNA is elevated in the aged human hippocampus with dementia when there is a history of traumatic brain injury [412], and PDE9A expression is upregulated during cardiac hypertrophy and heart failure [413].

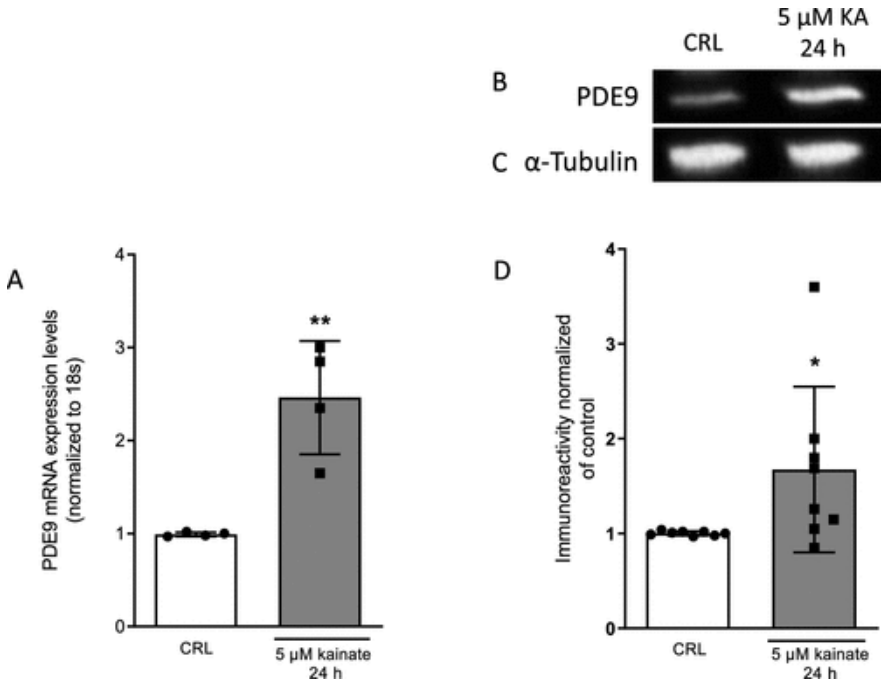

*Figure 59. PDE9A increased in organotypic hippocampal slice cultures exposed to KA. The mRNA levels of PDE9A were increased in slices treated with KA (A). Illustrative blots using antibodies directed against PDE9A (B) and β-tubulin (C). Quantitative analysis of immunoreactive bands reveals significant changes in PDE9A levels in slices treated with KA (D). Dot blots show the results of four (A) and eight (D) experiments from independent slice preparations, and each dot is the pool of four slices. *p < 0.05 and **p < 0.01 vs CRL (unpaired t-test).*

Using a different experimental technique, we assessed the effect of exposure to 5 µM KA for 24 h on the expression of PDE9A in the CA3 hippocampus by immunofluorescent staining and confocal microscopy. The qualitative confocal microscopy images (**Figure 60A-B2**) show that PDE9A expression was increased in CA3 SP of slices treated with KA (**Figure 60B-B2**) in comparison to CRL slices (**Figure 60A-A2**). As already published [414], in KA-treated slices, the morphology of neurons appeared altered, and numerous neurons showed a shrunken, elongated cytoplasm in comparison to controls, and we also observed morphological alterations in glial cells (see Figure S6A–E in the Supporting Information). The confocal images shown in **Figure 60D-D2**, which are magnifications of the framed areas in **Figure 60B-B2**, clearly demonstrate that PDE9A expression increased in CA3 pyramidal neurons that show signs of damage (**Figure 60C-C2**, open arrows).

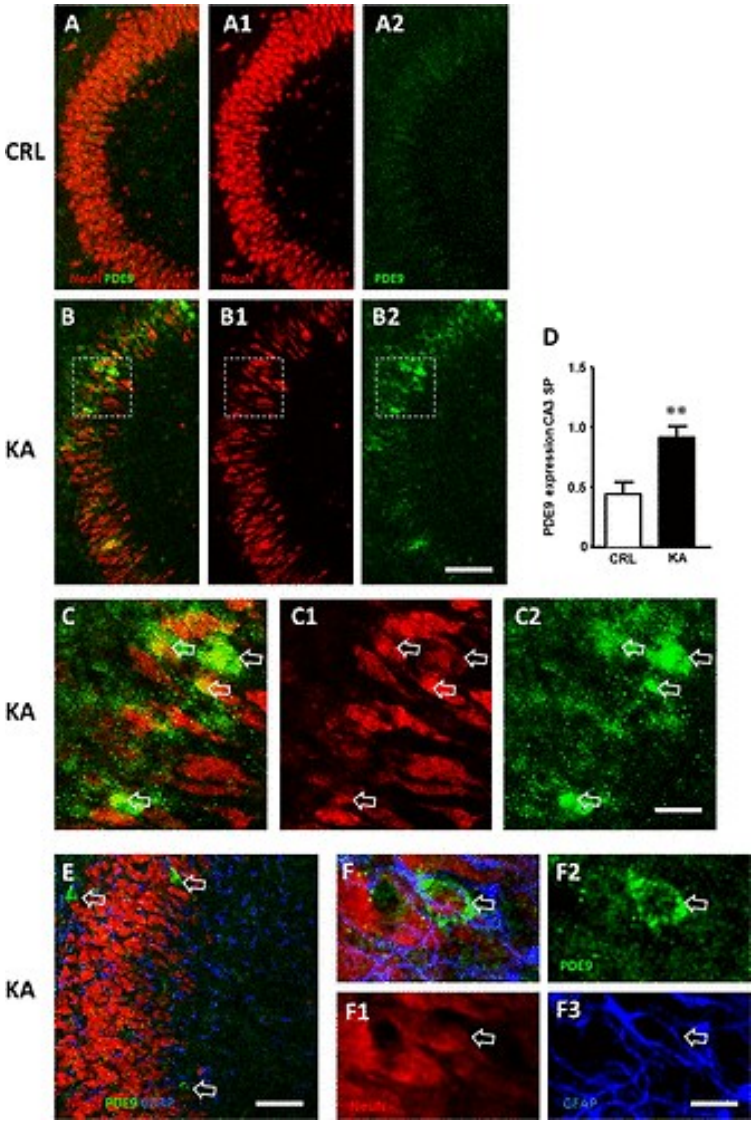

*Figure 60. (A-B2) Immunohistochemical assessment of neuronal damage and PDE9A expression in the CA3 hippocampus of organotypic slices after treatment with KA. (A1, B1) Representative confocal images of fluorescent immunostaining of NeuN-positive neurons in area CA3 of CRL (A1) and KA (B1) slices. (A2, B2) Representative confocal images of fluorescent immunostaining of PDE9A in area CA3 of CRL (A2) and KA-treated slices (B2). (A, B) Merge of the previous images. All images were captured with a 20× objective. Scale bar: 100 µm. (C-C2) Magnifications of the framed areas of the corresponding slice shown in B, B1, and B2. (C1) Immunostaining of NeuN showing the presence of damaged neurons with an elongated, shrunk cytoplasm. (C2) Immunostaining of PDE9A showing the expression of the enzyme in many CA3 pyramidal neurons (open arrows). (C) Merge of the two previous images (open arrows indicate neurons positive for PDE9A immunostaining). Scale bar: 25 µm. (D) Quantitative analysis of PDE9A immunostaining in CA3 SP (CRL n = 10 and KA n = 9). Statistical analysis: Student's t-test: **P < 0.01 KA vs CRL. (E-F3) Representative confocal images of triple immunofluorescent labeling of neurons (NeuN, red), PDE9A (green), and astrocytes (GFAP, blue) in CA3 of KA-treated slices captured with a 40× objective. Open arrows indicate PDE9A-positive pyramidal neurons. No colocalization with astrocytes was found. Scale bars: 70 µm (E) and 15 µm (F-F3).*

The quantitative analysis (**Figure 60D**) demonstrated that the treatment with KA significantly increased PDE9A expression in CA3 SP (Student's *t*-test: $^{**}p < 0.01$ KA vs CTR; CTR, $n = 10$; and KA, $n = 9$).

In addition, triple immunostaining demonstrated no colocalization of PDE9A expression with astrocytes in CA3 SP or SR in KA-treated slices (**Figure 60E-F3**). Furthermore, no colocalization of PDE9A with microglia was present in CA3 in organotypic slices treated with KA (Figure S6F in the Supporting Information). Consistent results from different approaches indicated that PDE9A may play a key role in brain degeneration. These data are in accordance with previous studies, which have localized PDE9A only in neuronal cells [415].

Assessment of PDE9A Inhibitory Activity

In the current study, the potential of DB987 was tested under the same conditions. Experimentally, PDE9A activity was evaluated using an enzymatic assay with increasing concentrations of the tested compound, and the results were expressed as percentages to calculate the IC_{50} values (**Figure 61**). An IC_{50} value of 5.35 nM was calculated for DB987, while the inhibitor potency observed with PF-04447943 was 14.00 nM, demonstrating that DB987 had a good affinity for the target.

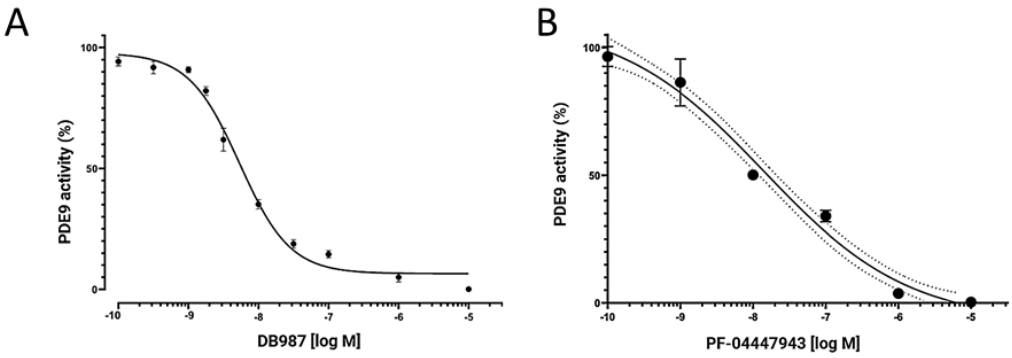

Figure 61. Concentration-dependent inhibitory activity of DB987 (A) and Pf-04447943 (B) on PDE9A in vitro. Results are shown as the mean of eight replicates ± SEM.

Effects of PDE9A Inhibitors on KA Neurotoxicity in Organotypic Hippocampal Slices

Based on previous studies, the reduction in the CA3 regions of organotypic hippocampal slices, caused by neuronal damage induced by KA exposure, was reduced after CBD administration, as indicated by PI fluorescence [414]. We also identified CBD as a drug-like PDE9A inhibitor through virtual screening and *in vitro* experiments. In this study, we observed that the studied PDE9A inhibitors did not induce damage in the CA3 area of slices at varying concentrations (**Figure 62A, B, C, and G**).

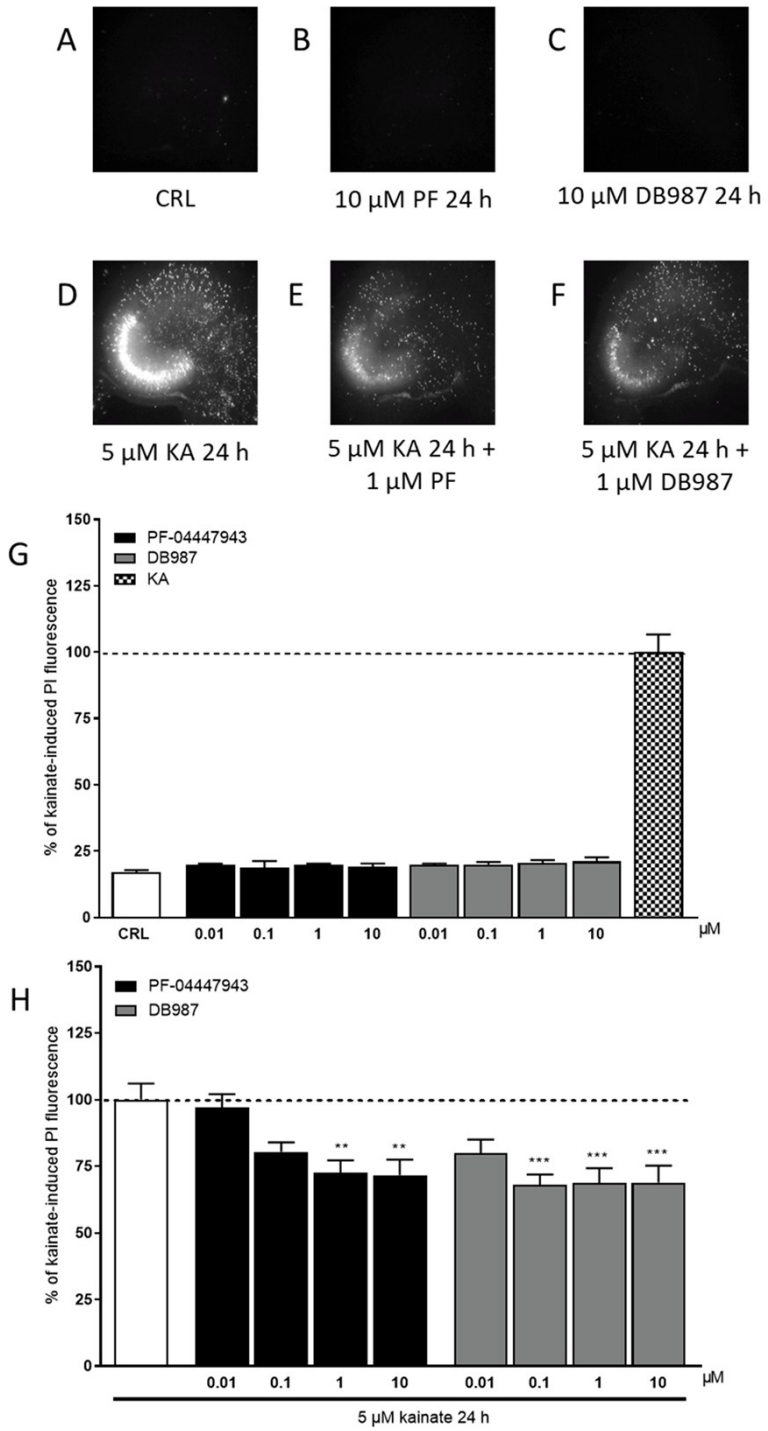

*Figure 62. Qualitative and quantitative analyses of the effects of PDE9A inhibitors in rat organotypic hippocampal slices under normal conditions or exposed to KA. (A) Hippocampal slice under normal conditions (background PI fluorescence), (B) slice exposed to 10 µM PF for 24 h, (C) slice exposed to 10 µM DB987 for 24 h, (D) slice exposed to 5 µM KA for 24 h displaying intense PI labeling in the CA3 subregion, and (E, F) CA3 damage induced by KA was attenuated by the presence of 1 µM PF and DB987. (G) PDE9A inhibitors alone did not induce side effects. (H) PDE9A inhibitors significantly attenuated CA3 damage in a dose-dependent manner. Bars represent the mean ± SEM of at least five experiments run in quadruplicate. **p < 0.01 and ***p < 0.001 vs KA (one-way ANOVA plus Dunnett's test).*

When the slices were incubated for 24 h with 5 μM KA, we observed a selective damage in the CA3 area (**Figure 62D**), in agreement with previous findings [414,416]. Treatment of slices with the PDE9A inhibitor PF-0447943 (0.01-1 μM) during the 24 h KA exposure significantly reduced neuronal death in a dose-dependent manner in CA3 at concentrations of 1 and 10 μM (**Figure 62E, H**). Importantly, we observed similar neuroprotective effects when the slices were incubated with the new PDE9A inhibitor DB987 (0.01–10 μM), which reduced the KA-induced damage at concentrations of 0.1–10 μM (**Figure 62F, H**), in accordance with the IC_{50} values obtained from the enzymatic assay.

In conclusion, computational studies were performed to evaluate the predicted binding affinity, stability, and interactions of a novel potential PDE9A ligand by molecular docking and MD simulations. Molecular docking analyses revealed that the highlighted semisynthetic compound, specifically the isoflavone DB987, interacts efficiently with the PDE9A catalytic site, and MD simulations confirmed the stability of the complex formed by the ligand. Then, we experimentally demonstrated that PDE9A was expressed in rat organotypic hippocampal slices and increased upon exposure to KA. Most importantly, the compound exhibited nanomolar inhibitory activity against PDE9A and reduced neuronal damage induced by KA *in vitro*. Taken together, the results of this study pave the way for more targeted development of new, semisynthetically obtainable, potential PDE inhibitors to be used against neurodegenerative diseases.

Materials and Methods

All the current data are published; readers can access the Supporting Information on the publication site [417].

Database Search

The considered database consists of 1632 compounds synthesized in-house. The database file, in SDF format, was directly loaded into Schrödinger Maestro version 13.4.134 and MMshare Version 6.0.134 Release 2022-4 on Platform Linux-X86_64: Maestro (Schrödinger, LLC, New York, NY, USA 2021). The structures were prepared with the LigPrep tool under the OPLS4 force field using an Epik ionizer; all the ionization states were generated in the 7 ± 2 pH range, including the possible metal states, leading to a total of 3150 molecules, which were analyzed with the QikProp tool to predict the pharmacokinetic properties [63,418,419]. The molecules having more than one violation of the "Lipinski's rule of five" were discarded, reducing the number of possible hits to 1762 [395]. These molecules were then filtered based on their chemical structure, and to perform this step, we loaded the SDF file retrieved from Schrödinger in ChemFinder Version 20.1.1 (ChemOffice, PerkinElmer Informatics, Inc. Waltham, MA, USA, 2020), and we used the chromone-based query (**Figure 56**) to screen the compounds, which were reduced to 441. Then, the molecules were loaded into Schrödinger to perform the docking study as described in the following paragraphs. The complexes resulting from the docking experiments were visually inspected, and the 20 molecules with the best poses, considering the docking score, were selected. The hit compounds retrieved physically from the database following the preliminary virtual screening were subjected to a solubility test. A 10 mM stock solution of the compounds was prepared in DMSO, and they were then diluted to 100 μM solutions in H_2O. Then, three additional 1:10 dilution steps were performed in phosphate-buffered saline (PBS, pH 7.4) to achieve a concentration range of 1 nM, ensuring adequate solubility of the compounds for the *in vitro* test.

Molecular Docking

The human PDE9A 3D structure was obtained from the RCSB Protein Data Bank (PDB, http://www.rcsb.org, accessed January 30, 2023). PDE9A in complex with inhibitor PF-04447943, entry PDB ID 4E90, was selected (resolution 2.50 Å).

The preparation step was performed through the Protein Preparation Workflow tool. Default parameters were selected, for example, adding hydrogens, assigning disulfide bonds, adding missing side chains using Prime, removing waters, adjusting charges, and minimizing the convergence of heavy atoms to RMSD under the OPLS4 force field [63].

Ligands were prepared for docking with the LigPrep tool under the OPLS4 force field. Possible ionization and metal binding states at target pH 7.0 ± 2.0 were generated with an Epik ionizer [419].

The binding poses of PF-04447943 and DB987 in complex with PDE9A were obtained through molecular docking calculations using Glide [300,301]. Ligands and receptors were prepared as described in the previous paragraphs.

The docking protocol consisted of rigid receptor and flexible ligand sampling, which was performed under the OPLS4 force field using standard precision (SP) with default settings like 0.80 scaling factor for the ligand atom van der Waals radius, 0.15 partial range cutoff, adding Epik state penalties to the docking score, generation of one pose per ligand, and performing post-docking minimization for generated poses [418].

The receptor grid was prepared with the Receptor Grid Generation tool included in Schrödinger, with default settings [300]. After identifying the best poses, the RMSD value was used to validate the adopted method using the rmsd.py script. A score under 2.50 Å was considered to indicate that the analysis was sufficiently accurate. In this study, an RMSD value of 1.18 Å was obtained. The obtained poses were evaluated using the GlideScore (GScore) scoring function, expressed in −kcal/mol, and by inspecting the interactions established between ligands and PDE9A. For interaction analysis, only residues within 5 Å in the binding pocket were considered.

Molecular Dynamics

MD simulations were performed using the GPU-accelerated Desmond tool of Schrödinger LLC (Schrödinger Release 2023-1: Desmond Molecular Dynamics System, D. E. Shaw Research, New York, NY, USA, 2021; Maestro-Desmond Interoperability Tools, Schrödinger, New York, NY, USA, 2021). The best protein–ligand complexes retrieved from the SP molecular docking step were used to prepare the solvated system to perform MD.

By using System Builder, all three complexes were solvated using the explicit TIP3P water model. Periodic boundary conditions were set with an orthorhombic box shape

of 10 × 10 × 10 Å. During ion placement, Na^+ ions were used to neutralize the system, a concentration of 0.15 M of NaCl was set, and an exclusion zone with 20 Å from the ligand was added. A run of 500 ns was performed for each complex under the OPLS4 force field with the temperature set at 300 K and pressure at 1.0 bar. Further, the Martyna–Tuckerman–Klein chain coupling scheme with an isotropic coupling constant of 2.0 ps for the pressure control and the Nosé–Hoover chain coupling scheme for the temperature control (NPT ensemble) were used. The cutoff radius in the Coulomb interactions was 9.0 Å. A RESPA integrator was set with time steps of 2.0 fs for bonded interactions and 6.0 fs for near and far interactions, respectively. Trajectories were saved at 500 ps intervals for analysis [420].

To analyze interactions between ligands and PDE9A, the Simulation Interaction Diagram tool and RMSD/RMSF evaluation were used. When ligand–protein contacts were evaluated, a contact strength threshold value of 30% was considered for all the analyses.

Chemicals and Biological Materials

Tissue culture reagents were obtained from Gibco-BRL (San Giuliano Milanese, MI, Italy) and Sigma (St. Louis, MO, USA). PF-0447943was purchased from Sigma (St. Louis, MO, USA). Our group previously reported the synthesis of DB987 [406].

Assessment of PDE9A Inhibitory Activity

To assess the inhibitory activity of DB987 against full-length recombinant human PDE9A (PDE9AA, SignalChem, Richmond, Canada), the PDE-Glo phosphodiesterase assay (Promega Corp., Madison, WI, USA) was used as previously reported [393]. The compound was dissolved in DMSO and mixed with the PDE-Glo reaction buffer at a v/v ratio of 1:5. Aliquots of PDE-Glo reaction buffer with appropriate amounts of human recombinant PDE9A were placed in separate wells of a 96-well plate (PerkinElmer, Milan, Italy). Subsequently, the solution (5 µL) containing a PDE inhibitor and 12.5 µL of cGMP solution as a substrate was added to each well. Each time after the addition of the solutions, the plates were gently shaken on a 3D rotator to ensure that the content was evenly distributed over the bottom of each well (PS-M3D Variable Speed/Angle, Multi-Function 3D Rotator, Kisker Biotech GmbH & Co. KG, Steinfurt, Germany). The samples were incubated for 90 min at room temperature. Then, PDE-Glo Termination Buffer and PDE-Glo Detection Solution (12.5 µL) were added to each well. After incubation (20 min, room temperature) and the addition of Kinase-Glo Reagent (50 µL) to each well, the

luminescence of each sample was measured by a microplate scintillation and luminescence counter reader, TopCountNXT (Packard, Ramsey, MN, USA). IC_{50} values were estimated through nonlinear regression using Prism v.8 for Windows (GraphPad Software, San Diego, CA, USA). Experiments were performed in eight replicates.

Animals

Male and female Wistar rat pups (7–9 days old) were purchased from Charles River (MI, Italy). Animals were housed at 23 ± 1 °C under a 12 h light–dark cycle (lights on at 07:00) and were fed a standard laboratory diet with ad libitum access to water. The experimental protocols were approved by the Animal Care Committee of the Department of Health Sciences, University of Florence (17E9C.N.GSO/2021).

The experimental procedures were conducted in accordance with the ARRIVE guidelines and were authorized by the Italian Ministry of Health. The ethical policy of the University of Florence complies with Directive 2010/63/EU of the European Parliament and with Italian Regulation DL 26/2014 on the protection of animals used for scientific purposes. According to the law, all efforts were made to fulfill the principle of the 3 Rs.

Preparation of Rat Organotypic Hippocampal Slice Cultures

Organotypic hippocampal slice cultures were prepared as previously reported [421]. Briefly, hippocampi were removed from the brains of 7–9 day old Wistar rat pups (Charles River, Milan, Italy), and transverse slices (420 μm) were prepared using a McIlwain tissue chopper and then transferred onto 30 mm-diameter semiporous membranes inserts (Millicell-CM PICM03050; Millipore, Milan, Italy; four slices per insert), which were placed in six-well tissue culture plates containing 1.2 mL of medium per well. The culture medium compound is composed of 50% Eagle's minimal essential medium, 25% heat-inactivated horse serum, 25% Hanks' balanced salt solution, 5 mg/mL glucose, 2 mM l-glutamine, and 3.75 mg/mL amphotericin B. Slices were maintained at 37 °C in an incubator in an atmosphere of humidified air and 5% CO_2 for 2 weeks.

During the incubation period, the slices mature and become ready for the experiments. The slices were incubated for 24 h with 5 μM kainic acid (KA) in the presence or absence of PDE9A inhibitors. KA concentration and incubation time were chosen based on previous studies, and a selective damage was induced in CA3 [414,416,422]. The slices were incubated for 24 with PF-0447943 (0.01–1 μM) or DB987 (0.01–10 μM), alone or in

combination with 5 μM KA. Cell death was evaluated using the fluorescent dye propidium iodide (PI, 5 μg/mL), and fluorescence was viewed using an inverted fluorescence microscope (Olympus IX-50; Solent Scientific, Segensworth, UK) equipped with a xenon arc lamp, a low-power objective (4×), and a rhodamine filter. Images were digitized using a video image obtained by a CCD camera (Diagnostic Instruments Inc., Sterling Heights, MI, USA) controlled by software (InCyt Im1TM; Intracellular Imaging Inc., Cincinnati, OH, USA). Images were analyzed by using morphometric analysis software. Cellular death induced by KA in the CA3 hippocampal subfields was quantified by the image software (ImageJ; NIH, Bethesda, MD, USA) detecting the optical density of PI fluorescence (the fluorescence measured in KA-exposed slices in the CA3 region was taken as 100%) [414,423].

Evaluation of PDE9A Gene Expression by Quantitative Real-Time Polymerase Chain Reaction

Total RNA was isolated from organotypic hippocampal slices (four slices for the sample) using Trizol reagent (Life Technologies, Carlsbad, CA, USA). 1 μg of RNA was retrotranscribed using *iScript* (Bio-Rad, Milan, Italy). Real-time polymerase chain reaction (RT-PCR) was performed as reported [424,425]. The following primers were used: PDE9A rat: forward 5′-TCAGAGCGAACTCCCTACAAGGTGAG-3′ and reverse 5′-CTCCACCACTTTGAGTCCTTCCAATTCC-3′; 18S rat: forward 5′-GGCGGCTTTGGTGACTCTAGATAACC-3′ and reverse 5′-CCTGCTGCCTTCCTTGGATGTGG-3′.

Western Blot Analysis

Western blotting was conducted as previously reported [416]. Four slices of the sample were dissolved in 1% SDS. BCA (bicinchoninic acid) protein assay was used to quantify the total protein levels. Lysates (20 μg/lane of protein) were resolved by electrophoresis on a 4–20% SDS-polyacrylamide gel (Bio-Rad Laboratories, Hercules, CA, USA) and transferred onto nitrocellulose membranes. After blocking, the blots were incubated overnight at 4 °C with rabbit-polyclonal anti-PDE9A (Millipore, Burlington, Massachusetts, USA) diluted 1:1000 in TBS-T containing 5% nonfat dry milk. β-Tubulin was used as a loading control (monoclonal antibody) purchased from Sigma (St Louis, MO, USA). Immunodetection was performed with HRP-conjugated secondary antibodies

(1:2000) antimouse or antirabbit IgG from donkey (Amersham Biosciences, Little Chalfont, UK) in TBS-T containing 5% nonfat dry milk. After the membranes and reactive bands were washed, they were detected using chemiluminescence (ECLplus; Euroclone, Padova, Italy). Quantity One analysis software was used for quantitative analysis (Bio-Rad, Hercules, CA, USA). Results are presented as the mean standard error of the mean (SEM) of different gels and expressed as AU-, which depicts the ratio between the levels of target protein expression and β-tubulin normalized to basal levels.

Fluorescence Immunohistochemistry

At the end of treatments with KA, the organotypic hippocampal slices were harvested and fixed overnight (O/N) in ice-cold paraformaldehyde (4% in PBS). The following day, slices were placed in a sucrose solution (18% in PBS) for at least 2 days and then conserved in an anti-freezing solution at −20 °C until used for immunohistochemistry. Immunohistochemistry was performed with the free-floating method as previously reported [414,426,427].

First day: Hippocampal slices were placed in a multi-well and incubated for 60 min with blocking buffer (BB) containing 10% normal goat serum. The slices were then incubated overnight at 4 °C under slight agitation with a mouse anti-NeuN to immunostain neurons (1:400 in BB; product code #MAB377, Millipore, Billerica, MA, USA) and a rabbit anti-PDE9A antibody to immunostain PDE9A (1:100; code ABN32, Merck, Darmstadt, DE), dissolved in BB.

Second day: Slices were incubated for 2 h at room temperature in the dark with AlexaFluor 555 donkey antimouse (1:400 in BB; product code #A31570, Thermo Fisher Scientific, Waltham, MA, USA). Slices were then incubated for 2 h at room temperature in the dark with AlexaFluor 555 donkey antimouse plus AlexaFluor 488 donkey antirabbit (1:400 in BB; product code #A21206, Thermo Fisher Scientific). Astrocytes were immunostained using a mouse anti-GFAP antibody conjugated with the fluorochrome Alexa Fluor 488 for 2 h at room temperature in the dark (1:500; code MAB3402X, Millipore). The slices were mounted onto gelatin-coated slides using Vectashield mounting medium with DAPI (Product Code #H-1200, Vectashield, Burlingame, CA, U.S.A.). Slices were observed under a LEICA TCS SP5 confocal laser scanning microscope (Leica Microsystems CMS GmbH, Mannheim, Germany) equipped with 20×, 40×, and 63×

objectives (*z* step of 1.2 µm, 0.6 µm, or 0.3 µm, respectively). Confocal scans were acquired, keeping all parameters constant.

Quantitative Analyses for Immunohistochemical Experiments

Image analyses were performed with ImageJ software (NIH, Bethesda, MD, USA) on z-stack projections of the region of interest, corresponding to area CA3. We quantified the number of NeuN-positive neurons in the CA3 Stratum Pyramidalis (SP). PDE9A and GFAP immunofluorescence in CA3 SP were detected by setting a fixed threshold level and quantifying the positive pixels above threshold with the ImageJ threshold tool, and were expressed as percent-positive pixels/total pixels. Astrocyte branches were measured in accordance with Cerbai et al. by quantifying only the number of branches longer than 70 µm and expressing their density as branches/mm^2 [428].

Statistical Analysis

Data are presented as means ± SEM of *n* experiments. The statistical significance of differences between PI fluorescence intensity data was analyzed using one-way ANOVA with a post hoc Dunnett's t-test for multiple comparisons. Student's t-test statistically analyzed RT-qPCR, western blot, and immunohistochemistry data. All statistical calculations were performed using GraphPad PRISM v. Eight for Windows (GraphPad Software, San Diego, CA, USA). A probability value (*P*) of <0.05 was considered significant.

3.3 Rational Design of DB987 for Targeting Neuroinflammation

Based on the results of DB987 identification, the search for new PDE9A inhibitors proceeded by fragmenting DB987 through a structure-activity relationship study using a database available in the laboratory. The selection criterion was based on structural affinity with DB987, achieved through modification of pomiferin, a natural flavonoid extracted from *Maclura pomifera*. Pomiferin has been demonstrated to be a neuroprotective compound in rat hippocampal slices (IC_{50} of 5.35 nM), where neuroinflammation was induced by KA exposure.

In silico studies enabled the fragmentation of DB987 to identify new substructures with a similar biological effect. Out of the 672 molecules present in the library, only 27 compounds were identified to be sub-structurally similar to DB987. A screening on the DB987 Subset was performed using *in silico* tools, such as molecular docking and molecular dynamics simulations, which enabled us to identify BS560 and BS586, quercetin-derivative compounds, as the best PDE9A binders. Then, PDE9A inhibition was assessed using a recently developed HPLC-based method, which identified BS560 as the best PDE9A inhibitor. In this context, my work mainly focused on performing computational studies, which are being evaluated in collaboration with the University of Florence.

Results and Discussion

Building on the findings from our publication, in which DB987, a derivatized pomiferine, was identified as a potent PDE9A binder and inhibitor (IC_{50} = 5.35 nM), we performed a substructural search analysis using this compound as a reference scaffold (**Figure 63**) [406,417]. Our objective was to identify more effective PDE9A inhibitors capable of mitigating neuronal inflammation, a hallmark of numerous neurodegenerative disorders, such as AD and PD, in which PDE9A expression is increased [429,430].

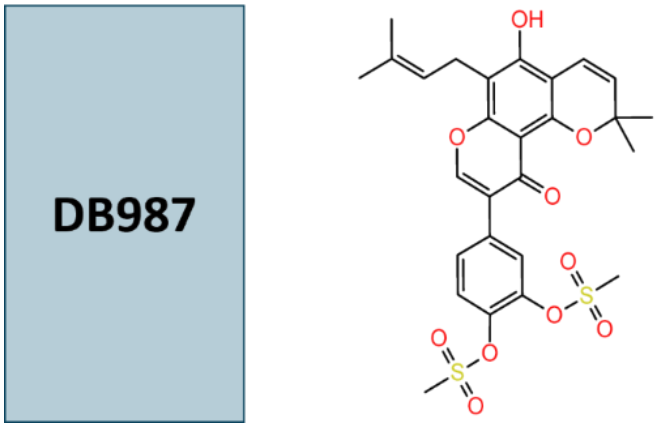

Figure 63. Structure of DB987 used as a reference for query generation.

To identify structural queries deriving from DB987, a minimum number of carbon atoms equal to 8 and the presence of at least two heteroatoms were used. These allowed the generation of 6 queries (A to F) in which a natural scaffold, such as coumarins, was present (**Figure 64**). Generated queries were then used to screen the in-house database, which comprised 672 compounds. Of these, only 27 molecules matched the search criteria and were used to perform molecular docking analysis.

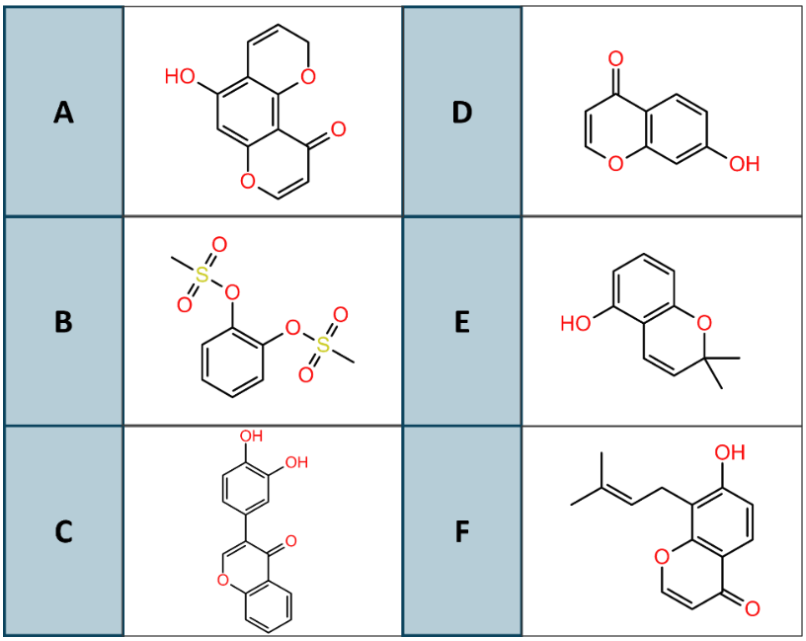

Figure 64. Queries obtained from DB987.

Molecular docking

The top 5 binders (excluding BS579, which is considered an internal control) resulting from molecular docking (BS590, BS563, BS586, BS579, BS570, and BS560) were evaluated in terms of docking score and the nature of their interaction established with the target.

Since PF-04447943 formed strong hydrogen bonds and hydrophobic interactions with Gln453 and Phe456, these residues were used as a screening criterion, thereby allowing the identification of compounds BS586 and BS560, a quercetin and a 6-bromo-quercetin derivative. The 3D structure consisting of a crystallized PDE9A enzyme and the cognate ligand PF-04447943 was retrieved from the RCSB Protein Data Bank (PDB ID: 4E90). In the context of this structure, it can be noted that PF-04447943 established good hydrogen bonds and hydrophobic interactions with key residues like Gln453 and Phe456, supporting the relevance of these two residues [388,417]. DB987 (−8.782 kcal/mol) established a hydrogen bond with His296, where the Hε2 atom of His296 served as the donor and the carbonyl oxygen (O16) of the methanesulfonate group, which acted as the acceptor, thereby resulting in a strong hydrogen bond with a length of 1.86 Å (**Figure 65A**). Similarly, hydrogen atoms Hδ21 of Asn300 and H of Asn301 functioned as donors in hydrogen bonds with the carbonyl oxygens O38 and O37 of the methanesulfonate moieties, at distances of 2.68 Å and 2.44 Å, respectively. Two additional key interactions contributed to the stabilization of DB987, reinforcing its potential as a promising starting compound. One involved the hydroxyl oxygen (O19) of DB987 serving as a hydrogen bond acceptor with the Oε1 atom of Gln453, exhibiting a bond length of 1.77 Å (thus indicating a strong interaction). Another relevant interaction included a π–π stacking interaction between aromatic ring A of the isoflavone scaffold and the aromatic side chain of Phe456, with a ring-to-ring distance of 3.59 Å. Compound BS586 (−9.088 kcal/mol) exhibited interactions between its B ring and both key residues (**Figure 65B**). A hydrogen bond in which oxygen in the hydroxyl group (O20) served as acceptor for the interaction with the Hε22 in Gln453 (1.95 Å). Additionally, B ring established a π–π stacking interaction with the phenyl ring in Phe456 (4.17 Å) and a hydrogen bond between O22 in the hydroxyl moiety of B ring and the carbonyl moiety in Ile403 backbone (1.88 Å). Then, A ring allowed for the formation of a π–π stacking interaction with the imidazole ring in His252 sidechain (5.08 Å), and a C ring allowed for salt bridges and metal coordination formation between atom O19 and Zn^{2+} and Mg^{2+} present in the M pocket. Then, among the top compounds evaluated

through molecular docking, BS560 (-8.360 kcal/mol) stood out for the interactions it established with key residues Gln453 and Phe456 (**Figure 65C**). Two hydrogen bonds were formed between O21 and O23 in the B ring and acted as donors to the Oε1 atom of the Gln453 side chain, with bond lengths of 1.96 Å and 2.08 Å, respectively. The same ring established π–π stacking interaction with the Phe456 side chain (4.08 Å). Further, ring A contributed in BS560 through a hydrogen bond between backbone Thr363 and O7 (2.67 Å) and by a π–π stacking interaction with the imidazole in His252 (5.05 Å). Compounds BS590 (-9.550 kcal/mol), BS563 (-9.177 kcal/mol), and BS570 (-8.607 kcal/mol) were discarded since they did not establish relevant interactions with both PDE9A key residues.

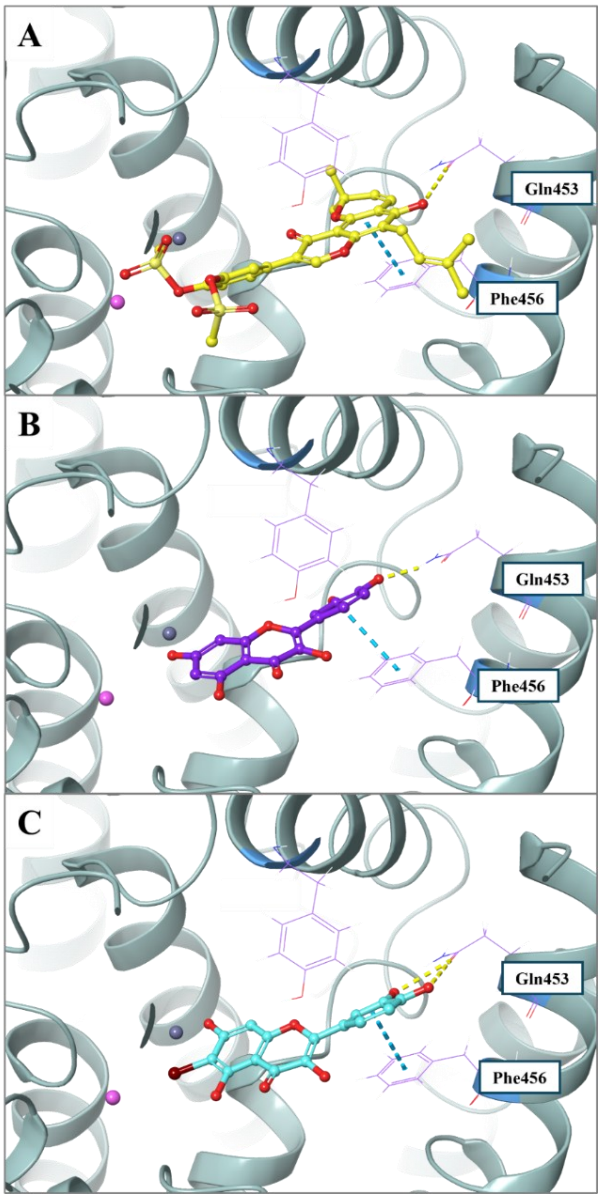

Figure 65. Docking conformations of DB987 (A), BS586 (B), and BS560 (C), showing key interactions with Gln453 (highlighted in yellow for hydrogen bonding) and Phe456 (highlighted in light blue for π–π stacking).

MD Simulations

To evaluate whether the interactions established during molecular docking formed a transient or a stable complex, classical MD simulations were performed, using the docked poses of PDE9A/BS586 and PDE9A/BS560 as starting points for 500 ns simulations. For PDE9A/BS586, the trajectories showed strong stability in both the protein and ligand systems, with only minor fluctuations (**Figure 66A**). By examining interactions that last in 30% of the simulation time, the rings A and C in the ligand are well inserted into the M and H pockets, where they interact through π-cation and π-π stacking interactions with ring A and Lys399. Then, the O19 forms interactions with Zn^{2+}, Asp293, His256, Asp402, and His292, suggesting a good insertion into the M pocket. Furthermore, the interaction between Hε22 in Gln453 and O5 in BS586 contributes to maintaining the stability of the complex. When checking B ring in BS586 showed a highly stable and rigid structure given by a set of hydrogen bonds partially mediated by water molecules between Glu406, Ala413, Asn405, and O20, and between Ile403 and O22. The set of these interactions effectively minimized fluctuations in BS586, keeping it stably within the binding pocket throughout the simulation.

Then, the PDE9A/BS560 complex was evaluated. Unlike BS586, during the first 150 ns, the RMSD plot of the complex showed major oscillations, which were attenuated during the simulation. Furthermore, RMSD analysis of the final frames revealed a greater oscillation of the protein at 460 ns, which was attributed to the C-terminal helix (residues 481-503) (**Figure 66B**). By examining the interactions present in at least 30% of the simulation, a metal coordination center was identified between Zn^{2+} in the protein, Br, and the O7 atoms in ring A, which supported the interactions with Asp293, His256, His292, and Asp402. Further, O5 in ring A established a hydrogen bond with Thr363. Then, ring C interacted with Tyr424 aromatic ring *via* a π-π stacking interaction, and O11 displayed a water-mediated hydrogen bond with Asp364, and a hydrogen bond with Met365 was established for 34% of the simulation. Another relevant interaction between Gln453 and the O23 atom in ring B was detected, suggesting a stabilizing effect of the ring in the complex. Different from BS586, BS560 had a spike associated with the B ring in the RMSF profile attributable to the rotation of the single C15-C16 bond. An analysis of the key residues during the simulations of both BS586 and BS560 reveals apparent differences between the two compounds. In the case of the PDE9A/BS586 complex, initial hydrogen bonds formed between Tyr424 and the C ring of the ligand, while Gln453 and Phe456

remained uninvolved throughout the simulation. Over time, Tyr424 gradually reoriented and moved away, reducing the potential for further interactions. Although Phe456 stayed close to the ligand, its orientation was not ideal for stable binding. In contrast, Gln453, although it does not make direct contact, helps stabilize the ligand through water-mediated hydrogen bonds. As a result, while the complex remained structurally stable, its configuration offers limited support for a potential inhibitory effect on PDE9A. Conversely, the orientation of the bromine atom toward the M pocket strongly favors halogen bond formation, aiding in the stabilization of the quercetin scaffold. In the PDE9A/BS560 complex simulation, the Tyr424 residue (important for PDE9A inhibition) positions its side chain parallel to the ligand's C ring, promoting a π–π stacking interaction; likewise, as with the B ring and the side chain of Phe456 [431]. These stacking interactions help stabilize the binding site geometry and correctly orient Gln453, enabling the formation of stable hydrogen bonds.

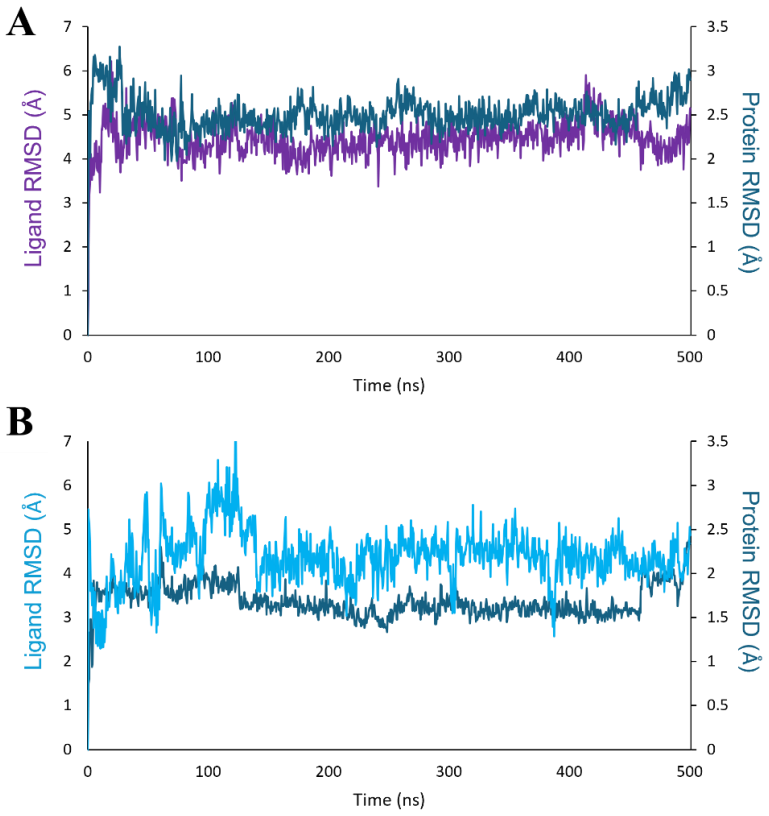

Figure 66. RMSD profiles for PDE9A (in blue) in complex with BS586 (A) and BS560 (B).

3.4 Future Perspectives on PDE9A as Therapeutic Target

Phosphodiesterase 9 localization in cytoplasm and nucleus: the gateway to selective targeting in neuroprotection?

The umbrella term NDD covers conditions involving progressive loss of nervous system cells, affecting over 50 million worldwide. These disorders involve complex factors and mechanisms, often relying on cell signaling pathways with second messengers like cAMP and cGMP to maintain homeostasis. Several effectors like PKA, PKG, PDEs, and scaffold proteins regulate signaling duration and amplitude. cAMP production results from Gs activation of G-protein-coupled receptors and increased species such as CO^2/HCO_3^-, Ca^{2+}, and ATP. Gs activates transmembrane and soluble adenylate cyclases, raising intracellular cAMP. PKA-I and PKA-II, stimulated by cAMP, activate proteins or modulate kinase pathways via phosphorylation. PKA-I inhibits lymphocyte proliferation and immune response; PKA-II influences neuronal gene expression, motor learning, lipolysis, and sperm motility. Their functional differences stem from differences in expression levels, localization, and binding to scaffold proteins. Their tissue-specific roles are linked to spatiotemporal localization supported by A- and G-kinase anchoring proteins (AKAPs and GKAPs that anchor PKA, PDEs, and phosphatases [432]. This complex connects PKA to several receptors and subcellular structures, including the endoplasmic reticulum (AKAP-100), mitochondria (AKAP-84), and nucleus (AKAP-95), leading to the formation of signalosomes and enabling efficient sensing and functioning of cAMP in various subcellular locations. Importantly, cAMP can regulate gene expression through the phosphorylation of the nuclear transcription factor nitric oxide/cGMP/cAMP-response element-binding protein, which is correlated with proliferation, survival, differentiation, neurogenesis, and neuronal plasticity in neurons. Another crucial second messenger is cGMP. Soluble and particulate guanylate cyclases produce it in response to nitric oxide and natriuretic peptides. Additionally, cGMP is related to PKG-I and PKG-II, as well as PDEs, serving as effectors. PKG-I and PKG-II are distinguished by cellular localization, given that PKG-I is highly expressed in platelets, smooth muscle, cardiomyocytes, and many endothelial and neuronal cells, while PKG-II is mainly expressed in the intestine, kidney, and brain cells. PKG is the major intracellular cGMP target in many cell types, but high cGMP concentrations can cross-activate PKA. It is challenging to identify endogenous substrates for PKG, as it is typically expressed at levels that are 10 to 100-fold lower than

those of PKA. Again, PKG is reported to be scaffolded by GKAPs, which are involved in compartmentalization and control the formation of cGMP-based signalosomes [433]. For instance, PKG-I is mainly localized in the cytoplasm, but it is also involved in nuclear translocation events, thus supporting cGMP-mediated gene expression. Notably, more than 50 genes and transcription factors are directly or indirectly influenced by cGMP signaling (e.g., antiapoptotic effects mediated by Bcl-2 or Bcl-2–associated proteins in neuronal cells and activation/inhibition of MAP kinase pathways) [434]. PDEs are known as major effectors of cAMP and cGMP, as they hydrolyze their 3′-phosphate bonds to generate 5′-AMP and 5′-GMP, respectively. Given the pathophysiological importance of cGMP and cAMP, it is pivotal to fully understand their regulation mechanisms, which contribute to both the CNS and peripheral homeostasis. Among them, PDE9A stands out as it has the highest affinity for cGMP (K_m = 70–170 nM), compared to cAMP (K_m = 230 mM). This protein is expressed from the PDE9A gene, which is located on chromosome 21q22.3, and includes over 20 exons. Currently, more than 15 isoforms generated from alternative splicing are reported. Such species distinguish themselves in different tissues and subcellular distribution, thus suggesting cGMP regulation more subtly. Interestingly, PDE catalytic sites are conserved among families, and the main differences can be found in the regulatory N-terminal domain, which might define cellular and subcellular distribution. PDE9A is not an exception, as its N-terminal domain is reported to facilitate its possible localization. In this sense, a different expression pattern for PDE9A6/13 and PDE9A1 regarding their cellular distribution was reported by Wang et al., which stated that PDE9A mRNA is expressed at the highest rate in the brain, bladder, spleen, kidney, and small intestine [384]. The authors found that PDE9A1 exhibited mostly a nuclear localization, while PDE9A6/13 were preponderantly in the cytoplasm fraction. This difference may be explained by the presence of a nuclear localization signal in PDE9A1, identified as a pat7 motif, which defines the ability to translocate across the nuclear membrane. Pat7 is a well-defined residue pattern that starts with a proline that is followed within 3 residues by a basic segment containing at least 3 lysine/arginine residues. Nuclear localization signal is required for the action of nuclear transport proteins, which recognize macromolecules allowed to translocate in the nucleus with consequences in gene expression. However, there are different studies reporting that these translocation events in PDEs context can be mediated by other scaffold proteins such as β2-arrestin and karyopherins [435]. Targeting karyopherins, due to their pivotal role in regulating nuclear events, is an attractive

pharmacological strategy: selinexor is a karyopherin (exportin-1; XPO1) inhibitor approved as an antineoplastic agent, while its derivative eltanexor is currently investigated for PD [436]. Since PDE9A variants have similar enzymatic properties but differential tissue distribution and subcellular localization, and considering the abovementioned evidence, it is tempting to speculate that PDE9A1 could have a unique role in regulating events through the hydrolysis of compartmentalized cGMP pools, which in turn modulate gene expression via cGMP-effector systems. For instance, in the CNS, it is known that PDE9A-regulated cGMP signaling is involved in synaptic plasticity, even if the mechanism related to compartmentalized cGMP has not been fully elucidated yet. Patel et al. showed that PDE9A expression and subcellular localization change across the life span in a manner that is isoform, brain-region, and age specific [412]. It must be noted that in recent years, two mechanisms involving the nuclear translocation of other PDEs have been described. In this regard, PDE1A is mostly enriched in the nuclear fraction of vascular smooth muscle cells, while PDE1C is reported to be more present in the cytoplasm. Nagel et al. (2006) found that PDE1A inhibition led to an alteration of the cell cycle since the reduction of its nuclear expression significantly increased the number of apoptotic cells through the rise of phosphorylated p53 levels. This suggests the pivotal role of PDE1A and PDE1C and their different impacts on the regulation of basal cGMP homeostasis in vascular smooth muscle cells [437].

A similar process was reported by Martinez et al. for another isoform of the PDE4 family, since PDE4D5, from the PDE4D cAMP-hydrolyzing family, was identified to be enriched in the nuclei of cortical and hippocampal neurons [438]. On the other hand, PDE4D8 and PDE4D9 were mainly detected in the cytoplasm. It must be noted that memory and learning are supported by the activation of the expression of immediate early genes promoted by G-protein-coupled receptors. In this work, the authors showed that β2-adrenergic receptor (β2AR) stimulation induced the export of PDE4D5 from the nucleus. Further, they discovered that phosphorylated-β2AR endocytosis, mediated by G-protein-coupled receptor kinases, is implicated in the arrestin3-dependent nuclear export of PDE4D5. This mechanism may aim at limiting nuclear cAMP hydrolysis and promoting nuclear signaling and gene expression in hippocampal neurons. Inhibition of the Arrestin3-PDE4D5 complex did not affect β2AR endocytosis, while direct PDE4 inhibition rescued β2AR-induced nuclear cAMP signaling and improved memory deficits in mice.

These studies further highlighted the translocation events of PDEs as a mechanism to promote second messenger signaling in specific subcellular locations, particularly in the nucleus. The abovementioned PDEs share the ability to cross the nuclear membrane in response to stimuli, and these mechanisms could be comparable with those of PDE9A1 (**Figure 67**). In fact, the unique nuclear localization of PDE9A1, regulated by the pat7 motif, differentiates PDE9A1 from other PDE9A splice variants and other cGMP-hydrolyzing PDE families and implies a potential role of PDE9A1 in the regulation of nuclear events.

PDE9A plays an important role in the proliferation, differentiation, and apoptosis of cells via intracellular cGMP signaling. These effects are more visible in tissues where PDE9A is more expressed. Indeed, pathophysiological disorders could also be addressed to PDE9A expression alterations. This might be the case of cancers in which PDE9A is considered a potential prognostic marker. In this context, PDE9A is reported to be enriched in prostate and breast cancer cells, in which the inhibition of this enzyme increases the number of apoptotic cells. Currently, it is not clear if these effects are related to nuclear or cytoplasmic events; thus, more studies are required to define which PDE9A isoform is involved in the observed effects.

Still, more efforts are needed to understand the subcellular localization of PDE9A, its interaction with other scaffold proteins, and how it influences cGMP signaling at both nuclear and cytoplasmic levels. Considering the potential PDE9A interaction network with other proteins, based on the Human Protein Atlas (proteinatlas.org) interactome, proteins of different classes stand out. Additionally, it is interesting to note that these are classified as nuclear or cytoplasmic, and are related to different pathways (Cryptochrome Circadian Regulator 2, related to circadian rhythm; CDC Like Kinase 1, a prognostic marker in urothelial cancer; Tripartite Motif Containing 32, involved in liver and head and neck cancers), suggesting possible specific interactions for PDE9A1 or PDE9A6/13 at nuclear or cytoplasmic levels, respectively.

Moreover, since PDE9A is also involved in synaptic plasticity due to its expression in the CNS, several clinical trials enrolling PDE9A inhibitors have been carried out for different brain disorders. As cAMP-response element-binding protein signaling is downregulated in these conditions, EISAI company recently developed E2027, a selective PDE9A inhibitor that is currently involved in a Phase 2 study for patients affected by dementia with Lewy bodies. A single dose of E2027 was already reported to increase cGMP

levels in cerebrospinal fluid during Phase 1 [439]. Additionally, our group recently demonstrated the potential of PDE9A inhibitors in neuroprotection [393,440].

Thus, this could represent an attractive topic for future drug development, and considering that nowadays drug discovery heavily relies on structure-based computer-aided drug design, it is important to point out that 3D structures of the targets are needed. Unfortunately, there are still some caveats. In the case of available structures of PDE9A1, its N-terminal domain is not entirely resolved. It is possible that the region containing the pat7 motif, the potential target for neuroprotective drug development, behaves like an intrinsically disordered protein that needs an interactor to reach structural stability.

The first question that arises is whether PDE9A1 mechanisms can parallel those reported for PDE1A and PDE4D5, and which scaffold proteins are involved in these processes. Once these events are fully characterized, the possibility of targeting the N-terminal domain, and Pat7 in particular, to regulate the intracellular trafficking of PDE9A with drug candidates should be explored. Future drug discovery efforts should rely on these findings to pave the way for a more accurate design of therapeutic candidates, aiming to influence nuclear or cytoplasmic PDE9A-related events specifically.

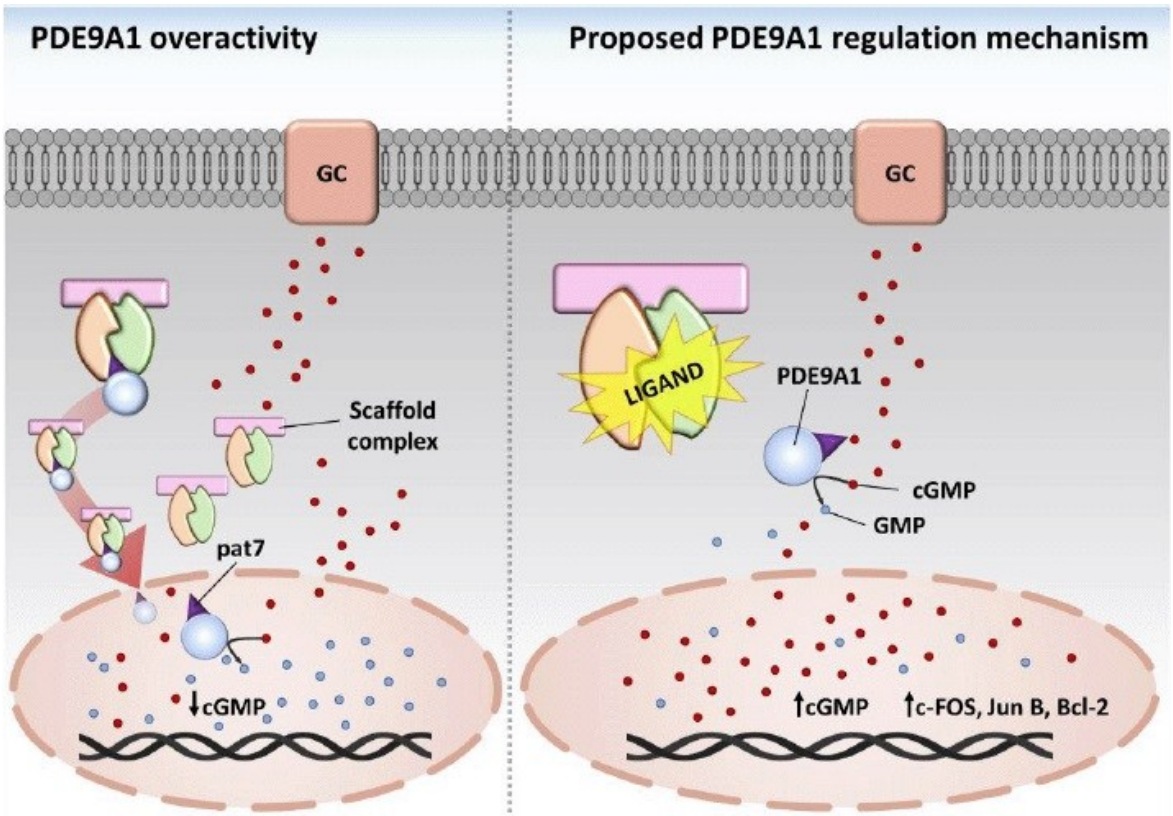

Figure 67. Regulation of nuclear cGMP signaling by preventing PDE9A1 nuclear localization. In the left panel, a case in which PDE9A1 is overactivated is depicted: guanylate cyclase produces cGMP, while PDE9A1 is transferred into the nucleus thanks to the scaffold complex, and this results in increased cGMP hydrolysis in the nucleus. In the right panel, the proposed mechanism for the regulation of nuclear cGMP-related events is represented: an inhibitor of the binding of PDE9A1 to the scaffold complex prevents nuclear translocation of the enzyme, thus resulting in a local increase of cGMP levels. Created with Microsoft PowerPoint Version 2108 (build 14332.20706) using figures from Servier Medical Art, licensed under Creative Commons Attribution 4.0 Unported License. Bcl-2: B-cell lymphoma 2; c-FOS: Finkel–Biskis–Jinkins osteosarcoma proto-oncogene; cGMP: cyclic guanosine 3',5'-monophosphate; GC: guanylate cyclase; GMP: guanosine 3',5'-monophosphate; Jun B: transcription factor encoded by the JUNB gene; pat7: residue pattern 7; PDE9A1: phosphodiesterase 9A isoform 1; Scaffold Complex: comprises scaffold proteins. Image from [441].

Therapeutic Approaches Interfering with Nuclear Localization Signals: An Emerging Strategy for CNS-Related Diseases

This article highlights the importance of the karyopherin-dependent system, aiming to identify new potential targets for the development of therapeutic approaches in the field of CNS diseases. For this reason, a literature search was performed, and 150 publications were retrieved using query strings that contained the words “karyopherin”, “phosphodiesterase”, “CNS”, “drug discovery”, “protein-protein interaction”, and their combinations. Neurological disorders currently attract special attention from the perspective of drug treatment. Although methods for drug research and development are constantly evolving, identifying molecules that can target the CNS remains an open challenge [442–444]. For every disease, it is challenging to discover effective and safe drugs, which depend on a combination of variables. In the case of CNS diseases, this is further exacerbated by the fact that a comprehensive understanding of the complex underlying biology is lacking. Furthermore, the absence of specific biomarkers is reflected by a high failure rate that drug identification encounters in this area compared to its peripheral counterpart [445]. Moreover, already available approaches in most cases are limited to giving relief to patients through symptomatic treatments rather than completely resolving the pathological conditions [444,445]. The World Health Organization (WHO) has stated that brain disorders

fall within the top 10 causes of mortality worldwide, and that, within these conditions, NDDs represent the main group [446].

Both cancer (e.g., glioma) and NDDs (e.g., PD and AD) exert a destructive force at the level of the anatomical components, and a variety of symptoms reflect this. Although these differ in incidence, mortality, and etiology, few markers allow their identification. In this case, one of the main reasons stems from the localization of affected cell populations, which makes the availability of diagnostic markers, to date, limited [447–449]. The complexity in efficiently treating CNS cancer and NDDs is supported by their resistance to therapy, making them more challenging to treat. Because of this, few drugs have reached the market to date.

Successful drug discovery and development depend on a detailed knowledge of pathophysiological mechanisms. In this context, one of the most difficult hurdles to overcome is the location of CNS targets that are protected by the blood-brain barrier (BBB) [450]. BBB is a vascularized semipermeable barrier acting as a protection system for CNS

functional units like neurons, astrocytes, and pericytes, which are constantly supplied by nutrients, deprived of waste, and protected by exogenous molecules. The position of BBB allows it to play a pivotal role in the CNS, making it one of the most important aspects to consider in drug design from medicinal chemistry studies. Indeed, the ability of ligands to cross the BBB is a crucial parameter to consider in the drug discovery process [395,451–454]. The fine regulation that the BBB does is given by active and passive transport. Although passive diffusion of small lipophilic molecules is a major mechanism of penetration for CNS drugs, efflux pumps often transport the compounds, preventing their access to the CNS [455]. Usually, these mechanisms rely on several transporters belonging to the ATP-binding cassette (ABC) transporter family, such as P-glycoprotein (P-gp), breast cancer resistance protein (BCRP), and members of the multidrug resistance protein (MRP) subfamily, which are highly expressed and determine an active transport that leads to a reduction in the effective concentration of molecules within the CNS [456–458]. From a medicinal chemistry point of view, capturing every feature that can enable the effective migration of molecules into the brain is crucial to the progress of CNS drug discovery [459,460]. For CNS ligand design, it is relevant to consider several aspects that involve physicochemical properties (e.g., solubility and size), pharmacokinetics, and pharmacodynamics, and try to assess whether they are substrates for efflux pumps or not. Over the years, several rules have been proposed to standardize and summarize the features that ligands should fulfill to access the CNS by crossing the BBB [461]. This exploration led to the definition of a subgroup defined as “CNS chemical space,” which has seen several changes over the years. The first benchmark against which the chemical space for CNS drug candidates was explored was Lipinski's rule of five, which summarizes the features that a molecule must possess to be associated with oral bioavailability [462,463]. Although this rule allowed for the identification of several promising compounds with good approximation, analysis of the CNS chemical space has led to the optimization of the parameters needed for CNS drugs, resulting in the application of stricter rules. Indeed, these drugs occupy a considerably more limited chemical space compared to drugs directed at the peripheral counterparts [460,464]. One of the most important physicochemical properties that this allowed us to find was the lipophilicity. An increase in this property is reported to be an increment in the *in vitro* potency. In contrast, extremely high lipophilicity values fall back to low solubility and an increase in the number of unwanted activities [465]. Then, the hydrogen bonding potential for a drug is essential since an increase in it

reduces lower passive permeability, and this runs in parallel with a higher possibility of recognition by P-gp efflux pumps [466]. Further, even the number of hydrogen bond acceptors and donors (respectively, HBA and HBD) is pivotal for CNS targeting. In this context, Pajouhesh and Lenz proposed the following guidelines for successful CNS drug candidates: HBD < 3, HBA < 7, and total hydrogen bonds < 8 [467]. Accordingly, a reduction in HBD capacity is one of the most frequently reported medicinal chemistry strategies for improving brain exposure [468]. Another evaluated aspect is the polar surface area (PSA) of a small molecule that can be calculated in different ways. Molecules with a PSA > 140 Å2 generally have poor gut permeability, leading to low oral bioavailability [469]. However, reflecting the differences in the gut and BBB permeability as well as plasma and brain tissue binding, PSA values for CNS penetrant compounds tend to be considerably lower. A comparative analysis of marketed CNS and non-CNS drug properties led Van de Waterbeemd to propose a PSA value lower than 90 $Å^2$ as a cutoff for optimal CNS exposure [470].

Based on a similar analysis performed on a different data set, Kelder suggested an even stricter cutoff of PSA comprised between 60-70 $Å^2$ [471]. These parameters, discovered over the years, confirmed how the exploration of CNS chemical space still needs to find an optimum for treating CNS diseases [472–474]. The goal of finding new strategies that can circumvent the issue of BBB penetration to reach the CNS targets has led to the use of alternative small molecules, such as peptides, that nowadays allow us to achieve pioneering results for treating CNS cancers and NDDs [475–479]. Different classes of CNS-selective peptides have been designed, and their main features regard BBB crossing. Among these, there are cell-penetrating, neuroprotective, and anti-inflammatory peptides, and their main goal is to mimic specific recognition regions present in their targets. In the group of strategies employed for an alternative CNS targeting, natural and synthetic peptides are one of the most studied approaches [477,480]. Natural peptides can come from humans, plants, and animals. Within this category, several examples can be considered, and the main ones are carnosine, amylin, RI-OR2, QBP1, ED11 (WO2014057484A1), and their derivatives [476,481–486]. Many identified synthetic peptides need to undergo further modifications to improve their pharmacokinetic properties before clinical application. Hence, after the target is known, it is essential to rely on structure-activity relationship (SAR) studies to characterize active binding domains of the target.

3.4.1 Karyopherins as Novel CNS Targets

Several groups attempted to unravel these mechanisms, and, in this context, many pathophysiological processes were identified to deregulate intracellular transfer, thus altering cell homeostasis at nuclear or cytoplasmic levels. These two cellular compartments are known to be constantly communicating through the karyopherin (Kap) shuttle system; hence, medicinal chemists try to identify and develop efficient Kap shuttle-interfering ligands [487]. This system allows the transport of macromolecules (defined as "cargoes") with the aim of shuttling them from the cytoplasm to the nucleus or vice versa, depending on cell demands. Nuclear pore complexes (NPCs) components are referred to as nucleoporins, and to form a functional NPC, ~600 copies of ~30 nucleoporins are required [488]. NPCs were thought to be involved only in transport activities, but multiple studies highlighted their involvement in other biological events such as transcriptional control, small ubiquitin-related modifier homeostasis, cell cycle progression, chromatin organization, and RNA biogenesis [489]. The active process transports nearly all macromolecules in and out of the nucleus with the help of transport signals and the Kap protein superfamily. Kaps specifically bind transport signals found on cargoes and translocate them through the NPC channel. The most studied transport signals are found on nuclear protein cargoes. Such signals consist of short amino acid sequences called "nuclear localization sequences" (NLSs; for import) or "nuclear export sequences" (NESs; for export) that are found within their structures [490]. The Kaps family is divided into two major groups: Kaps-α and Kaps-β. The former directly recognizes NLSs and NESs on the cargoes, acting as an adaptor protein between cargoes and Kaps-β. The latter recognizes Kaps-α/cargo complexes and subsequently binds NPCs, leading to translocation events [488]. Kaps-α are classified in three subfamilies, α1 (IMPα1, IMPα8), α2 (IMPα3, IMPα4), and α3 (IMPα5, IMPα6, IMPα7), depending on differences in their amino acid sequence, defining cargo selectivity. These subfamilies generally present a conserved region containing ten helical armadillo repeats, a C-terminal domain which is involved in the exit from the nuclear environment toward the cytoplasmic one, and an N-terminal domain involved in the recognition of NLSs of the specific cargoes through the presence of the importin β binding (IBB) domain responsible for the interaction with Kaps-β [491,492]. On the other hand, from a structural point of view, Kap-β is divided in two main regions: a common N-terminal binding site involved in the release of cargoes and a C-terminal domain characterized by 18-20 tandem huntingtin, elongation factor 3, protein phosphatase

2A, and TOR1 (HEAT) motifs composed by pairs of antiparallel α-helices connected by a turn, all organized into a flexible right-handed solenoid structure [492]. This architecture is pivotal since it gives Kaps-β the ability to bind multiple interactors, such as Kaps-α, cargoes, and intrinsically disordered proteins (IDPs) at the same time [492–495]. The directions in which Kaps-β transport their cargoes lead to their classification in three categories: importins (towards the nucleus), exportins (towards the cytoplasm) and biportins (both directions). Currently, at least twenty human Kaps-β are known, of which 10 are importins (IMP or IPO; IMPβ, Transportin/Karyopherin-β2 (KAPβ2), Transportin 2/ Karyopherin-β2b, Transportin 3/Transportin-SR, IPO4, IPO5, IPO7, IPO8, IPO9, IPO11) (**Table 7**), 5 are exportins (XPO; Chromatin Region Maintenance 1 CRM1/XPO1, Cellular Apoptosis Susceptibility/XPO2, XPOT, XPO5, XPO6) (**Table 8**), 3 are biportins (IPO13, XPO4, XPO7) (**Table 9**), while the role of the other two (RanBP6, RanBP17) has yet to be determined (**Table 10**) [496]. Like most intracellular transport, Kap-mediated regulation requires energy, and in these processes, the RanGTPase family is crucial [490]. These are GTPases that function as a molecular switch, converting the active GTP-bound and inactive GDP-bound complexes (**Figure 68**) [497]. Their dual role in both cellular compartments leads to a gradient within the cell that allows the dissociation of cargoes from their shuttles both in the nucleus and cytoplasm [498,499]. As a result, Kaps are involved in physiological processes like mitosis and gene transcription, while several studies have reported their contribution to pathophysiological events like cancer, NDDs, and viral infections [490,492,500,501]. Given the importance that nuclear transport has, the involved proteins might be considered attractive druggable targets.

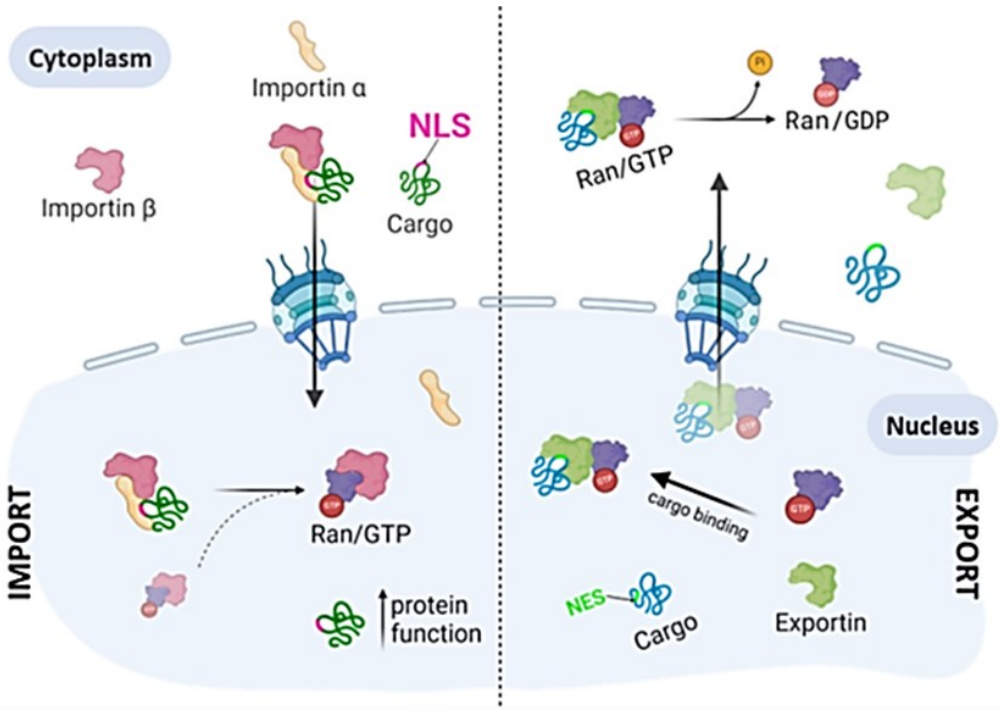

Figure 68. Representation of importin/exportin-mediated nucleocytoplasmic transport of macromolecules. Nuclear import of cargoes (left panel) occurs through Importin-α, which binds to the NLS within cargo proteins, then a ternary complex forms in the cytoplasm by binding to Importin β and allows the nuclear entry. Next, the binding of RanGTP and Importin β in the nucleus allows for the dissociation of the complex and protein functioning. For nuclear export (right panel), RanGTP stimulates binding of exportin to an NES-containing cargo protein in the nucleus, then the complex is exported to the cytoplasm, where hydrolysis of RanGTP to RanGDP results in complex disassembly. (A higher resolution/colour version of this figure is available in the electronic copy of the article). Image from [502].

Kap	Other names	Isoforms	Cargoes
Importin-β (IMPβ)	Kapβ1, KPNB1, IPO1, IMB1, IPOB, p97, NTF97	2	Many cargoes through the adaptors Impα1 and Snurportin-1, SREBP-2, NFκB, TFEB, PD-L1
Transportin 1/Karyopherin-β2 (KAPβ2)	Impβ2, KPNB2, IPO2, TNPO1, TRN1	3	FUS, hnRNP-A1, TDP-43, β-catenin, BAP1
Transportin 2/Karyopherin-β2b (KAPβ2b)	Impβ2b, KPNB2B, IPO3, TNPO2, TRN2	2	hnRNP A1, TDP-43, FUS
Transportin 3/Transportin-SR (TNPO3)	TrnSR, TrnSR2, Trn3, Imp12, IPO12	4	ASF/SF2, CPSF6, CIRBP, HIV virus
Importin 4 (IPO4)	RanBP4, Imp4, Imp4b	2	Histones H3 and H4, Vitamin D receptor
Importin 5 (IPO5)	Impβ3, Kapβ3, RanBP5, KPNB3, Imp5, IMB3	3	Ribosomal proteins, histone H3, influenza A virus RNA polymerase subunit PB1
Importin 7 (IPO7)	RanBP7, IPO7	1	Histone H1, HIV reverse transcription complex (RTC), SMAD1, Yap1, DNA plasmids
Importin 8 (IPO8)	RanBP8, Imp8	2	cap-free eIF4E, SMAD4, microRNAs
Importin 9 (IPO9)	RanBP9, Imp9	1	ARID3A, PFKP, histones H2A and H2B
Importin 11 (IPO11)	RanBP11, Imp11	2	BZW1/2, β-catenin, PTEN

*Table 7. Overview of importins, their isoforms, and some of their related cargoes known in the literature. *Abbreviations: SREBP-2: Sterol regulatory element-binding proteins 2; TFEB: Transcription factor EB; PD-L1: Programmed death-ligand 1; FUS: Fused in sarcoma; hnRNP-A1:Heterogeneous nuclear ribonucleoprotein A1; TDP-43: Transactive response DNA binding protein 43 kDa (TAR DNA-binding protein 43; BAP1: BRCA1 associated protein 1; ASF/SF2: Serine/arginine-rich splicing factor 1; CPSF6: Cleavage And Polyadenylation Specific Factor 6; CIRBP: Cold-inducible RNA-binding protein; HIV: human immunodeficiency virus; SMAD1: Suppressor of mother against decapentaplegic; YAP1: yes-associated protein 1; elF4E: Eukaryotic translation initiation factor 4E; ARID3A: AT-rich interactive domain-containing protein 3A; PFKP: Phosphofructokinase, platelet; BZW1/2: Basic Leucine Zipper And W2 Domains 1; PTEN: Phosphatase and Tensin Homolog. Image from [502].*

Kap	Other names	Isoforms	Cargoes
Chromatin Region Maintenance 1/Exportin 1 (CRM1/XPO1)	Exp1, emb	1	p53, FOXO, Survivin, TFEB, cGAS
Cellular Apoptosis Susceptibility/Exportin 2 (CAS/XPO2)	Exp2, CSE1L, Impα re-exporter	4	Impα1-7
Exportin-t (XPOT)	Exp-T, XPO3	1	aminoacylated tRNAs
Exportin 5 (XPO5)	Exp5, RanBP21	1	Pre-miRNA, tRNA, hairpin RNA, RNA coexported proteins
Exportin 6 (XPO6)	Exp6, RanBP20	2	Nuclear actin

*Table 8. Table 2. Overview of exportins, their isoforms, and their cargoes known in the literature. *Abbreviations: p53: tumoral protein 53; FOXO: Forkhead box O3; cGAS: Cyclic GMP-AMP synthase. Image from [502].*

Kap	Other names	Isoforms	Cargoes
Importin 13 (IPO13)	Kap13, RanBP13, IPO13	1	**Import cargo**: Mago-Y14, Ubc9 **Export cargo**: eIF1A
Exportin 4 (XPO4)	Exp4	1	**Import cargo**: Sox2, SRY **Export cargo**: eIF5A1, eIF5A2, Smad3
Exportin 7 (XPO7)	Exp7, RanBP16	1	RhoGAP1, 14-3-3σ, p65

*Table 9. Overview of biportins, their isoforms, and some of their related cargoes known in the literature. *Abbreviations: Mago-Y14: Mago nashi; Ubc9: ubiquitin conjugating enzyme; Sox2: SRY-Box Transcription Factor 2; SRY: Sex -determining region Y protein; RhoGAP1: Rho GTPase-activating protein 1, p65: nuclear factor NF-kappa-B p65 subunit. Image from [502].*

KAP	OTHER NAMES	ISOFORMS	CARGOES
RANBP6	**NA**	**1**	Putative cargo: STAT3
RANBP17	**NA**	**2**	-

*Table 10. Overview of unknown karyopherins and their isoforms known in the literature. *Abbreviations: STAT3: Signal Transducer and Activator of Transcription 3. Image from [502].*

3.4.2. Small molecules and peptides for targeting KAP-mediated activities

Given these premises, regulating Kaps-mediated intracellular transport might be an alternative path to explore in the quest for new therapeutic options. As will be discussed in the following sections, some of these approaches aimed at interfering with the Kaps/cargoes recognition at different levels with both small molecules and/or peptides [503]. In particular, some of the cases that have stood out mainly relied on IMPα/β-dependent transport, on the inhibition of cargoes recognized by the IMPα/β complex, and on the inhibition of XPO-dependent transport [504,505].

3.4.2.1. IMPα/β-dependent Transport Inhibitors

IMPα and IMPβ inhibitors prevent the import of cargoes. Among IMPα inhibitors, small molecules like ivermectin [506] and gossypol were reported in the literature [507,508]. Selective targeting of IMPα5 by ivermectin was described to reduce the import of hypoxia-inducible factor 1 subunit α (HIF1α) and its related translational and angiogenic events. Further, synthetic inhibitor peptides like bimax1, bimax2, and N50 are found to bind IMPα with high affinity (K_d in pM range) and mimic the natural NLS sequence of proteins [509–511]. The sequence of bimax1 (GSRRRRPRKRPLEWDEDEEPPRKRKRLW) and bimax2 (GSRRRRRRKRKREWDDDDDPPKKRRRLD) attempted to resemble a typical bipartite cNLS consensus region in IMPα independently of the presence of IMPβ. Results demonstrated that these peptides were able to disrupt the protein-protein interaction, interfering with Retinoblastoma-like protein 1 (p107) involved in cell cycle regulation and tumor suppression, and with Protein Inhibitor of Activated STAT Y (PIASy) involved in cell proliferation and transcriptional activity [512,513]. N50 (VQRKRQKLMP) is a synthetic peptide selective for IMPα, and in particular for IMPα5 (K_d in the nM range), which can mimic the NLS pattern PKKKRKV and it is reported to modulate the import of proinflammatory cargoes like nuclear factor kappa-light-chain enhancer of activated B cells (NF-κB), Signal transducer and activator of transcription 1 (STAT1) and Activator protein 1 (AP-1) [511]. On the other hand, a higher number of small molecules and fewer peptides that exert their actions as IMPβ inhibitors are reported in the literature [514]. In this group, karyostatin 1A reduces the Nuclear factor of activated T-cells (NFAT) nuclear import based on IMPα/β but does not affect NFAT XPO1-dependent nuclear export in HeLa cells. Furthermore, importazole (IPZ) is reported to have selectivity in myeloma cell lines since

the inhibition of NF-κB nuclear import induced apoptosis. This mechanism of action (MoA) is reported to occur with a similar selectivity toward NFAT target [515,516]. Moreover, IPZ was known to be effective at peripheral levels, and consequently, Pathak and colleagues reported its activity in the CNS at the level of hippocampal cells derived from C57/Black 6, where IMPβ-mediated nuclear import was prevented. Further, IPZ reduced cell viability in glioblastoma (GBM) cell lines. In this work, both Ran-positive (VTC-103) and Ran-negative (VTC-037) primary GBM cell lines were evaluated. As expected, since RanGTPase is implicated in IMPβ-mediated transport, VTC-103 cell lines were more sensitive to IPZ [517–519]. Moreover, similar results were obtained on different human GBM cell lines (U-87 MG, U-251 MG, A-172 MG, and SHG-44) by inducing apoptotic events. Other small molecules like INI-43, INI-60, 58H5-6, genkwadaphnin (DD1), and its derivative DD1-Br were reported [145,216,516,520–522]. The latter, a brominated derivative of the natural diterpene DD1, has been recently reported to be able to significantly reduce the nuclear import of transcription factors such as Cellular myelocytomatosis oncogene (c-MYC), E2 transcription Factor 1 (E2F1), androgen receptor (AR), Forkhead box protein M1 (FOXM1), and coactivators like proliferating cell nuclear antigen (PCNA), cAMP response element-binding protein (CREB) and PARK7 Parkinsonism associated deglycase (PARK7) by targeting IMPβ1 in C4-2B prostate cancer cell line. A novelty in the field is represented by goyazensolide, a natural sesquiterpene lactone identified as the first covalent IPO5 inhibitor [523]. Interestingly, this compound was found to be effective in reducing cell viability in human GBM cell lines U-87 MG and T98-G and was able to successfully cross a BBB mimic membrane, showing potential as a candidate for GBM treatment. Recently, a steroidal lactone, withaferin A, has been reported as another covalent binder of IPO5, on which more studies need to be done to unravel its MoA (**Figure 69A**) [524].

3.4.2.1.1 Cargo-specific IMPα/β Inhibitors: an Application for Viral Therapeutics

One of the explored fields of application for cargo/IMPα/β complex disruption regards viral proteins. Several drugs have been identified that prevent the entry of viral proteins into the host nuclear environment, thereby inhibiting viral replication. In this regard, several synthetic steroids like mifepristone, budesonide, and flunisolide belong to this group. Their MoA relies on targeting the NLS region of human immunodeficiency virus type 1 (HIV-1) integrase, blocking its nuclear import, and potentially inhibiting the

transport of the HIV pre-integration complex into the nucleus. Furthermore, fenretinide is a promising antiviral effective against flaviviruses, such as Dengue, Zika virus, and West Nile viruses, by targeting their non-structural protein 5 (NS5) and blocking their nuclear translocation (**Figure 69B**) [525–528].

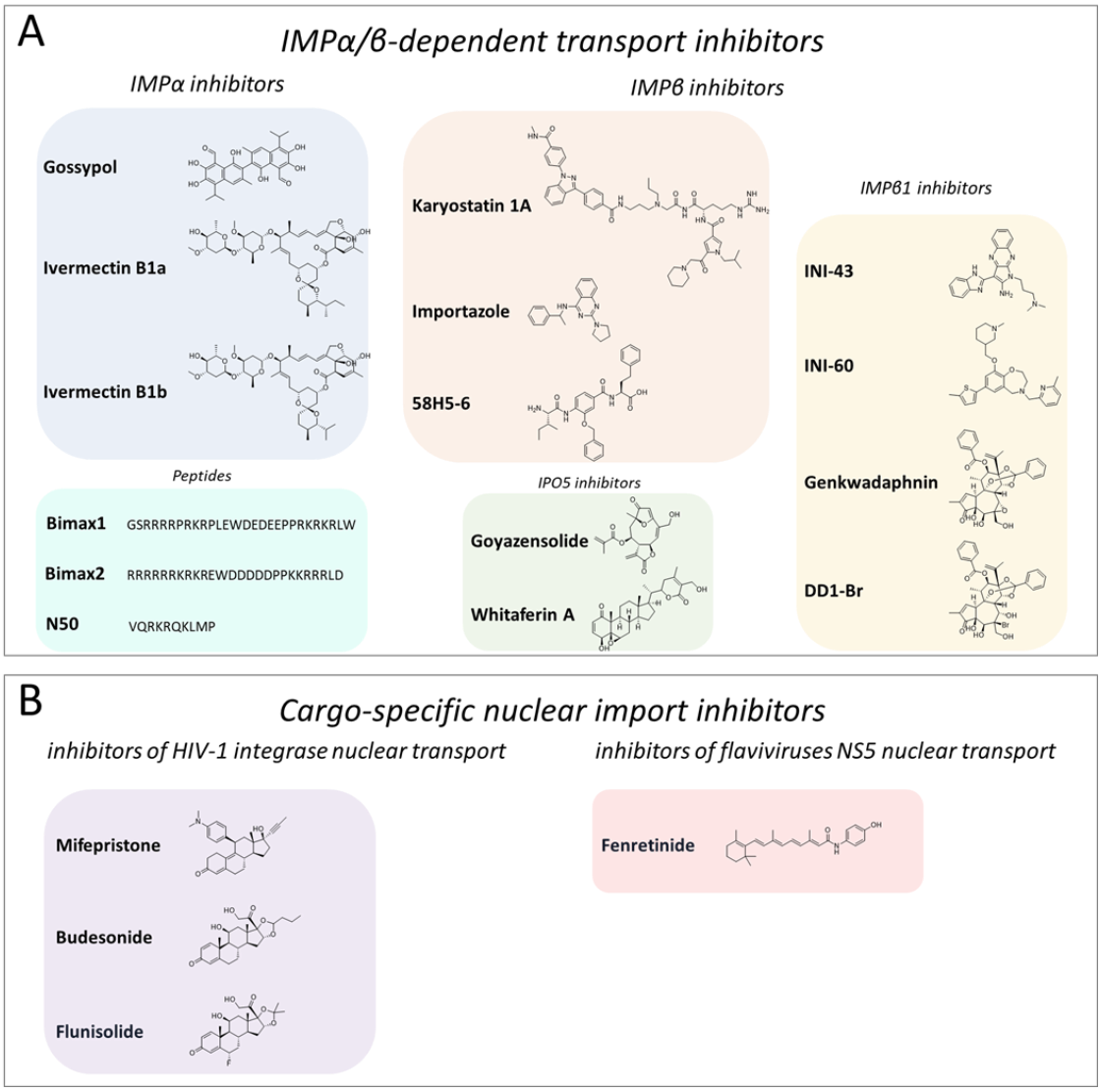

Figure 69. IMPα/β-dependent and cargo-specific nuclear import inhibitors. A) IMPα inhibitors can be small molecules (gossypol, ivermectin B1a and B1b) or peptides (bimax1, bimax2, N50). IMPβ can be divided into non-selective, IMPβ-specific, or selective for IPO5. B) Cargo-specific nuclear import inhibitors can be classified in inhibitors of HIV-1 integrase nuclear transport (mifepristone, budesonide, flunisolide) and inhibitors of flaviviruses NS5 nuclear transport (fenretinide). Image from [502].

3.4.2 XPO-dependent Transport Inhibitors

The XPO-dependent transport inhibitor class includes drugs that interfere with the nuclear export process. Most of these compounds specifically target XPO1, which is currently the most characterized exportin. From the structural point of view, the XPO1 binding site was characterized in 2010 by Güttler and colleagues, and it was found that a

set of five pockets (φ0-φ4) compose the binding site and recognize different NES peptides [528]. However, a new pocket was discovered recently. It is called φ1* since it is found below φ1[529]. The first compound reported as an XPO1 inhibitor is leptomycin B (LMB), a natural polyketide that selectively alkylates Cys528 of human XPO1, thus inhibiting its nuclear export activity [530,531]. Furthermore, LMB is also reported to inhibit NF-κB activity by blocking an NF-κB inhibitor (IκB-α) degradation via XPO1 inhibition in HeLa cells [532,533]. Due to high toxicity issues, including nausea, vomiting, severe anorexia, and malaise, LMB was discontinued from the Phase I clinical trial that enrolled patients with a wide variety of cancer types [534–536]. Anguinomycins C and D are natural polyketides structurally like LMB that inhibit XPO1 through the same mechanism as LMB [537]. Goniothalamin and its derivatives covalently bind XPO1 in a hydrophobic cleft that recognizes the NESs of its cargoes [538,539]. Moreover, it is reported that these compounds in HeLa cells inhibit the cytoplasmic Right open reading frame 2 protein kinase (Rio2-kinase) involved in ribosome biogenesis, which relies on nuclear export [540]. Interestingly, LMB, anguinomycins, goniothalamin, and their derivatives are characterized by the presence of an unsaturated δ-lactone ring that acts as a Michael acceptor, which is involved in a Michael addition reaction with the thiol moiety of Cys528, a nucleophilic group, thus acting as a Michael donor. This was also predicted through computational studies (e.g., covalent docking), providing further evidence of the importance of the lactone ring in XPO1 covalent inhibitors. Differently, other small molecules like curcumin and its analogue dibenzylideneacetone are other compounds identified as XPO1 inhibitors that behave as Michael acceptors, allowing for covalent interaction with Cys528. Related biological events include the block of NF-κB, myeloid differentiation protein 2 (MD2), protein kinase B/mammalian target of rapamycin (Akt/mTOR), and STAT3 signaling pathways, inhibition of Forkhead box protein O1 (FOXO1) export in the cytoplasm, and upregulation of p73 and p27 [535,541,542]. Interestingly, a hydrogenated metabolite of curcumin, octahydrocurcumin (OHC), showed anticancer activity in an H22 tumor-bearing mouse model by inducing cell apoptosis through p53 upregulation and murine double minute 2 (MDM2) downregulation. However, OHC distinguishes itself by not being a Michael acceptor and not a covalent binder with Cys528, thus requiring more studies to unravel its MoA [543]. Curcumin was also tested in combination with proteasome inhibitors (bortezomib, carfilzomib, or ixazomib) or immunomodulatory drugs against multiple myeloma (thalidomide, lenalidomide, or pomalidomide) in 15 dexamethasone

intolerant multiple myeloma patients, showing a better tolerance and diarrhea as the only side effect in two patients, that was managed by lowering the dose or temporarily suspend the therapy [536,544]. Plumbagin, a natural naphthoquinone, is another XPO1 covalent inhibitor selective for Cys528 binding. It prevents NF-κB activation and IκBα degradation through XPO1 inhibition, and can disrupt XPO1 complexes with FOXO1, p21, p53, and p73. Plumbagin is also being investigated as a potential therapeutic agent in prostate and non-small cell LC [545–547]. Furthermore, CBS9106 (felezonexor) and its derivative S109 are the first reversible XPO1 covalent inhibitors selective for Cys528 reported in the literature [548]. Due to their relevance, several clinical studies were done, and, in this context, felezonexor was completed in Phase I clinical trials (NCT02667873, NCT05795192, NCT05522868) where patients affected by solid tumors were involved. The patients involved in these clinical trials showed adverse events, including nausea, vomiting, fatigue, decreased appetite, diarrhea, acute renal injury, and neutropenia [549]. Avoiding XPO1 permanent inhibition is preferable since the majority of highly toxic effects could be attributed to covalent binding. Subsequently, a new series of compounds called selective inhibitors of nuclear export (SINEs), which are reversible covalent inhibitors, was developed. KPT-127, KPT-185, KPT-205, KPT-225, KPT-227, KPT-249, KPT-251, KPT-276, KPT-301, KPT-330 (selinexor), KPT-335 (verdinexor), and KPT-8602 (eltanexor) belong to this class and are characterized by the presence of an N-azolylacrylate scaffold, that was previously found in PKF050-638, a small molecule that inhibits the XPO1-dependant nuclear export of HIV-1 Rev, a protein which is required for HIV replication. SINEs have been the most successful drug candidate class in this context so far. Indeed, selinexor has received FDA approval for the treatment of refractory multiple myeloma and diffuse large B-cell lymphoma [550–555]. Moreover, SINEs, especially selinexor and eltanexor, are being investigated *in vitro* and/or *in vivo* for their application against solid cancers. In this context, KPT-127 and KPT-205 were investigated for pancreatic and prostate cancers, KPT-225 and KPT-301 for prostate cancers; KPT-227 for pancreatic cancers; verdinexor for neuroblastoma and esophageal cancers, and KPT-185, KPT-251, KPT-276, selinexor, and eltanexor for various cancers. Furthermore, SINEs are investigated in brain cancers, and eltanexor has been highlighted as a promising anti-PD compound [436,556,557]. In particular, Liu et al. found that eltanexor inhibits the activation of the NF-κB pathway and the NLRP3 inflammasome by inhibiting the nuclear transport of p65 NF-κB subunit, an IMPα3 and IMPα4 cargo, thus resulting in an attenuation of

Lipopolysaccharides-induced peripheral inflammation and 1-methyl-4-phenyl-1,2,3,6-tetrahydro pyridine (MPTP)-induced neuroinflammation. Moreover, selinexor has been involved in many clinical trials against glioblastoma, the most common brain cancer, in combination with standard of care therapy with encouraging results (NCT04216329, NCT04421378, NCT01986348, NCT05432804) [558–560,560–562]. However, the administration of selinexor, a first-generation SINE, is associated with many side effects, such as thrombocytopenia, fatigue, nausea, anemia, hyponatremia; while eltanexor, a second-generation SINE, show a similar adverse effect profile, but with lower incidence and severity of fatigue, nausea and hyponatremia, thus the development of non-covalent inhibitors has become important to try to reduce these effects [563,564]. Moreover, in several cases, cancer patients show mutations in XPO1 that alter the presence of Cys528. This reflects a reduction in the efficacy of Cys528-selective drugs, leading to resistance to SINEs and, in general, to covalent Cystargeting binders. Therefore, the development of XPO1 inhibitors that are also effective against Cys528 mutants became an attractive perspective. Indeed, in 2021, NCI-1, the first noncovalent XPO1 inhibitor, was presented. It was designed by combining the dimethylbutyl group of CBS9106 and the (3,5-bis(trifluoromethyl)phenyl)sulfinyl group of LFS-829, a different XPO1 inhibitor. However, since NCI-1 has a Michael acceptor group, it can also covalently bind XPO1 if Cys528 is not mutated. NCI-1 showed anticancer activity towards various cancer cell lines and also against XPO1-Cys528Ser-transfected HeLa cells, which are resistant to covalent inhibitors [565]. Two aminoratjadone derivatives, KL1 and KL2, and zafirlukast (ZAF) have been discovered in this context [216,566,567]. KL1 and KL2 do not contain any Michael acceptor group; thus, they cannot covalently bind Cys528 in XPO1. However, unlike NCI-1, they show sensitivity to the Cys528Ser mutation, probably because serine is a polar amino acid, while Cys528 was predicted to be involved in hydrophobic interaction with these compounds. KL1 and KL2 showed anticancer activity against HeLa and colorectal cancer cell lines, including HCT116 and RKO [567]. ZAF was identified as an XPO1 non-covalent inhibitor in a drug repurposing study involving both *in silico* and *in vitro* approaches. ZAF, as in the case of KL1 and KL2, does not contain any Michael acceptor group and thus cannot covalently bind Cys528. However, unlike the aminoratjadone derivatives, ZAF is insensitive to the Cys528Ser mutation, as in the case of NCI-1. Moreover, ZAF showed anticancer activity against HGC27 cells, a human gastric carcinoma cell line [568]. In a recent study, Li and colleagues [529] identified various non-

covalent XPO1 binders characterized by the same scaffold. Interestingly, they noted that one of those compounds, B28, bound to XPO1 at a different site, a previously hidden pocket, with a binding mode never observed in other XPO1 inhibitors. Indeed, it was noted that B28 bound the pockets φ3, φ2, and φ1*, while usually XPO1 non-covalent ligands bind at least three pockets between φ0, φ1, φ2, φ3, and φ4. However, B28 did not show anticancer activity against HeLa cells, leading to the synthesis of B28 derivatives based on SAR, of which three, G1, G8, and G9, showed anticancer activity towards various cancer cell lines. SAR analyses revealed that in ring A, meta, and ortho substitutions were optimal since they allow the interaction with φ2 (ortho position) and φ3 (meta position). It was also noted that in these positions, bulky moieties were preferable over smaller ones. Considering ring B, they found that ortho substitutions were not favorable and that the best substituents were Br and Cl in the para position, allowing molecules to insert in φ1* (**Figure 70**). The development of non-covalent ligands, in addition to their efficacy in cases of Cys528 mutations, may also be beneficial in reducing side effects, which are problematic for reversible covalent inhibitors, such as SINEs. Nevertheless, more studies are needed to clarify this point.

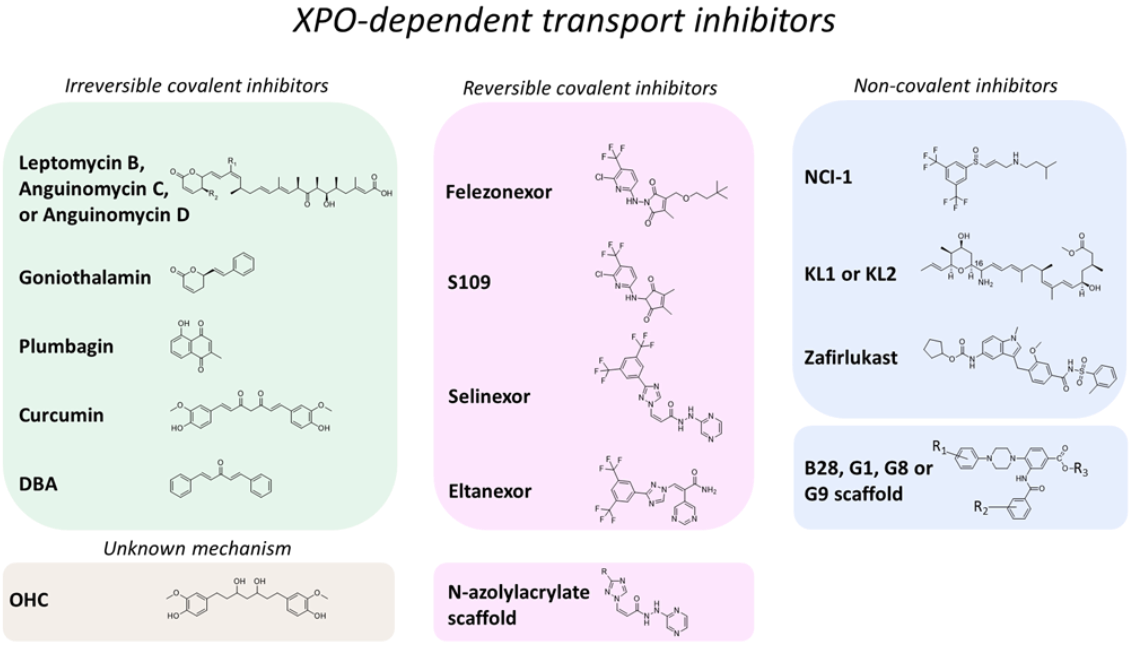

Figure 70. XPO-dependent transport inhibitors. They can be divided into irreversible (leptomycin B (R_1=C_2H_5, R_2=CH_3), anguinomycin C (R_1=CH_3, R_2=H) anguinomycin D (R_1=C_2H_5, R_2=H), goniothalamin, plumbagin, curcumin, DBA) and reversible (felezonexor, S109, selinexor (presenting an N-azolylacrylate scaffold, as most of the other SINEs), eltanexor and the other SINEs) covalent inhibitors and non-covalent inhibitors (NC-1, KL1 (16R), KL2 (16S), zafirlukast, B28 (R_1= CH_3 in meta and ortho, R_2= Br in para, R_3= H), G1 (R_1= CF_3 in meta and ortho, R_2= Cl in para, R_3= H), G8 (R_1= CF_3 in meta and ortho, R_2= Br in para,

R_3= H) and G9 (R_1= CF_3 in both meta positions, R_2= Br, R_3=H). The OHC mechanism is yet to be determined. Image from [502].

3.4.3 Karyopherin-mediated treatments: future perspectives

Most of the abovementioned evidence was supported by *in silico* studies. Over the years, several structural experiments, including those conducted by X-ray diffraction, NMR, and Cryo-EM, have enabled the acquisition of structural information about importins, exportins, cargoes, and their respective ligands. In this context, several records were added to the Protein Data Bank repository (https://www.rcsb.org/), and this information led to the unraveling of some features about their binding modes. Furthermore, ligand-based studies were conducted, enabling the expansion of knowledge about potential derivatives of covalent and non-covalent binders for importins and exportins. In this context, SAR studies were pivotal for increasing the possibility of finding reliable candidates. Promising compounds such as eltanexor are being investigated in the field of PD. Despite the numerous limitations in NDDs drug discovery, such as BBB permeability, susceptibility to P-gp, and molecular weight, several research groups are attempting to expand the knowledge about the selectivity of these molecular targets to resolve brain pathological conditions. A family of proteins for which the mechanisms of nuclear transport have been reported to be Kap-mediated and to be involved in the regulation of their activity is one of the PDEs.

In particular, this has been reported for PDE1A and PDE4D5 [437,438], and it is under investigation for PDE9A [441], which is one of the appealing targets for epilepsy, AD, Huntington disease, vascular dementia, breast tumors, and prostate cancers [381,382,417,569–571]. In more detail, PDE9A is reported to have several isoforms, with some being exclusively cytoplasmic, nuclear, or dual [384]. This different localization was attributed to the sequence, and in the case of isoform PDE9A1, an NLS region, named Pat7, was found. Interestingly, PDE9A6/13 does not contain any NLS, and an exclusive cytoplasmic localization was reported. These features could be attributed to different causes, but the possibility that PDE9A1 could be a cargo for importins or exportins cannot be ruled out. Combined, these pieces of evidence pave the way for investigating the possible Kap/PDE9A interaction in more detail and possibly identify a new class of selective ligands, given the relevant biological role of PDE9A in cancer and NDDs.

Conclusion

This mini-review aimed to highlight the emerging role of drugs targeting the Kap-shuttle system in the context of CNS diseases, including cancers and NDDs. Given the relevance that the Kap-shuttle system has at the level of intracellular regulation, several studies are attempting to identify and characterize possible Kap families important for CNS biology. The search for new small molecules and peptides has gained momentum in recent years, leading to the initiation of important clinical trials for anti-tumor drugs. Regarding NDDs resolving drugs, further studies are needed to identify new molecules within the CNS drug chemical space, which is still not fully explored. Although many discovered ligands imply a treatment for peripheral targets, some of them are being investigated for CNS applications, as in the case of brain tumors (e.g., GBM) and NDDs (e.g., PD, amyotrophic lateral sclerosis, and frontotemporal dementia) [572]. Furthermore, with the continuous advancement of artificial intelligence-based methods, the landscape of drug discovery has undergone a significant transformation, particularly through substantial progress in 3D protein structure prediction and the expansion of the CNS-chemical space. Key aspects of structure-based studies, such as the accuracy of predicted models (e.g., AlphaFold 3) [573], as well as the speed and cost-efficiency of calculations, have significantly expanded and enriched the chemical space of CNS-targeting molecules [574]. All these elements contribute to achieving results with greater precision and reliability. In the intricate world of karyopherin-dependent systems, where each small piece of the puzzle plays a crucial role, computational studies may hold the key to developing and optimizing Kap-selective drugs, paving the way for entirely new categories of therapeutics. Indeed, future research efforts should focus on a deeper exploration of this target category to identify new CNS-selective drugs.

4. Side projects 2: Computer-aided drug design applied to natural compounds-based drug discovery

Natural products have been a cornerstone of medicine, from ancient herbal remedies to the discovery of major drugs like morphine and quinine. Their importance has peaked across several therapeutic areas, including cancer, infections, cardiovascular (e.g., statins), and multiple sclerosis (e.g., fingolimod) [575,576].

Natural products have unique features compared to conventional synthetic molecules, providing both benefits and challenges in drug discovery, also because they are known for their vast scaffold diversity and structural complexity.

These three years of PhD have also been used to explore potential applications of natural products as ligands for targets across different therapeutic areas. These include acetylcholinesterase for AD, sarcoplasmic/endoplasmic reticulum Ca^{2+}-ATPase (SERCA) for rheumatoid arthritis, Urate oxidase (Uox) as an antifungal target, epidermal growth factor receptor kinase (EGFRk) involved in tumor processes, and α-glucosidase related to the pathogenesis of diabetes mellitus.

4.1 Mechanistic investigation on compounds from Amorpha fruticosa L. targeting acetylcholinesterase

Formation of beta amyloid deposits, oxidative stress, and impaired cholinergic transmission are among the proposed mechanisms involved in AD [577]. Drugs such as donepezil inhibit acetylcholinesterase (AChE), and by sustaining the cholinergic tone, they combat the symptoms of cognitive decline associated with AD [578]. While innovative monoclonal antibodies targeting beta amyloid are encountering safety and regulatory issues [579], the search for small molecules as therapeutic tools is wide open. In this connection, natural products represent chemically diverse compounds with potential applications against AD, and computational techniques aid the translation of traditional knowledge on plants' bioactivity into medicinal chemistry [399,580–582]. Amorpha *fruticosa* L., known as 'false indigo', belongs to Fabaceae and is commonly found in the northern hemisphere [583]. Phenols with cytotoxic activity [584,585] and polysaccharides with cosmetic applications [586] were identified in this plant. In the context of ad, its rotenoids were studied as inhibitors of tyrosinase, which is overexpressed in neurodegenerative diseases [587], and compounds from the same class were recently shown to inhibit butyrylcholinesterase (BChE) and AChE [588].

Results and Discussion

The composition of the different parts of A. *fruticosa* has been explored in the last decade, highlighting rotenoids, flavonoids, sterols, cinnamic acid analogues, polyamine derivatives, and stilbenoids as the main chemical categories. Throughout the years, nearly a hundred different molecules have been described to be contained in the extracts of A. fruticose [584,588,589]. In particular, the leaves contain bioactive compounds belonging to several classes of the different abovementioned scaffolds. Thus, in the current study, we rationally selected 15 compounds reported to be present in the leaves to build a small set of molecules to be investigated *in silico* as possible AChE inhibitors. Specifically, we included rotenoids, flavones, and isoflavones (both aglycones and glycosylated compounds), sterols, and cinnamic acid derivatives, which we considered representative of the main chemical classes contained in A. *fruticosa*. The compounds studied in this work were: (1) tephrosin, (2) 6α,12α-dehydrodeguelin, (3) vitexin, (4) Afrormosin-7-O-β-D-glucopyranoside, (5) 2″-O-α-L-Rhamnopyranosyl-isovitexin, (6) rutin, (7) Chryseriol, (8) 7-O-Methylluteolin, (9) Trans-p-coumaric acid, (10) 2-benzyl-4,6-dihydroxybenzoic acid-4-O-β-D-glucopyranoside, (11) Formononetin, (12) Quercetin, (13) Apigenin, (14) β-Sitosterol, and (15) β-daucosterol. On the other hand, the growing chemodiversity of A. *fruticosa* components is evidenced by the burgeoning literature on this topic. In particular, scientific papers focusing on the characterization of extracts from flowers and leaves were very recently published [586,590,591]. Thus, it cannot be ruled out that the panel of compounds tested in this work may not encompass all the potentially interesting species in the plant. Nevertheless, as mentioned above, the selection of such compounds for the virtual screening study was performed by us mainly based on the work by Cui and colleagues, in which bioactive compounds were identified in leaves [584]. Only a limited number of reports appeared in the literature describing the inhibitory effect of A. *fruticosa* extracts and isolated compounds on AChE to date. Concerning *in vitro* data, a preliminary study by Zheleva-Dimitrova and colleagues reported that methanolic extracts of leaves and fruits showed inhibitory activity against AChE of 25.43% ± 0.16 and 48.86% ± 0.55, respectively, at a concentration of 0.17 mg/mL. In this case, the authors speculated that the effect may have been related to the presence of hydroxycinnamic derivatives in the extract [592]. In a recent study by Jankovská and colleagues, the authors reported the extraction of five putrescine and spermidine derivatives, as well as five rotenoids, from the methanolic extracts of A. *fruticosa* flowers. In this context, isolated rotenoid derivatives exhibited

limited inhibitory activity against AChE as they inhibited the enzyme between 17.9% ± 5.9 and 22.4% ± 4.9 at a concentration of 100 µM [588]. Nevertheless, the structural details of the binding mode were not studied. Additionally, it must be noted that structurally related rotenoids extracted from Millettia *pachycarpa*, including deguelin and tephrosin (1), were reported to inhibit AChE in the µM range (with IC_{50} values of 126.70 ± 1.83 and 127.18 ± 21.37 µM for these two molecules, respectively). In the same research work, the two compounds were defined as "inactive" on BChE [593]. Thus, only limited data can be retrieved in the literature concerning inhibitory activity of A. *fruticosa* components, as, to the best of our knowledge, the abovementioned works represent the few examples of extracts or isolated compounds tested for their AChE inhibitory activity. Consequently, computational medicinal chemistry approaches could guide the identification of novel, potentially interesting small molecules to be tested *in vitro* in a subsequent step. The current work was conceived as a CADD study applied to the identification of components present in the leaves of A. *fruticosa* among a panel of 15 molecules constituted as described above. According to this approach, the compounds were first screened for their chemical properties to identify those with 'drug-like' features and structural hallmarks matching the requirements for interaction with AChE, which were assessed through target prediction and molecular docking studies. The compound resulting from the point of intersection of these different simulations, i.e., the molecule showing a promising predicted pharmacokinetic profile and docking score, was further studied using more advanced computational techniques, including molecular dynamics simulations and ligand-based machine learning-aided toxicity studies. More in detail, the first steps of our virtual screening approach consisted of calculating physicochemical descriptors relevant for oral bioavailability and CNS permeation [463], and in the ligand-based target prediction to assess the presence of AChE among the retrieved putative macromolecular interactors. The rotenoid 6α,12α-dehydrodeguelin (2), trans-p-coumaric acid (9), and formononetin (11) were predicted as 'drug-like' molecules (i.e., possessing the ideal physicochemical properties to be orally bioavailable as reported in **Table 11**).

Compound	MW g/mol	LogP	RB	HBA	HBD	Lipinski violations	GI permeation	BBB permeation
1	410.42	1.13	2	7	1	0	High	No
2	392.40	1.75	2	6	0	0	High	Yes
3	432.38	-2.02	3	10	7	1	Low	No
4	460.43	-1.18	6	10	4	0	Low	No
5	578.52	-3.36	5	14	9	3	Low	No
6	610.52	-3.89	6	16	10	3	Low	No
7	300.26	0.22	2	6	3	0	High	No
8	300.26	0.22	2	6	3	0	High	No
9	164.16	1.28	2	3	2	0	High	Yes
10	406.38	-0.33	6	9	6	1	Low	No
11	268.26	1.33	2	4	1	0	High	Yes
12	302.24	-0.56	1	7	5	0	High	No
13	270.24	0.52	1	5	3	0	High	No
14	414.71	6.73	6	1	1	1	Low	No
15	576.85	3.96	9	6	4	1	Low	No

Table 11. Calculated physicochemical descriptors according to SwissADME. The values are referred to as molecular weight (MW), partition coefficient (LogP), rotatable bonds (RB), H-bond acceptors and donors (HBA, HBD), number of violations of the Lipinski rule, permeation through the gastrointestinal tract (GI), and blood-brain barrier (BBB).

Additionally, based on target prediction studies that work on the structural comparison between the investigated ligands and known molecules for which macromolecular targets have been characterized in the literature, 11 out of 15 compounds, including (2), were highlighted as potential interactors of AChE [594,595]. The results of this study are shown in **Table 12**.

Compound	Predicted interaction with AChE	Probability
1	**No**	**n.a.**
2	**Yes**	**Low**
3	**No**	**n.a.**
4	**Yes**	**Low**
5	**Yes**	**Low**
6	**Yes**	**High**
7	**Yes**	**Low**
8	**Yes**	**Low**
9	**No**	**n.a.**
10	**No**	**n.a.**
11	**Yes**	**Low**
12	**Yes**	**High**
13	**Yes**	**High**
14	**Yes**	**Low**
15	**Yes**	**Low**

Table 12. Prediction of the interaction with acetylcholinesterase (AChE) according to SwissTargetPrediction. "Yes" or "No" indicates if the protein was among the list of predicted targets, and the probability is expressed as follows: "Low" if < 30%, "Average" if between 30% and 70%, "High" if > 70%.

Then, molecular docking was used to study the binding of the 15 molecules with AChE (PDB ID 4EY7). The protocol was validated by redocking the cognate ligand, donepezil (**Figure 71**), using both blind and site-specific algorithms, which perform conformational searches across the entire target or within the defined binding site, respectively. Coordinates of search grids are reported in *Materials and Methods*. The simulations showed that the compounds preferentially interact with the same region of the protein targeted by donepezil. β-Sitosterol (14), (2), and apigenin (13) exhibited the best docking scores, as indicated by the values listed in **Table 13**.

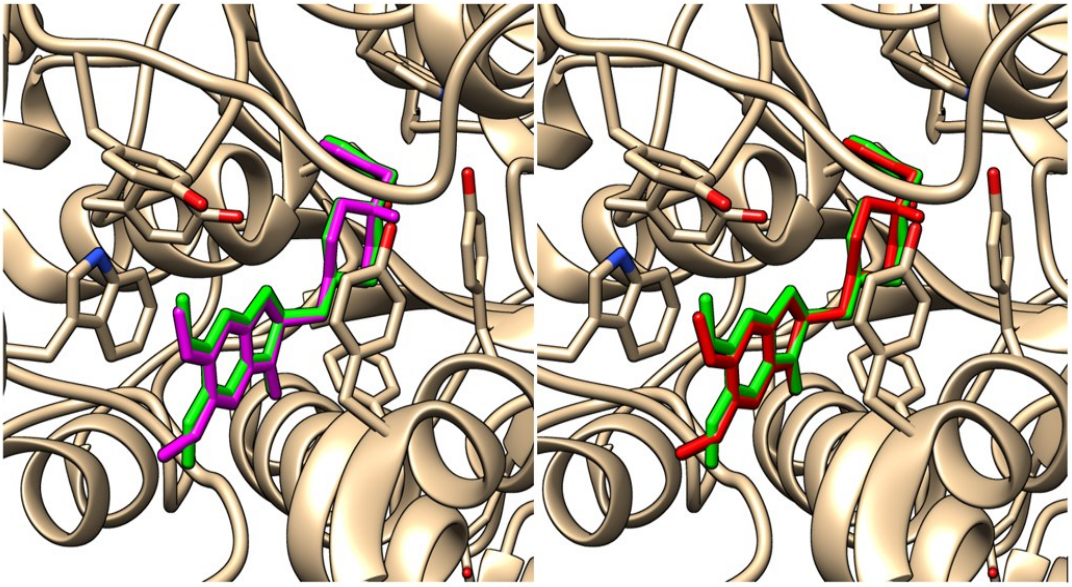

Figure 71. Comparison of cognate ligand poses (green) and blind (purple) or site-specific (red) re-docked donepezil. Root mean square deviation (RMSD) values: 1.484 Å (blind), 0.987 Å (site-specific).

Compound	Blind (kcal/mol)	Site-specific (kcal/mol)
Donepezil	-12.2	-12.1
6α.12α-dehydrodeguelin	-10.8	-10.8
Afrormosin-7-O-β-D-glucopyranoside	-9.5	-9.6
2-O-α-L-Rhamnopyranosyl-isovitexin	-8.7	-9.7
Rutin	-9.1	-9.8
Chryseriol	-10.0	-10.0
7-O-Methylluteolin	-9.9	-9.8
Formononetin	-10.0	-10.1
Quercetin	-9.5	-9.5
Apigenin	-10.2	-10.2
β-Sitosterol	-11.1	-11.2
β-daucosterol	-9.8	-9.9

Table 13. Calculated binding energy according to blind and site-specific docking experiments. The values for re-docked donepezil are reported for reference.

Considering these screening steps, (2) was identified as the most promising compound through this first set of computational studies based on the combined results. Indeed, this compound was identified as a drug-like molecule by ligand-based calculations, and AChE was among its predicted targets. It showed a promising score in docking studies towards the enzyme (-10.8 kcal/mol). Thus, (2) was selected for a more accurate analysis of the interaction with the macromolecular target. Ser203, Glu334, and His447 constitute the 'catalytic triad' enabling the catalytic mechanism of AChE, since they are involved in the hydrolysis of the neurotransmitter to acetate and choline in the catalytic site [596,597]. Donepezil directly binds His447, and the 6α,12α-dehydrodeguelin (2) docking pose shows a proximity to this residue (**Figure 72**), potentially impairing the catalytic activity.

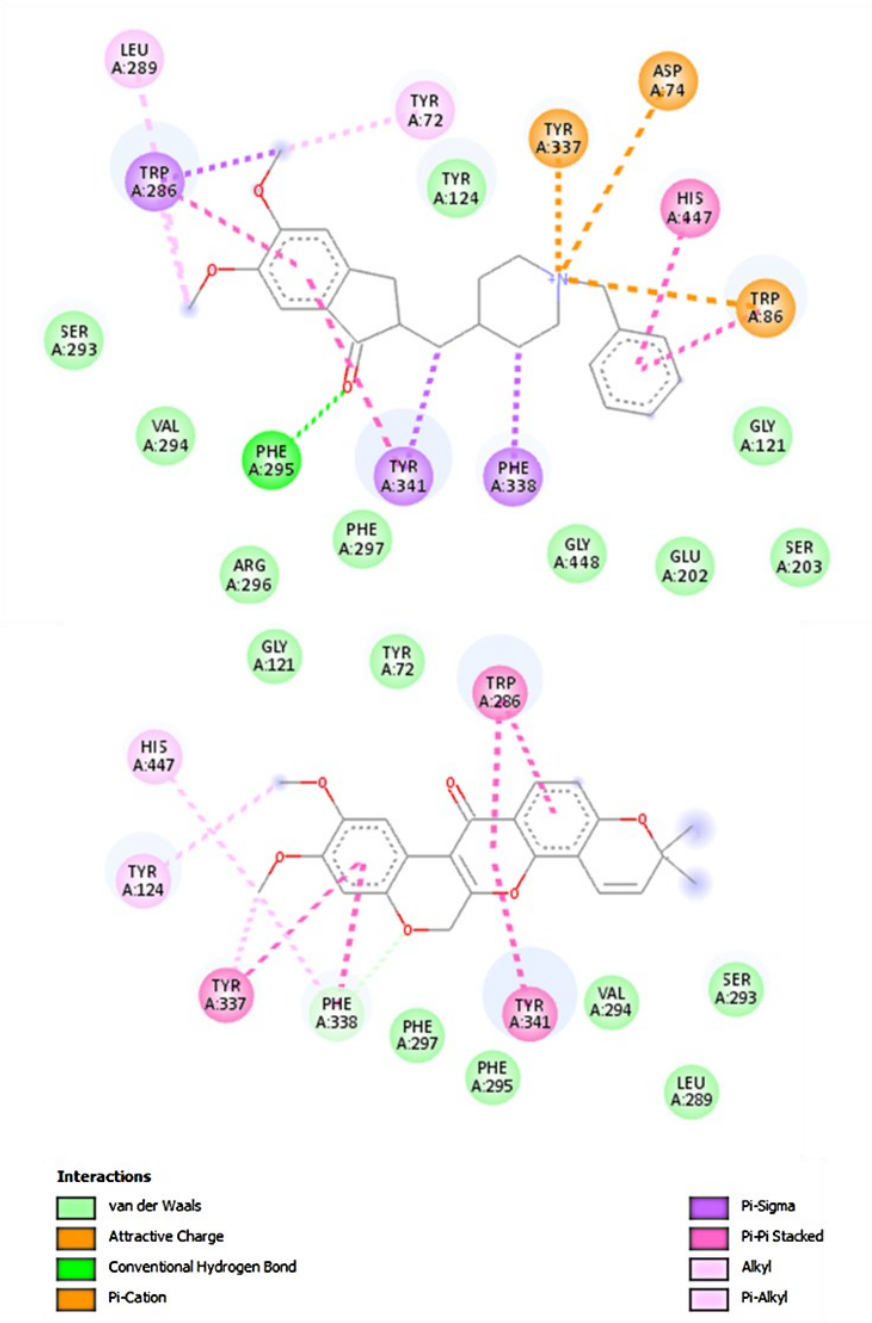

Figure 72. Comparison of the interaction pattern of donepezil (upper panel) and of 6α,12α-dehydrodeguelin (lower panel) in terms of involved residues in the binding site (BIOVIA, Dassault Systèmes, Discovery Studio, v24.1.0.23298, San Diego: Dassault Systèmes, 2024).

Molecular dynamics simulations (250 ns) demonstrated that (2) forms a stable complex with AChE. Throughout the simulation, the molecule maintains its position in the binding site, and the resulting trajectories are reported in **Figures 73 and 74**.

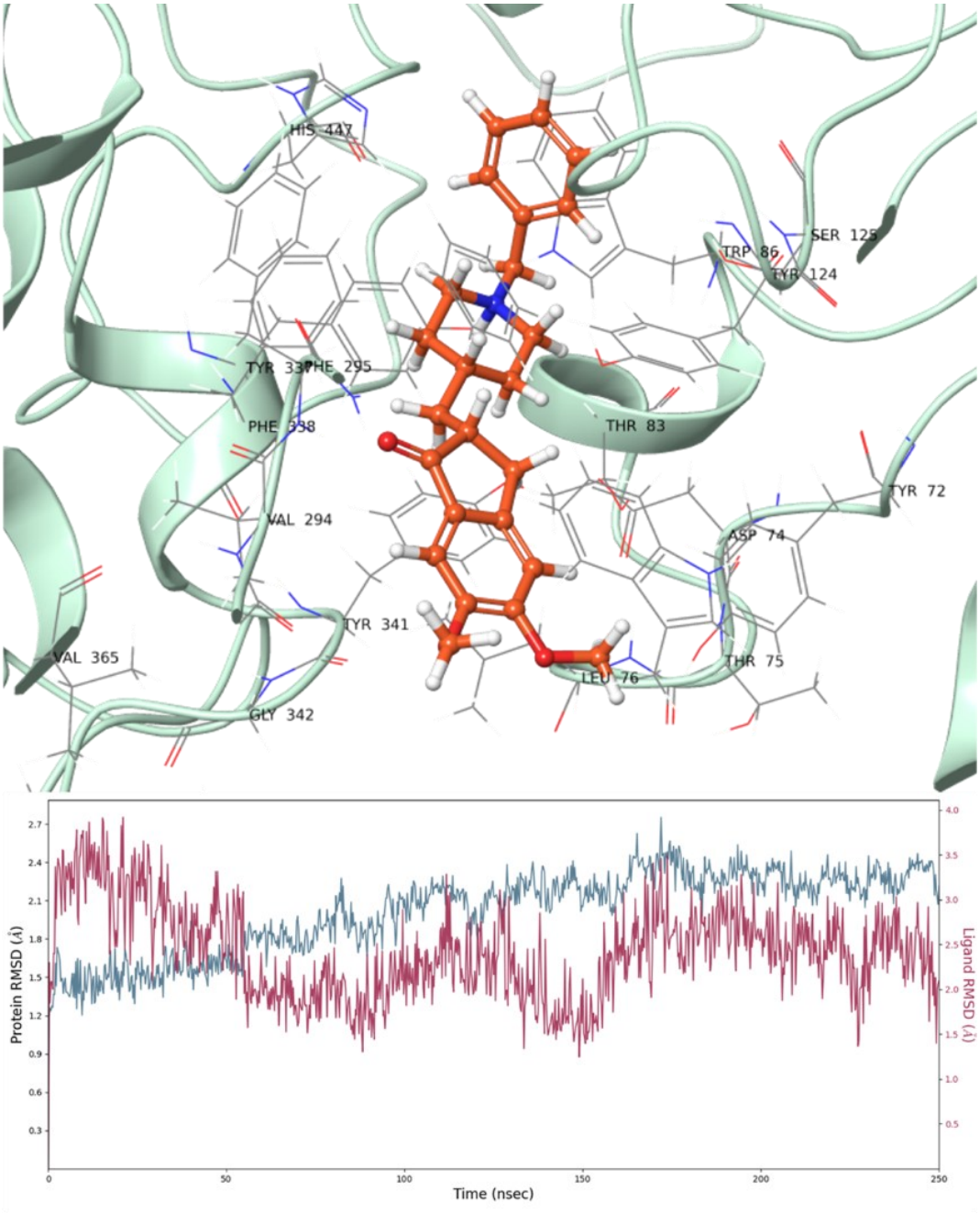

Figure 73. (Upper panel) Docking pose of donepezil. (Lower panel) Trajectories retrieved from MD simulations showing the RMSD of the donepezil/AChE systems over the simulation time. The plots for the heavy atoms of the ligand are depicted in blue (aligned with the protein), while the plots for protein C-alphas are depicted in red.

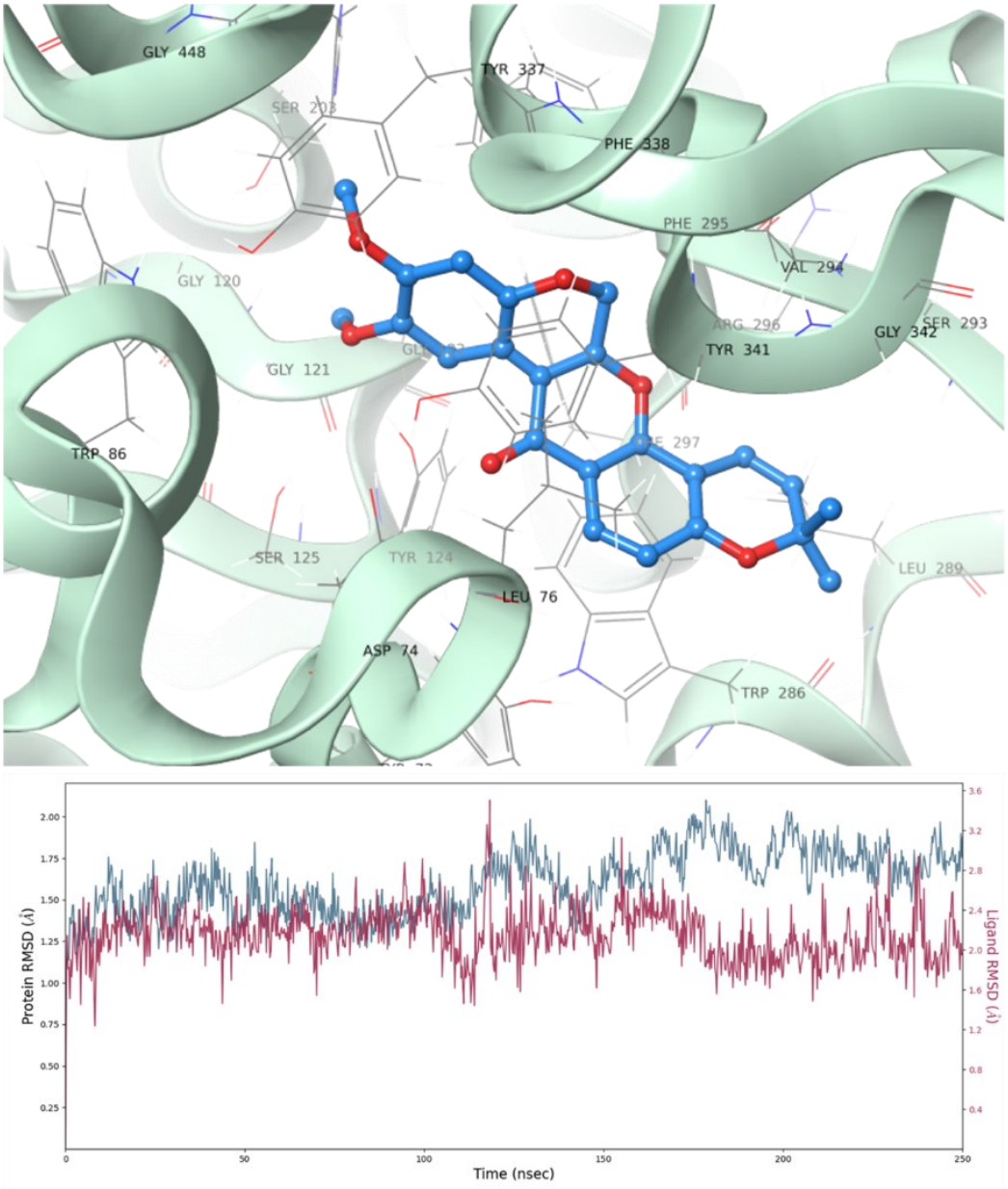

Figure 74. (Upper panel) Docking pose of (2). (Lower panel) Trajectories retrieved from MD simulations showing the RMSD of the 6α,12α-dehydrodeguelin/AChE systems over the simulation time. The plots for the heavy atoms of the ligand are depicted in blue (aligned with the protein), while the plots for protein C-alphas are depicted in red.

Relevant interactions were observed and, as depicted in **Figure 75**, a hydrogen bond between (2) and His447 was established, further confirming the selection of the molecule. Indeed, this residue is of fundamental importance because it is part of the catalytic triad (Ser203, Glu334, and His447). Since the compound interacts with the catalytic site, (2) may represent a competitive inhibitor.

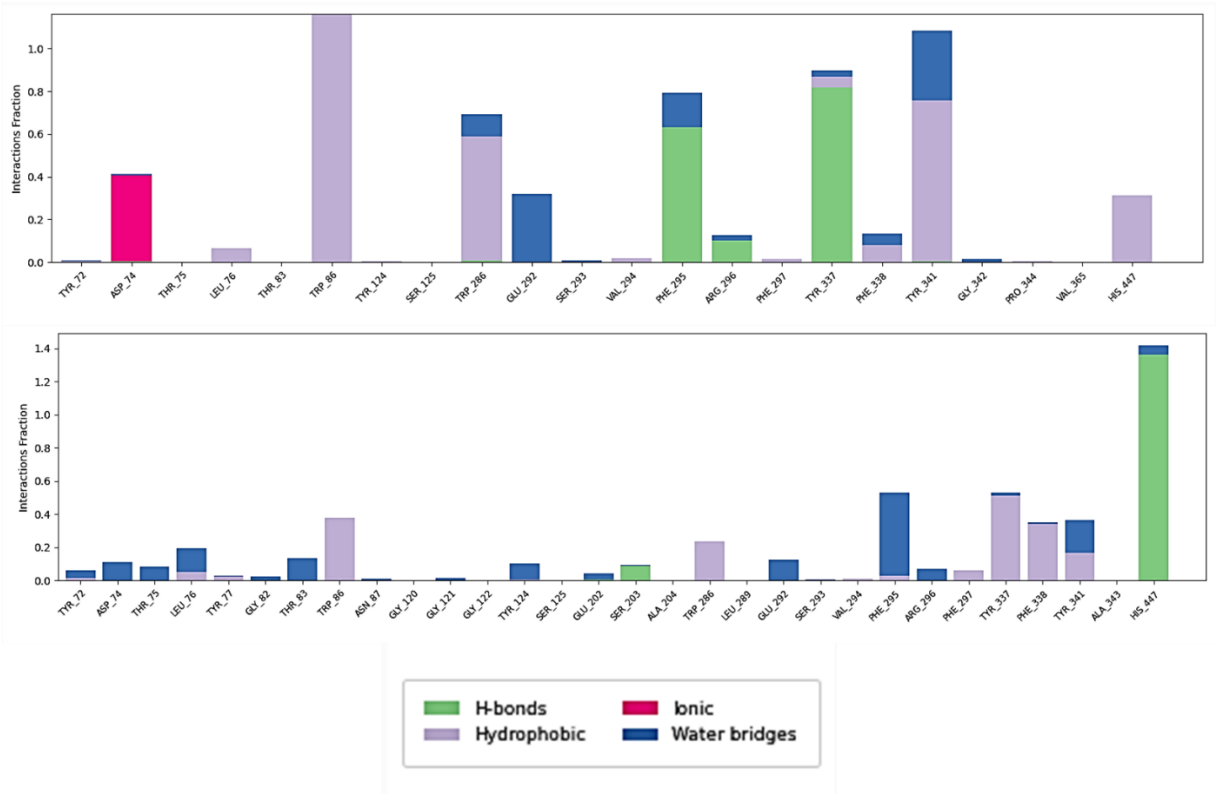

Figure 75. Overview of the interaction fraction throughout the simulation (250 ns) for donepezil (upper panel) and 6α,12α-dehydrodeguelin (lower panel).

Additionally, according to ligand-based machine learning-aided toxicity studies, 6α,12α-dehydrodeguelin (2) was predicted to fall within class 5 of the Globally Harmonized System (GHS) of Classification and Labelling of Chemicals [598], which comprehends 'substances which are of relatively low acute toxicity hazard but which, under certain circumstances, may present a danger to vulnerable populations'. While the main 'red flags' identified for the compound consisted of potential immunotoxicity, BBB toxicity, ecotoxicity, and the interaction with CYP2D6 and CYP2C9, the molecule was not predicted to affect the main "toxicity targets". Additionally, methoxy groups and double bonds were identified as metabolic hotspots for CYP2D6 and CYP2C9 [599]. Machine learning-based prediction of metabolism confirmed O-dealkylation and double bond epoxidation as possible pathways (**Figure 76**) [600,601].

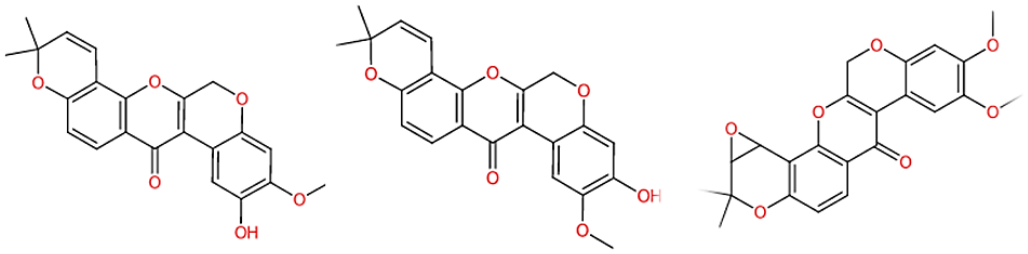

Figure 76. Predicted metabolites of 6α,12α-dehydrodeguelin.

Materials and Methods

All the current data are published; readers can access the Supporting Information on the publication site [602]

Molecular Docking

The 3D X-ray crystal structure of the target in complex with donepezil was retrieved from the RCSB Protein Data Bank (www.rcsb.org, PDB ID 4EY7; resolution 2.35 Å). The structures were prepared using the DockPrep tool of UCSF Chimera [603]. Ligands were built and optimized using Avogadro [604]. The blind and site-specific molecular docking studies were performed using AutoDock Vina [605]. The search grids for blind and site-specific docking simulations were set according to the parameters reported below.

	Blind				Site-specific		
	x	y	z		x	y	z
Center	-3.53	-37.90	34.64	Center	-10.23	-44.94	28.98
Size (Å)	54.81	59.49	72.48	Size (Å)	30.92	35.72	34.01

Docking simulation was carried out with default Vina parameters, in which the number of generated docking poses was set to 8, and the docking energy conformation value was expressed in kcal/mol. To validate the docking protocol, the cognate ligand was re-docked using both blind and site-specific approaches. Docking score and root mean square deviation (RMSD) were computed, giving the following values: -12.2 kcal/mol and 1.484 Å (blind), -12.1 kcal/mol and 0.987 Å (site-specific).

Molecular Dynamics

Molecular dynamics (MD) simulations were performed using the GPU-accelerated Desmond tool of Schrödinger LLC (Schrödinger Release 2023-1: Desmond Molecular Dynamics System, D. E. Shaw Research, New York, NY, USA, 2021; Maestro-Desmond Interoperability Tools, Schrödinger, New York, NY, USA, 2021). The best protein-ligand complex retrieved from the docking step was used to prepare the solvated system to perform MD [420]. By using the System Builder tool [420], both complexes were solvated using the explicit TIP3P water model. Periodic boundary conditions were set with an orthorhombic box shape with a buffer size of 8 × 8 × 8 Å. During ion placement, Na^+ ions

were used to neutralize the system, and a concentration of 0.15 M of NaCl was set. A minimization step was performed prior to MD simulation, which consisted of a 250 ns run under the OPLS4 force field with the temperature set at 300 K and pressure at 1.0 bar. Further, the Martyna–Tuckerman–Klein chain coupling scheme with an isotropic coupling constant of 2.0 ps for the pressure control and the Nosé–Hoover chain coupling scheme for the temperature control (NPT ensemble), and a relaxation time of 1.0 ps were used. The cutoff radius in the Coulomb interactions was 9.0 Å. A RESPA integrator was set with a time step of 2.0, 2.0, and 6.0 fs, respectively, for bonded interactions and near and far interactions. Trajectories were saved at 250 ps intervals for analysis. With the aim of analyzing interactions between ligand and target, the Simulation Interaction Diagram tool was used to evaluate molecular dynamics trajectories; here, a contact strength of 20% was considered for all the analyses.

Prediction of Physicochemical Descriptors

For the studied compounds, physicochemical descriptors relevant for drug-likeness, ADME parameters, and pharmacokinetic properties were predicted using the SwissADME tool (www.swissadme.ch) [594]. In particular, parameters related to Lipinski's rule were considered [463].

Prediction of Targets

The prediction of potential macromolecular targets for the studied molecules was performed using the SwissTargetPrediction tool [595].

Prediction of Metabolism and Toxicity

The selected compound, namely 6α,12α-dehydrodeguelin, was further investigated by means of computational tools for its potential toxicity using ProTox [606,607]. Interaction with cytochromes was simulated by using SMARTCyp 3.0 [599] and BioTransformer 3.0 [600,601].

4.2 SERCA inhibitors: (2R,4aS,6aS,12bR,14aS,14bR)-N-(2-(2-(2-(2-Azidoethoxy) ethoxy)ethoxy)ethyl)-10-hydroxy-2,4a,6a,9,12b,14ahexamethyl-11-oxo-1,2,3,4,4a,5,6,6a,11,12b,13,14,14a,14btetradecahydropicene-2-carboxamide

Recently, celastrol (**1**) has gained prominence as a drug candidate because of its potential therapeutic properties. Sourced from the roots of *Tripterygium wilfordii*, a traditional Chinese medicinal plant steeped in centuries-old practices of traditional Chinese medicine, **1** has become a focal point for scientific exploration. Although **1** has been part of traditional Chinese medical culture for the treatment of various disorders for several generations, this molecule has only gained importance in the last ten years due to its beneficial pharmacological effects, as revealed by investigations on its molecular mechanisms undertaken during this period.

Notably, **1** exhibits a multitude of beneficial properties, including anti-inflammatory [608–611]. Additionally, celastrol has demonstrated anticancer activity [612], as well as efficacy in combating neuronal degeneration and addressing obesity. Indeed, one of the most captivating features of compound **1** is its ability to regulate cellular signaling pathways that are pivotal in disease progression. Studies have shown that celastrol can inhibit the activation of nuclear factor-kappa B (NF-κB), Hsp90-Cdc37, and sarco-endoplasmic reticulum (SR) Ca^{2+} transport ATPase (SERCA) [613–615].

Rheumatoid arthritis (RA) is a systemic, chronic, autoimmune inflammatory disease that primarily affects the joints. This condition has a worldwide prevalence of 0.25% to 1%. Given the debilitating nature of this condition, many efforts have been made to find a definitive solution that can alleviate its symptoms. The pathogenesis of RA is complex and not fully understood, since a variety of cell populations (e.g., macrophages, lymphocytes, and fibroblasts) and molecules are involved in these mechanisms [616]. Among these, Ca^{2+} plays a pivotal role, as it significantly contributes to autoimmunity and the subsequent progression of the disease. One of the effectors dependent on the presence of Ca^{2+} is SERCA. The importance of this protein has also been demonstrated in other pathologies, such as tumors. To this extent, research has shown that SERCA inhibitors (e.g., thapsigargin) prompt the accumulation of cytosolic and mitochondrial Ca^{2+}, along with ATP depletion, potentially triggering various signaling pathways that culminate in the demise of cancer cells. Additionally, SERCA is a noteworthy anti-arthritic target. Several studies report that its pharmacological inhibition led to beneficial effects in the field of RA

[617]. To this end, celastrol was investigated for its SERCA-inhibitory activity, as it has been reported to reduce bone damage and suppress autoimmune arthritis.

Although celastrol shows promising potential, further research is necessary to fully understand its mechanisms of action and potential side effects. While its therapeutic benefits are recognized, certain drawbacks, including elevated toxicity, limited water solubility, and stability issues, limit its broader clinical use.

To overcome these limitations, medicinal chemists have shown interest in organic synthetic and semi-synthetic approaches to produce novel celastrol active derivatives (**Figure 77**, panel ii). Simple modifications, such as esterification or amidation of the C29-carboxylic acid (**Figure 77**, panel i), were employed to improve solubility, mitigate toxicity, and discover new activities of celastrol analogues. Furthermore, to enhance the efficacy of these new analogues, targeted nanodelivery systems are being developed [618]. These innovative approaches aim to regulate drug release and bioavailability, while also reducing systemic toxicity. Several strategies are implied in this context, including the use of nanoparticles (NPs), liposomes, and micelles. The process of chemically linking an insoluble drug with a hydrophilic polymer can induce self-assembly into NPs, thereby enhancing the apparent solubility and optimizing the drug's pharmacokinetics. The PEG azide nanodelivery system demonstrates enhanced efficiency in targeted drug delivery, highlighting its potential for therapeutic applications [619].

In this context, this study elucidates the synthesis and computational investigations of a celastrol derivative, wherein the scaffold has been intricately linked to a specific moiety, PEG azide (**3**) (**Figure 78**). A future application could be the use of this derivative to perform profiling studies. This could be performed by coupling these analogues to biotin linkers through the Staudinger−Bertozzi reaction or by using click chemistry, conjugating various molecular weights of short-chain PEG to a small molecule drug [620–622].

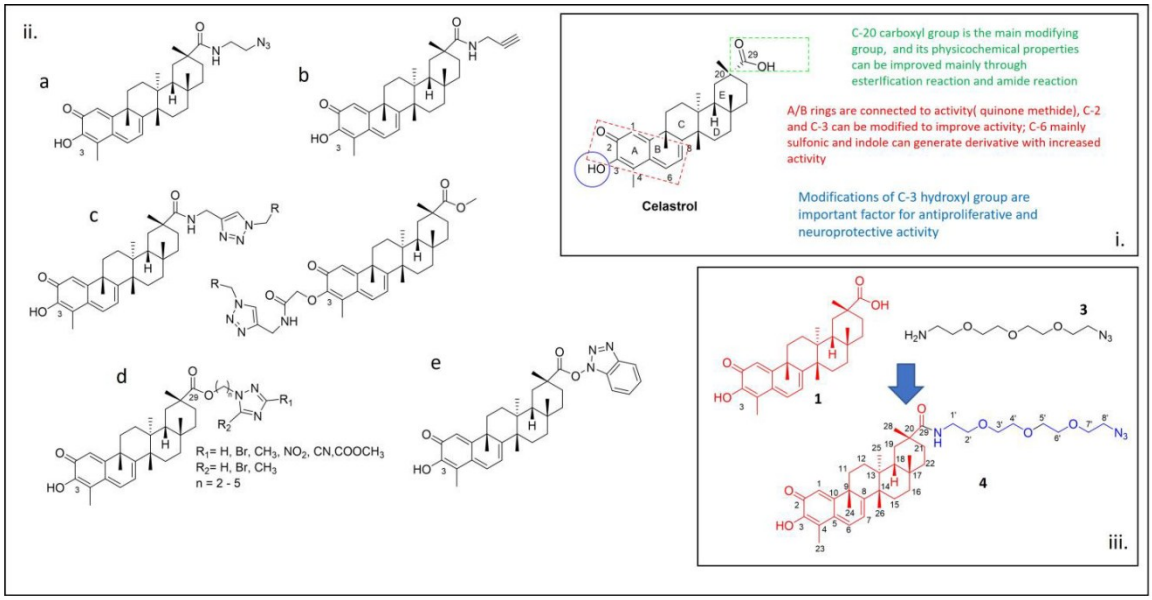

Figure 77. ***(i)*** *Functional groups of celastrol (**1**) that are important for its biological activity.* ***(ii)*** *Example of celastrol derivatives reported in the literature: (a) [623], (b) [624], and 1,2,3 and 1,2,4-triazol celastrol derivatives, (c) [625], (d) [626], and (e) [627].* ***(iii)*** *Chemical structures of 11-Azido-3,6,9-trioxaundecan-1-amine (**3**) and compound **4** are reported in the inset of the figure.*

Results and Discussion

The synthetic route for (2R,4aS,6aS,12bR,14aS,14bR)-N-(2-(2-(2-(2-azidoethoxy)ethoxy)ethoxy)ethyl)-10-hydroxy-2,4a,6a,9,12b,14a-hexamethyl-11-oxo-1,2,3,4,4a,5,6,6a,11,12b,13,14,14a,14b-tetradecahydropicene-2-carboxamide started from the preparation of the precursor (3, **Figure 78a**).

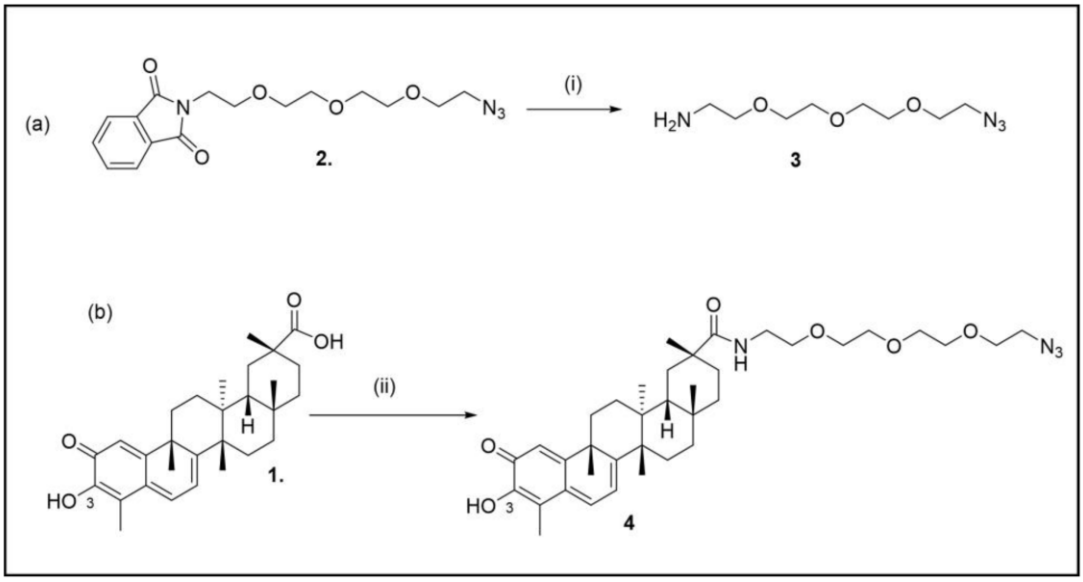

Figure 78. ***(a)*** *Synthesis of 11-Azido-3,6,9-trioxaundecan-1-amine 3 (i) ethanol, hydrazine monohydrate, 4 h, 85 °C.* ***(b)*** *Synthesis of (2R,4aS,6aS,12bR,14aS,14bR)-N-(2-(2-(2-(2-azidoethoxy)ethoxy)ethoxy)ethyl)-10-hydroxy-2,4a,6a,9,12b,14a-hexamethyl-11-oxo-1,2,3,4,4a,5,6,6a,11,12b,13,14,14a,14b-*

*tetradecahydropicene-2-carboxamide (ii) **3**, EDC hydrochloride (3 equiv.), HOBt (3 equiv.), CH_2Cl_2, room temperature for 12-8 h.*

Isoindoline-1,3-dione, or phthalimide, constitutes an important group of chemical compounds. It serves as an $^{-}NH_2$-synthon, allowing the preparation of primary amines, and is used to prepare amine PEG. In particular, following the protocol reported in the literature [628], 11-azido-3,6,9-trioxaundecan-1-amine 3 was prepared by the reaction of 2-(2-(2-(2-(2-azidoethoxy)ethoxy)ethoxy)ethyl)isoindoline-1,3-dione **2** in ethanol with hydrazine monohydrate by Gabriel synthesis. The structure of **3** was determined by ^{1}H-, ^{13}C-NMR, and DEPT-135 spectra.

11-Azido-3,6,9-trioxaundecan-1-amine **3** was used as a starting compound by a coupling reaction using HOBt/EDC/TEA as the activation conditions, using a modified protocol reported by Pang et al. [629]. The EDC reagent and its urea byproduct are water-soluble, so the byproducts are removed by aqueous extraction.

A solution of celastrol in CH_2Cl_2 was prepared, to which HOBt and EDC hydrochloride were added, together with three equivalents of intermediate 3 (**Figure 78, step b**), and compound **4** was isolated in a high yield. Subsequently, the chemical structure of compound **4** was confirmed by NMR, IR, UV, and mass spectrometry analysis. Concerning the NMR analysis, the ^{1}H-NMR spectrum showed peaks associated with the methylene groups 2′-6′ in the region δH 3.29–3.68 ppm and a peak at δH 3.39 ppm associated with azide CH_2, thus supporting the formation of the expected product. Regarding the ^{13}C-NMR signals, the disappearance of peculiar peaks of carboxylic acid at 182 ppm of compound **1**, and the appearance of the peak at 178.3 ppm of the amide were probably the most relevant features to verify the reaction with the PEG azide. Of note, six signals in the region δC 70.7–69.5 123 ppm were attributed to the carbons 2′-6′.

Heteronuclear single quantum coherence spectroscopy (HSQC), correlation spectroscopy (^{1}H-^{1}H-COSY), and distortionless enhancement by polarization transfer (DEPT-135, DEPT-90, and DEPT-45) were also used to assign ^{13}C signals of compound **4**. The ^{13}C-NMR spectrum of **4** exhibited 37 carbon signals, which were classified by DEPT experiments as six methyl groups, fifteen methylene groups, four methine groups, and twelve quaternary carbons.

The IR spectrum of compound **4** showed characteristic N–H stretching at 3332 cm^{-1}, C–H stretching at 2931 and 2870 cm^{-1}, and secondary amide stretching at 1643 cm^{-1}

compared to **1**. Other vibrational peaks at 1442 cm^{-1} were attributed to the O–H bending in the amide.

The strongest band found at 1288 and 1103 cm^{-1} could be assigned to the characteristic C–O stretching vibrations of the aliphatic ether group of polyethylene glycol.

Moreover, the disappearance of the C=O stretching of carboxylic acid confirms the reaction at position 29, while the appearance of the N=N=N stretching peak of **4** at 2106 cm^{-1} supports the presence of the azide.

The UV spectrum of **4** was also recorded for further characterization, showing an absorption peak at 228 nm and another lower absorption peak at 420 nm (n→π transition). An HRMS value of **4** was also obtained for further characterization, validating the proposed structure determined by NMR spectra.

To assess whether compound **4** could be a good candidate as a SERCA inhibitor, we performed computational studies to determine its binding mode with SERCA (**Figure 79**).

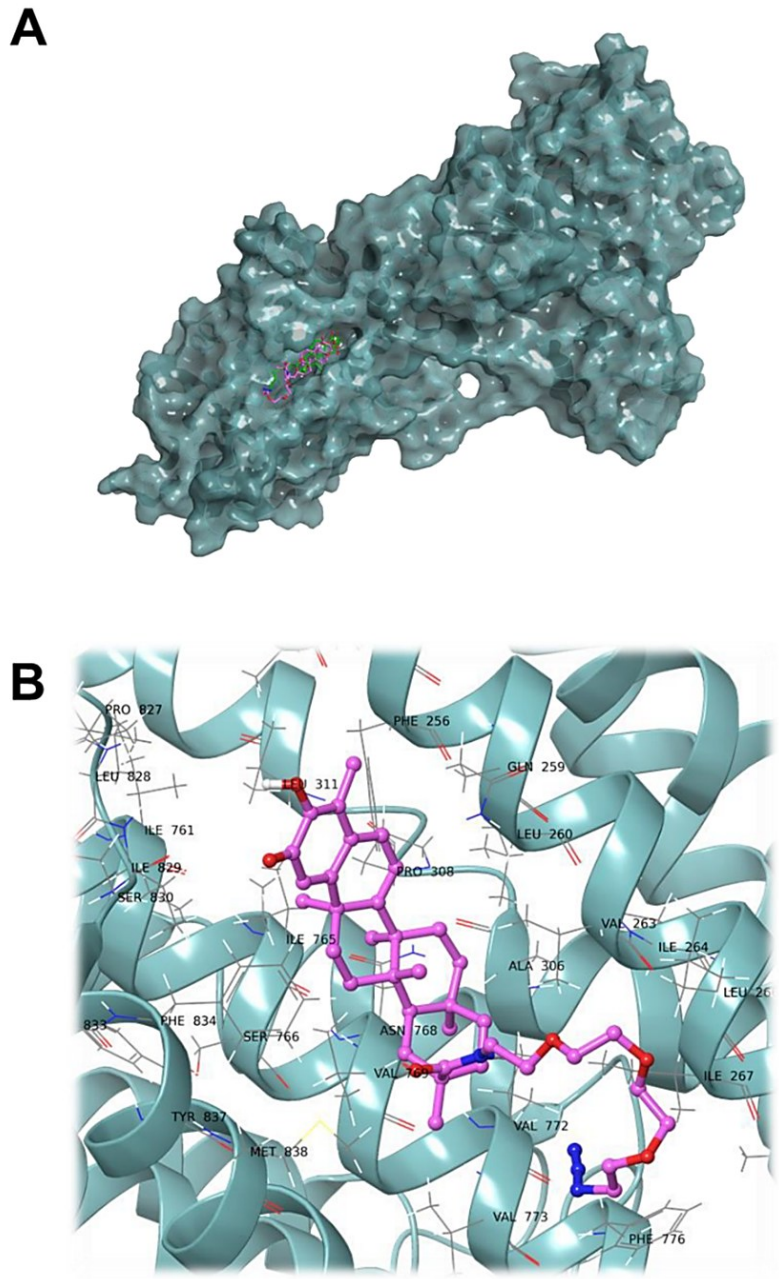

*Figure 79. Predicted interaction motif for compound **4** (pink) and co-crystallized pose of thapsigargin (green) within SERCA binding site (PDB ID: 1IWO) (**A**). Detailed view of the best-docked pose of **4** (magenta) in the binding site of SERCA. Residues located in a zone of 5 Å radius from the center of the ligand have been labeled (**B**).*

A site-specific molecular docking technique was adopted to investigate the interaction motif of compound **4** with SERCA preliminarily. For this reason, the X-ray crystallographic structure of SERCA in complex with thapsigargin was considered (PDB ID: 1IWO) [630]. The robustness of the docking protocol used was evaluated by re-docking thapsigargin to the SERCA binding site and by comparing the docked pose (−8.6 kcal/mol) with the co-crystallized ligand. Further, a root-mean-square deviation (RMSD) value of

1.1056 Å was obtained, hence supporting the accuracy of the protocol (**Figure 79A**). Then, the same protocol was adopted to evaluate the binding mode of compound **4** and celastrol into the same binding site of thapsigargin. A calculated binding energy value of −7.2 kcal/mol was computed for compound **4** (**Figure 79B**), while celastrol reported a docking score of −9.6 kcal/mol. The studied molecule, namely compound **4**, interacts with the binding pocket targeted by thapsigargin through a partially similar binding motif. It must be noted, anyway, that the two compounds are chemically different and are based on different scaffolds. Nevertheless, the docking pose analysis shows co-localization of the hydrophobic parts of the molecules. In **Figure 79B**, the residues within interaction distance (<5 Å) have been labelled. As can be seen in the model, the binding pocket is indeed rich in hydrophobic residues (e.g., Ile, Leu, Val, Phe), which are targeted by both compounds.

Considering potential pharmacological uses, compound **4** was assessed for its physicochemical properties and oral bioavailability using ligand-based predictive modeling [631]. The analysis of these computations revealed that compound **4** violates one of the parameters of Lipinski's rule, indicating the necessity for further refinement to meet comprehensive drug-like standards (**Figure 80**). Thus, even if the compound shows a promising binding mode towards SERCA and a high binding affinity, it may exhibit poor bioavailability. Therefore, parameters such as molecular weight and TPSA should be improved before further studies.

Name	MW	MLogP	HBA	HBD	TPSA (Å^2)	nRtB	nviolations
Lipinsky's rule	≤500	<4.15	≤10	≤5	<75	≤10	**0**
1	450.62	5.06	4	2	74.60	1	**1**
4	650.85	2.18	9	2	143.84	14	**1**

Figure 80. Physicochemical properties of compounds 1 and 4 were calculated by SwissADME. MW: Molecular weight. HBA: Number of hydrogen-bond acceptors. HBD: Number of hydrogen-bond donors. TPSA: topological polar surface area; nRtB: Number of rotatable bonds. Violations: number of Lipinki's rule violations.

Materials and Methods

Chemistry

Silica gel (FCP 230–400 mesh) was used for column chromatography. Thin-layer chromatography was carried out on Merck precoated silica gel 60 F_{254} plates and visualized with phosphomolybdic acid, iodine, or a UV–visible lamp.

All chemicals were purchased from Bide Pharmatech, Ltd. (Shanghai, China) and J & K Scientific (Hong Kong, China). ^{1}H-NMR and ^{13}C-NMR spectra were collected in $CDCl_3$ and DMSO at 25 °C on a Bruker Ascend®-600 NMR spectrometer (600 MHz for ^{1}H and 150 MHz for ^{13}C). All chemical shifts were reported in the standard δ notation of parts per million using the peak of residual proton signals of $CDCl_3$ as an internal reference ($CDCl_3$, δ_C 77.2 ppm, δ_H 7.26 ppm). High-resolution mass spectra (HRMS) were measured using electrospray ionization (ESI). The measurements were performed in a positive ion mode (interface capillary voltage 4500 V); the mass-to-charge ratio was set from *m*/*z* 50 to 3000 Da; external/internal calibration was conducted using an electrospray calibration solution. HRMS analyses were performed by an Agilent 6230 ESI time-of-flight (TOF) mass spectrometer with an Agilent C18 column (4.6 mm × 150 mm, 3.5 μm). The mobile phase was isocratic (water + 0.01% TFA; CH_3CN) at a flow rate of 0.35 mL/min. The peaks were determined at 254 nm using a UV detector.

UV analysis was performed on a Shimadzu UV–2600 with a 1 cm quartz cell and a slit width of 2.0 nm. The analysis was conducted using wavelengths in the range of 200–700 nm.

The FT-IR analysis was performed using a Shimadzu IRAffinity-1S (Osaka, Japan) with a frequency range of 4000–500 cm^{-1} equipped with a SPECAC ATR accessory.

Synthesis of 11-Azido-3,6,9-trioxaundecan-1-amine (3)

To a solution of 2-(2-(2-(2-(2-azidoethoxy)ethoxy)ethoxy)ethyl)isoindoline-1,3-dione (0.479 g, 1.376 mmol, 1.0 eq) in ethanol (25 mL) hydrazine monohydrate (0.3480 g, 6.96 mmol, 5.0 eq) was added, and the reaction mixture was allowed to stir for 4 h at 85 °C. After cooling down to RT, the precipitate was filtered off, and the filtrate was evaporated under reduced pressure. The residue was dissolved in a small amount of ethanol (ca. 20 mL), and the solution was cooled down to 0 °C. The resulting precipitate was filtered off, and the filtrate was evaporated under reduced pressure. The residue was loaded onto

silica and purified by silica gel column chromatography (ethyl acetate:cyclohexane, 1:1 → 2:1) to obtain 2-{2-[2-(2-azidoethoxy)ethoxy]ethoxy}ethan-1-amine (quantitative) as a light yellow oil. The yield was 80% δ_H (600MHz, $CDCl_3$) 3.70–3.63 (10H, m, H3–H7), 3.61 (2H, t, H2), 3.42 (2H, m, H8), 2.98 (2H, t, H1); δ_C (150 MHz, CDCl3): δ = 71.6 (C2), 70.9, 70.9, 70.8, 70.5, 70.3 (C3-C7), 51 (C8), 41.4 (C1); ESI-MS *m/z* 219.44 $[M + H]^+$ (calcd. for $C_8H_{19}N_4O_3^+$, *m/z* 219.42). The spectral characteristics are consistent with those of **3** in the literature [632].

Synthesis of (2R,4aS,6aS,12bR,14aS,14bR)10-hydroxy-N-(4-((6-methoxyquinolin-8-yl)amino)pentyl)-2,4a,6a,9,12b,14a-hexamethyl-11-oxo-1,2,3,4,4a,5,6,6a,11,12b,13,14,14a,14b-tetradecahydropicene-2-carboxamide (4)

To a CH_2Cl_2 (6 mL) solution of celastrol (45 mg, 0.10 mmol), HOBT (41 mg, 0.30 mmol), and EDC-HCl (57 mg, 0.30 mmol) were added under ice/salt-bath (5 °C) conditions. Then, Et_3N (70 µL) was added after 20 min, and the solution was stirred at 5 °C for 1 h. Then, **3** was added, and the mixture was stirred at room temperature for 12–18 h. The mixture was washed thrice with water, and the organic phase was collected, dried over anhydrous Na_2SO_4, filtered, and concentrated in vacuo to give the crude product. The purification was implemented by chromatography on a silica gel column (eluents: from CH_2Cl_2 to 5% MeOH). The yield was 80%, δ_H (600 MHz, $CDCl_3$) 0.64 (3H, s, CH_3), 0.99 (1H, d, H-22), 1.12 (3H, s, CH_3), 1.15 (3H, s, CH_3), 1.26 (3H, s, CH_3), 1.44 (3H, s, CH_3), 1.49–1.70 (7H, m), 1.82–1.92 (3H, m), 1.94–2.15 (4H, m), 2.21 (3H, s, CH_3), 2.44 (1H, t, H–19), 3.29–3.34 (2H, m), 3.39 (2H, t, CH_2), 3.44–3.50 (2H, m, CH_2), 3.57–3.59 (2H, m, CH_2), 3.63–3.68 (8H, m, CH_2), 6.23 (1H, br, NH), 6.33 (1H, d, H-7), 6.52 (1H, s, H-1), 7.00 (1H, d, H-6) ppm; δ_C (150 MHz, $CDCl_3$) 10.2 (CH_3), 18.3 (CH_3), 21.7 (CH_3), 28.6, 29.4, 30.0, 30.9, 31.1, 31.6, 33.5, 33.7, 34.9, 36.4, 38.1, 39.1, 39.3, 40.2, 43.0, 44.4, 45.0, 50.6, 69.5, 70.0, 70.1, 70.5, 70.6, 70.7, 117.0, 118.0, 119.5, 127.4, 134.0 146.0, 164.7, 170.2, 177.7, 178.3 ppm; ESI-MS m/z 651.41 $[M + H]^+$ (calcd. for $C_{37}H_{55}N_4O_6^+$, m/z 651.41); UV (CH_2Cl_2) peaks at 228 and 424 nm; IR (FTIR) 3332, 2931, 2870, 2360, 2106, 1643, 1589, 1442, 1288 and 1103 cm^{-1}.

Computational Studies

The 3D X-ray crystal structure of SR Ca^{2+}-ATPase complexed with thapsigargin (TG1) was retrieved from the RCSB Protein Data Bank (www.rcsb.org; accessed on 24

January 2024; PDB ID 1IWO, resolution 3.10 Å) and used in agreement with previous studies [633].

Prior to conducting site-specific docking studies, SERCA was prepared, and selected chains were isolated and considered. Further, the obtained structure was processed through the DockPrep tool of Chimera to fix missing residues in the receptor eventually. Ligands were built and optimized using Avogadro [604].

The site-specific molecular docking study was performed using AutoDock Vina. The search grid was set according to the following parameters: x = −4.5190, y = −25.0079, z = 9.5195; size: 30.000 × 30.000 × 30.000 Å. Docking simulation was carried out with default Vina parameters; the number of generated docking poses was set to 8, and the docking energy conformation value was expressed in -kcal/mol. After identifying of the best poses, the root-mean-square deviation (RMSD) value was used to validate the adopted method with the *rmsd.py* script, and a score under 2.50 Å was deemed sufficient to consider the analysis accurate. In the case of this study, an RMSD value of 1.1056 Å was obtained. Schrödinger Release 2023-1: Maestro, Schrödinger, LLC, New York, NY, 2023 was used to produce the artworks.

Conclusions

This study introduces the synthesis of a celastrol derivative that can be utilized for profiling studies or applications in click chemistry. NMR, UV, IR, and mass spectrometry were used to characterize the synthesized compound. Computational studies were also employed to assess the binding mode of the compound within the receptor. Molecular docking results revealed a similarity in the binding mode of thapsigargin and compound **4**, with similar docking scores also observed. Although ADME profiling reported one violation of Lipinski's rule, the characterization of compound **4** provides a promising starting point for further optimization steps.

4.3 Antifungal and Antiproliferative Activity of Pistagremic Acid and Flavonoids Extracted from the Galls of Pistacia chinensis subsp. Integerrima

Since ancient times, humans have been familiar with the beneficial roles and pharmacological potential of medicinal herbs in traditional medicine. However, many applications of these plants and spices still require scientific rationalization by fully understanding the underlying molecular mechanisms [634,635]. In this connection, Pistacia chinensis subsp. *integerrima* (J.L. Stewart) Rech. f. from the *Anacardiaceae* family represents an example of a plant of folkloric usage, also known as zebrawood, that has not been thoroughly investigated. Various parts of this single-stemmed, deciduous, multi-branched tree have therapeutic uses described in traditional medicine, which are related to its antimicrobial, anticancer, antioxidant, anti-inflammatory, analgesic, antidiarrheal, and muscle relaxant properties [636,637]. From a chemical point of view, several classes of bioactive phyto-components are contained in different parts of P. *chinensis*, including steroids, flavonoids, terpenoids, tannins, and phenolic compounds [637]. In the current work, we focused our attention on galls, which are abnormal growths in plants formed in response to stressors. These structures often represent reservoirs of peculiar metabolites, which may be endowed with specific biological roles, such as antimicrobial activity. In the case of P. *chinensis*, these parts are traditionally used for aromatic purposes, but also to treat diarrhea, infections, and pain. The triterpene pistagremic acid (1) is one of the main components extracted from P. *chinensis* galls, but it can also be retrieved in its roots and barks. P. *chinensis* galls also contain flavonoids, such as apigenin (2) and sakuranetin (3) that we studied in the current report, and which contribute in conferring antiproliferative, anti-infective, and antioxidant potential to the plant and to its extracts. This study aims to evaluate, by means of *in vitro* tests, the antifungal properties of the defatted methanolic extract of P. *chinensis* galls and of the 3 cited molecules, consisting in a triterpene and 2 flavonoids, isolated by column chromatography. The samples were tested against a panel of 6 different, biologically relevant fungal strains, namely Aspergillus *flavus*, Candida *albicans*, Candida *glabrata*, Fusarium *solani*, Microsporum *canis,* and Trichoderma *longibrachiatum*. Moreover, the antiproliferative activity of the extract and of the compounds was evaluated in human liver, kidney, lung, and ovarian cancer cell lines. Then, we used docking and molecular dynamics studies to aid the rationalization of the biological results, based on information on the interaction motifs of the isolated compounds with two

relevant targets for their antifungal and antiproliferative activity, namely A. *flavus* urate oxidase (Uox) and the epidermal growth factor receptor kinase (EGFRk) domain. Eventually, ligand-based computational studies were employed to assess the drug-likeness of the compounds.

Results and Discussion

Throughout the years, the use of this multipotential plant in various contexts prompted the researchers to isolate and further test the single constituents for their different pharmacological effects. In the current study, the extract and isolated compounds (1-3) were investigated for their antifungal and anticancer properties. In fact, even in the modern era, several fungicidal and fungistatic, as well as anticancer, agents are available; however, side effects, toxicity, and resistance limit their application.

To isolate compounds 1–3, the extract obtained from galls was defatted and then subjected to silica gel column chromatography, which afforded pistagremic acid (1), apigenin (2), and sakuranetin (3) in yields of 0.38%, 0.35%, and 0.35%, respectively. The chemical structures of the isolated compounds are reported in **Figure 81**, and the detailed procedure for their isolation is described in the *Methods section*.

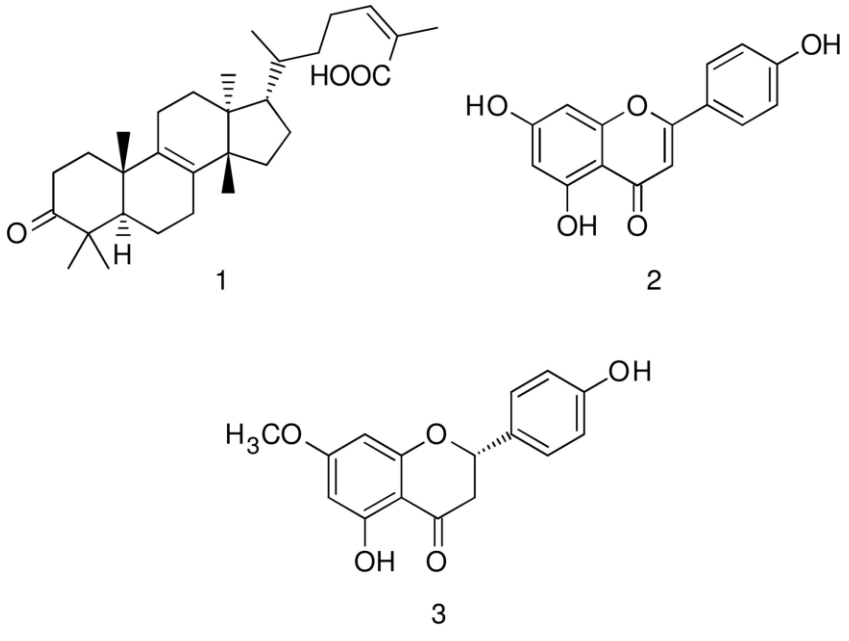

Figure 81. Chemical structures of pistagremic acid (1), apigenin (2), and sakuranetin (3), the compounds isolated from P. chinensis galls and studied in this paper.

P. *chinensis* and its extract were previously reported to possess antimicrobial properties [638], but the involvement of single components still has to be elucidated. In

fact, our group previously investigated the antifungal role of pistagremic acid (1), but in this research work, we expanded the test panel of fungal strains.

Thus, the antifungal activity of the defatted methanolic extract of P. *chinensis* galls and of the isolated compounds was evaluated against A. *flavus*, C. *albicans*, C. *glabrata*, F. *solani*, M. *canis,* and T. *logifusus*. The results are reported in **Table 14**, and depending on the strain, amphotericin B or miconazole was used as a positive control, as indicated. The minimum inhibitory concentration (MIC) of the reference compounds for the fungal strains tested in this research work is reported in **Table 15**.

The antifungal activity of compounds 1–3 is expressed as percent zone of inhibition, with the zone of inhibition achieved with standard drugs set at 100%. This data representation mode is widely used because it is convenient for directly comparing the bioactivity of different compounds. Overall, isolated compounds exhibited higher inhibitory activity compared to the extract, and interestingly, flavonoids 2 and 3 were also active against the strains to which the extract was ineffective. This may be related to the concentration that such compounds have in the extract itself. The best result was observed for compound 2, which showed good inhibitory activity (49.54 % of the positive control) against A. *flavus*. Indeed, apigenin has previously been reported to possess antifungal activity against C. *albicans*, likely due to its interference with mitochondrial calcium signaling [639]. Similarly, the other flavonoid, compound 3, showed a 44.13% zone of inhibition against the same strain. In fact, this methoxylated flavanone is known as a "chemical defense" produced by the plant to combat infections under stress conditions. Thus, this result aligns with the reported bioactivity. Importantly, compound 1, which is also chemically distinct, showed a distinct inhibitory profile and blocked the growth of T. *longibrachiatum* more efficiently (45.23%).

	Zone of inhibition (%)			
	Extract	**1**	**2**	**3**
A. *flavus*	30.23 ± 1.65	45.09 ± 1.23	49.54 ± 1.00	44.13 ± 0.59
C. *albicans*	-	-	29.32 ± 0.39	36.22 ± 0.66
C. *glabrata*	15.43 ± 1.23	18.55 ± 1.00	-	42.32 ± 0.73
F. *solani*	-	-	38.44 ± 0.43	-
M. *canis*	18.32 ± 1.02	20.09 ± 1.05	-	-
T. *longibrachiatum*	30.44 ± 1.43	45.23 ± 1.54	36.54 ± 0.66	24.43 ± 0.32

Table 14. Antifungal effect of the P. chinensis extract and of the isolated compounds (1-3) in terms of percent zone of inhibition. Amphotericin B was used as a positive control in the case of A. flavus, while miconazole was used for the other strains. Results represent the mean of three different experimental readings.

	STD	MIC (µg/mL)
A. *flavus*	Amphotericin B	20.20 ± 0.06
C. *albicans*	Miconazole	110.81 ± 0.21
C. *glabrata*	Miconazole	110.84 ± 0.18
F. *solani*	Miconazole	73.25 ± 0.21
M. *canis*	Miconazole	98.43 ± 0.87
T. *logifusus*	Miconazole	87.79 ± 0.29

Table 15. Minimum inhibitory concentration (MIC) was determined for the reference compounds (STD) against the fungal strains tested in this study.

Then, the extract and isolated compounds were tested for antiproliferative activity against a panel of human cancer cell lines, including HepG2 (liver), A498 (kidney), NCI-H226 (lung), and 2780AD (ovary). Various compounds demonstrated different levels of anticancer effects against the tested cells, and the results are summarized in **Table 16**. In these experiments, the antiproliferative effect was compared to that of the standard drug doxorubicin. Even though apigenin and sakuranetin are more widely studied anticancer compounds [640–642], a remarkable antiproliferative activity was noted for pistagremic

acid (1) on Hep G2 cells, with an IC_{50} value in the same order of magnitude as the positive control. Importantly, the highest effect was observed against the multidrug-resistant 2780AD ovarian cancer cell line, where pistagremic acid (1) remained the most active molecule. Thus, these preliminary findings support the potential of the isolated compounds, particularly compound 1, as antiproliferative agents.

	IC_{50} (µg/mL)				
	Extract	**1**	**2**	**3**	**Doxorubicin**
Hep G2	110.87 ± 1.65	17.87 ± 0.65	89.01 ± 1.00	104.76 ± 1.2	7.64 ± 0.43
A498	180.76 ± 1.23	170.54 ± 0.50	154.76 ± 1.32	190.65 ± 1.76	97.87 ± 0.32
NCI-H226	112.87 ± 1.44	98.09 ± 0.33	108.23 ± 1.08	118.87 ± 1.32	63.09 ± 0.2
2780AD	0.98 ± 1.64	0.76 ± 0.30	0.91 ± 1.07	0.90 ± 1.20	0.21 ± 0.09

Table 16. Antiproliferative effect of the P. chinensis extract and of the isolated compounds. Results represent the mean of three experiments.

It is interesting to note that, according to the results, different chemical components appear to be responsible for distinct bioactivity profiles. Indeed, these observations are in line with previous findings that showed that pistagremic acid (1) is a broad-spectrum cytotoxic compound [643]. It must also be noted that pistagremic acid (1) has already been reported to reverse multidrug resistance mediated by P-glycoprotein [644], suggesting that this compound could act as a multitarget anticancer agent. Thus, the P. *chinensis* extract and the isolated compounds significantly blocked the growth of the various tested fungi. This indicates that the antifungal potential of the tested plant may be due to its bioactive components, particularly flavonoids 2 and 3. On the other hand, the anticancer effects of these molecules are also worth mentioning, especially for compound 1, which encourages us to study further the antifungal and antiproliferative effects of these isolated compounds (1-3). It is also worth noting that identifying the biological targets of compounds with empirically confirmed biological activity can be a challenging task. Moreover, the observed *in vitro* effects may result from the simultaneous contribution of multiple biological targets. Nevertheless, the availability of numerous protein 3D structures, combined with advances

in virtual screening, has spurred the development of *in silico* approaches that accelerate drug discovery [645]. In this context, molecular docking is a computational tool of primary relevance for studying intermolecular interactions between a receptor and a ligand. It finds application in structure-based virtual screening for the discovery of potentially active compounds and for a better understanding of the molecular mechanisms underlying biological activity [646]. In this study, Uox is an enzyme involved in regulating metabolic pathways and plays a role in fungal virulence. Thus, interfering with its functioning could represent a strategy for blocking fungi growth [647,648]. Consequently, the isolated compounds were docked to the enzyme's 3D structure. In particular, apigenin (2) showed the best docking score (-6.34 kcal/mol) towards Uox from A. *flavus* (PDB ID: 1R51). Calculated binding energy values of -3.09 and -4.77 kcal/mol were computed for pistagremic acid (1) and sakuranetin (3), respectively. This result is particularly notable, as compound 2 was also identified as the most promising antifungal agent in the *in vitro* screening. Thus, the interactions between Uox and apigenin (2) were further evaluated. Uox is a globular tetrameric enzyme constituted of monomers composed of two structurally equivalent domains named tunneling-fold (T-fold) [647]. To perform their function, two conserved residues (glutamine or glutamate) are present in the N-terminal end of the first monomer. The sequences in the Uox family share 30–50% identity. This leads to the presence of conserved residues, among which it is notable that histidines and cysteines, two important residues often involved in oxidation processes, are absent. Among them, 15 functionally conserved residues are found near the active site. Phe159 and Leu170 constitute a hydrophobic basement below the substrate; Leu170 is located at the entrance cavity and may help in the arrangement of the ligand. Two relevant residues involved in hydrogen bonding are Arg176 and Gln228. Other important residues are Gln158, Ser226, Asn223, and Asn254, which contribute to the enzyme's inhibitory process through π-π, hydrogen-bond, and water-mediated interactions. Residues on the adjacent monomer also support them. A relevant aspect for Uox is the presence of water molecules in the active site that, through hydrogen bonds with residues Ser226, Asn254, His256, and Tyr257, is involved in the functioning of Uox. With respect to the information retrieved from the literature [649,650], what we observed during the evaluation of the interactions established in docking simulation is that relevant residues like Arg176, Val227, and Gln228 are involved in the Uox/apigenin complex. The -NH2 moiety bound to Cζ in Arg176 establishes a hydrogen bond (2.16 Å) with the present O18 contained in the heterocycle.

Then, the Oε1-Cδ in Gln228 interacted with the O18 of apigenin (2) through a hydrogen bond interaction (1.68 Å). Lastly, the same group interacted via another hydrogen bond (2.09 Å) with the N Cα atom of Val227 (**Figure 82A**). Furthermore, the isolated compounds were docked against a widely studied anticancer drug target. EGFR is a tyrosine kinase receptor located in the epithelial cell membrane. Endogenous ligands stimulate its activation, triggering signaling cascades that regulate normal cellular functions. Nevertheless, besides normal conditions, EGFR can be overexpressed, and in this case, its activation can promote excessive stimulation of cascades mediating angiogenesis, growth, and progression of tumors, and metastasis [651]. Consequently, throughout the years, medicinal chemists focused their attention on the identification of EGFR inhibitors, and several compounds were approved by the FDA [652]. Moreover, it must be noted that EGFR is listed among the putative anticancer targets of apigenin (2) [640]. Thus, by means of a docking study, we also investigated the binding of the compounds to EGFRk (**Figure 82B**, PDB ID: 1M17). A calculated binding energy value of -3.90 kcal/mol was computed for compound 1, while better results were recorded for flavonoids 2 and 3 (-8.19 and -6.67 kcal/mol, respectively). In this case, it was not possible to identify a clear correlation with the experimental data, in which compound 1 outperformed the flavonoids. It must be pointed out that, as will be discussed in the following, several other macromolecular interactors could mediate the activity of the compound. From a structural point of view, EGFRk comprises almost 50% of the EGFR intracellular fraction. This rearranges into a bilobate-fold conformation. Usually, it consists of three lobes: the NH2-terminal lobe (N-lobe), the ATP-binding pocket located between N- and C-lobes where ATP, ATP analogues, and ATP competitors reside, and a terminal-COOH lobe (C-lobe). Many are the important residues for the functioning of the enzyme, like Gly695 and Gly700 (which form the glycine-rich nucleotide phosphate-binding loop). Then, the C-lobe contains the amino acid sequence Leu955-Val956-Ile957 (LVI motif). Further other residues like Gly672, Arg681, Ile682, Lys721, and Glu738. Further, in the A-loop in EGFRk, residues Glu842, Tyr845, and Glu844 are pivotal for EGFR function. Other important residues for the establishment of interactions between EGFRk/substrate are Leu718, Val726, Ala743, Leu792, Met793, Met769, Thr766, and Cys751 [653,654]. The evaluation of interactions obtained from molecular docking was also performed in this case for compound 1 and, interestingly, a hydrogen-bond interaction (1.70 Å) between the NH Cα of Met769 and the carboxylic group of pistagremic acid (1) was established (**Figure**

82B). Furthermore, the interactions of the most promising compounds according to the results of *the in vitro test were* studied in a more detailed way by means of molecular dynamics. In both simulations, the best-docked poses were used as the starting point.

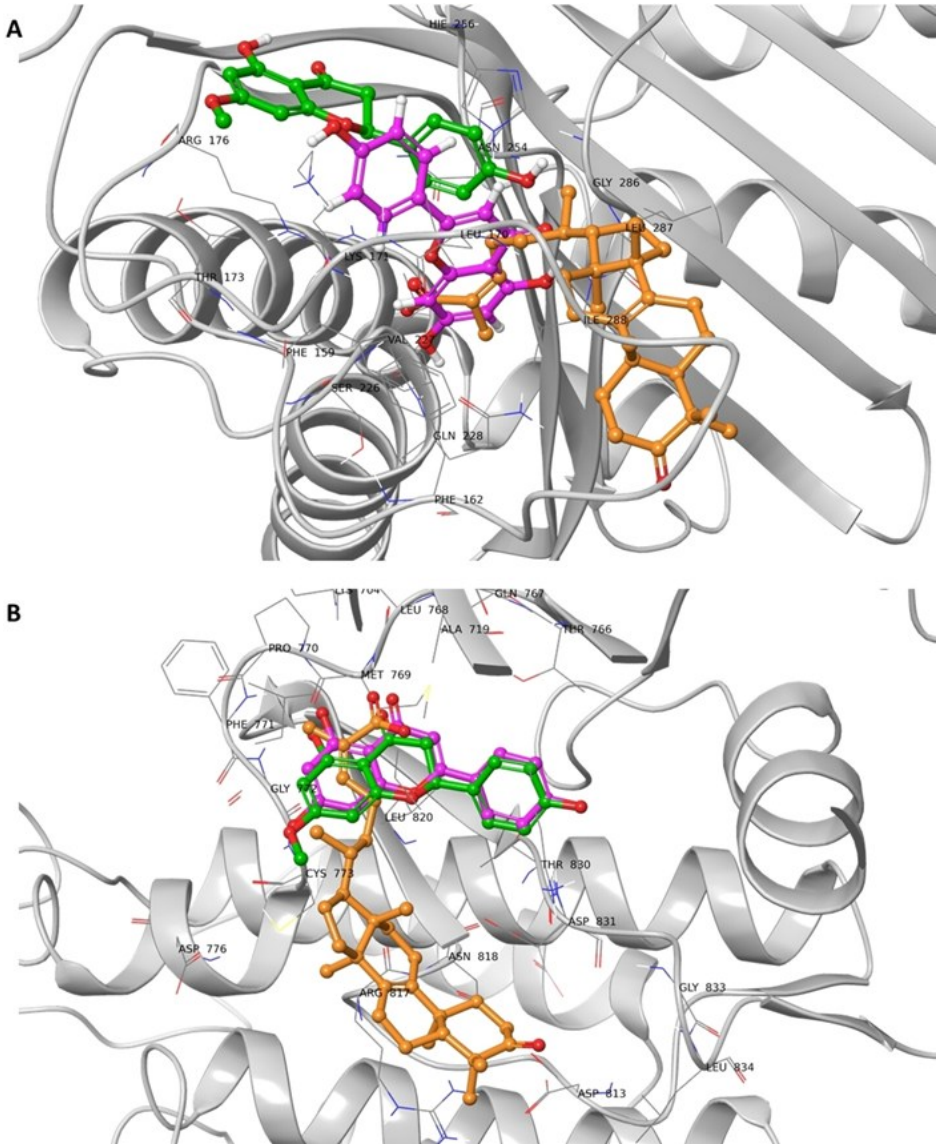

Figure 82. Predicted interaction motif for pistagremic acid (1, orange), apigenin (2, pink), and sakuranetin (3, green) with A. flavus Uox (A). Predicted interaction motif for pistagremic acid (1, orange), apigenin (2, pink), and sakuranetin (3, green) with EGFRk (B).

The analysis revealed that three main events characterized the dynamic simulation of the complex Uox/apigenin. During the first event, which matches with the initial part of the run, there is the presence of purely stable fluctuations made possible thanks to the π-π interactions and hydrogen bonds with Phe159, Val227, Gln228, and Phe258, where some of these are the same that emerged in molecular docking evaluation. The second situation coincides with the simulation period, which ranges from 10 to 175 ns. Further fluctuations

occur and then converge in the stability of the complex, and at this stage, the ligand establishes interactions with residues His256 and Tyr257. Finally, the third event is characterized by the ligand that fluctuates from the binding site with the aim of reacquiring previously observed interactions during molecular docking, such as the one with Gln228, important for Uox activity (**Figure 83**).

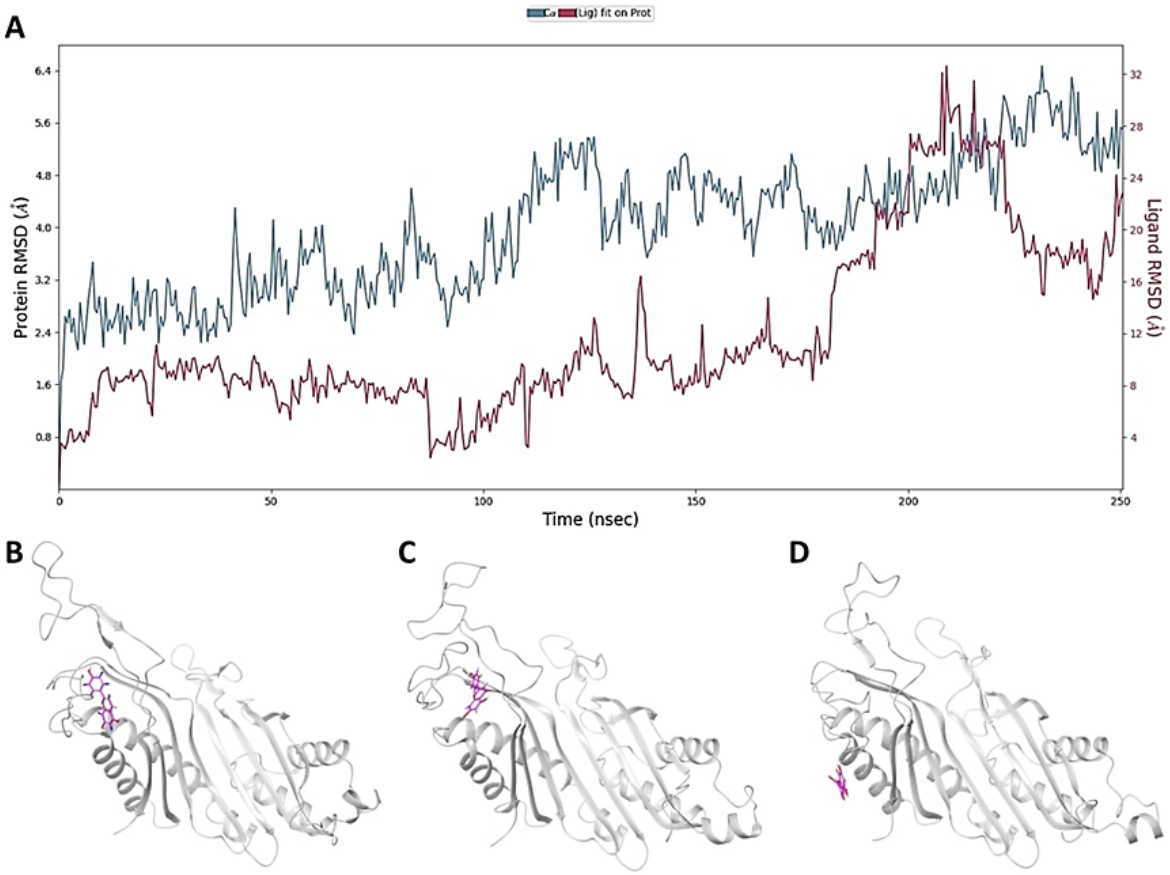

Figure 83. Trajectories retrieved from MD simulation showing the (root-mean-square deviation) RMSD of the Uox/apigenin system over the simulation time. The plot for the heavy atoms of the ligand is depicted in red (aligned with the protein), while the plot for protein C-alphas is depicted in blue (A). Snapshots of Uox/apigenin complex relative to frame 1 (0 ns, B), frame 175 (87.5 ns, C), and frame 470 (235 ns, D).

Then, the dynamics simulation of the complex EGFRk/pistagremic acid was analyzed, which highlighted overall system stability. Beyond an event involving the first part of the simulation, ranging from 0 to 60 ns, where the ligand oscillates with the aim of stabilizing itself in the binding pocket, the rest of the simulation is stable over time (**Figure 84**). The remaining portion of the simulation shows that the carboxyl group present in pistagremic acid (1) establishes the largest number of interactions. Looking more in detail, we have seen that these interactions evolve over time; going from a first moment where there is a hydrogen bond with Met769 to a second moment where this is replaced by another

interaction with Lys704; both residues, as reported in the literature, are relevant for inhibitory activity of EGFRk.

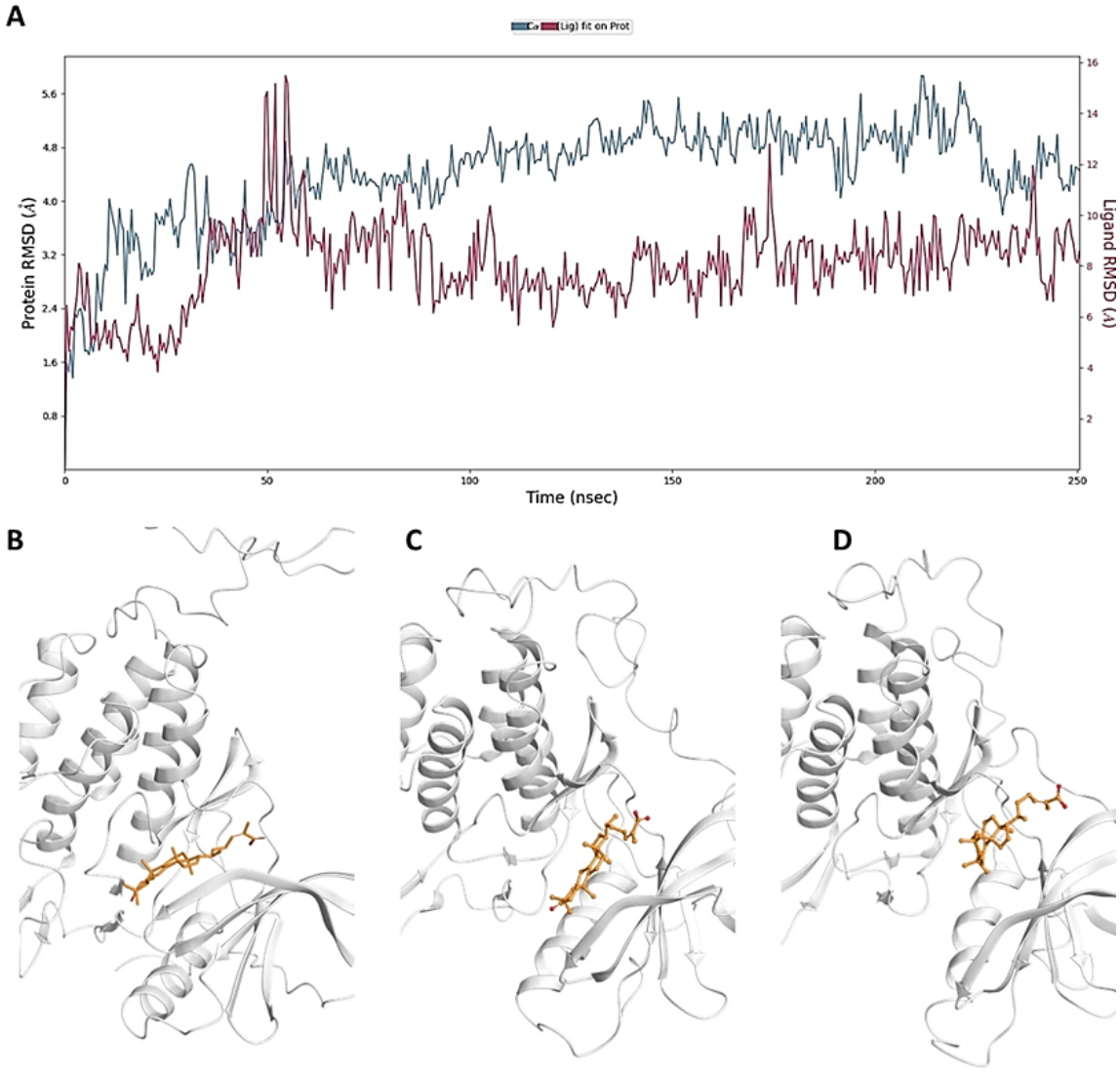

Figure 84. Trajectories retrieved from MD simulation showing the RMSD of the EGFRk/pistagremic acid system over the simulation time. The plot for the heavy atoms of the ligand is depicted in red (aligned with the protein), while the plot for protein C-alphas is depicted in blue. For the RMSD plot, residues Arg953-Pro995 were not considered due to high (root-mean-square fluctuation) RMSF values observed for that portion of the macromolecule (A, see Figure S4 in the Supporting Information). Snapshots of EGFRk/pistagremic complex relative to frame 1 (0 ns, B), frame 250 (125 ns, C), and frame 470 (235 ns, D).

In a ligand-based approach, the SwissADME web service was used to compute a set of physicochemical descriptors known to be relevant to ADME parameters and pharmacokinetic properties [631]. Such features allow for a preliminary evaluation, using computational tools, of whether a molecule possesses the chemical properties required for oral administration. Their ideal values are summarized in Lipinski's rule, which states that the compound should possess no more than 5 hydrogen bond donors, no more than 10

hydrogen bond acceptors, a molecular weight below 500 Da, and an octanol/ water partition coefficient (LogP) that does not exceed 5 [463]. Overall, pistagremic acid (1), apigenin (2), and sakuranetin (3) are considered drug-like compounds. In fact, only one violation of Lipinski's rule was predicted for compound 1 (LogP = 5.63), while flavonoids 2 and 3 showed no computed violations. Additionally, according to predicted physicochemical descriptors, 1 is characterized by a low water solubility and poor absorption through the gastrointestinal (GI) tract. On the other hand, flavonoids 2 and 3 are highly water-soluble and GI-permeant.

As demonstrated in previous parts of this study, the tested compounds showed promising anti-infective and antiproliferative activity *in vitro*. Nevertheless, in the context of drug discovery, potential off-targets must be considered. In our ligand-based study, SwissTargetPrediction was used to foresee other potential macromolecular interactors that could mediate side effects. The results of the simulation, carried out using the Homo *sapiens* target database, indicated that pistagremic acid (1) could bind to estrogen alpha and beta receptors with a probability of 0.79/1.

On the other hand, NADPH oxidase 4, CDK5, xanthine dehydrogenase, monoamine oxidase, cytochrome P450 19 A1, and estrogen receptor alpha were highlighted as potential targets of apigenin (2) with a probability of 1/1. Eventually, taste receptor type 2 member 31 and adenosine A3 receptor were retrieved as interactors for sakuranetin (3) with a probability of 1/1. Again, estrogen receptor beta was present among the records with a moderate probability (0.42/1). While little information is available in the literature on the bioactivity of pistagremic acid (1), flavonoids 2 and 3 were previously reported as modulators of estrogen receptors [655,656]. Thus, computational predictions are in line with experimental data: the influence of this extract and such isolated compounds on the estrogen pathway cannot be ruled out. They must be considered in view of their development as therapeutic agents.

Conclusions

In this work, we reported the isolation of three bioactive molecules, consisting in pistagremic acid (1) and flavonoids 2 and 3. The extract and the isolated compounds exhibited varying degrees of antifungal activity against relevant fungal strains, including A. *flavus*, C. *albicans*, C. *glabrata*, F. *solani*, M. *canis*, and T. *longibrachiatum*. In particular, the flavonoids were identified as the most promising compounds in this test.

Furthermore, the same samples showed varying anticancer effects across a panel of human cancer cell lines. Notably, the maximum effect was observed against the multidrug-resistant 2780AD ovarian cancer cells. In this case, pistagremic acid (1) outperformed the flavonoids in terms of antiproliferative activity. Computational studies were used to investigate the molecular mechanisms underlying the observed biological activity, and the simulation results are at least partially consistent with the experimental data. MD simulation showed that, in both cases, the most promising ligands targeted key residues in the receptors' binding pockets. Nevertheless, according to ligand-based simulations, potential involvement of the estrogen pathway cannot be ruled out. In conclusion, this study highlights a distinct bioactivity profile for the triterpene and flavonoid constituents of P. *chinensis* galls and underscores the potential of plant-synthesized small molecules as "chemical defense". Most importantly, a good agreement between experimental data and simulations was observed. Thus, the results support the different traditional therapeutic applications of this plant and pave the way for the future development and optimization of pistagremic acid (1) as an anticancer agent and of P. *chinensis* flavonoids 2 and 3 for their antifungal properties.

Materials and Methods

All the current data are published; readers can access the Supporting Information on the publication site [657].

Extraction and isolation of compounds

The fresh galls of P. *chinensis* (Pistacia *chinensis* subsp. *integerrima* (J.L. Stewart) Rech. f.) were collected in the month of July from the garden of Islamia College, Peshawar, KP, Pakistan. The plant specimen was identified by Dr. Abdur Rashid, chairman of the Botany Department of Peshawar University, KP, Pakistan. After identification, the voucher specimen UOS/Bot (20037) was deposited in the herbarium of the above-mentioned Department. The extraction and spectroscopic characterization were performed according to a previously reported procedure [658]. Antifungal assay The evaluation of the antifungal effect of the extract and of the isolated constituents was conducted according to a previously published procedure [659]. The fungal strains A. *flavus* (ATCC 32611), C. *albicans* (ATCC 2091), C. *glabrata* (ATCC 90030), F. *solani* (ATCC 11712), M. *canis* (ATCC 11622), and T. *longibrachiatum* (ATC 18648) were provided by the Institute of Chemical Sciences, University of Peshawar, KP, Pakistan. Stock solutions of the compounds to be tested and of the extract were prepared in DMSO (22 mg/mL).

Autoclaved Sabouraud Dextrose Agar (SDA) medium (4 mL) was used for the preparation of the assay, and it was mixed with 66.6 µL of stock solutions, leading to a final concentration of 400 µg/mL of the samples. The solidified tubes were inoculated with 7-day-old cultures of fungal strains. Amphotericin B and miconazole were used as positive controls at the same concentration, while DMSO was used as a negative control. The MIC, which is the lowest concentration of the samples that visually shows the absence of growth [660], was assessed for the standard drugs used as controls, and the results are reported in the Supporting Information.

The antifungal effect of extracts and compounds was calculated as the percent zone of inhibition, considering the inhibition achieved with standard drugs as 100 %. In general, the zone of inhibition is the diameter of the growth-inhibited zone surrounding the discs [660], and the percent zone of inhibition is calculated by the ratio between the diameter measured for test compound and the diameter for the standard drug, multiplied by 100. The results were expressed as mean of three assays standard deviation. Graph Pad PRISM 6 was used for data analysis.

Antiproliferative activity

The anticancer potential of the extract and of the isolated constituents was assessed through the MTT test. The Gibco RPMI 1640 medium was supplemented with streptomycin sulfate (100 g/ mL), penicillin sodium (100 g/mL), sodium bicarbonate (2 mg/mL), and fetal bovine serum (10 %). The human cancer cell lines, i.e., Hep G2 (liver, ATCC HB-8065), A-498 (kidney, ATCC HTB-44), NCI H226 (lung, ATCC CRL-5826), and 2780AD (ovary, ATCC TCP-1021), were used for this assay, and the inhibition of the growth of these cells was tested upon exposure to extract/compounds following a standard procedure.[40] Doxorubicin was used as a positive control, while DMSO was used as a negative control, and no growth inhibition was observed for the samples treated with the negative control. Cells were examined after 48 h of incubation and the IC_{50} was calculated from triplicates. The results were expressed as the mean of three assays standard deviation. Graph Pad PRISM 6 was used for data analysis.

Molecular docking

The 3D structures of the considered targets were obtained from the Protein Data Bank (PDB, www.rcsb.org, accessed 11 September 2023). The Uox models of A. *flavus* (PDB ID: 1R51) and EGFRk (PDB ID: 1M17) were used in the simulations, in agreement with previous studies [649,661]. The preparation step was done through the Protein Preparation Wizard tool. The assignment of disulfide bonds, adding missing side chains using Prime, removing waters, adjusting charges, and minimizing the convergence of heavy atoms to RMSD under the OPLS4 force field was done [63]. In the case of Uox from A. *flavus* (PDB ID: 1R51), the pH for the preparation step has been set to 8; this was chosen with the aim of reproducing the best pH of the peroxisome environment [662]. For the same reason, the preparation of the EGFR kinase domain (PDB ID: 1M17) was performed at pH 7.4 [654]. The structures of ligands were prepared with the LigPrep tool under the OPLS4 force field by using an Epik Ionizer. All the ionization states were generated in the 8.0 ± 0.3 pH for the case of Uox investigation, while a pH set to 7.4 ± 2.0 was chosen for the EGFRk case. Binding poses of complexes Uox/apigenin and EGFRk/pistagremic acid were obtained by molecular docking calculations through Glide tool [300,301]. The Receptor grid was generated using the Receptor Grid Generation tool in Schrödinger with default settings. Docking protocol consisted of rigid receptor and flexible ligand sampling; this was performed under the OPLS4 force field using standard precision (SP) with default settings

like adding Epik state penalties to the docking score, generation of one pose per ligand, 0.80 scaling factor, 0.15 partial range cutoff, the ligand atom Van der Waals radius, and performing post docking minimization for generated poses. After the identification of the best poses, the RMSD value was used to validate the molecular docking method used. This was done through the Superposition tool, and a score under 2.50 Å was admitted in order to consider the analysis sufficiently accurate [408]. The validation of the Uox/apigenin led to an RMSD value of 1.41 Å while the complex EGFRk/pistagremic acid reported an RMSD value of 1.94 Å. Once that the validation of the protocol was done, the GlideScore (GScore) scoring function (expressed in kcal/ mol) was used to evaluate the best-docked poses in energetic terms. Further, interactions established between receptors and their respective ligands were inspected through the Ligand Interaction tool. Only interactions within 5 Å in the binding pocket have been considered. Graphic representations were produced using Schrödinger (Schrödinger Release 2023–3: Maestro, Schrödinger, LLC, New York, NY, 2023).

Molecular dynamics

Molecular dynamics simulations were done by using the GPU-accelerated Desmond tool of Schrodinger LLC (Schrödinger Release 2023–1: Desmond Molecular Dynamics System, D.E.Shaw Research, New York, NY, USA, 2021. Maestro-Desmond Interoperability Tools, Schrödinger, New York, NY, USA 2021) [420]. Best-docked protein/ ligand complexes obtained through SP molecular docking were used to prepare and solvate the system to perform Molecular Dynamics simulations. Both complexes were solvated through the System Builder tool. Periodic boundary conditions were set with an orthorhombic box shape of 10×10×10 Å (for Uox/apigenin system) and 10×10×12 Å (for EGFRk/pistagremic acid). The solvation was done by using the TIP3P water model. For both complexes, Na^+ ions were used to neutralize the system, and a 0.15 M NaCl solution was used. For both complexes, a 250 ns run was performed under the OPLS4 force field, with pressure set at 1.01 bar and temperature at 303.15 K (for Uox/apigenin) and 310.15 K (for EGFRk/pistagremic acid). A RESPA integrator was set with the time step of 2.0, 2.0, and 6.0 fs, respectively, for bonded, near, and far interactions. The Martyna-Tobias-Klein chain coupling scheme with an isotropic coupling constant of 2.0 ps for the pressure control and the Nosé-Hoover chain coupling scheme for the temperature control (NPT ensemble) for 1.0 ps were used. Trajectories were saved every 500 ps interval for analysis. To evaluate

interactions between ligands and receptors, the Simulation Interaction Diagram Tool was used.

Ligand-based computational studies

Physicochemical descriptors used to predict drug-likeness, ADME parameters, and pharmacokinetic properties were computed using the SwissADME web service (www.swissadme.ch; Molecular Modeling Group, Swiss Institute of Bioinformatics, Lausanne, CH).[32] The SwissTargetPrediction web service was used to predict putative macromolecular interactors of the studied compounds (www.swisstargetprediction.ch, Molecular Modeling Group - Swiss Institute of Bioinformatics, Lausanne, CH) [595]. The following SMILES notations were used: C[C@@]12CC[C@@H](C(C)CC\C=C(\C)C(O) = O)[C@]2(C)CCC2 = C1CC[C@@H]1[C@]2(C)CCC(= O)C1(C)C (pistagremic acid, 1); O=C1C=C(Oc2cc(O)cc(O)c21)c1ccc(O)cc1 (apigenin, 2); O=C1CC(Oc2cc(cc(O)c21)OC)c1ccc(O)cc1 (sakuranetin, 3).

5. Conclusions and Future Perspectives

This doctoral thesis presents the research I conducted during my PhD project on the development of new ligands targeting G4s as heavily depicted in the literature, aromatic scaffolds that favors interactions with G4s, anthracenes have been investigated in my former laboratory over the years leading to the development of the anthracene-propargylamine scaffold, which, to increase selectivity for G4 over the canonical counterpart, was modified to a new di-substituted ligand. In this context, my work, performed using *in silico* tools such as molecular docking and dynamics, confirmed and unraveled the binding mode of the OAF89 ligand. Moreover, in my former lab, several analytical workflows, primarily based on ESI-MS and NMR spectroscopy, were developed over the years to characterize G4-ligand interactions. This was also the case for OAF89, which, due to its good selectivity and interaction profile with Tel23 structure, was tested *in vitro* in lung cancer cell lines of different natures. Despite the promising binding and selectivity profile, this step marked a turning point, defined by toxicity issues, which highlighted the need to modify the ligand's structure further rationally.

Then, still referring to the literature, the class of flavonoid-derived compounds was investigated as G4 binders using both computational and in vitro methods, which revealed that isoflavones could be promising scaffolds for developing selective G4 binders and stabilizers. Starting from a previous structure-activity relationship (SAR) work in which these compounds underwent several derivatizations with several substituents, such as the tosyl moiety, these were tested, and the latter showed increased selectivity for G4 over dsDNA. Again, in this context, my work primarily focused on conducting *in silico* studies, which enabled us to demonstrate that tosylated derivatives interacted better with G4 differently than their natural precursors. Again, to confirm computational findings, NMR analysis was used to verify the relevance of the tosyl moiety.

Furthermore, over the years, computational studies have become a pivotal step in the scenario of G4 identification, serving as a key factor in the development and optimization of newly developed compounds. This was the case of AQA3, a dimeric ligand designed to function as a molecular tweezer, effective for G4 stabilization, especially in the parallel topology (known to be biologically relevant in telomere-dependent processes). A new branch in G4-ligand discovery has been established in our lab to identify, through a SAR-based study, new compounds that can prevent the self-stacking aspect and perform equally well as AQA3.

Then, due to the relevance that PDE9A gained over the years in both tumoral and neurodegenerative disease contexts, this target was investigated during my PhD as a therapeutic target, respectively, in the context of CNS diseases. During the years, several compounds have been synthesized, characterized, and stored in the in-house database of Prof. Gianoncelli (which I implemented in my first year of PhD). From this, the database was used to identify PDE9A inhibitors through several screening steps (e.g., assessing druglikeness and using a chromone query as a parameter), which allowed for the reduction of the number of compounds to be evaluated. Then, PDE9A binders were identified through molecular docking, where the top 20 compounds were then screened in an *in vitro* solubility test, as this is a pivotal parameter considered in the preliminary steps of drug discovery. All information led to the identification of DB987, for which a stable complex was identified through MD simulation. For testing the inhibitory activity of the compound, *in vitro* tests demonstrated high inhibitory activity (IC_{50} of 5 nM), comparable to that of the control PF-04447943, which has an IC_{50} of 14 nM. To demonstrate the biological activity of DB987, it was used to treat organotypic hippocampal slices subjected to neuronal damage caused by kainate exposure, enabling the recovery of neurons. Due to the good results obtained with DB987 in terms of potency and biological activity, a study on SAR began in my third year. The hit compound was fragmented into several substructures, leading to the selection of six queries used to further screen our in-house database, which allowed the identification of 27 compounds that underwent a docking-based screening step and manual inspection of the obtained poses. Ligands able to interact with key residues for PDE9A activity (Gln453 and Phe456), yielded BS586 and BS560, a quercetin and a 6-bromo quercetin, respectively were selected for further *in vitro* studies. In collaboration with the University of Florence, a new application for PDE9A inhibitors has been proposed, as it is reported that neuroinflammation states (as observed in models induced by LPS exposure) in mixed glial cells are characterized by increased levels of PDE9A. Although their findings are considered preliminary, BS560 and BS586 are reported to play a role in the significant reduction of the inflamed state.

As can be deduced from this 3-year PhD work, apart from some cases, the presence of natural compounds as direct or indirect bioactive agents in various applications has been extensively studied, especially in my case, through computational means, especially for the case of G4s, where flavonoids (more drug-like than anthracene counterparts) were found to be suitable stabilizers for telomeric G4s. Now that some of these ligands have been

explored, *in vitro* analysis is needed to test their bioactivity. Future studies to identify suitable compounds are in progress for both G4 and PDE9A targets, intending to find more non-toxic compounds (especially for OAF89). Furthermore, new targets are under investigation since new evidence for specific G4s in cancer-related contexts has been identified in the literature. Evidence on PDE9A isoforms enabled us to initiate a new branch of research in our lab, where binding sites in protein-protein interaction proteins are evaluated and targeted with natural or nature-derived compounds.

In conclusion, throughout my PhD, I participated in a series of works that established collaborations (both national and international) (see *Produced Literature*).

Abbreviations

Abbreviation	Full Name
3D	Three-Dimensional
AI	Artificial Intelligence
ALS	Amyotrophic Lateral Sclerosis
BA	Binding Affinity
CADD	Computer-Aided Drug Design
CCS	Collisional Cross Section
CD	Circular Dichroism
CID	Collision-Induced Dissociation
CNS	Central Nervous System Diseases
CX-3543	Quarfloxin
CX-5461	Pidnarulex
DC	Direct Current
DNA	Deoxyribonucleic Acid
dsDNA	Double-Stranded DNA
EHSS	Exact Hard Sphere Scattering
ESI	Electrospray Ionization
FDA	Food And Drug Administration
G4	G-Quadruplex
HTS	High-Throughput Screening
HTVS	High-Throughput Virtual Screening
IC_{50}	Half Inhibitory Concentration
IMMS	Ion-Mobility Mass Spectrometry
LBDD	Ligand-Based Drug Design
LC	Lung Cancer
LJ	Lennard-Jones
m	Mass
MD	Molecular Dynamics
ML	Machine Learning
MTTK	Martyna-Tobias-Tuckerman-Klein

NDD	Neurodegenerative Diseases
NDI	Naphthalene Diimides
NH_4OAc	Ammonium Acetate
NMR	Nuclear Magnetic Resonance
NOE	Nuclear Overhauser Effect
OAF89	9,10-Bis[(4-(2-Hydroxyethyl)Piperazine-1-Yl)Prop-2-Yne-1-Yl]Anthracene
P	Pressure
PA	Project Approximation
PBCs	Periodic Boundary Conditions
PD	Pharmacodynamics
PDB	Protein Data Bank
PDE9A	Phosphodiesterase 9
PDS	Pyridostatin
PK	Pharmacokinetics
PQS	Putative G4 Sequences
QN-302	Sop1812
QSAR	Quantitative Structure-Activity Relationship
RF	Radio Frequency
RMSD	Root-Mean-Square Deviation
RMSF	Root-Mean-Square Fluctuation
RNA	Ribonucleic Acid
RoG	Radius Of Gyration
SAXS	Small-Angle X-Ray Scattering
SBDD	Structure-Based Drug Design
STD	Saturation Transfer Difference
T	Temperature
TERRA	Telomeric Repeat-Containing RNA
ThT	Thioflavin T

TIMS	Trapped Ion Mobility Mass Spectrometry
TM	Trajectory Method
TOF	Time-Of-Flight
TRF2	Telomere-Binding Protein
V	Volume
VdW	Van Der Waals
z	Charge
ΔG	Docking Score

6. Produced literature

Fai, L.K.; M. Anyanwu; Ai, J.; Xie, Y.; Gianoncelli, A.; Ribaudo, G.; Coghi, P. 4-(4-(((1H-Benzo[d][1,2,3]Triazol-1-Yl)Oxy)Methyl)-1H-1,2,3-Triazol-1-Yl)-7-Chloroquinoline. Molbank 2022, **2022**, M1404, doi:10.3390/m1404..

Jiang, A.; M. Anyanwu; Leong, K.; Li, J.; Gianoncelli, A.; Coghi, P.; Ribaudo, G. 3-[(1H-Benzo[d][1,2,3]Triazol-1-Yl)Oxy]Propyl 9-Hydroxy-5a,5b,8,8,11a-Pentamethyl-1-(Prop-1-En-2-Yl)Icosahydro-3aH-Cyclopenta[a]Chrysene-3a-Carboxylate. Molbank 2022, **2022**, M1419, doi:10.3390/m1419..

Landucci, E.; Ribaudo, G.; Anyanwu, M.; Oselladore, E.; Giannangeli, M.; Mazzantini, C.; Lana, D.; Giovannini, M.G.; Memo, M.; Pellegrini-Giampietro, D.E.; et al. Virtual Screening-Accelerated Discovery of a Phosphodiesterase 9 Inhibitor with Neuroprotective Effects in the Kainate Toxicity In Vitro Model. ACS Chemical Neuroscience **2023**, 14, 3826–3838, doi:10.1021/acschemneuro.3c00431..

Mastinu, A.; Anyanwu, M.; Carone, M.; Abate, G.; Bonini, S.A.; Peron, G.; Tirelli, E.; Pucci, M.; Ribaudo, G.; Oselladore, E.; et al. The Bright Side of Psychedelics: Latest Advances and Challenges in Neuropharmacology. International Journal of Molecular Sciences **2023**, 24, 1329, doi:10.3390/ijms24021329..

Rauf, A.; Anyanwu, M.; Aliiri, A.A.; Alanazi, H. a. H.; Alharbi, A.M.A.; Wadood, A.; Aljohani, A.S.M.; Muhammad, N.; Samad, A.; Shah, S.U.A.; et al. Antifungal and Antiproliferative Activity of Pistagremic Acid and Flavonoids Extracted from the Galls of Pistacia Chinensis Subsp. Integerrima. Chemistry & Biodiversity **2023**, 21, e202301815, doi:10.1002/cbdv.202301815..

M. Anyanwu, M. Giannangeli, X.-X. Fan, P. Coghi, G. Ribaudo, and A. Gianoncelli, "9,10-Bis[(4-(2-hydroxyethyl)piperazine-1-yl)prop2-yne-1-yl]anthracene: G-Quadruplex Selectivity and Anticancer Activity," *ACS Medicinal Chemistry Letters*, vol. 15, no. 9, pp. 1615–1619, Aug. **2024**, doi: 10.1021/acsmedchemlett.4c00340.

Rauf *et al.*, "Dinaphthodiospyrol H: a natural α-glucosidase inhibitor extracted from Diospyros kaki L.f," *Natural Product Research*, pp. 1–5, Sep. **2024**, doi: 10.1080/14786419.2024.2397725.

G. Ribaudo *et al.*, "G-Quadruplex DNA as a macromolecular target for Semi-Synthetic isoflavones bearing B-Ring tosylation," *Macromol—A Journal of Macromolecular Research*, vol. 4, no. 3, pp. 556–565, Aug. **2024**, doi: 10.3390/macromol4030033.

G. Yuzhu *et al.*, "(2R,4aS,6aS,12bR,14aS,14bR)-N-(2-(2-(2-(2-azidoethoxy)ethoxy)ethoxy)ethyl)-10-hydroxy-2,4a,6a,9,12b,14a-hexamethyl-11-oxo-1,2,3,4,4a,5,6,6a,11,12b,13,14,14a,14b-tetradecahydropicene-2-carboxamide," *Molbank*, vol. 2024, no. 2, p. M1800, Apr. **2024**, doi: 10.3390/m1800.

G. Ribaudo, M. Giannangeli, M. Anyanwu, and A. Gianoncelli, "Phosphodiesterase 9 localization in cytoplasm and nucleus: the gateway to selective targeting in neuroprotection?" *Neural Regeneration Research*, vol. 20, no. 6, pp. 1701–1702, Jul. **2024**, doi: 10.4103/nrr.nrr-d-24-00373.

M. Anyanwu, M. Giannangeli, A. Gianoncelli, and G. Ribaudo, "Therapeutic Approaches Interfering with Nuclear Localization Signals: An Emerging Strategy for CNS-Related Diseases," *Current Neuropharmacology*, vol. 23, Jul. **2025**, doi: 10.2174/011570159x384321250627071259.

E. Durosini, M. Anyanwu, T. Vendrame, A. Gianoncelli, and G. Ribaudo, "Mechanistic investigation on compounds from Amorpha *fruticosa* L. targeting acetylcholinesterase," *Natural Product Research*, pp. 1–6, Apr. **2025**, doi: 10.1080/14786419.2025.2495856.

G. Ribaudo, M.A. Pagano, M. Anyanwu, M. Giannangeli; M. Vezzoli, A. Visentin, F. Frezzato, L. Trentin, A.M. Brunati, A. Gianoncelli. "Interplay between Protein Phosphatase 2A (PP2A) and SE Translocation (SET) as Macromolecular Target of Anticancer Compounds: A Combined Computational and Experimental Study".

Macromol—A Journal of Macromolecular Research **2025**, 5, 43, doi:10.3390/macromol5030043.

M. Giannangeli, N. Dal Ponte, M. Anyanwu, M.B. Romanello, E. Mucenji, R. Rigo, G. Ribaudo,* C. Sissi,* and A. Gianoncelli. “Enhancing G-Quadruplex Binding: Rational Design and Biophysical Evaluation of Dimeric Ligands”. Chemistry - A European Journal – **2025**, e03128, doi:10.1002/chem.202503128.

7. References

1. Hughes, J.; Rees, S.; Kalindjian, S.; Philpott, K. Principles of Early Drug Discovery. *British Journal of Pharmacology* **2011**, *162*, 1239–1249, doi:10.1111/j.1476-5381.2010.01127.x.
2. Gashaw, I.; Ellinghaus, P.; Sommer, A.; Asadullah, K. What Makes a Good Drug Target? *Drug Discovery Today* **2012**, *17*, S24–S30, doi:10.1016/j.drudis.2011.12.008.
3. Mohs, R.C.; Greig, N.H. Drug Discovery and Development: Role of Basic Biological Research. *Alzheimers Dement (N Y)* **2017**, *3*, 651–657, doi:10.1016/j.trci.2017.10.005.
4. Bassani, D.; Moro, S. Past, Present, and Future Perspectives on Computer-Aided Drug Design Methodologies. *Molecules* **2023**, *28*, 3906, doi:10.3390/molecules28093906.
5. Hefti, F.F. Requirements for a Lead Compound to Become a Clinical Candidate. *BMC Neurosci* **2008**, *9*, S7, doi:10.1186/1471-2202-9-S3-S7.
6. Singh, N.; Vayer, P.; Tanwar, S.; Poyet, J.-L.; Tsaioun, K.; Villoutreix, B.O. Drug Discovery and Development: Introduction to the General Public and Patient Groups. *Front. Drug Discov.* **2023**, *3*, doi:10.3389/fddsv.2023.1201419.
7. Kandi, V.; Vadakedath, S.; Kandi, V.; Vadakedath, S. Clinical Trials and Clinical Research: A Comprehensive Review. *Cureus* **2023**, *15*, doi:10.7759/cureus.35077.
8. Perez, K.L.; López-López, E.; Soulage, F.; Felix, E.; Medina-Franco, J.L.; Miranda-Quintana, R.A. Growth vs. Diversity: A Time-Evolution Analysis of the Chemical Space 2025.
9. Reymond, J.-L. The Chemical Space Project. *Acc. Chem. Res.* **2015**, *48*, 722–730, doi:10.1021/ar500432k.
10. Kirkpatrick, P.; Ellis, C. Chemical Space. *Nature* **2004**, *432*, 823–823, doi:10.1038/432823a.
11. Sliwoski, G.; Kothiwale, S.; Meiler, J.; Lowe, E.W. Computational Methods in Drug Discovery. *Pharmacological Reviews* **2014**, *66*, 334–395, doi:10.1124/pr.112.007336.
12. Moro, S.; Bacilieri, M.; Deflorian, F. Combining Ligand-Based and Structure-Based Drug Design in the Virtual Screening Arena. *Expert Opinion on Drug Discovery* **2007**, *2*, 37–49, doi:10.1517/17460441.2.1.37.
13. Pandey, M.; Fernandez, M.; Gentile, F.; Isayev, O.; Tropsha, A.; Stern, A.C.; Cherkasov, A. The Transformational Role of GPU Computing and Deep Learning in Drug Discovery. *Nat Mach Intell* **2022**, *4*, 211–221, doi:10.1038/s42256-022-00463-x.
14. Yu, W.; MacKerell, A.D. Computer-Aided Drug Design Methods. *Methods Mol Biol* **2017**, *1520*, 85–106, doi:10.1007/978-1-4939-6634-9_5.
15. von Itzstein, M. The War against Influenza: Discovery and Development of Sialidase Inhibitors. *Nat Rev Drug Discov* **2007**, *6*, 967–974, doi:10.1038/nrd2400.
16. Kitchen, D.B.; Decornez, H.; Furr, J.R.; Bajorath, J. Docking and Scoring in Virtual Screening for Drug Discovery: Methods and Applications. *Nat Rev Drug Discov* **2004**, *3*, 935–949, doi:10.1038/nrd1549.

17. Schneider, G. Automating Drug Discovery. *Nat Rev Drug Discov* **2018**, *17*, 97–113, doi:10.1038/nrd.2017.232.
18. Mak, K.-K.; Pichika, M.R. Artificial Intelligence in Drug Development: Present Status and Future Prospects. *Drug Discovery Today* **2019**, *24*, 773–780, doi:10.1016/j.drudis.2018.11.014.
19. Murmu, A.; Győrffy, B. Artificial Intelligence Methods Available for Cancer Research. *Front. Med.* **2024**, *18*, 778–797, doi:10.1007/s11684-024-1085-3.
20. Leelananda, S.P.; Lindert, S. Computational Methods in Drug Discovery. *Beilstein J. Org. Chem.* **2016**, *12*, 2694–2718, doi:10.3762/bjoc.12.267.
21. Ferreira, L.; dos Santos, R.; Oliva, G.; Andricopulo, A. Molecular Docking and Structure-Based Drug Design Strategies. *Molecules* **2015**, *20*, 13384–13421, doi:10.3390/molecules200713384.
22. Batool, M.; Ahmad, B.; Choi, S. A Structure-Based Drug Discovery Paradigm. *Int J Mol Sci* **2019**, *20*, 2783, doi:10.3390/ijms20112783.
23. Muhammed, M.T.; Aki-Yalcin, E. Homology Modeling in Drug Discovery: Overview, Current Applications, and Future Perspectives. *Chemical Biology & Drug Design* **2019**, *93*, 12–20, doi:10.1111/cbdd.13388.
24. Berman, H.M. The Protein Data Bank. *Nucleic Acids Research* **2000**, *28*, 235–242, doi:10.1093/nar/28.1.235.
25. Kelley, L.A.; Sternberg, M.J.E. Protein Structure Prediction on the Web: A Case Study Using the Phyre Server. *Nat Protoc* **2009**, *4*, 363–371, doi:10.1038/nprot.2009.2.
26. Roy, A.; Kucukural, A.; Zhang, Y. I-TASSER: A Unified Platform for Automated Protein Structure and Function Prediction. *Nat Protoc* **2010**, *5*, 725–738, doi:10.1038/nprot.2010.5.
27. Söding, J. Protein Homology Detection by HMM–HMM Comparison. *Bioinformatics* **2005**, *21*, 951–960, doi:10.1093/bioinformatics/bti125.
28. Raman, S.; Vernon, R.; Thompson, J.; Tyka, M.; Sadreyev, R.; Pei, J.; Kim, D.; Kellogg, E.; DiMaio, F.; Lange, O.; et al. Structure Prediction for CASP8 with All-Atom Refinement Using Rosetta. *Proteins: Structure, Function, and Bioinformatics* **2009**, *77*, 89–99, doi:10.1002/prot.22540.
29. Jumper, J.; Evans, R.; Pritzel, A.; Green, T.; Figurnov, M.; Ronneberger, O.; Tunyasuvunakool, K.; Bates, R.; Žídek, A.; Potapenko, A.; et al. Highly Accurate Protein Structure Prediction with AlphaFold. *Nature* **2021**, *596*, 583–589, doi:10.1038/s41586-021-03819-2.
30. Tunyasuvunakool, K.; Adler, J.; Wu, Z.; Green, T.; Zielinski, M.; Žídek, A.; Bridgland, A.; Cowie, A.; Meyer, C.; Laydon, A.; et al. Highly Accurate Protein Structure Prediction for the Human Proteome. *Nature* **2021**, *596*, 590–596, doi:10.1038/s41586-021-03828-1.
31. Evans, R.; O'Neill, M.; Pritzel, A.; Antropova, N.; Senior, A.; Green, T.; Žídek, A.; Bates, R.; Blackwell, S.; Yim, J.; et al. Protein Complex Prediction with AlphaFold-Multimer 2021.

32. Chan, H.C.S.; Shan, H.; Dahoun, T.; Vogel, H.; Yuan, S. Advancing Drug Discovery via Artificial Intelligence. *Trends in Pharmacological Sciences* **2019**, *40*, 592–604, doi:10.1016/j.tips.2019.06.004.
33. Barrio-Hernandez, I.; Yeo, J.; Jänes, J.; Mirdita, M.; Gilchrist, C.L.M.; Wein, T.; Varadi, M.; Velankar, S.; Beltrao, P.; Steinegger, M. Clustering Predicted Structures at the Scale of the Known Protein Universe. *Nature* **2023**, *622*, 637–645, doi:10.1038/s41586-023-06510-w.
34. Bordin, N.; Sillitoe, I.; Nallapareddy, V.; Rauer, C.; Lam, S.D.; Waman, V.P.; Sen, N.; Heinzinger, M.; Littmann, M.; Kim, S.; et al. AlphaFold2 Reveals Commonalities and Novelties in Protein Structure Space for 21 Model Organisms. *Commun Biol* **2023**, *6*, 160, doi:10.1038/s42003-023-04488-9.
35. David, A.; Islam, S.; Tankhilevich, E.; Sternberg, M.J.E. The AlphaFold Database of Protein Structures: A Biologist's Guide. *Journal of Molecular Biology* **2022**, *434*, 167336, doi:10.1016/j.jmb.2021.167336.
36. Zheng, Z.; Zeng, Y.; Lai, K.; Liao, B.; Li, P.; Tan, C.S.H. Protein Painting for Structural and Binding Site Analysis via Intracellular Lysine Reactivity Profiling with O-Phthalaldehyde. *Chem. Sci.* **2024**, *15*, 6064–6075, doi:10.1039/D4SC00032C.
37. Guo, C.; Li, X.; Xu, H.; Yu, J.; Li, J.; Lin, D. Structural Basis for Suramin Binding to the C-Terminal Domain of the SARS-CoV-2 Nucleocapsid Protein. *Acta Biochim Biophys Sin (Shanghai)* **2025**, doi:10.3724/abbs.2025182.
38. Aggarwal, R.; Gupta, A.; Chelur, V.; Jawahar, C.V.; Priyakumar, U.D. DeepPocket: Ligand Binding Site Detection and Segmentation Using 3D Convolutional Neural Networks. *J. Chem. Inf. Model.* **2022**, *62*, 5069–5079, doi:10.1021/acs.jcim.1c00799.
39. Su, H.; Liu, M.; Sun, S.; Peng, Z.; Yang, J. Improving the Prediction of Protein–Nucleic Acids Binding Residues via Multiple Sequence Profiles and the Consensus of Complementary Methods. *Bioinformatics* **2019**, *35*, 930–936, doi:10.1093/bioinformatics/bty756.
40. Methods for the Prediction of Protein-Ligand Binding Sites for Structure-Based Drug Design and Virtual Ligand Screening. *Current Protein & Peptide Science 7*, 395–406, doi:10.2174/138920306778559386.
41. Xia, Y.; Pan, X.; Shen, H.-B. A Comprehensive Survey on Protein-Ligand Binding Site Prediction. *Current Opinion in Structural Biology* **2024**, *86*, 102793, doi:10.1016/j.sbi.2024.102793.
42. Levitt, D.G.; Banaszak, L.J. POCKET: A Computer Graphies Method for Identifying and Displaying Protein Cavities and Their Surrounding Amino Acids. *Journal of Molecular Graphics* **1992**, *10*, 229–234, doi:10.1016/0263-7855(92)80074-N.
43. Laurie, A.T.R.; Jackson, R.M. Q-SiteFinder: An Energy-Based Method for the Prediction of Protein-Ligand Binding Sites. *Bioinformatics* **2005**, *21*, 1908–1916, doi:10.1093/bioinformatics/bti315.
44. Jain, A.N.; Nicholls, A. Recommendations for Evaluation of Computational Methods. *J Comput Aided Mol Des* **2008**, *22*, 133–139, doi:10.1007/s10822-008-9196-5.

45. Huang, S.-Y.; Zou, X. Advances and Challenges in Protein-Ligand Docking. *Int J Mol Sci* **2010**, *11*, 3016–3034, doi:10.3390/ijms11083016.
46. Agu, P.C.; Afiukwa, C.A.; Orji, O.U.; Ezeh, E.M.; Ofoke, I.H.; Ogbu, C.O.; Ugwuja, E.I.; Aja, P.M. Molecular Docking as a Tool for the Discovery of Molecular Targets of Nutraceuticals in Diseases Management. *Sci Rep* **2023**, *13*, 13398, doi:10.1038/s41598-023-40160-2.
47. Liu, M.; Wang, S. MCDOCK: A Monte Carlo Simulation Approach to the Molecular Docking Problem. *J Comput Aided Mol Des* **1999**, *13*, 435–451, doi:10.1023/A:1008005918983.
48. Brooijmans, N.; Kuntz, I.D. Molecular Recognition and Docking Algorithms. *Annu Rev Biophys Biomol Struct* **2003**, *32*, 335–373, doi:10.1146/annurev.biophys.32.110601.142532.
49. Liu, J.; Wang, R. Classification of Current Scoring Functions. *J. Chem. Inf. Model.* **2015**, *55*, 475–482, doi:10.1021/ci500731a.
50. Guedes, I.A.; Pereira, F.S.S.; Dardenne, L.E. Empirical Scoring Functions for Structure-Based Virtual Screening: Applications, Critical Aspects, and Challenges. *Front. Pharmacol.* **2018**, *9*, doi:10.3389/fphar.2018.01089.
51. Pavan, M.; Menin, S.; Bassani, D.; Sturlese, M.; Moro, S. Implementing a Scoring Function Based on Interaction Fingerprint for Autogrow4: Protein Kinase CK1δ as a Case Study. *Front. Mol. Biosci.* **2022**, *9*, doi:10.3389/fmolb.2022.909499.
52. Genheden, S.; Ryde, U. The MM/PBSA and MM/GBSA Methods to Estimate Ligand-Binding Affinities. *Expert Opinion on Drug Discovery* **2015**, *10*, 449–461, doi:10.1517/17460441.2015.1032936.
53. Jones, G.; Willett, P.; Glen, R.C.; Leach, A.R.; Taylor, R. Development and Validation of a Genetic Algorithm for Flexible Docking. *J Mol Biol* **1997**, *267*, 727–748, doi:10.1006/jmbi.1996.0897.
54. Morris, G.M.; Huey, R.; Lindstrom, W.; Sanner, M.F.; Belew, R.K.; Goodsell, D.S.; Olson, A.J. AutoDock4 and AutoDockTools4: Automated Docking with Selective Receptor Flexibility. *J Comput Chem* **2009**, *30*, 2785–2791, doi:10.1002/jcc.21256.
55. Li, Y.; Zhang, X.; Cao, D. The Role of Shape Complementarity in the Protein-Protein Interactions. *Sci Rep* **2013**, *3*, 3271, doi:10.1038/srep03271.
56. Salmaso, V.; Moro, S. Bridging Molecular Docking to Molecular Dynamics in Exploring Ligand-Protein Recognition Process: An Overview. *Front. Pharmacol.* **2018**, *9*, 923, doi:10.3389/fphar.2018.00923.
57. Li, H.; Sze, K.-H.; Lu, G.; Ballester, P.J. Machine-Learning Scoring Functions for Structure-Based Virtual Screening. *WIREs Computational Molecular Science* **2021**, *11*, e1478, doi:10.1002/wcms.1478.
58. Zheng, W.; Wuyun, Q.; Li, Y.; Liu, Q.; Zhou, X.; Peng, C.; Zhu, Y.; Freddolino, L.; Zhang, Y. Deep-Learning-Based Single-Domain and Multidomain Protein Structure Prediction with D-I-TASSER. *Nat Biotechnol* **2025**, 1–13, doi:10.1038/s41587-025-02654-4.

59. Kim, S.; Chen, J.; Cheng, T.; Gindulyte, A.; He, J.; He, S.; Li, Q.; Shoemaker, B.A.; Thiessen, P.A.; Yu, B.; et al. PubChem 2025 Update. *Nucleic Acids Research* **2025**, *53*, D1516–D1525, doi:10.1093/nar/gkae1059.
60. Tingle, B.I.; Tang, K.G.; Castanon, M.; Gutierrez, J.J.; Khurelbaatar, M.; Dandarchuluun, C.; Moroz, Y.S.; Irwin, J.J. ZINC-22─A Free Multi-Billion-Scale Database of Tangible Compounds for Ligand Discovery. *J. Chem. Inf. Model.* **2023**, *63*, 1166–1176, doi:10.1021/acs.jcim.2c01253.
61. Chandrasekhar, V.; Rajan, K.; Kanakam, S.R.S.; Sharma, N.; Weißenborn, V.; Schaub, J.; Steinbeck, C. COCONUT 2.0: A Comprehensive Overhaul and Curation of the Collection of Open Natural Products Database. *Nucleic Acids Res* **2025**, *53*, D634–D643, doi:10.1093/nar/gkae1063.
62. Hunter, A.D. ACD/ChemSketch 1.0 (Freeware); ACD/ChemSketch 2.0 and Its Tautomers, Dictionary, and 3D Plug-Ins; ACD/HNMR 2.0; ACD/CNMR 2.0. *J. Chem. Educ.* **1997**, *74*, 905, doi:10.1021/ed074p905.
63. Madhavi Sastry, G.; Adzhigirey, M.; Day, T.; Annabhimoju, R.; Sherman, W. Protein and Ligand Preparation: Parameters, Protocols, and Influence on Virtual Screening Enrichments. *J Comput Aided Mol Des* **2013**, *27*, 221–234, doi:10.1007/s10822-013-9644-8.
64. Chaudhary, K.K.; Mishra, N. A Review on Molecular Docking: Novel Tool for Drug Discovery. *chemistry* **2016**, doi:10.47739/2334-1831/1029.
65. Flachsenberg, F.; Ehrt, C.; Gutermuth, T.; Rarey, M. Redocking the PDB. *J. Chem. Inf. Model.* **2024**, *64*, 219–237, doi:10.1021/acs.jcim.3c01573.
66. Spahn, V.; Del Vecchio, G.; Labuz, D.; Rodriguez-Gaztelumendi, A.; Massaly, N.; Temp, J.; Durmaz, V.; Sabri, P.; Reidelbach, M.; Machelska, H.; et al. A Nontoxic Pain Killer Designed by Modeling of Pathological Receptor Conformations. *Science* **2017**, *355*, 966–969, doi:10.1126/science.aai8636.
67. Hollingsworth, S.A.; Dror, R.O. Molecular Dynamics Simulation for All. *Neuron* **2018**, *99*, 1129–1143, doi:10.1016/j.neuron.2018.08.011.
68. Parry, W. Ergodic Theory. In *Time Series and Statistics*; Eatwell, J., Milgate, M., Newman, P., Eds.; Palgrave Macmillan UK: London, 1990; pp. 73–81 ISBN 978-1-349-20865-4.
69. Oostenbrink, C.; Villa, A.; Mark, A.E.; van Gunsteren, W.F. A Biomolecular Force Field Based on the Free Enthalpy of Hydration and Solvation: The GROMOS Force-Field Parameter Sets 53A5 and 53A6. *J Comput Chem* **2004**, *25*, 1656–1676, doi:10.1002/jcc.20090.
70. MacKerell, A.D.Jr.; Bashford, D.; Bellott, M.; Dunbrack, R.L.Jr.; Evanseck, J.D.; Field, M.J.; Fischer, S.; Gao, J.; Guo, H.; Ha, S.; et al. All-Atom Empirical Potential for Molecular Modeling and Dynamics Studies of Proteins. *J. Phys. Chem. B* **1998**, *102*, 3586–3616, doi:10.1021/jp973084f.
71. Cornell, W.D.; Cieplak, P.; Bayly, C.I.; Gould, I.R.; Merz, K.M.; Ferguson, D.M.; Spellmeyer, D.C.; Fox, T.; Caldwell, J.W.; Kollman, P.A. A Second Generation

Force Field for the Simulation of Proteins, Nucleic Acids, and Organic Molecules. *J. Am. Chem. Soc.* **1995**, *117*, 5179–5197, doi:10.1021/ja00124a002.
72. Jorgensen, W.L.; Tirado-Rives, J. The OPLS [Optimized Potentials for Liquid Simulations] Potential Functions for Proteins, Energy Minimizations for Crystals of Cyclic Peptides and Crambin. *J. Am. Chem. Soc.* **1988**, *110*, 1657–1666, doi:10.1021/ja00214a001.
73. Newberry, R.W.; Raines, R.T. Secondary Forces in Protein Folding. *ACS Chem. Biol.* **2019**, *14*, 1677–1686, doi:10.1021/acschembio.9b00339.
74. Evans, D.J.; Holian, B.L. The Nose–Hoover Thermostat. *J. Chem. Phys.* **1985**, *83*, 4069–4074, doi:10.1063/1.449071.
75. Janek, J.; Kolafa, J. Novel Barostat Implementation for Molecular Dynamics. *J. Chem. Phys.* **2024**, *160*, 184111, doi:10.1063/5.0193281.
76. Wassenaar, T.A.; Mark, A.E. The Effect of Box Shape on the Dynamic Properties of Proteins Simulated under Periodic Boundary Conditions. *Journal of Computational Chemistry* **2006**, *27*, 316–325, doi:10.1002/jcc.20341.
77. Tsuchida, E. Revisiting the Minimum Image Locus Method for Calculating the Radial Distribution Functions. *Computational and Theoretical Chemistry* **2023**, *1227*, 114256, doi:10.1016/j.comptc.2023.114256.
78. Toukmaji, A.Y.; Board, J.A. Ewald Summation Techniques in Perspective: A Survey. *Computer Physics Communications* **1996**, *95*, 73–92, doi:10.1016/0010-4655(96)00016-1.
79. Fincham, D. Leapfrog Rotational Algorithms. *Molecular Simulation* **1992**, *8*, 165–178, doi:10.1080/08927029208022474.
80. Vyas, D.R.; Ottino, J.M.; Lueptow, R.M.; Umbanhowar, P.B. Improved Velocity-Verlet Algorithm for the Discrete Element Method. *Computer Physics Communications* **2025**, *310*, 109524, doi:10.1016/j.cpc.2025.109524.
81. Song, X.; Bao, L.; Feng, C.; Huang, Q.; Zhang, F.; Gao, X.; Han, R. Accurate Prediction of Protein Structural Flexibility by Deep Learning Integrating Intricate Atomic Structures and Cryo-EM Density Information. *Nat Commun* **2024**, *15*, 5538, doi:10.1038/s41467-024-49858-x.
82. Kumari, N.; Hasija, Y. CADD: - Exploring the Digital Frontier in Drug Designing. In Proceedings of the 2024 3rd International Conference on Computational Modelling, Simulation and Optimization (ICCMSO); June 2024; pp. 272–277.
83. Bender, A.; Jenkins, J.L.; Scheiber, J.; Sukuru, S.C.K.; Glick, M.; Davies, J.W. How Similar Are Similarity Searching Methods? A Principal Component Analysis of Molecular Descriptor Space. *J. Chem. Inf. Model.* **2009**, *49*, 108–119, doi:10.1021/ci800249s.
84. MAEHLE, A.-H. “Receptive Substances”: John Newport Langley (1852–1925) and His Path to a Receptor Theory of Drug Action. *Med Hist* **2004**, *48*, 153–174, doi:10.1017/s0025727300000090.

85. Tripathi, A.; Bankaitis, V.A. Molecular Docking: From Lock and Key to Combination Lock. *J Mol Med Clin Appl* **2017**, *2*, 10.16966/2575-0305.106, doi:10.16966/2575-0305.106.
86. Seidel, T.; Schuetz, D.A.; Garon, A.; Langer, T. The Pharmacophore Concept and Its Applications in Computer-Aided Drug Design. *Prog Chem Org Nat Prod* **2019**, *110*, 99–141, doi:10.1007/978-3-030-14632-0_4.
87. Zhao, S.; Li, X.; Peng, W.; Wang, L.; Ye, W.; Zhao, Y.; Yin, W.; Chen, W.-D.; Li, W.; Wang, Y.-D. Ligand-Based Pharmacophore Modeling, Virtual Screening and Biological Evaluation to Identify Novel TGR5 Agonists. *RSC Adv.* **2021**, *11*, 9403–9409, doi:10.1039/D0RA10168K.
88. Gao, Q.; Yang, L.; Zhu, Y. Pharmacophore Based Drug Design Approach as a Practical Process in Drug Discovery. *Current Computer-Aided Drug Design 6*, 37–49, doi:10.2174/157340910790980151.
89. Voet, A.; Qing, X.; Lee, X.Y.; De Raeymaecker, J.; Tame, J.; Zhang, K.; De Maeyer, M. Pharmacophore Modeling: Advances, Limitations, and Current Utility in Drug Discovery. *JRLCR* **2014**, 81, doi:10.2147/JRLCR.S46843.
90. Mysinger, M.M.; Carchia, M.; Irwin, John.J.; Shoichet, B.K. Directory of Useful Decoys, Enhanced (DUD-E): Better Ligands and Decoys for Better Benchmarking. *J. Med. Chem.* **2012**, *55*, 6582–6594, doi:10.1021/jm300687e.
91. Giordano, D.; Biancaniello, C.; Argenio, M.A.; Facchiano, A. Drug Design by Pharmacophore and Virtual Screening Approach. *Pharmaceuticals* **2022**, *15*, 646, doi:10.3390/ph15050646.
92. Dixon, S.L.; Smondyrev, A.M.; Rao, S.N. PHASE: A Novel Approach to Pharmacophore Modeling and 3D Database Searching. *Chem Biol Drug Des* **2006**, *67*, 370–372, doi:10.1111/j.1747-0285.2006.00384.x.
93. Kebarle, P.; Peschke, M. On the Mechanisms by Which the Charged Droplets Produced by Electrospray Lead to Gas Phase Ions. *Analytica Chimica Acta* **2000**, *406*, 11–35, doi:10.1016/S0003-2670(99)00598-X.
94. Hanrieder, J. Cerebrum Illuminans: Mass Spectrometric Analysis of Protein and Peptide Dynamics in Neurological Diseases.
95. Introduction to Mass Analyzers Available online: https://www.shimadzu.com/an/service-support/technical-support/analysis-basics/fundamental/mass_analyzers.html (accessed on 16 October 2025).
96. Yang, Z.; Ren, Z.; Cheng, Y.; Sun, W.; Xi, Z.; Jia, W.; Li, G.; Wang, Y.; Guo, M.; Li, D. Review and Prospect on Portable Mass Spectrometer for Recent Applications. *Vacuum* **2022**, *199*, 110889, doi:10.1016/j.vacuum.2022.110889.
97. Fernandez-Lima, F.A.; Kaplan, D.A.; Park, M.A. Note: Integration of Trapped Ion Mobility Spectrometry with Mass Spectrometry. *Rev. Sci. Instrum.* **2011**, *82*, doi:10.1063/1.3665933.
98. Shaffer, S.A.; Tang, K.; Anderson, G.A.; Prior, D.C.; Udseth, H.R.; Smith, R.D. A Novel Ion Funnel for Focusing Ions at Elevated Pressure Using Electrospray Ionization Mass Spectrometry. *RAPID COMMUN. MASS SPECTROM.* **1997**, *11*,

1813–1817, doi:10.1002/(SICI)1097-0231(19971030)11:16%3C1813::AID-RCM87%3E3.0.CO;2-D.
99. Ridgeway, M.E.; Lubeck, M.; Jordens, J.; Mann, M.; Park, M.A. Trapped Ion Mobility Spectrometry: A Short Review. *International Journal of Mass Spectrometry* **2018**, *425*, 22–35, doi:10.1016/j.ijms.2018.01.006.
100. Largy, E.; König, A.; Ghosh, A.; Ghosh, D.; Benabou, S.; Rosu, F.; Gabelica, V. Mass Spectrometry of Nucleic Acid Noncovalent Complexes. *Chem. Rev.* **2022**, *122*, 7720–7839, doi:10.1021/acs.chemrev.1c00386.
101. Wyttenbach, T.; von Helden, G.; Batka, J.J.; Carlat, D.; Bowers, M.T. Effect of the Long-Range Potential on Ion Mobility Measurements. *J. Am. Soc. Mass Spectrom.* **1997**, *8*, 275–282, doi:10.1016/S1044-0305(96)00236-X.
102. Mesleh, M.F.; Hunter, J.M.; Shvartsburg, A.A.; Schatz, G.C.; Jarrold, M.F. Structural Information from Ion Mobility Measurements: Effects of the Long-Range Potential. *J. Phys. Chem.* **1996**, *100*, 16082–16086, doi:10.1021/jp961623v.
103. Shvartsburg, A.A.; Schatz, G.C.; Jarrold, M.F. Mobilities of Carbon Cluster Ions: Critical Importance of the Molecular Attractive Potential. *J. Chem. Phys.* **1998**, *108*, 2416–2423, doi:10.1063/1.475625.
104. Kartowikromo, K.Y.; Olajide, O.E.; Hamid, A.M. Collision Cross Section (CCS) Measurement and Prediction Methods in Omics. *J Mass Spectrom* **2023**, *58*, e4973, doi:10.1002/jms.4973.
105. Myers, C.A.; D'Esposito, R.J.; Fabris, D.; Ranganathan, S.V.; Chen, A.A. CoSIMS: An Optimized Trajectory-Based Collision Simulator for Ion Mobility Spectrometry. *J. Phys. Chem. B* **2019**, *123*, 4347–4357, doi:10.1021/acs.jpcb.9b01018.
106. Gabelica, V.; Marklund, E. Fundamentals of Ion Mobility Spectrometry. *Current Opinion in Chemical Biology* **2018**, *42*, 51–59, doi:10.1016/j.cbpa.2017.10.022.
107. Rabi, I.I. A New Method of Measuring Nuclear Magnetic Moment. *Phys. Rev.* **1938**, *53*, 318, doi:10.1103/PhysRev.53.318.
108. NMR Spectroscopy Principles, Interpreting an NMR Spectrum and Common Problems Available online: http://www.technologynetworks.com/analysis/articles/nmr-spectroscopy-principles-interpreting-an-nmr-spectrum-and-common-problems-355891 (accessed on 20 October 2025).
109. Ben-Tal, Y.; Boaler, P.J.; Dale, H.J.A.; Dooley, R.E.; Fohn, N.A.; Gao, Y.; García-Domínguez, A.; Grant, K.M.; Hall, A.M.R.; Hayes, H.L.D.; et al. Mechanistic Analysis by NMR Spectroscopy: A Users Guide. *Progress in Nuclear Magnetic Resonance Spectroscopy* **2022**, *129*, 28–106, doi:10.1016/j.pnmrs.2022.01.001.
110. Hosur, R.V.; Kakita, V.M.R. Fourier Transform NMR. In *A Graduate Course in NMR Spectroscopy*; Hosur, R.V., Kakita, V.M.R., Eds.; Springer International Publishing: Cham, 2022; pp. 89–142 ISBN 978-3-030-88769-8.

111. Dumez, J.-N. Spatial Encoding and Spatial Selection Methods in High-Resolution NMR Spectroscopy. *Progress in Nuclear Magnetic Resonance Spectroscopy* **2018**, *109*, 101–134, doi:10.1016/j.pnmrs.2018.08.001.
112. Sedaghat Doost, A.; Akbari, M.; Stevens, C.V.; Setiowati, A.D.; Van der Meeren, P. A Review on Nuclear Overhauser Enhancement (NOE) and Rotating-Frame Overhauser Effect (ROE) NMR Techniques in Food Science: Basic Principles and Applications. *Trends in Food Science & Technology* **2019**, *86*, 16–24, doi:10.1016/j.tifs.2019.02.001.
113. Viegas, A.; Manso, J.; Nobrega, F.L.; Cabrita, E.J. Saturation-Transfer Difference (STD) NMR: A Simple and Fast Method for Ligand Screening and Characterization of Protein Binding. *J. Chem. Educ.* **2011**, *88*, 990–994, doi:10.1021/ed101169t.
114. Finan, C.; Gaulton, A.; Kruger, F.A.; Lumbers, R.T.; Shah, T.; Engmann, J.; Galver, L.; Kelley, R.; Karlsson, A.; Santos, R.; et al. The Druggable Genome and Support for Target Identification and Validation in Drug Development. *Science Translational Medicine* **2017**, *9*, eaag1166, doi:10.1126/scitranslmed.aag1166.
115. Minchin, S.; Lodge, J. Understanding Biochemistry: Structure and Function of Nucleic Acids. *Essays Biochem* **2019**, *63*, 433–456, doi:10.1042/EBC20180038.
116. Cobb, M.; Comfort, N. What Rosalind Franklin Truly Contributed to the Discovery of DNA's Structure. *Nature* **2023**, *616*, 657–660, doi:10.1038/d41586-023-01313-5.
117. Watson, J.D.; Crick, F.H.C. Molecular Structure of Nucleic Acids: A Structure for Deoxyribose Nucleic Acid. *Nature* **1953**, *171*, 737–738, doi:10.1038/171737a0.
118. Gellert, M.; Lipsett, M.N.; Davies, D.R. Helix Formation by Guanylic Acid. *Proceedings of the National Academy of Sciences* **1962**, *48*, 2013–2018, doi:10.1073/pnas.48.12.2013.
119. Burge, S.; Parkinson, G.N.; Hazel, P.; Todd, A.K.; Neidle, S. Quadruplex DNA: Sequence, Topology and Structure. *Nucleic Acids Research* **2006**, *34*, 5402–5415, doi:10.1093/nar/gkl655.
120. Phan, A.T.; Mergny, J.-L. Human Telomeric DNA: G-Quadruplex, i-Motif and Watson-Crick Double Helix. *Nucleic Acids Res* **2002**, *30*, 4618–4625, doi:10.1093/nar/gkf597.
121. Dumas, L.; Herviou, P.; Dassi, E.; Cammas, A.; Millevoi, S. G-Quadruplexes in RNA Biology: Recent Advances and Future Directions. *Trends Biochem Sci* **2021**, *46*, 270–283, doi:10.1016/j.tibs.2020.11.001.
122. Varshney, D.; Spiegel, J.; Zyner, K.; Tannahill, D.; Balasubramanian, S. The Regulation and Functions of DNA and RNA G-Quadruplexes. *Nat Rev Mol Cell Biol* **2020**, *21*, 459–474, doi:10.1038/s41580-020-0236-x.
123. Largy, E.; Mergny, J.-L.; Gabelica, V. Role of Alkali Metal Ions in G-Quadruplex Nucleic Acid Structure and Stability. *Met Ions Life Sci* **2016**, *16*, 203–258, doi:10.1007/978-3-319-21756-7_7.

124. Ma, Y.; Iida, K.; Nagasawa, K. Topologies of G-Quadruplex: Biological Functions and Regulation by Ligands. *Biochemical and Biophysical Research Communications* **2020**, *531*, 3–17, doi:10.1016/j.bbrc.2019.12.103.
125. Dvorkin, S.A.; Karsisiotis, A.I.; Webba da Silva, M. Encoding Canonical DNA Quadruplex Structure. *Science Advances* **2018**, *4*, eaat3007, doi:10.1126/sciadv.aat3007.
126. Todd, A.K. Highly Prevalent Putative Quadruplex Sequence Motifs in Human DNA. *Nucleic Acids Research* **2005**, *33*, 2901–2907, doi:10.1093/nar/gki553.
127. Huppert, J.L.; Balasubramanian, S. Prevalence of Quadruplexes in the Human Genome. *Nucleic Acids Res* **2005**, *33*, 2908–2916, doi:10.1093/nar/gki609.
128. Dell'Oca, M.C.; Quadri, R.; Bernini, G.M.; Menin, L.; Grasso, L.; Rondelli, D.; Yazici, O.; Sertic, S.; Marini, F.; Pellicioli, A.; et al. Spotlight on G-Quadruplexes: From Structure and Modulation to Physiological and Pathological Roles. *Int J Mol Sci* **2024**, *25*, 3162, doi:10.3390/ijms25063162.
129. Puig Lombardi, E.; Londoño-Vallejo, A. A Guide to Computational Methods for G-Quadruplex Prediction. *Nucleic Acids Research* **2020**, *48*, 1–15, doi:10.1093/nar/gkz1097.
130. Brázda, V.; Kolomazník, J.; Lýsek, J.; Bartas, M.; Fojta, M.; Šťastný, J.; Mergny, J.-L. G4Hunter Web Application: A Web Server for G-Quadruplex Prediction. *Bioinformatics* **2019**, *35*, 3493–3495, doi:10.1093/bioinformatics/btz087.
131. Hon, J.; Martínek, T.; Zendulka, J.; Lexa, M. Pqsfinder: An Exhaustive and Imperfection-Tolerant Search Tool for Potential Quadruplex-Forming Sequences in R. *Bioinformatics* **2017**, *33*, 3373–3379, doi:10.1093/bioinformatics/btx413.
132. Patro, L.P.P.; Kumar, A.; Kolimi, N.; Rathinavelan, T. 3D-NuS: A Web Server for Automated Modeling and Visualization of Non-Canonical 3-Dimensional Nucleic Acid Structures. *J Mol Biol* **2017**, *429*, 2438–2448, doi:10.1016/j.jmb.2017.06.013.
133. Kwok, C.K.; Marsico, G.; Sahakyan, A.B.; Chambers, V.S.; Balasubramanian, S. rG4-Seq Reveals Widespread Formation of G-Quadruplex Structures in the Human Transcriptome. *Nat Methods* **2016**, *13*, 841–844, doi:10.1038/nmeth.3965.
134. Chambers, V.S.; Marsico, G.; Boutell, J.M.; Di Antonio, M.; Smith, G.P.; Balasubramanian, S. High-Throughput Sequencing of DNA G-Quadruplex Structures in the Human Genome. *Nat Biotechnol* **2015**, *33*, 877–881, doi:10.1038/nbt.3295.
135. Marsico, G.; Chambers, V.S.; Sahakyan, A.B.; McCauley, P.; Boutell, J.M.; Antonio, M.D.; Balasubramanian, S. Whole Genome Experimental Maps of DNA G-Quadruplexes in Multiple Species. *Nucleic Acids Res* **2019**, *47*, 3862–3874, doi:10.1093/nar/gkz179.
136. Hosseini, M.; Palmer, A.; Manka, W.; Grady, P.G.S.; Patchigolla, V.; Bi, J.; O'Neill, R.J.; Chi, Z.; Aguiar, D. Deep Statistical Modelling of Nanopore Sequencing Translocation Times Reveals Latent Non-B DNA Structures. *Bioinformatics* **2023**, *39*, i242–i251, doi:10.1093/bioinformatics/btad220.
137. Kaya-Okur, H.S.; Wu, S.J.; Codomo, C.A.; Pledger, E.S.; Bryson, T.D.; Henikoff, J.G.; Ahmad, K.; Henikoff, S. CUT&Tag for Efficient Epigenomic Profiling of Small

Samples and Single Cells. *Nat Commun* **2019**, *10*, 1930, doi:10.1038/s41467-019-09982-5.
138. Li, C.; Wang, H.; Yin, Z.; Fang, P.; Xiao, R.; Xiang, Y.; Wang, W.; Li, Q.; Huang, B.; Huang, J.; et al. Ligand-Induced Native G-Quadruplex Stabilization Impairs Transcription Initiation. *Genome Res* **2021**, *31*, 1546–1560, doi:10.1101/gr.275431.121.
139. Sato, K.; Knipscheer, P. G-Quadruplex Resolution: From Molecular Mechanisms to Physiological Relevance. *DNA Repair* **2023**, *130*, 103552, doi:10.1016/j.dnarep.2023.103552.
140. Hui, W.W.I.; Simeone, A.; Zyner, K.G.; Tannahill, D.; Balasubramanian, S. Single-Cell Mapping of DNA G-Quadruplex Structures in Human Cancer Cells. *Sci Rep* **2021**, *11*, 23641, doi:10.1038/s41598-021-02943-3.
141. Campbell, N.H.; Parkinson, G.N. Crystallographic Studies of Quadruplex Nucleic Acids. *Methods* **2007**, *43*, 252–263, doi:10.1016/j.ymeth.2007.08.005.
142. Bao, H.-L.; Ishizuka, T.; Sakamoto, T.; Fujimoto, K.; Uechi, T.; Kenmochi, N.; Xu, Y. Characterization of Human Telomere RNA G-Quadruplex Structures in Vitro and in Living Cells Using 19F NMR Spectroscopy. *Nucleic Acids Res* **2017**, *45*, 5501–5511, doi:10.1093/nar/gkx109.
143. Vorlíčková, M.; Kejnovská, I.; Sagi, J.; Renčiuk, D.; Bednářová, K.; Motlová, J.; Kypr, J. Circular Dichroism and Guanine Quadruplexes. *Methods* **2012**, *57*, 64–75, doi:10.1016/j.ymeth.2012.03.011.
144. Simonsson, T.; Kubista, M.; Pecinka, P. DNA Tetraplex Formation in the Control Region of C-Myc. *Nucleic Acids Res* **1998**, *26*, 1167–1172, doi:10.1093/nar/26.5.1167.
145. Ambrus, G.; Whitby, L.R.; Singer, E.L.; Trott, O.; Choi, E.; Olson, A.J.; Boger, D.L.; Gerace, L. Small Molecule Peptidomimetic Inhibitors of Importin α/β Mediated Nuclear Transport. *Bioorganic & Medicinal Chemistry* **2010**, *18*, 7611–7620, doi:10.1016/j.bmc.2010.08.038.
146. Pagano, B.; Randazzo, A.; Fotticchia, I.; Novellino, E.; Petraccone, L.; Giancola, C. Differential Scanning Calorimetry to Investigate G-Quadruplexes Structural Stability. *Methods* **2013**, *64*, 43–51, doi:10.1016/j.ymeth.2013.02.018.
147. Fonzo, S.D.; Amato, J.; D'Aria, F.; Caterino, M.; D'Amico, F.; Gessini, A.; Brady, J.W.; Cesàro, A.; Pagano, B.; Giancola, C. Ligand Binding to G-Quadruplex DNA: New Insights from Ultraviolet Resonance Raman Spectroscopy. *Phys. Chem. Chem. Phys.* **2020**, *22*, 8128–8140, doi:10.1039/D0CP01022G.
148. Mergny, J.-L.; Lacroix, L. UV Melting of G-Quadruplexes. *Curr Protoc Nucleic Acid Chem* **2009**, *Chapter 17*, 17.1.1-17.1.15, doi:10.1002/0471142700.nc1701s37.
149. Luo, Y.; Granzhan, A.; Marquevielle, J.; Cucchiarini, A.; Lacroix, L.; Amrane, S.; Verga, D.; Mergny, J.-L. Guidelines for G-Quadruplexes: I. In Vitro Characterization. *Biochimie* **2023**, *214*, 5–23, doi:10.1016/j.biochi.2022.12.019.
150. Kejnovská, I.; Renčiuk, D.; Palacký, J.; Vorlíčková, M. CD Study of the G-Quadruplex Conformation. In *G-Quadruplex Nucleic Acids: Methods and Protocols*;

Yang, D., Lin, C., Eds.; Springer: New York, NY, 2019; pp. 25–44 ISBN 978-1-4939-9666-7.
151. Javadekar, S.M.; Nilavar, N.M.; Paranjape, A.; Das, K.; Raghavan, S.C. Characterization of G-Quadruplex Antibody Reveals Differential Specificity for G4 DNA Forms. *DNA Res* **2020**, *27*, dsaa024, doi:10.1093/dnares/dsaa024.
152. Schaffitzel, C.; Berger, I.; Postberg, J.; Hanes, J.; Lipps, H.J.; Plückthun, A. In Vitro Generated Antibodies Specific for Telomeric Guanine-Quadruplex DNA React with Stylonychia Lemnae Macronuclei. *Proceedings of the National Academy of Sciences* **2001**, *98*, 8572–8577, doi:10.1073/pnas.141229498.
153. Biffi, G.; Tannahill, D.; McCafferty, J.; Balasubramanian, S. Quantitative Visualization of DNA G-Quadruplex Structures in Human Cells. *Nat Chem* **2013**, *5*, 182–186, doi:10.1038/nchem.1548.
154. Biffi, G.; Di Antonio, M.; Tannahill, D.; Balasubramanian, S. Visualization and Selective Chemical Targeting of RNA G-Quadruplex Structures in the Cytoplasm of Human Cells. *Nat Chem* **2014**, *6*, 75–80, doi:10.1038/nchem.1805.
155. Liu, H.-Y.; Zhao, Q.; Zhang, T.-P.; Wu, Y.; Xiong, Y.-X.; Wang, S.-K.; Ge, Y.-L.; He, J.-H.; Lv, P.; Ou, T.-M.; et al. Conformation Selective Antibody Enables Genome Profiling and Leads to Discovery of Parallel G-Quadruplex in Human Telomeres. *Cell Chem Biol* **2016**, *23*, 1261–1270, doi:10.1016/j.chembiol.2016.08.013.
156. Kazemier, H.G.; Paeschke, K.; Lansdorp, P.M. Guanine Quadruplex Monoclonal Antibody 1H6 Cross-Reacts with Restrained Thymidine-Rich Single Stranded DNA. *Nucleic Acids Res* **2017**, *45*, 5913–5919, doi:10.1093/nar/gkx245.
157. Zyner, K.G.; Simeone, A.; Flynn, S.M.; Doyle, C.; Marsico, G.; Adhikari, S.; Portella, G.; Tannahill, D.; Balasubramanian, S. G-Quadruplex DNA Structures in Human Stem Cells and Differentiation. *Nat Commun* **2022**, *13*, 142, doi:10.1038/s41467-021-27719-1.
158. Hänsel-Hertsch, R.; Beraldi, D.; Lensing, S.V.; Marsico, G.; Zyner, K.; Parry, A.; Di Antonio, M.; Pike, J.; Kimura, H.; Narita, M.; et al. G-Quadruplex Structures Mark Human Regulatory Chromatin. *Nat Genet* **2016**, *48*, 1267–1272, doi:10.1038/ng.3662.
159. Hänsel-Hertsch, R.; Spiegel, J.; Marsico, G.; Tannahill, D.; Balasubramanian, S. Genome-Wide Mapping of Endogenous G-Quadruplex DNA Structures by Chromatin Immunoprecipitation and High-Throughput Sequencing. *Nat Protoc* **2018**, *13*, 551–564, doi:10.1038/nprot.2017.150.
160. Li, G.; Su, G.; Wang, Y.; Wang, W.; Shi, J.; Li, D.; Sui, G. Integrative Genomic Analyses of Promoter G-Quadruplexes Reveal Their Selective Constraint and Association with Gene Activation. *Commun Biol* **2023**, *6*, 625, doi:10.1038/s42003-023-05015-6.
161. Siddiqui-Jain, A.; Grand, C.L.; Bearss, D.J.; Hurley, L.H. Direct Evidence for a G-Quadruplex in a Promoter Region and Its Targeting with a Small Molecule to

Repress c-MYC Transcription. *Proceedings of the National Academy of Sciences* **2002**, *99*, 11593–11598, doi:10.1073/pnas.182256799.
162. Bejugam, M.; Sewitz, S.; Shirude, P.S.; Rodriguez, R.; Shahid, R.; Balasubramanian, S. Trisubstituted Isoalloxazines as a New Class of G-Quadruplex Binding Ligands: Small Molecule Regulation of c-Kit Oncogene Expression. *J Am Chem Soc* **2007**, *129*, 12926–12927, doi:10.1021/ja075881p.
163. Spiegel, J.; Cuesta, S.M.; Adhikari, S.; Hänsel-Hertsch, R.; Tannahill, D.; Balasubramanian, S. G-Quadruplexes Are Transcription Factor Binding Hubs in Human Chromatin. *Genome Biology* **2021**, *22*, 117, doi:10.1186/s13059-021-02324-z.
164. Gao, J.; Zybailov, B.L.; Byrd, A.K.; Griffin, W.C.; Chib, S.; Mackintosh, S.G.; Tackett, A.J.; Raney, K.D. Yeast Transcription Co-Activator Sub1 and Its Human Homolog PC4 Preferentially Bind to G-Quadruplex DNA. *Chem. Commun.* **2015**, *51*, 7242–7244, doi:10.1039/C5CC00742A.
165. Bai, L.; Morozov, A.V. Gene Regulation by Nucleosome Positioning. *Trends in Genetics* **2010**, *26*, 476–483, doi:10.1016/j.tig.2010.08.003.
166. Kharel, P.; Ivanov, P. RNA G-Quadruplexes and Stress: Emerging Mechanisms and Functions. *Trends in Cell Biology* **2024**, *34*, 771–784, doi:10.1016/j.tcb.2024.01.005.
167. Balaratnam, S.; Hettiarachchilage, M.; West, N.; Piontkivska, H.; Basu, S. A Secondary Structure within a Human piRNA Modulates Its Functionality. *Biochimie* **2019**, *157*, 72–80, doi:10.1016/j.biochi.2018.11.002.
168. Rouleau, S.G.; Garant, J.-M.; Bolduc, F.; Bisaillon, M.; Perreault, J.-P. G-Quadruplexes Influence Pri-microRNA Processing. *RNA Biol* **2018**, *15*, 198–206, doi:10.1080/15476286.2017.1405211.
169. Jayaraj, G.G.; Pandey, S.; Scaria, V.; Maiti, S. Potential G-Quadruplexes in the Human Long Non-Coding Transcriptome. *RNA Biol* **2012**, *9*, 81–86, doi:10.4161/rna.9.1.18047.
170. Huang, H.; Zhang, J.; Harvey, S.E.; Hu, X.; Cheng, C. RNA G-Quadruplex Secondary Structure Promotes Alternative Splicing via the RNA-Binding Protein hnRNPF. *Genes Dev* **2017**, *31*, 2296–2309, doi:10.1101/gad.305862.117.
171. Conlon, E.G.; Lu, L.; Sharma, A.; Yamazaki, T.; Tang, T.; Shneider, N.A.; Manley, J.L. The C9ORF72 GGGGCC Expansion Forms RNA G-Quadruplex Inclusions and Sequesters hnRNP H to Disrupt Splicing in ALS Brains. *eLife* **2016**, *5*, e17820, doi:10.7554/eLife.17820.
172. Wolfe, A.L.; Singh, K.; Zhong, Y.; Drewe, P.; Rajasekhar, V.K.; Sanghvi, V.R.; Mavrakis, K.J.; Jiang, M.; Roderick, J.E.; Van der Meulen, J.; et al. RNA G-Quadruplexes Cause eIF4A-Dependent Oncogene Translation in Cancer. *Nature* **2014**, *513*, 65–70, doi:10.1038/nature13485.
173. Kumari, S.; Bugaut, A.; Huppert, J.L.; Balasubramanian, S. An RNA G-Quadruplex in the 5’ UTR of the NRAS Proto-Oncogene Modulates Translation. *Nat Chem Biol* **2007**, *3*, 218–221, doi:10.1038/nchembio864.

174. Murat, P.; Marsico, G.; Herdy, B.; Ghanbarian, A.; Portella, G.; Balasubramanian, S. RNA G-Quadruplexes at Upstream Open Reading Frames Cause DHX36- and DHX9-Dependent Translation of Human mRNAs. *Genome Biology* **2018**, *19*, 229, doi:10.1186/s13059-018-1602-2.
175. Weitzmann, M.N.; Woodford, K.J.; Usdin, K. The Development and Use of a DNA Polymerase Arrest Assay for the Evaluation of Parameters Affecting Intrastrand Tetraplex Formation. *J Biol Chem* **1996**, *271*, 20958–20964, doi:10.1074/jbc.271.34.20958.
176. Kruisselbrink, E.; Guryev, V.; Brouwer, K.; Pontier, D.B.; Cuppen, E.; Tijsterman, M. Mutagenic Capacity of Endogenous G4 DNA Underlies Genome Instability in FANCJ-Defective C. Elegans. *Curr Biol* **2008**, *18*, 900–905, doi:10.1016/j.cub.2008.05.013.
177. Paeschke, K.; Capra, J.A.; Zakian, V.A. DNA Replication through G-Quadruplex Motifs Is Promoted by the *Saccharomyces Cerevisiae* Pif1 DNA Helicase. *Cell* **2011**, *145*, 678–691, doi:10.1016/j.cell.2011.04.015.
178. London, T.B.C.; Barber, L.J.; Mosedale, G.; Kelly, G.P.; Balasubramanian, S.; Hickson, I.D.; Boulton, S.J.; Hiom, K. FANCJ Is a Structure-Specific DNA Helicase Associated with the Maintenance of Genomic G/C Tracts. *J Biol Chem* **2008**, *283*, 36132–36139, doi:10.1074/jbc.M808152200.
179. Sarkies, P.; Reams, C.; Simpson, L.J.; Sale, J.E. Epigenetic Instability Due to Defective Replication of Structured DNA. *Mol Cell* **2010**, *40*, 703–713, doi:10.1016/j.molcel.2010.11.009.
180. Blackford, A.N.; Jackson, S.P. ATM, ATR, and DNA-PK: The Trinity at the Heart of the DNA Damage Response. *Mol Cell* **2017**, *66*, 801–817, doi:10.1016/j.molcel.2017.05.015.
181. Craig, A.; Scott, M.; Burch, L.; Smith, G.; Ball, K.; Hupp, T. Allosteric Effects Mediate CHK2 Phosphorylation of the P53 Transactivation Domain. *EMBO reports* **2003**, *4*, 787–792, doi:10.1038/sj.embor.embor901.
182. Guo, Z.; Kumagai, A.; Wang, S.X.; Dunphy, W.G. Requirement for Atr in Phosphorylation of Chk1 and Cell Cycle Regulation in Response to DNA Replication Blocks and UV-Damaged DNA in Xenopus Egg Extracts. *Genes Dev* **2000**, *14*, 2745–2756, doi:10.1101/gad.842500.
183. Linke, R.; Limmer, M.; Juranek, S.A.; Heine, A.; Paeschke, K. The Relevance of G-Quadruplexes for DNA Repair. *International Journal of Molecular Sciences* **2021**, *22*, 12599, doi:10.3390/ijms222212599.
184. Shiekh, S.; Kodikara, S.G.; Balci, H. Structure, Topology, and Stability of Multiple G-Quadruplexes in Long Telomeric Overhangs. *J Mol Biol* **2024**, *436*, 168205, doi:10.1016/j.jmb.2023.168205.
185. Shay, J.W.; Wright, W.E. Telomeres and Telomerase: Three Decades of Progress. *Nat Rev Genet* **2019**, *20*, 299–309, doi:10.1038/s41576-019-0099-1.

186. Xu, Y.; Komiyama, M. G-Quadruplexes in Human Telomere: Structures, Properties, and Applications. *Molecules* **2024**, *29*, 174, doi:10.3390/molecules29010174.
187. Xu, Y. Chemistry in Human Telomere Biology: Structure, Function and Targeting of Telomere DNA/RNA. *Chem Soc Rev* **2011**, *40*, 2719–2740, doi:10.1039/c0cs00134a.
188. Ou, T.; Lu, Y.; Tan, J.; Huang, Z.; Wong, K.-Y.; Gu, L. G-Quadruplexes: Targets in Anticancer Drug Design. *ChemMedChem* **2008**, *3*, 690–713, doi:10.1002/cmdc.200700300.
189. Schoeftner, S.; Blasco, M.A. Developmentally Regulated Transcription of Mammalian Telomeres by DNA-Dependent RNA Polymerase II. *Nat Cell Biol* **2008**, *10*, 228–236, doi:10.1038/ncb1685.
190. Luke, B.; Lingner, J. TERRA: Telomeric Repeat-containing RNA. *The EMBO Journal* **2009**, *28*, 2503–2510, doi:10.1038/emboj.2009.166.
191. Shrestha, P.; Jonchhe, S.; Emura, T.; Hidaka, K.; Endo, M.; Sugiyama, H.; Mao, H. Confined Space Facilitates G-Quadruplex Formation. *Nat Nanotechnol* **2017**, *12*, 582–588, doi:10.1038/nnano.2017.29.
192. Xu, Y.; Suzuki, Y.; Ito, K.; Komiyama, M. Telomeric Repeat-Containing RNA Structure in Living Cells. *Proceedings of the National Academy of Sciences* **2010**, *107*, 14579–14584, doi:10.1073/pnas.1001177107.
193. Bao, H.-L.; Xu, Y. Telomeric DNA–RNA-Hybrid G-Quadruplex Exists in Environmental Conditions of HeLa Cells. *Chem. Commun.* **2020**, *56*, 6547–6550, doi:10.1039/D0CC02053B.
194. Bryan, T.M. G-Quadruplexes at Telomeres: Friend or Foe? *Molecules* **2020**, *25*, 3686, doi:10.3390/molecules25163686.
195. Blackburn, E.H.; Greider, C.W.; Henderson, E.; Lee, M.S.; Shampay, J.; Shippen-Lentz, D. Recognition and Elongation of Telomeres by Telomerase. *Genome* **1989**, *31*, 553–560, doi:10.1139/g89-104.
196. Lim, C.J.; Cech, T.R. Shaping Human Telomeres: From Shelterin and CST Complexes to Telomeric Chromatin Organization. *Nat Rev Mol Cell Biol* **2021**, *22*, 283–298, doi:10.1038/s41580-021-00328-y.
197. de Lange, T. Shelterin-Mediated Telomere Protection. *Annu Rev Genet* **2018**, *52*, 223–247, doi:10.1146/annurev-genet-032918-021921.
198. Jack, A.; Kim, Y.; Strom, A.R.; Lee, D.S.W.; Williams, B.; Schaub, J.M.; Kellogg, E.H.; Finkelstein, I.J.; Ferro, L.S.; Yildiz, A.; et al. Compartmentalization of Telomeres through DNA-Scaffolded Phase Separation. *Developmental Cell* **2022**, *57*, 277-290.e9, doi:10.1016/j.devcel.2021.12.017.
199. Paeschke, K.; Juranek, S.; Simonsson, T.; Hempel, A.; Rhodes, D.; Lipps, H.J. Telomerase Recruitment by the Telomere End Binding Protein-Beta Facilitates G-Quadruplex DNA Unfolding in Ciliates. *Nat Struct Mol Biol* **2008**, *15*, 598–604, doi:10.1038/nsmb.1422.

200. Paeschke, K.; Simonsson, T.; Postberg, J.; Rhodes, D.; Lipps, H.J. Telomere End-Binding Proteins Control the Formation of G-Quadruplex DNA Structures in Vivo. *Nat Struct Mol Biol* **2005**, *12*, 847–854, doi:10.1038/nsmb982.
201. Phan, A.T. Human Telomeric G-Quadruplex: Structures of DNA and RNA Sequences. *FEBS J* **2010**, *277*, 1107–1117, doi:10.1111/j.1742-4658.2009.07464.x.
202. Wang, Y.; Patel, D.J. Solution Structure of the Human Telomeric Repeat d[AG3(T2AG3)3] G-Tetraplex. *Structure* **1993**, *1*, 263–282, doi:10.1016/0969-2126(93)90015-9.
203. Bao, H.-L.; Liu, H.-S.; Xu, Y. Hybrid-Type and Two-Tetrad Antiparallel Telomere DNA G-Quadruplex Structures in Living Human Cells. *Nucleic Acids Res* **2019**, *47*, 4940–4947, doi:10.1093/nar/gkz276.
204. Wu, G.; Chen, L.; Liu, W.; Yang, D. Molecular Recognition of the Hybrid-Type G-Quadruplexes in Human Telomeres. *Molecules* **2019**, *24*, 1578, doi:10.3390/molecules24081578.
205. Manna, S.; Sarkar, D.; Srivatsan, S.G. A Dual-App Nucleoside Probe Provides Structural Insights into the Human Telomeric Overhang in Live Cells. *J. Am. Chem. Soc.* **2018**, *140*, 12622–12633, doi:10.1021/jacs.8b08436.
206. Zhang, L.; Liu, H.; Shao, Y.; Lin, C.; Jia, H.; Chen, G.; Yang, D.; Wang, Y. Selective Lighting Up of Epiberberine Alkaloid Fluorescence by Fluorophore-Switching Aptamer and Stoichiometric Targeting of Human Telomeric DNA G-Quadruplex Multimer. *Anal. Chem.* **2015**, *87*, 730–737, doi:10.1021/ac503730j.
207. Calabrese, D.R.; Chen, X.; Leon, E.C.; Gaikwad, S.M.; Phyo, Z.; Hewitt, W.M.; Alden, S.; Hilimire, T.A.; He, F.; Michalowski, A.M.; et al. Chemical and Structural Studies Provide a Mechanistic Basis for Recognition of the MYC G-Quadruplex. *Nat Commun* **2018**, *9*, 4229, doi:10.1038/s41467-018-06315-w.
208. Chen, L.; Dickerhoff, J.; Sakai, S.; Yang, D. DNA G-Quadruplex in Human Telomeres and Oncogene Promoters: Structures, Functions, and Small Molecule Targeting. *Acc Chem Res* **2022**, *55*, 2628–2646, doi:10.1021/acs.accounts.2c00337.
209. Dickerhoff, J.; Dai, J.; Yang, D. Structural Recognition of the *MYC* Promoter G-Quadruplex by a Quinoline Derivative: Insights into Molecular Targeting of Parallel G-Quadruplexes. *Nucleic Acids Research* **2021**, *49*, 5905–5915, doi:10.1093/nar/gkab330.
210. Malina, J.; Scott, P.; Brabec, V. Stabilization of Human Telomeric RNA G-Quadruplex by the Water-Compatible Optically Pure and Biologically-Active Metallohelices. *Sci Rep* **2020**, *10*, 14543, doi:10.1038/s41598-020-71429-5.
211. Mendoza, O.; Porrini, M.; Salgado, G.F.; Gabelica, V.; Mergny, J.-L. Orienting Tetramolecular G-Quadruplex Formation: The Quest for the Elusive RNA Antiparallel Quadruplex. *Chemistry – A European Journal* **2015**, *21*, 6732–6739, doi:10.1002/chem.201500358.
212. Collie, G.W.; Haider, S.M.; Neidle, S.; Parkinson, G.N. A Crystallographic and Modelling Study of a Human Telomeric RNA (TERRA) Quadruplex. *Nucleic Acids Res* **2010**, *38*, 5569–5580, doi:10.1093/nar/gkq259.

213. Martadinata, H.; Phan, A.T. Structure of Propeller-Type Parallel-Stranded RNA G-Quadruplexes, Formed by Human Telomeric RNA Sequences in K+ Solution. *J. Am. Chem. Soc.* **2009**, *131*, 2570–2578, doi:10.1021/ja806592z.
214. Xu, Y.; Suzuki, Y.; Lönnberg, T.; Komiyama, M. Human Telomeric DNA Sequence-Specific Cleaving by G-Quadruplex Formation. *J. Am. Chem. Soc.* **2009**, *131*, 2871–2874, doi:10.1021/ja807313x.
215. Xiao, C.-D.; Shibata, T.; Yamamoto, Y.; Xu, Y. An Intramolecular Antiparallel G-Quadruplex Formed by Human Telomere RNA. *Chem. Commun.* **2018**, *54*, 3944–3946, doi:10.1039/C8CC01427B.
216. Huang, J.-L.; Yan, X.-L.; Huang, D.; Gan, L.; Gao, H.; Fan, R.-Z.; Li, S.; Yuan, F.-Y.; Zhu, X.; Tang, G.-H.; et al. Discovery of a Highly Potent and Orally Available Importin-B1 Inhibitor That Overcomes Enzalutamide-Resistance in Advanced Prostate Cancer. *Acta Pharmaceutica Sinica B* **2023**, *13*, 4934–4944, doi:10.1016/j.apsb.2023.07.017.
217. Asamitsu, S.; Yabuki, Y.; Ikenoshita, S.; Kawakubo, K.; Kawasaki, M.; Usuki, S.; Nakayama, Y.; Adachi, K.; Kugoh, H.; Ishii, K.; et al. CGG Repeat RNA G-Quadruplexes Interact with FMRpolyG to Cause Neuronal Dysfunction in Fragile X-Related Tremor/Ataxia Syndrome. *Science Advances* **2021**, *7*, eabd9440, doi:10.1126/sciadv.abd9440.
218. Ji, D.; Juhas, M.; Tsang, C.M.; Kwok, C.K.; Li, Y.; Zhang, Y. Discovery of G-Quadruplex-Forming Sequences in SARS-CoV-2. *Brief Bioinform* **2021**, *22*, 1150–1160, doi:10.1093/bib/bbaa114.
219. Xu, Y.; Suzuki, Y.; Ito, K.; Komiyama, M. Telomeric Repeat-Containing RNA Structure in Living Cells. *Proceedings of the National Academy of Sciences* **2010**, *107*, 14579–14584, doi:10.1073/pnas.1001177107.
220. Laguerre, A.; Stefan, L.; Larrouy, M.; Genest, D.; Novotna, J.; Pirrotta, M.; Monchaud, D. A Twice-As-Smart Synthetic G-Quartet: PyroTASQ Is Both a Smart Quadruplex Ligand and a Smart Fluorescent Probe. *J. Am. Chem. Soc.* **2014**, *136*, 12406–12414, doi:10.1021/ja506331x.
221. Bao, H.-L.; Ishizuka, T.; Yamashita, A.; Furukoji, E.; Asada, Y.; Xu, Y. Improving Thermodynamic Stability and Anticoagulant Activity of a Thrombin Binding Aptamer by Incorporation of 8-Trifluoromethyl-2′-Deoxyguanosine. *J. Med. Chem.* **2021**, *64*, 711–718, doi:10.1021/acs.jmedchem.0c01711.
222. Chen, X.-C.; Chen, S.-B.; Dai, J.; Yuan, J.-H.; Ou, T.-M.; Huang, Z.-S.; Tan, J.-H. Tracking the Dynamic Folding and Unfolding of RNA G-Quadruplexes in Live Cells. *Angewandte Chemie International Edition* **2018**, *57*, 4702–4706, doi:10.1002/anie.201801999.
223. Flynn, R.L.; Zou, L. ATR: A Master Conductor of Cellular Responses to DNA Replication Stress. *Trends Biochem Sci* **2011**, *36*, 133–140, doi:10.1016/j.tibs.2010.09.005.
224. Mei, Y.; Deng, Z.; Vladimirova, O.; Gulve, N.; Johnson, F.B.; Drosopoulos, W.C.; Schildkraut, C.L.; Lieberman, P.M. TERRA G-Quadruplex RNA Interaction

with TRF2 GAR Domain Is Required for Telomere Integrity. *Sci Rep* **2021**, *11*, 3509, doi:10.1038/s41598-021-82406-x.
225. Zhang, Y.; Huang, J.; Yu, K.; Cui, X. G-Quadruplexes Formation by the C9orf72 Nucleotide Repeat Expansion d(GGGGCC)n and Conformation Regulation by Fangchinoline. *Molecules* **2023**, *28*, 4671, doi:10.3390/molecules28124671.
226. Fay, M.M.; Anderson, P.J.; Ivanov, P. ALS/FTD-Associated C9ORF72 Repeat RNA Promotes Phase Transitions In Vitro and in Cells. *Cell Rep* **2017**, *21*, 3573–3584, doi:10.1016/j.celrep.2017.11.093.
227. van Wietmarschen, N.; Merzouk, S.; Halsema, N.; Spierings, D.C.J.; Guryev, V.; Lansdorp, P.M. BLM Helicase Suppresses Recombination at G-Quadruplex Motifs in Transcribed Genes. *Nat Commun* **2018**, *9*, 271, doi:10.1038/s41467-017-02760-1.
228. Hanahan, D.; Weinberg, R.A. Hallmarks of Cancer: The Next Generation. *Cell* **2011**, *144*, 646–674, doi:10.1016/j.cell.2011.02.013.
229. Brown, S.; Swafford, K.; McCrury, M.; Nasrin, F.; Gragg, C.Q.; Chavan, A.; Roy Choudhury, S.; Dickerhoff, J.; Yang, D.; Kendrick, S. G-Quadruplex and i-Motif DNA Structures Form in the Promoter of the Key Innate Immune Adaptor MYD88. *Cell Rep Phys Sci* **2025**, *6*, 102560, doi:10.1016/j.xcrp.2025.102560.
230. Guneri, D.; Morris, C.J.; Ding, Y.; Craggs, T.D.; Smith, S.S.; Waller, Z.A.E. G-Quadruplexes Act as an On/Off Switch While i-Motifs Regulate Insulin Expression in Reporter Gene Assays 2025, 2025.05.02.651924.
231. Burkhart, I.; McKenney, V.R.; Wirmer-Bartoschek, J.; Grün, J.T.; Heckel, A.; Schwalbe, H. Structural Insights into Spare-Tire DNA G-Quadruplex from the Human VEGF Promoter. *ACS Chem. Biol.* **2025**, *20*, 1417–1425, doi:10.1021/acschembio.5c00226.
232. Wen, L.; Han, Z.; Li, J.; Du, Y. C-MYC and HIF1α Promoter G-Quadruplexes Dependent Metabolic Regulation Mechanism of Berberine in Colon Cancer. *J Gastrointest Oncol* **2022**, *13*, 1152–1168, doi:10.21037/jgo-22-389.
233. Bahls, B.; Aljnadi, I.M.; Emídio, R.; Mendes, E.; Paulo, A. G-Quadruplexes in c-MYC Promoter as Targets for Cancer Therapy. *Biomedicines* **2023**, *11*, 969, doi:10.3390/biomedicines11030969.
234. Mazzini, S.; Gargallo, R.; Musso, L.; De Santis, F.; Aviñó, A.; Scaglioni, L.; Eritja, R.; Di Nicola, M.; Zunino, F.; Amatulli, A.; et al. Stabilization of C-KIT G-Quadruplex DNA Structures by the RNA Polymerase I Inhibitors BMH-21 and BA-41. *Int J Mol Sci* **2019**, *20*, 4927, doi:10.3390/ijms20194927.
235. Wang, K.-B.; Liu, Y.; Li, J.; Xiao, C.; Wang, Y.; Gu, W.; Li, Y.; Xia, Y.-Z.; Yan, T.; Yang, M.-H.; et al. Structural Insight into the Bulge-Containing KRAS Oncogene Promoter G-Quadruplex Bound to Berberine and Coptisine. *Nat Commun* **2022**, *13*, 6016, doi:10.1038/s41467-022-33761-4.
236. Agrawal, P.; Lin, C.; Mathad, R.I.; Carver, M.; Yang, D. The Major G-Quadruplex Formed in the Human BCL-2 Proximal Promoter Adopts a Parallel Structure with a 13-Nt Loop in K+ Solution. *J. Am. Chem. Soc.* **2014**, *136*, 1750–1753, doi:10.1021/ja4118945.

237. Figueiredo, J.; Mergny, J.-L.; Cruz, C. G-Quadruplex Ligands in Cancer Therapy: Progress, Challenges, and Clinical Perspectives. *Life Sciences* **2024**, *340*, 122481, doi:10.1016/j.lfs.2024.122481.
238. Drygin, D.; Siddiqui-Jain, A.; O'Brien, S.; Schwaebe, M.; Lin, A.; Bliesath, J.; Ho, C.B.; Proffitt, C.; Trent, K.; Whitten, J.P.; et al. Anticancer Activity of CX-3543: A Direct Inhibitor of rRNA Biogenesis. *Cancer Research* **2009**, *69*, 7653–7661, doi:10.1158/0008-5472.CAN-09-1304.
239. Ahmed, A.A.; Greenhalf, W.; Palmer, D.H.; Williams, N.; Worthington, J.; Arshad, T.; Haider, S.; Alexandrou, E.; Guneri, D.; Waller, Z.A.E.; et al. The Potent G-Quadruplex-Binding Compound QN-302 Downregulates S100P Gene Expression in Cells and in an In Vivo Model of Pancreatic Cancer. *Molecules* **2023**, *28*, 2452, doi:10.3390/molecules28062452.
240. Umar, M.I.; Ji, D.; Chan, C.-Y.; Kwok, C.K. G-Quadruplex-Based Fluorescent Turn-On Ligands and Aptamers: From Development to Applications. *Molecules* **2019**, *24*, 2416, doi:10.3390/molecules24132416.
241. Duarte, A.R.; Cadoni, E.; Ressurreição, A.S.; Moreira, R.; Paulo, A. Design of Modular G-Quadruplex Ligands. *ChemMedChem* **2018**, *13*, 869–893, doi:10.1002/cmdc.201700747.
242. Monchaud, D.; Teulade-Fichou, M.-P. A Hitchhiker's Guide to G-Quadruplex Ligands. *Org. Biomol. Chem.* **2008**, *6*, 627–636, doi:10.1039/B714772B.
243. Alessandrini, I.; Recagni, M.; Zaffaroni, N.; Folini, M. On the Road to Fight Cancer: The Potential of G-Quadruplex Ligands as Novel Therapeutic Agents. *International Journal of Molecular Sciences* **2021**, *22*, 5947, doi:10.3390/ijms22115947.
244. Dickerhoff, J.; Warnecke, K.R.; Wang, K.; Deng, N.; Yang, D. Evaluating Molecular Docking Software for Small Molecule Binding to G-Quadruplex DNA. *Int J Mol Sci* **2021**, *22*, 10801, doi:10.3390/ijms221910801.
245. Yang, Q.-F.; Wang, X.-R.; Wang, Y.-H.; Wu, X.-H.; Shi, R.-Y.; Wang, Y.-X.; Zhu, H.-N.; Yang, S.; Tang, Y.-L.; Li, F. G4LDB 3.0: A Database for Discovering and Studying G-Quadruplex and i-Motif Ligands. *Nucleic Acids Res* **2025**, *53*, D91–D98, doi:10.1093/nar/gkae835.
246. Sun, Z.-Y.; Wang, X.-N.; Cheng, S.-Q.; Su, X.-X.; Ou, T.-M. Developing Novel G-Quadruplex Ligands: From Interaction with Nucleic Acids to Interfering with Nucleic Acid–Protein Interaction. *Molecules* **2019**, *24*, 396, doi:10.3390/molecules24030396.
247. Neidle, S. Human Telomeric G-Quadruplex: The Current Status of Telomeric G-Quadruplexes as Therapeutic Targets in Human Cancer: G-Quadruplexes as Cancer Drug Targets. *FEBS Journal* **2010**, *277*, 1118–1125, doi:10.1111/j.1742-4658.2009.07463.x.
248. Taetz, S.; Baldes, C.; Mürdter, T.E.; Kleideiter, E.; Piotrowska, K.; Bock, U.; Haltner-Ukomadu, E.; Mueller, J.; Huwer, H.; Schaefer, U.F.; et al.

Biopharmaceutical Characterization of the Telomerase Inhibitor BRACO19. *Pharm Res* **2006**, *23*, 1031–1037, doi:10.1007/s11095-006-0026-y.
249. Machireddy, B.; Sullivan, H.-J.; Wu, C. Binding of BRACO19 to a Telomeric G-Quadruplex DNA Probed by All-Atom Molecular Dynamics Simulations with Explicit Solvent. *Molecules* **2019**, *24*, 1010, doi:10.3390/molecules24061010.
250. Harrison, R.J.; Cuesta, J.; Chessari, G.; Read, M.A.; Basra, S.K.; Reszka, A.P.; Morrell, J.; Gowan, S.M.; Incles, C.M.; Tanious, F.A.; et al. Trisubstituted Acridine Derivatives as Potent and Selective Telomerase Inhibitors. *J Med Chem* **2003**, *46*, 4463–4476, doi:10.1021/jm0308693.
251. Burger, A.M.; Dai, F.; Schultes, C.M.; Reszka, A.P.; Moore, M.J.; Double, J.A.; Neidle, S. The G-Quadruplex-Interactive Molecule BRACO-19 Inhibits Tumor Growth, Consistent with Telomere Targeting and Interference with Telomerase Function. *Cancer Res* **2005**, *65*, 1489–1496, doi:10.1158/0008-5472.CAN-04-2910.
252. Gunaratnam, M.; Green, C.; Moreira, J.B.; Moorhouse, A.D.; Kelland, L.R.; Moses, J.E.; Neidle, S. G-Quadruplex Compounds and Cis-Platin Act Synergistically to Inhibit Cancer Cell Growth in Vitro and in Vivo. *Biochem Pharmacol* **2009**, *78*, 115–122, doi:10.1016/j.bcp.2009.03.018.
253. Iachettini, S.; Stevens, M.F.; Frigerio, M.; Hummersone, M.G.; Hutchinson, I.; Garner, T.P.; Searle, M.S.; Wilson, D.W.; Munde, M.; Nanjunda, R.; et al. On and Off-Target Effects of Telomere Uncapping G-Quadruplex Selective Ligands Based on Pentacyclic Acridinium Salts. *Journal of Experimental & Clinical Cancer Research* **2013**, *32*, 68, doi:10.1186/1756-9966-32-68.
254. Rizzo, A.; Iachettini, S.; Zizza, P.; Cingolani, C.; Porru, M.; Artuso, S.; Stevens, M.; Hummersone, M.; Biroccio, A.; Salvati, E.; et al. Identification of Novel RHPS4-Derivative Ligands with Improved Toxicological Profiles and Telomere-Targeting Activities. *J Exp Clin Cancer Res* **2014**, *33*, 81, doi:10.1186/s13046-014-0081-x.
255. Wang, K.-B.; Elsayed, M.S.A.; Wu, G.; Deng, N.; Cushman, M.; Yang, D. Indenoisoquinoline Topoisomerase Inhibitors Strongly Bind and Stabilize the MYC Promoter G-Quadruplex and Downregulate MYC. *J. Am. Chem. Soc.* **2019**, *141*, 11059–11070, doi:10.1021/jacs.9b02679.
256. Xu, H.; Di Antonio, M.; McKinney, S.; Mathew, V.; Ho, B.; O'Neil, N.J.; Santos, N.D.; Silvester, J.; Wei, V.; Garcia, J.; et al. CX-5461 Is a DNA G-Quadruplex Stabilizer with Selective Lethality in BRCA1/2 Deficient Tumours. *Nat Commun* **2017**, *8*, 14432, doi:10.1038/ncomms14432.
257. Haddach, M.; Schwaebe, M.K.; Michaux, J.; Nagasawa, J.; O'Brien, S.E.; Whitten, J.P.; Pierre, F.; Kerdoncuff, P.; Darjania, L.; Stansfield, R.; et al. Discovery of CX-5461, the First Direct and Selective Inhibitor of RNA Polymerase I, for Cancer Therapeutics. *ACS Med. Chem. Lett.* **2012**, *3*, 602–606, doi:10.1021/ml300110s.
258. Gunaratnam, M.; de la Fuente, M.; Hampel, S.M.; Todd, A.K.; Reszka, A.P.; Schätzlein, A.; Neidle, S. Targeting Pancreatic Cancer with a G-Quadruplex Ligand. *Bioorg Med Chem* **2011**, *19*, 7151–7157, doi:10.1016/j.bmc.2011.09.055.

259. Hampel, S.M.; Sidibe, A.; Gunaratnam, M.; Riou, J.-F.; Neidle, S. Tetrasubstituted Naphthalene Diimide Ligands with Selectivity for Telomeric G-Quadruplexes and Cancer Cells. *Bioorg Med Chem Lett* **2010**, *20*, 6459–6463, doi:10.1016/j.bmcl.2010.09.066.
260. Micco, M.; Collie, G.W.; Dale, A.G.; Ohnmacht, S.A.; Pazitna, I.; Gunaratnam, M.; Reszka, A.P.; Neidle, S. Structure-Based Design and Evaluation of Naphthalene Diimide G-Quadruplex Ligands as Telomere Targeting Agents in Pancreatic Cancer Cells. *J Med Chem* **2013**, *56*, 2959–2974, doi:10.1021/jm301899y.
261. Marchetti, C.; Zyner, K.G.; Ohnmacht, S.A.; Robson, M.; Haider, S.M.; Morton, J.P.; Marsico, G.; Vo, T.; Laughlin-Toth, S.; Ahmed, A.A.; et al. Targeting Multiple Effector Pathways in Pancreatic Ductal Adenocarcinoma with a G-Quadruplex-Binding Small Molecule. *J. Med. Chem.* **2018**, *61*, 2500–2517, doi:10.1021/acs.jmedchem.7b01781.
262. Makohon-Moore, A.P.; Zhang, M.; Reiter, J.G.; Bozic, I.; Allen, B.; Kundu, D.; Chatterjee, K.; Wong, F.; Jiao, Y.; Kohutek, Z.A.; et al. Limited Heterogeneity of Known Driver Gene Mutations among the Metastases of Individual Patients with Pancreatic Cancer. *Nat Genet* **2017**, *49*, 358–366, doi:10.1038/ng.3764.
263. Ahmed, A.A.; Angell, R.; Oxenford, S.; Worthington, J.; Williams, N.; Barton, N.; Fowler, T.G.; O'Flynn, D.E.; Sunose, M.; McConville, M.; et al. Asymmetrically Substituted Quadruplex-Binding Naphthalene Diimide Showing Potent Activity in Pancreatic Cancer Models. *ACS Med. Chem. Lett.* **2020**, *11*, 1634–1644, doi:10.1021/acsmedchemlett.0c00317.
264. Herdy, B.; Mayer, C.; Varshney, D.; Marsico, G.; Murat, P.; Taylor, C.; D'Santos, C.; Tannahill, D.; Balasubramanian, S. Analysis of NRAS RNA G-Quadruplex Binding Proteins Reveals DDX3X as a Novel Interactor of Cellular G-Quadruplex Containing Transcripts. *Nucleic Acids Res* **2018**, *46*, 11592–11604, doi:10.1093/nar/gky861.
265. Barral, A.; Déjardin, J. Telomeric Chromatin and TERRA. *J Mol Biol* **2020**, *432*, 4244–4256, doi:10.1016/j.jmb.2020.03.003.
266. Xu, S.; Li, Q.; Xiang, J.; Yang, Q.; Sun, H.; Guan, A.; Wang, L.; Liu, Y.; Yu, L.; Shi, Y.; et al. Directly Lighting up RNA G-Quadruplexes from Test Tubes to Living Human Cells. *Nucleic Acids Res* **2015**, *43*, 9575–9586, doi:10.1093/nar/gkv1040.
267. Malgowska, M.; Czajczynska, K.; Gudanis, D.; Tworak, A.; Gdaniec, Z. Overview of the RNA G-Quadruplex Structures. *Acta Biochim Pol* **2016**, *63*, 609–621, doi:10.18388/abp.2016_1335.
268. Tassinari, M.; Richter, S.N.; Gandellini, P. Biological Relevance and Therapeutic Potential of G-Quadruplex Structures in the Human Noncoding Transcriptome. *Nucleic Acids Res* **2021**, *49*, 3617–3633, doi:10.1093/nar/gkab127.
269. Ghosh, A.; Ekka, M.K.; Tawani, A.; Kumar, A.; Chakraborty, D.; Maiti, S. Restoration of miRNA-149 Expression by TmPyP4 Induced Unfolding of Quadruplex within Its Precursor. *Biochemistry* **2019**, *58*, 514–525, doi:10.1021/acs.biochem.8b00880.

270. Zamiri, B.; Reddy, K.; Macgregor, R.B.; Pearson, C.E. TMPyP4 Porphyrin Distorts RNA G-Quadruplex Structures of the Disease-Associated r(GGGGCC)n Repeat of the C9orf72 Gene and Blocks Interaction of RNA-Binding Proteins. *J Biol Chem* **2014**, *289*, 4653–4659, doi:10.1074/jbc.C113.502336.
271. Endoh, T.; Rode, A.B.; Takahashi, S.; Kataoka, Y.; Kuwahara, M.; Sugimoto, N. Real-Time Monitoring of G-Quadruplex Formation during Transcription. *Anal. Chem.* **2016**, *88*, 1984–1989, doi:10.1021/acs.analchem.5b04396.
272. Chen, S.-B.; Hu, M.-H.; Liu, G.-C.; Wang, J.; Ou, T.-M.; Gu, L.-Q.; Huang, Z.-S.; Tan, J.-H. Visualization of NRAS RNA G-Quadruplex Structures in Cells with an Engineered Fluorogenic Hybridization Probe. *J. Am. Chem. Soc.* **2016**, *138*, 10382–10385, doi:10.1021/jacs.6b04799.
273. Yu, Y.; Luo, Y.; Fang, Z.; Teng, W.; Yu, Y.; Tian, J.; Guo, P.; Xu, R.; Wu, J.; Li, Y. <p>Mechanism of Sanguinarine in Inhibiting Macrophages to Promote Metastasis and Proliferation of Lung Cancer via Modulating the Exosomes in A549 Cells</P>. *OTT* **2020**, *13*, 8989–9003, doi:10.2147/OTT.S261054.
274. Zhang, S.; Leng, T.; Zhang, Q.; Zhao, Q.; Nie, X.; Yang, L. Sanguinarine Inhibits Epithelial Ovarian Cancer Development via Regulating Long Non-Coding RNA CASC2-EIF4A3 Axis and/or Inhibiting NF-κB Signaling or PI3K/AKT/mTOR Pathway. *Biomedicine & Pharmacotherapy* **2018**, *102*, 302–308, doi:10.1016/j.biopha.2018.03.071.
275. Song, J.; Perreault, J.-P.; Topisirovic, I.; Richard, S. RNA G-Quadruplexes and Their Potential Regulatory Roles in Translation. *Translation (Austin)* **2016**, *4*, e1244031, doi:10.1080/21690731.2016.1244031.
276. Halder, K.; Largy, E.; Benzler, M.; Teulade-Fichou, M.-P.; Hartig, J.S. Efficient Suppression of Gene Expression by Targeting 5'-UTR-Based RNA Quadruplexes with Bisquinolinium Compounds. *Chembiochem* **2011**, *12*, 1663–1668, doi:10.1002/cbic.201100228.
277. Katsuda, Y.; Sato, S.-I.; Asano, L.; Morimura, Y.; Furuta, T.; Sugiyama, H.; Hagihara, M.; Uesugi, M. A Small Molecule That Represses Translation of G-Quadruplex-Containing mRNA. *J Am Chem Soc* **2016**, *138*, 9037–9040, doi:10.1021/jacs.6b04506.
278. Rocca, R.; Talarico, C.; Moraca, F.; Costa, G.; Romeo, I.; Ortuso, F.; Alcaro, S.; Artese, A. Molecular Recognition of a Carboxy Pyridostatin toward G-Quadruplex Structures: Why Does It Prefer RNA? *Chem Biol Drug Des* **2017**, *90*, 919–925, doi:10.1111/cbdd.13015.
279. Tao, Y.; Zheng, Y.; Zhai, Q.; Wei, D. Recent Advances in the Development of Small Molecules Targeting RNA G-Quadruplexes for Drug Discovery. *Bioorg Chem* **2021**, *110*, 104804, doi:10.1016/j.bioorg.2021.104804.
280. Peng, W.; Sun, Z.-Y.; Zhang, Q.; Cheng, S.-Q.; Wang, S.-K.; Wang, X.-N.; Kuang, G.-T.; Su, X.-X.; Tan, J.-H.; Huang, Z.-S.; et al. Design, Synthesis, and Evaluation of Novel p-(Methylthio)Styryl Substituted Quindoline Derivatives as

Neuroblastoma RAS (NRAS) Repressors via Specific Stabilizing the RNA G-Quadruplex. *J Med Chem* **2018**, *61*, 6629–6646, doi:10.1021/acs.jmedchem.8b00257.
281. Santos, T.; Salgado, G.F.; Cabrita, E.J.; Cruz, C. G-Quadruplexes and Their Ligands: Biophysical Methods to Unravel G-Quadruplex/Ligand Interactions. *Pharmaceuticals (Basel)* **2021**, *14*, 769, doi:10.3390/ph14080769.
282. Rosu, F.; De Pauw, E.; Gabelica, V. Electrospray Mass Spectrometry to Study Drug-Nucleic Acids Interactions. *Biochimie* **2008**, *90*, 1074–1087, doi:10.1016/j.biochi.2008.01.005.
283. Li, H. Mass Spectroscopic Study of G-Quadruplex. In *G-Quadruplex Nucleic Acids: Methods and Protocols*; Yang, D., Lin, C., Eds.; Springer: New York, NY, 2019; pp. 105–116 ISBN 978-1-4939-9666-7.
284. Monchaud, D.; Allain, C.; Bertrand, H.; Smargiasso, N.; Rosu, F.; Gabelica, V.; De Cian, A.; Mergny, J.-L.; Teulade-Fichou, M.-P. Ligands Playing Musical Chairs with G-Quadruplex DNA: A Rapid and Simple Displacement Assay for Identifying Selective G-Quadruplex Binders. *Biochimie* **2008**, *90*, 1207–1223, doi:10.1016/j.biochi.2008.02.019.
285. Yuan, G.; Zhang, Q.; Zhou, J.; Li, H. Mass Spectrometry of G-Quadruplex DNA: Formation, Recognition, Property, Conversion, and Conformation. *Mass Spectrom Rev* **2011**, *30*, 1121–1142, doi:10.1002/mas.20315.
286. Carrasco, C.; Rosu, F.; Gabelica, V.; Houssier, C.; De Pauw, E.; Garbay-Jaureguiberry, C.; Roques, B.; Wilson, W.D.; Chaires, J.B.; Waring, M.J.; et al. Tight Binding of the Antitumor Drug Ditercalinium to Quadruplex DNA. *ChemBioChem* **2002**, *3*, 1235–1241, doi:10.1002/1439-7633(20021202)3:12%3C1235::AID-CBIC1235%3E3.0.CO;2-I.
287. Lombardo, C.M.; Martínez, I.S.; Haider, S.; Gabelica, V.; Pauw, E.D.; Moses, J.E.; Neidle, S. Structure-Based Design of Selective High-Affinity Telomeric Quadruplex-Binding Ligands. *Chem. Commun.* **2010**, *46*, 9116–9118, doi:10.1039/C0CC02917C.
288. Gabelica, V. Determination of Equilibrium Association Constants of Ligand-DNA Complexes by Electrospray Mass Spectrometry. *Methods Mol Biol* **2010**, *613*, 89–101, doi:10.1007/978-1-60327-418-0_6.
289. Tan, W.; Zhou, J.; Yuan, G. Electrospray Ionization Mass Spectrometry Probing of Binding Affinity of Berbamine, a Flexible Cyclic Alkaloid from Traditional Chinese Medicine, with G-Quadruplex DNA. *Rapid Commun Mass Spectrom* **2014**, *28*, 143–147, doi:10.1002/rcm.6763.
290. Yuan, G.; Zhang, Q.; Zhou, J.; Li, H. Mass Spectrometry of G-Quadruplex DNA: Formation, Recognition, Property, Conversion, and Conformation. *Mass Spectrom Rev* **2011**, *30*, 1121–1142, doi:10.1002/mas.20315.
291. Ribaudo, G.; Ongaro, A.; Oselladore, E.; Memo, M.; Gianoncelli, A. Combining Electrospray Mass Spectrometry (ESI-MS) and Computational Techniques in the Assessment of G-Quadruplex Ligands: A Hybrid Approach to Optimize Hit

Discovery. *J. Med. Chem.* **2021**, *64*, 13174–13190, doi:10.1021/acs.jmedchem.1c00962.
292. Rosu, F.; Gabelica, V.; Smargiasso, N.; Mazzucchelli, G.; Shin-Ya, K.; De Pauw, E. Cation Involvement in Telomestatin Binding to G-Quadruplex DNA. *J Nucleic Acids* **2010**, *2010*, 121259, doi:10.4061/2010/121259.
293. Hill, D.W.; Baveghems, C.L.; Albaugh, D.R.; Kormos, T.M.; Lai, S.; Ng, H.K.; Grant, D.F. Correlation of Ecom50 Values between Mass Spectrometers: Effect of Collision Cell Radiofrequency Voltage on Calculated Survival Yield. *Rapid Communications in Mass Spectrometry* **2012**, *26*, 2303–2310, doi:10.1002/rcm.6353.
294. Rosu, F.; Nguyen, C.-H.; De Pauw, E.; Gabelica, V. Ligand Binding Mode to Duplex and Triplex DNA Assessed by Combining Electrospray Tandem Mass Spectrometry and Molecular Modeling. *J Am Soc Mass Spectrom* **2007**, *18*, 1052–1062, doi:10.1016/j.jasms.2007.03.010.
295. Caceres-Cortes, J.; Falk, B.; Mueller, L.; Dhar, T.G.M. Perspectives on Nuclear Magnetic Resonance Spectroscopy in Drug Discovery Research. *J. Med. Chem.* **2024**, *67*, 1701–1733, doi:10.1021/acs.jmedchem.3c02389.
296. Dalvit, C.; Fogliatto, G.; Stewart, A.; Veronesi, M.; Stockman, B. WaterLOGSY as a Method for Primary NMR Screening: Practical Aspects and Range of Applicability. *J Biomol NMR* **2001**, *21*, 349–359, doi:10.1023/a:1013302231549.
297. Kerkour, A.; Mergny, J.-L.; Salgado, G.F. NMR Based Model of Human Telomeric Repeat G-Quadruplex in Complex with 2,4,6-Triarylpyridine Family Ligand. *Biochim Biophys Acta Gen Subj* **2017**, *1861*, 1293–1302, doi:10.1016/j.bbagen.2016.12.016.
298. Alcaro, S.; Musetti, C.; Distinto, S.; Casatti, M.; Zagotto, G.; Artese, A.; Parrotta, L.; Moraca, F.; Costa, G.; Ortuso, F.; et al. Identification and Characterization of New DNA G-Quadruplex Binders Selected by a Combination of Ligand and Structure-Based Virtual Screening Approaches. *J Med Chem* **2013**, *56*, 843–855, doi:10.1021/jm3013486.
299. Ranjan, N.; Andreasen, K.F.; Arora, Y.; Xue, L.; Arya, D.P. Surface Dependent Dual Recognition of a G-Quadruplex DNA With Neomycin-Intercalator Conjugates. *Front Chem* **2020**, *8*, 60, doi:10.3389/fchem.2020.00060.
300. Halgren, T.A.; Murphy, R.B.; Friesner, R.A.; Beard, H.S.; Frye, L.L.; Pollard, W.T.; Banks, J.L. Glide: A New Approach for Rapid, Accurate Docking and Scoring. 2. Enrichment Factors in Database Screening. *J. Med. Chem.* **2004**, *47*, 1750–1759, doi:10.1021/jm030644s.
301. Friesner, R.A.; Murphy, R.B.; Repasky, M.P.; Frye, L.L.; Greenwood, J.R.; Halgren, T.A.; Sanschagrin, P.C.; Mainz, D.T. Extra Precision Glide: Docking and Scoring Incorporating a Model of Hydrophobic Enclosure for Protein−Ligand Complexes. *J. Med. Chem.* **2006**, *49*, 6177–6196, doi:10.1021/jm051256o.
302. Artese, A.; Costa, G.; Ortuso, F.; Parrotta, L.; Alcaro, S. Identification of New Natural DNA G-Quadruplex Binders Selected by a Structure-Based Virtual Screening Approach. *Molecules* **2013**, *18*, 12051–12070, doi:10.3390/molecules181012051.

303. Reznichenko, O.; Leclercq, D.; Franco Pinto, J.; Mouawad, L.; Gabelica, V.; Granzhan, A. Optimization of G-Quadruplex Ligands through a SAR Study Combining Parallel Synthesis and Screening of Cationic Bis(Acylhydrazones). *Chemistry* **2023**, *29*, e202202427, doi:10.1002/chem.202202427.
304. Moraca, F.; Arciuolo, V.; Marzano, S.; Napolitano, F.; Castellano, G.; D'Aria, F.; Di Porzio, A.; Landolfi, L.; Catalanotti, B.; Randazzo, A.; et al. Repurposing FDA-Approved Drugs to Target G-Quadruplexes in Breast Cancer. *European Journal of Medicinal Chemistry* **2025**, *285*, 117245, doi:10.1016/j.ejmech.2025.117245.
305. Ivanova, L.; Tammiku-Taul, J.; García-Sosa, A.T.; Sidorova, Y.; Saarma, M.; Karelson, M. Molecular Dynamics Simulations of the Interactions between Glial Cell Line-Derived Neurotrophic Factor Family Receptor GFRα1 and Small-Molecule Ligands. *ACS Omega* **2018**, *3*, 11407–11414, doi:10.1021/acsomega.8b01524.
306. Case, D.A.; Aktulga, H.M.; Belfon, K.; Cerutti, D.S.; Cisneros, G.A.; Cruzeiro, V.W.D.; Forouzesh, N.; Giese, T.J.; Götz, A.W.; Gohlke, H.; et al. AmberTools. *J. Chem. Inf. Model.* **2023**, *63*, 6183–6191, doi:10.1021/acs.jcim.3c01153.
307. Li, N.; Gao, Y.; Qiu, F.; Zhu, T. Benchmark Force Fields for the Molecular Dynamic Simulation of G-Quadruplexes. *Molecules* **2021**, *26*, 5379, doi:10.3390/molecules26175379.
308. Knappeová, B.; Mlýnský, V.; Pykal, M.; Šponer, J.; Banáš, P.; Otyepka, M.; Krepl, M. Comprehensive Assessment of Force-Field Performance in Molecular Dynamics Simulations of DNA/RNA Hybrid Duplexes. *J Chem Theory Comput* **2024**, *20*, 6917–6929, doi:10.1021/acs.jctc.4c00601.
309. Machireddy, B.; Sullivan, H.-J.; Wu, C. Binding of BRACO19 to a Telomeric G-Quadruplex DNA Probed by All-Atom Molecular Dynamics Simulations with Explicit Solvent. *Molecules* **2019**, *24*, 1010, doi:10.3390/molecules24061010.
310. Tawani, A.; Mishra, S.K.; Kumar, A. Structural Insight for the Recognition of G-Quadruplex Structure at Human c-Myc Promoter Sequence by Flavonoid Quercetin. *Sci Rep* **2017**, *7*, 3600, doi:10.1038/s41598-017-03906-3.
311. Nasiri, H.R.; Bell, N.M.; McLuckie, K.I.E.; Husby, J.; Abell, C.; Neidle, S.; Balasubramanian, S. Targeting a C-MYC G-Quadruplex DNA with a Fragment Library. *Chem. Commun.* **2014**, *50*, 1704–1707, doi:10.1039/C3CC48390H.
312. Neidle, S.; Thurston, D.E. Chemical Approaches to the Discovery and Development of Cancer Therapies. *Nat Rev Cancer* **2005**, *5*, 285–296, doi:10.1038/nrc1587.
313. Hasnat, H.; Shompa, S.A.; Islam, Md.M.; Alam, S.; Richi, F.T.; Emon, N.U.; Ashrafi, S.; Ahmed, N.U.; Chowdhury, Md.N.R.; Fatema, N.; et al. Flavonoids: A Treasure House of Prospective Pharmacological Potentials. *Heliyon* **2024**, *10*, e27533, doi:10.1016/j.heliyon.2024.e27533.
314. Ali, M.R.; Sadoqi, M.; Møller, S.G.; Boutajangout, A.; Mezei, M. Assessing the Binding of Cholinesterase Inhibitors by Docking and Molecular Dynamics Studies. *Journal of Molecular Graphics and Modelling* **2017**, *76*, 36–42, doi:10.1016/j.jmgm.2017.06.027.

315. Ribaudo, G.; Vendrame, T.; Bova, S. Isoflavones from *Maclura Pomifera* : Structural Elucidation and *in Silico* Evaluation of Their Interaction with PDE5. *Natural Product Research* **2017**, *31*, 1988–1994, doi:10.1080/14786419.2016.1269101.
316. Gavathiotis, E.; Searle, M.S. Structure of the Parallel-Stranded DNA Quadruplex d(TTAGGGT)4 Containing the Human Telomeric Repeat: Evidence for A-Tetrad Formation from NMR and Molecular Dynamics Simulations. *Org Biomol Chem* **2003**, *1*, 1650–1656, doi:10.1039/b300845m.
317. Ribaudo, G.; Oselladore, E.; Ongaro, A.; Zagotto, G.; Memo, M.; Gianoncelli, A. Enhanced G-Quadruplex Selectivity of Flavonoid Glycoside Rutin over Quercetin. *Natural Product Research* **2020**, 1–5, doi:10.1080/14786419.2020.1859505.
318. Bhattacharjee, S.; Chakraborty, S.; Chorell, E.; Sengupta, P.K.; Bhowmik, S. Importance of the Hydroxyl Substituents in the B-Ring of Plant Flavonols on Their Preferential Binding Interactions with VEGF G-Quadruplex DNA: Multi-Spectroscopic and Molecular Modeling Studies. *Int J Biol Macromol* **2018**, *118*, 629–639, doi:10.1016/j.ijbiomac.2018.06.115.
319. Bag, S.; Burman, M.D.; Bhowmik, S. Structural Insights and Shedding Light on Preferential Interactions of Dietary Flavonoids with G-Quadruplex DNA Structures: A New Horizon. *Heliyon* **2023**, *9*, e13959, doi:10.1016/j.heliyon.2023.e13959.
320. Ribaudo, G.; Ongaro, A.; Zagotto, G.; Memo, M.; Gianoncelli, A. Evidence on Selective Binding to G-Quadruplex DNA of Isoflavones from Maclura Pomifera by Mass Spectrometry and Molecular Docking. *Natural Product Research* **2021**, *35*, 2583–2587, doi:10.1080/14786419.2019.1680670.
321. Ribaudo, G.; Anyanwu, M.; Giannangeli, M.; Oselladore, E.; Ongaro, A.; Memo, M.; Gianoncelli, A. G-Quadruplex DNA as a Macromolecular Target for Semi-Synthetic Isoflavones Bearing B-Ring Tosylation. *Macromol* **2024**, *4*, 556–565, doi:10.3390/macromol4030033.
322. Siegel, M.M. Early Discovery Drug Screening Using Mass Spectrometry. *Curr Top Med Chem* **2002**, *2*, 13–33, doi:10.2174/1568026023394551.
323. Ribaudo, G.; Scalabrin, M.; Pavan, V.; Fabris, D.; Zagotto, G. Constrained Bisantrene Derivatives as G-Quadruplex Binders. *Arkivoc* **2016**, *2016*, 145–160, doi:10.3998/ark.5550190.p009.394.
324. Ongaro, A.; Desiderati, G.; Oselladore, E.; Auricchio, D.; Memo, M.; Ribaudo, G.; Sissi, C.; Gianoncelli, A. Amino-Acid-Anthraquinone Click Chemistry Conjugates Selectively Target Human Telomeric G-Quadruplexes. *ChemMedChem* **2022**, *17*, e202100665, doi:10.1002/cmdc.202100665.
325. Cubrilovic, D.; Biela, A.; Sielaff, F.; Steinmetzer, T.; Klebe, G.; Zenobi, R. Quantifying Protein-Ligand Binding Constants Using Electrospray Ionization Mass Spectrometry: A Systematic Binding Affinity Study of a Series of Hydrophobically Modified Trypsin Inhibitors. *J Am Soc Mass Spectrom* **2012**, *23*, 1768–1777, doi:10.1007/s13361-012-0451-6.

326. Ribaudo, G.; Ongaro, A.; Zagotto, G.; Memo, M.; Gianoncelli, A. Photoactivated Semi-Synthetic Derivative of Osajin Selectively Interacts with G-Quadruplex DNA. *Natural Product Research* **2022**, *36*, 405–410, doi:10.1080/14786419.2020.1768087.
327. Mazzitelli, C.L.; Brodbelt, J.S.; Kern, J.T.; Rodriguez, M.; Kerwin, S.M. Evaluation of Binding of Perylene Diimide and Benzannulated Perylene Diimide Ligands to DNA by Electrospray Ionization Mass Spectrometry. *J Am Soc Mass Spectrom* **2006**, *17*, 593–604, doi:10.1016/j.jasms.2005.12.011.
328. Ribaudo, G.; Ongaro, A.; Zagotto, G.; Memo, M.; Gianoncelli, A. Photoactivated Semi-Synthetic Derivative of Osajin Selectively Interacts with G-Quadruplex DNA. *Natural Product Research* **2022**, *36*, 405–410, doi:10.1080/14786419.2020.1768087.
329. Torvinen, M.; Kalenius, E.; Sansone, F.; Casnati, A.; Jänis, J. Noncovalent Complexation of Monoamine Neurotransmitters and Related Ammonium Ions by Tetramethoxy Tetraglucosylcalix[4]Arene. *J. Am. Soc. Mass Spectrom.* **2012**, *23*, 359–365, doi:10.1007/s13361-011-0289-3.
330. Gu, W.; Lin, Z.; Zhao, S.; Wang, G.; Shen, Z.; Liu, W.; Cai, Y.; Wang, K.; Wan, C.C.; Yan, T. Research Progress on G-Quadruplexes in Human Telomeres and Human Telomerase Reverse Transcriptase (hTERT) Promoter. *Oxid Med Cell Longev* **2022**, *2022*, 2905663, doi:10.1155/2022/2905663.
331. Xu, N.; Yang, H.; Cui, M.; Song, F.; Liu, Z.; Liu, S. Evaluation of Alkaloids Binding to the Parallel Quadruplex Structure [d(TGGGGT)]4 by Electrospray Ionization Mass Spectrometry. *Journal of Mass Spectrometry* **2012**, *47*, 694–700, doi:10.1002/jms.2997.
332. Pagano, B.; Amato, J.; Iaccarino, N.; Cingolani, C.; Zizza, P.; Biroccio, A.; Novellino, E.; Randazzo, A. Looking for Efficient G-Quadruplex Ligands: Evidence for Selective Stabilizing Properties and Telomere Damage by Drug-like Molecules. *ChemMedChem* **2015**, *10*, 640–649, doi:10.1002/cmdc.201402552.
333. Li, K.; Yatsunyk, L.; Neidle, S. Water Spines and Networks in G-Quadruplex Structures. *Nucleic Acids Res* **2021**, *49*, 519–528, doi:10.1093/nar/gkaa1177.
334. Proceedings of the 2006 ACM/IEEE Conference on Supercomputing Available online: https://dl.acm.org/doi/proceedings/10.1145/1188455 (accessed on 22 October 2025).
335. Wang, J.; Cieplak, P.; Kollman, P.A. How well does a restrained electrostatic potential (RESP) model perform in calculating conformational energies of organic and biological molecules? *Journal of Computational Chemistry* **2000**, *21*, 1049–1074, doi:10.1002/1096-987X(200009)21:12%3C1049::AID-JCC3%3E3.0.CO;2-F.
336. Zgarbová, M.; Šponer, J.; Otyepka, M.; Cheatham, T.E.; Galindo-Murillo, R.; Jurečka, P. Refinement of the Sugar-Phosphate Backbone Torsion Beta for AMBER Force Fields Improves the Description of Z- and B-DNA. *J Chem Theory Comput* **2015**, *11*, 5723–5736, doi:10.1021/acs.jctc.5b00716.
337. Pérez, A.; Marchán, I.; Svozil, D.; Sponer, J.; Cheatham, T.E.; Laughton, C.A.; Orozco, M. Refinement of the AMBER Force Field for Nucleic Acids: Improving the

Description of Alpha/Gamma Conformers. *Biophys J* **2007**, *92*, 3817–3829, doi:10.1529/biophysj.106.097782.
338. Martino, L.; Virno, A.; Pagano, B.; Virgilio, A.; Di Micco, S.; Galeone, A.; Giancola, C.; Bifulco, G.; Mayol, L.; Randazzo, A. Structural and Thermodynamic Studies of the Interaction of Distamycin A with the Parallel Quadruplex Structure [d(TGGGGT)]4. *J. Am. Chem. Soc.* **2007**, *129*, 16048–16056, doi:10.1021/ja075710k.
339. Ribaudo, G.; Anyanwu, M.; Giannangeli, M.; Oselladore, E.; Ongaro, A.; Memo, M.; Gianoncelli, A. G-Quadruplex DNA as a Macromolecular Target for Semi-Synthetic Isoflavones Bearing B-Ring Tosylation. *Macromol* **2024**, *4*, 556–565, doi:10.3390/macromol4030033.
340. Kozurková, M.; Sabolová, D.; Paulíková, H.; Janovec, L.; Kristian, P.; Bajdichová, M.; Busa, J.; Podhradský, D.; Imrich, J. DNA Binding Properties and Evaluation of Cytotoxic Activity of 9,10-Bis-N-Substituted (Aminomethyl)Anthracenes. *Int J Biol Macromol* **2007**, *41*, 415–422, doi:10.1016/j.ijbiomac.2007.05.013.
341. Folini, M.; Pivetta, C.; Zagotto, G.; De Marco, C.; Palumbo, M.; Zaffaroni, N.; Sissi, C. Remarkable Interference with Telomeric Function by a G-Quadruplex Selective Bisantrene Regioisomer. *Biochem Pharmacol* **2010**, *79*, 1781–1790, doi:10.1016/j.bcp.2010.02.018.
342. Gama, S.; Rodrigues, I.; Mendes, F.; Santos, I.C.; Gabano, E.; Klejevskaja, B.; Gonzalez-Garcia, J.; Ravera, M.; Vilar, R.; Paulo, A. Anthracene-Terpyridine Metal Complexes as New G-Quadruplex DNA Binders. *Journal of Inorganic Biochemistry* **2016**, *160*, 275–286, doi:10.1016/j.jinorgbio.2016.04.002.
343. Coban, T.; Robertson, C.; Schwikkard, S.; Singer, R.; LeGresley, A. Synthesis and Evaluation of Bis(Imino)Anthracene Derivatives as G-Quadruplex Ligands. *RSC Med. Chem.* **2021**, *12*, 751–757, doi:10.1039/D0MD00428F.
344. Asamitsu, S.; Bando, T.; Sugiyama, H. Ligand Design to Acquire Specificity to Intended G-Quadruplex Structures. *Chemistry – A European Journal* **2019**, *25*, 417–430, doi:10.1002/chem.201802691.
345. Ongaro, A.; Ribaudo, G.; Zagotto, G.; Memo, M.; Gianoncelli, A. Synthesis via A3 Coupling Reaction of Anthracene-Propargylamine as a New Scaffold for the Interaction with DNA. *ChemistrySelect* **2019**, *4*, 13138–13142, doi:10.1002/slct.201902975.
346. Sanchez-Martin, V.; Lopez-Pujante, C.; Soriano-Rodriguez, M.; Garcia-Salcedo, J.A. An Updated Focus on Quadruplex Structures as Potential Therapeutic Targets in Cancer. *Int J Mol Sci* **2020**, *21*, 8900, doi:10.3390/ijms21238900.
347. Figueiredo, J.; Djavaheri-Mergny, M.; Ferret, L.; Mergny, J.-L.; Cruz, C. Harnessing G-Quadruplex Ligands for Lung Cancer Treatment: A Comprehensive Overview. *Drug Discovery Today* **2023**, *28*, 103808, doi:10.1016/j.drudis.2023.103808.

348. Ribaudo, G.; Ongaro, A.; Oselladore, E.; Zagotto, G.; Memo, M.; Gianoncelli, A. 9,10-Bis[(4-(2-Hydroxyethyl)Piperazine-1-Yl)Prop-2-Yne-1-Yl]Anthracene: Synthesis and G-Quadruplex Selectivity. *Molbank* **2020**, *2020*, M1138, doi:10.3390/M1138.
349. Dai, J.; Carver, M.; Punchihewa, C.; Jones, R.A.; Yang, D. Structure of the Hybrid-2 Type Intramolecular Human Telomeric G-Quadruplex in K+ Solution: Insights into Structure Polymorphism of the Human Telomeric Sequence. *Nucleic Acids Res* **2007**, *35*, 4927–4940, doi:10.1093/nar/gkm522.
350. Mayer, M.; Meyer, B. Characterization of Ligand Binding by Saturation Transfer Difference NMR Spectroscopy. *Angewandte Chemie International Edition* **1999**, *38*, 1784–1788, doi:10.1002/(SICI)1521-3773(19990614)38:12%3C1784::AID-ANIE1784%3E3.0.CO;2-Q.
351. Di Micco, S.; Bassarello, C.; Bifulco, G.; Riccio, R.; Gomez-Paloma, L. Differential-Frequency Saturation Transfer Difference NMR Spectroscopy Allows the Detection of Different Ligand–DNA Binding Modes. *Angewandte Chemie International Edition* **2006**, *45*, 224–228, doi:10.1002/anie.200501344.
352. Maity, S.; Gundampati, R.K.; Suresh Kumar, T.K. NMR Methods to Characterize Protein-Ligand Interactions. *Natural Product Communications* **2019**, *14*, 1934578X19849296, doi:10.1177/1934578X19849296.
353. Raingeval, C.; Cala, O.; Brion, B.; Le Borgne, M.; Hubbard, R.E.; Krimm, I. 1D NMR WaterLOGSY as an Efficient Method for Fragment-Based Lead Discovery. *Journal of Enzyme Inhibition and Medicinal Chemistry* **2019**, *34*, 1218–1225, doi:10.1080/14756366.2019.1636235.
354. Anyanwu, M.; Giannangeli, M.; Fan, X.-X.; Coghi, P.; Ribaudo, G.; Gianoncelli, A. 9,10-Bis[(4-(2-Hydroxyethyl)Piperazine-1-Yl)Prop2-Yne-1-Yl]Anthracene: G-Quadruplex Selectivity and Anticancer Activity. *ACS Medicinal Chemistry Letters* **2024**, *15*, 1615–1619, doi:10.1021/acsmedchemlett.4c00340.
355. Maji, B.; Kumar, K.; Muniyappa, K.; Bhattacharya, S. New Dimeric Carbazole–Benzimidazole Mixed Ligands for the Stabilization of Human Telomeric G-Quadruplex DNA and as Telomerase Inhibitors. A Remarkable Influence of the Spacer. *Org. Biomol. Chem.* **2015**, *13*, 8335–8348, doi:10.1039/C5OB00675A.
356. Pasangha, C.H.; Kishore, N. Unveiling the Multifaceted Interactions of Antitumor Drug Mitoxantrone with Ct-DNA through Biophysical and in Silico Studies. *International Journal of Biological Macromolecules* **2024**, *280*, 135813, doi:10.1016/j.ijbiomac.2024.135813.
357. Kreft, D.; Wang, Y.; Rattay, M.; Toensing, K.; Anselmetti, D. Binding Mechanism of Anti-Cancer Chemotherapeutic Drug Mitoxantrone to DNA Characterized by Magnetic Tweezers. *J Nanobiotechnol* **2018**, *16*, 56, doi:10.1186/s12951-018-0381-y.
358. Parkinson, G.N.; Lee, M.P.H.; Neidle, S. Crystal Structure of Parallel Quadruplexes from Human Telomeric DNA. *Nature* **2002**, *417*, 876–880, doi:10.1038/nature755.

359. Dai, J.; Carver, M.; Punchihewa, C.; Jones, R.A.; Yang, D. Structure of the Hybrid-2 Type Intramolecular Human Telomeric G-Quadruplex in K+ Solution: Insights into Structure Polymorphism of the Human Telomeric Sequence. *Nucleic Acids Res.* **2007**, *35*, 4927–4940, doi:10.1093/nar/gkm522.
360. Wang, Y.; Patel, D.J. Solution Structure of the Human Telomeric Repeat d[AG3(T2AG3)3] G-Tetraplex. *Structure* **1993**, *1*, 263–282, doi:10.1016/0969-2126(93)90015-9.
361. Giannangeli, M.; Ponte, N.D.; Anyanwu, M.; Romanello, M.B.; Mucenji, E.; Rigo, R.; Ribaudo, G.; Sissi, C.; Gianoncelli, A. Enhancing G-Quadruplex Binding: Rational Design and Biophysical Evaluation of Dimeric Ligands. *Chemistry – A European Journal n/a*, e03128, doi:10.1002/chem.202503128.
362. Lamptey, R.N.L.; Chaulagain, B.; Trivedi, R.; Gothwal, A.; Layek, B.; Singh, J. A Review of the Common Neurodegenerative Disorders: Current Therapeutic Approaches and the Potential Role of Nanotherapeutics. *Int J Mol Sci* **2022**, *23*, 1851, doi:10.3390/ijms23031851.
363. Hague, S.M. Neurodegenerative Disorders: Parkinson's Disease and Huntington's Disease. *Journal of Neurology, Neurosurgery & Psychiatry* **2005**, *76*, 1058–1063, doi:10.1136/jnnp.2004.060186.
364. Li, Q.; Liao, Q.; Qi, S.; Huang, H.; He, S.; Lyu, W.; Liang, J.; Qin, H.; Cheng, Z.; Yu, F.; et al. Opportunities and Perspectives of Small Molecular Phosphodiesterase Inhibitors in Neurodegenerative Diseases. *European Journal of Medicinal Chemistry* **2024**, *271*, 116386, doi:10.1016/j.ejmech.2024.116386.
365. Delhaye, S.; Bardoni, B. Role of Phosphodiesterases in the Pathophysiology of Neurodevelopmental Disorders. *Mol Psychiatry* **2021**, *26*, 4570–4582, doi:10.1038/s41380-020-00997-9.
366. Ahammed, M.S.; Wang, X. Promoting Proteostasis by cAMP/PKA and cGMP/PKG. *Trends in Molecular Medicine* **2025**, *31*, 224–239, doi:10.1016/j.molmed.2024.10.006.
367. Li, Z.-H.; Cui, D.; Qiu, C.-J.; Song, X.-J. Cyclic Nucleotide Signaling in Sensory Neuron Hyperexcitability and Chronic Pain after Nerve Injury. *Neurobiology of Pain* **2019**, *6*, 100028, doi:10.1016/j.ynpai.2019.100028.
368. Bollen, E.; Puzzo, D.; Rutten, K.; Privitera, L.; De Vry, J.; Vanmierlo, T.; Kenis, G.; Palmeri, A.; D'Hooge, R.; Balschun, D.; et al. Improved Long-Term Memory via Enhancing cGMP-PKG Signaling Requires cAMP-PKA Signaling. *Neuropsychopharmacol* **2014**, *39*, 2497–2505, doi:10.1038/npp.2014.106.
369. Kim, J.; Kaang, B.-K. Cyclic AMP Response Element-Binding Protein (CREB) Transcription Factor in Astrocytic Synaptic Communication. *Front. Synaptic Neurosci.* **2023**, *14*, 1059918, doi:10.3389/fnsyn.2022.1059918.
370. Gupta, A.K.; Gupta, S.; Mehan, S.; Khan, Z.; Das Gupta, G.; Narula, A.S. Exploring the Connection Between BDNF/TrkB and AC/cAMP/PKA/CREB Signaling Pathways: Potential for Neuroprotection and Therapeutic Targets for

Neurological Disorders. *Mol Neurobiol* **2025**, *62*, 14627–14659, doi:10.1007/s12035-025-05001-5.
371. Hutson, P.H.; Finger, E.N.; Magliaro, B.C.; Smith, S.M.; Converso, A.; Sanderson, P.E.; Mullins, D.; Hyde, L.A.; Eschle, B.K.; Turnbull, Z.; et al. The Selective Phosphodiesterase 9 (PDE9) Inhibitor PF-04447943 (6-[(3S,4S)-4-Methyl-1-(Pyrimidin-2-Ylmethyl)Pyrrolidin-3-Yl]-1-(Tetrahydro-2H-Pyran-4-Yl)-1,5-Dihydro-4H-Pyrazolo[3,4-d]Pyrimidin-4-One) Enhances Synaptic Plasticity and Cognitive Function in Rodents. *Neuropharmacology* **2011**, *61*, 665–676, doi:10.1016/j.neuropharm.2011.05.009.
372. Blokland, A.; Heckman, P.; Vanmierlo, T.; Schreiber, R.; Paes, D.; Prickaerts, J. Phosphodiesterase Type 4 Inhibition in CNS Diseases. *Trends in Pharmacological Sciences* **2019**, *40*, 971–985, doi:10.1016/j.tips.2019.10.006.
373. AlRuwaili, R.; Al-kuraishy, H.M.; Alruwaili, M.; Khalifa, A.K.; Alexiou, A.; Papadakis, M.; Saad, H.M.; Batiha, G.E.-S. The Potential Therapeutic Effect of Phosphodiesterase 5 Inhibitors in the Acute Ischemic Stroke (AIS). *Mol Cell Biochem* **2024**, *479*, 1267–1278, doi:10.1007/s11010-023-04793-1.
374. Bender, A.T.; Beavo, J.A. Cyclic Nucleotide Phosphodiesterases: Molecular Regulation to Clinical Use. *Pharmacological Reviews* **2006**, *58*, 488–520, doi:10.1124/pr.58.3.5.
375. Fisher, D.A.; Smith, J.F.; Pillar, J.S.; Denis, S.H.St.; Cheng, J.B. Isolation and Characterization of PDE9A, a Novel Human cGMP-Specific Phosphodiesterase. *Journal of Biological Chemistry* **1998**, *273*, 15559–15564, doi:10.1074/jbc.273.25.15559.
376. Soderling, S.H.; Bayuga, S.J.; Beavo, J.A. Identification and Characterization of a Novel Family of Cyclic Nucleotide Phosphodiesterases. *Journal of Biological Chemistry* **1998**, *273*, 15553–15558, doi:10.1074/jbc.273.25.15553.
377. Zheng, L.; Zhou, Z.-Z. An Overview of Phosphodiesterase 9 Inhibitors: Insights from Skeletal Structure, Pharmacophores, and Therapeutic Potential. *European Journal of Medicinal Chemistry* **2023**, *259*, 115682, doi:10.1016/j.ejmech.2023.115682.
378. Singh, N.; Patra, S. Phosphodiesterase 9: Insights from Protein Structure and Role in Therapeutics. *Life Sciences* **2014**, *106*, 1–11, doi:10.1016/j.lfs.2014.04.007.
379. Vardigan, J.D.; Converso, A.; Hutson, P.H.; Uslaner, J.M. The Selective Phosphodiesterase 9 (PDE9) Inhibitor PF-04447943 Attenuates a Scopolamine-Induced Deficit in a Novel Rodent Attention Task. *J. Neurogenet.* **2011**, *25*, 120–126, doi:10.3109/01677063.2011.630494.
380. You, J.; Liu, X.; Bao, Y.; Shen, Z.; Wang, Q.; He, G.; Lu, J.; Zhang, J.; Chen, J.; Liu, P. A Novel Phosphodiesterase 9A Inhibitor LW33 Protects against Ischemic Stroke through the cGMP/PKG/CREB Pathway. *European Journal of Pharmacology* **2022**, *925*, 174987, doi:10.1016/j.ejphar.2022.174987.
381. Tropea, M.R.; Gulisano, W.; Vacanti, V.; Arancio, O.; Puzzo, D.; Palmeri, A. Nitric Oxide/cGMP/CREB Pathway and Amyloid-Beta Crosstalk: From Physiology

to Alzheimer's Disease. *Free Radical Biology and Medicine* **2022**, *193*, 657–668, doi:10.1016/j.freeradbiomed.2022.11.022.
382. Saravani, R.; Karami-Tehrani, F.; Hashemi, M.; Aghaei, M.; Edalat, R. Inhibition of Phosphodiestrase 9 Induces c GMP Accumulation and Apoptosis in Human Breast Cancer Cell Lines, MCF -7 and MDA - MB -468. *Cell Proliferation* **2012**, *45*, 199–206, doi:10.1111/j.1365-2184.2012.00819.x.
383. Rentero, C.; Monfort, A.; Puigdomènech, P. Identification and Distribution of Different mRNA Variants Produced by Differential Splicing in the Human Phosphodiesterase 9A Gene. *Biochemical and Biophysical Research Communications* **2003**, *301*, 686–692, doi:10.1016/S0006-291X(03)00021-4.
384. Wang, P.; Wu, P.; Egan, R.W.; Billah, M.M. Identification and Characterization of a New Human Type 9 cGMP-Specific Phosphodiesterase Splice Variant (PDE9A5). *Gene* **2003**, *314*, 15–27, doi:10.1016/S0378-1119(03)00733-9.
385. Lakics, V.; Karran, E.H.; Boess, F.G. Quantitative Comparison of Phosphodiesterase mRNA Distribution in Human Brain and Peripheral Tissues. *Neuropharmacology* **2010**, *59*, 367–374, doi:10.1016/j.neuropharm.2010.05.004.
386. Hou, J.; Xu, J.; Liu, M.; Zhao, R.; Luo, H.-B.; Ke, H. Structural Asymmetry of Phosphodiesterase-9, Potential Protonation of a Glutamic Acid, and Role of the Invariant Glutamine. *PLoS ONE* **2011**, *6*, e18092, doi:10.1371/journal.pone.0018092.
387. Huai, Q.; Wang, H.; Zhang, W.; Colman, R.W.; Robinson, H.; Ke, H. Crystal Structure of Phosphodiesterase 9 Shows Orientation Variation of Inhibitor 3-Isobutyl-1-Methylxanthine Binding. *Proc. Natl. Acad. Sci. U.S.A.* **2004**, *101*, 9624–9629, doi:10.1073/pnas.0401120101.
388. Verhoest, P.R.; Fonseca, K.R.; Hou, X.; Proulx-LaFrance, C.; Corman, M.; Helal, C.J.; Claffey, M.M.; Tuttle, J.B.; Coffman, K.J.; Liu, S.; et al. Design and Discovery of 6-[(3S,4S)-4-Methyl-1-(Pyrimidin-2-Ylmethyl)Pyrrolidin-3-Yl]-1-(Tetrahydro-2H-Pyran-4-Yl)-1,5-Dihydro-4H-Pyrazolo[3,4-d]Pyrimidin-4-One (PF-04447943), a Selective Brain Penetrant PDE9A Inhibitor for the Treatment of Cognitive Disorders. *J. Med. Chem.* **2012**, *55*, 9045–9054, doi:10.1021/jm3007799.
389. Zhang, C.; Zhou, Q.; Wu, X.-N.; Huang, Y.-D.; Zhou, J.; Lai, Z.; Wu, Y.; Luo, H.-B. Discovery of Novel PDE9A Inhibitors with Antioxidant Activities for Treatment of Alzheimer's Disease. *J. Enzyme Inhib. Med. Chem.* **2018**, *33*, 260–270, doi:10.1080/14756366.2017.1412315.
390. Li, J.; Liu, C.-N.; Wei, N.; Li, X.-D.; Liu, Y.-Y.; Yang, R.; Jia, Y.-J. Protective Effects of BAY 73-6691, a Selective Inhibitor of Phosphodiesterase 9, on Amyloid-β Peptides-Induced Oxidative Stress in in-Vivo and in-Vitro Models of Alzheimer's Disease. *Brain Research* **2016**, *1642*, 327–335, doi:10.1016/j.brainres.2016.04.011.
391. Boland, K.; Moschetti, V.; Dansirikul, C.; Pichereau, S.; Gheyle, L.; Runge, F.; Zimdahl-Gelling, H.; Sand, M. A Phase I, Randomized, Proof-of-clinical-mechanism Study Assessing the Pharmacokinetics and Pharmacodynamics of the Oral PDE9A Inhibitor BI 409306 in Healthy Male Volunteers. *Human Psychopharmacology* **2017**, *32*, e2569, doi:10.1002/hup.2569.

392. Zhang, P.; Jiang, M.-Y.; Le, M.-L.; Zhang, B.; Zhou, Q.; Wu, Y.; Zhang, C.; Luo, H.-B. Design, Synthesis and Evaluation of Pyrazolopyrimidinone Derivatives as Novel PDE9A Inhibitors for Treatment of Alzheimer's Disease. *Bioorganic & Medicinal Chemistry Letters* **2020**, *30*, 127254, doi:10.1016/j.bmcl.2020.127254.
393. Ribaudo, G.; Landucci, E.; Giannangeli, M.; Mazzantini, C.; Maccarinelli, G.; Mastinu, A.; Bonini, S.A.; Memo, M.; Pellegrini-Giampietro, D.E.; Gianoncelli, A. Virtual Screening and in Vitro Experiments Highlight Cannabidiol as a Drug-like Phosphodiesterase 9 Inhibitor. *European Journal of Neuroscience* **2023**, *57*, 1954–1965, doi:10.1111/ejn.15869.
394. Singh, N.; Saravanan, P.; Thakur, M.S.; Patra, S. Development of Xanthine Based Inhibitors Targeting Phosphodiesterase 9A. *LDDD* **2017**, *14*, 1122–1137, doi:10.2174/1570180813666161102125423.
395. Lipinski, C.A. Drug-like Properties and the Causes of Poor Solubility and Poor Permeability. *Journal of Pharmacological and Toxicological Methods* **2000**, *44*, 235–249, doi:10.1016/S1056-8719(00)00107-6.
396. Prickaerts, J.; Heckman, P.R.A.; Blokland, A. Investigational Phosphodiesterase Inhibitors in Phase I and Phase II Clinical Trials for Alzheimer's Disease. *Expert Opinion on Investigational Drugs* **2017**, *26*, 1033–1048, doi:10.1080/13543784.2017.1364360.
397. Kumar, A.; Sharma, V.; Singh, V.P.; Kaundal, M.; Gupta, M.K.; Bariwal, J.; Deshmukh, R. Herbs to Curb Cyclic Nucleotide Phosphodiesterase and Their Potential Role in Alzheimer's Disease. *Mechanisms of Ageing and Development* **2015**, *149*, 75–87, doi:10.1016/j.mad.2015.05.009.
398. Rahimi, R.; Ghiasi, S.; Azimi, H.; Fakhari, S.; Abdollahi, M. A Review of the Herbal Phosphodiesterase Inhibitors; Future Perspective of New Drugs. *Cytokine* **2010**, *49*, 123–129, doi:10.1016/j.cyto.2009.11.005.
399. Zanforlin, E.; Zagotto, G.; Ribaudo, G. The Medicinal Chemistry of Natural and Semisynthetic Compounds against Parkinson's and Huntington's Diseases. *ACS Chem. Neurosci.* **2017**, *8*, 2356–2368, doi:10.1021/acschemneuro.7b00283.
400. Temkitthawon, P.; Viyoch, J.; Limpeanchob, N.; Pongamornkul, W.; Sirikul, C.; Kumpila, A.; Suwanborirux, K.; Ingkaninan, K. Screening for Phosphodiesterase Inhibitory Activity of Thai Medicinal Plants. *Journal of Ethnopharmacology* **2008**, *119*, 214–217, doi:10.1016/j.jep.2008.05.034.
401. Pohanka, M. The Perspective of Caffeine and Caffeine Derived Compounds in Therapy. *BLL* **2015**, *116*, 520–530, doi:10.4149/BLL_2015_106.
402. Ribaudo, G.; Pagano, M.A.; Pavan, V.; Redaelli, M.; Zorzan, M.; Pezzani, R.; Mucignat-Caretta, C.; Vendrame, T.; Bova, S.; Zagotto, G. Semi-Synthetic Derivatives of Natural Isoflavones from *Maclura Pomifera* as a Novel Class of PDE-5A Inhibitors. *Fitoterapia* **2015**, *105*, 132–138, doi:10.1016/j.fitote.2015.06.020.
403. Ongaro, A.; Zagotto, G.; Memo, M.; Gianoncelli, A.; Ribaudo, G. Natural Phosphodiesterase 5 (PDE5) Inhibitors: A Computational Approach. *Natural Product Research* **2021**, *35*, 1648–1653, doi:10.1080/14786419.2019.1619726.

404. Oselladore, E.; Ongaro, A.; Zagotto, G.; Memo, M.; Ribaudo, G.; Gianoncelli, A. Combinatorial Library Generation, Molecular Docking and Molecular Dynamics Simulations for Enhancing the Isoflavone Scaffold in Phosphodiesterase Inhibition. *New J. Chem.* **2020**, *44*, 19472–19488, doi:10.1039/D0NJ02537B.
405. Ribaudo, G.; Memo, M.; Gianoncelli, A. A Perspective on Natural and Nature-Inspired Small Molecules Targeting Phosphodiesterase 9 (PDE9): Chances and Challenges against Neurodegeneration. *Pharmaceuticals* **2021**, *14*, 58, doi:10.3390/ph14010058.
406. Ribaudo, G.; Coghi, P.; Zanforlin, E.; Law, B.Y.K.; Wu, Y.Y.J.; Han, Y.; Qiu, A.C.; Qu, Y.Q.; Zagotto, G.; Wong, V.K.W. Semi-Synthetic Isoflavones as BACE-1 Inhibitors against Alzheimer's Disease. *Bioorganic Chemistry* **2019**, *87*, 474–483, doi:10.1016/j.bioorg.2019.03.034.
407. Berman, H.M.; Westbrook, J.; Feng, Z.; Gilliland, G.; Bhat, T.N.; Weissig, H.; Shindyalov, I.N.; Bourne, P.E. The Protein Data Bank. *Nucleic Acids Research* **2000**, *28*, 235–242, doi:10.1093/nar/28.1.235.
408. Kuzmanic, A.; Zagrovic, B. Determination of Ensemble-Average Pairwise Root Mean-Square Deviation from Experimental B-Factors. *Biophysical Journal* **2010**, *98*, 861–871, doi:10.1016/j.bpj.2009.11.011.
409. Shao, Y.; Huang, M.; Cui, W.; Feng, L.-J.; Wu, Y.; Cai, Y.; Li, Z.; Zhu, X.; Liu, P.; Wan, Y.; et al. Discovery of a Phosphodiesterase 9A Inhibitor as a Potential Hypoglycemic Agent. *J. Med. Chem.* **2014**, *57*, 10304–10313, doi:Sivakumar%20et%20al%202021.
410. Sivakumar, D.; Mudedla, S.; Jang, S.; Kim, H.; Park, H.; Choi, Y.; Oh, J.; Wu, S. Computational Study on Selective PDE9 Inhibitors on PDE9-Mg/Mg, PDE9-Zn/Mg, and PDE9-Zn/Zn Systems. *Biomolecules* **2021**, *11*, 709, doi:10.3390/biom11050709.
411. Jiang, A.; Anyanwu, M.; Leong, K.; Li, J.; Gianoncelli, A.; Coghi, P.; Ribaudo, G. 3-[(1H-Benzo[d][1,2,3]Triazol-1-Yl)Oxy]Propyl 9-Hydroxy-5a,5b,8,8,11a-Pentamethyl-1-(Prop-1-En-2-Yl)Icosahydro-3aH-Cyclopenta[a]Chrysene-3a-Carboxylate. *MolBank* **2022**, *2022*, doi:10.3390/M1419.
412. Patel, N.S.; Klett, J.; Pilarzyk, K.; Lee, D.I.; Kass, D.; Menniti, F.S.; Kelly, M.P. Identification of New PDE9A Isoforms and How Their Expression and Subcellular Compartmentalization in the Brain Change across the Life Span. *Neurobiology of Aging* **2018**, *65*, 217–234, doi:10.1016/j.neurobiolaging.2018.01.019.
413. Wang, P.; Li, Z.; Cai, S.; Li, J.; He, P.; Huang, Y.; Feng, G.; Luo, H.; Chen, S.; Liu, P. C33(S), a Novel PDE9A Inhibitor, Protects against Rat Cardiac Hypertrophy through Upregulating cGMP Signaling. *Acta Pharmacol Sin* **2017**, *38*, 1257–1268, doi:10.1038/aps.2017.38.
414. Landucci, E.; Mazzantini, C.; Lana, D.; Calvani, M.; Magni, G.; Giovannini, M.G.; Pellegrini-Giampietro, D.E. Cannabidiol Inhibits Microglia Activation and Mitigates Neuronal Damage Induced by Kainate in an In-Vitro Seizure Model. *Neurobiology of Disease* **2022**, *174*, 105895, doi:10.1016/j.nbd.2022.105895.

415. Van Staveren, W.C.G.; Steinbusch, H.W.M.; Markerink-van Ittersum, M.; Behrends, S.; De Vente, J. Species Differences in the Localization of cGMP-producing and NO-responsive Elements in the Mouse and Rat Hippocampus Using cGMP Immunocytochemistry. *Eur J of Neuroscience* **2004**, *19*, 2155–2168, doi:10.1111/j.0953-816X.2004.03327.x.
416. Landucci, E.; Mazzantini, C.; Buonvicino, D.; Pellegrini-Giampietro, D.E.; Bergonzi, M.C. Neuroprotective Effects of Thymoquinone by the Modulation of ER Stress and Apoptotic Pathway in In Vitro Model of Excitotoxicity. *Molecules* **2021**, *26*, 1592, doi:10.3390/molecules26061592.
417. Landucci, E.; Ribaudo, G.; Anyanwu, M.; Oselladore, E.; Giannangeli, M.; Mazzantini, C.; Lana, D.; Giovannini, M.G.; Memo, M.; Pellegrini-Giampietro, D.E.; et al. Virtual Screening-Accelerated Discovery of a Phosphodiesterase 9 Inhibitor with Neuroprotective Effects in the Kainate Toxicity In Vitro Model. *ACS Chemical Neuroscience* **2023**, *14*, 3826–3838, doi:10.1021/acschemneuro.3c00431.
418. Lu, C.; Wu, C.; Ghoreishi, D.; Chen, W.; Wang, L.; Damm, W.; Ross, G.A.; Dahlgren, M.K.; Russell, E.; Von Bargen, C.D.; et al. OPLS4: Improving Force Field Accuracy on Challenging Regimes of Chemical Space. *J. Chem. Theory Comput.* **2021**, *17*, 4291–4300, doi:10.1021/acs.jctc.1c00302.
419. Shelley, J.C.; Cholleti, A.; Frye, L.L.; Greenwood, J.R.; Timlin, M.R.; Uchimaya, M. Epik: A Software Program for pK a Prediction and Protonation State Generation for Drug-like Molecules. *J Comput Aided Mol Des* **2007**, *21*, 681–691, doi:10.1007/s10822-007-9133-z.
420. Bowers, K.J.; Sacerdoti, F.D.; Salmon, J.K.; Shan, Y.; Shaw, D.E.; Chow, E.; Xu, H.; Dror, R.O.; Eastwood, M.P.; Gregersen, B.A.; et al. Molecular Dynamics--- Scalable Algorithms for Molecular Dynamics Simulations on Commodity Clusters. In Proceedings of the Proceedings of the 2006 ACM/IEEE conference on Supercomputing - SC '06; ACM Press: Tampa, Florida, 2006; p. 84.
421. Gerace, E.; Landucci, E.; Scartabelli, T.; Moroni, F.; Pellegrini-Giampietro, D.E. Rat Hippocampal Slice Culture Models for the Evaluation of Neuroprotective Agents. In *Neurotrophic Factors: Methods and Protocols*; Skaper, S.D., Ed.; Humana Press: Totowa, NJ, 2012; pp. 343–354 ISBN 978-1-61779-536-7.
422. Holopainen, I. Mechanisms of Kainate-Induced Region-Specific Neuronal Death in Immature Organotypic Hippocampal Slice Cultures. *Neurochemistry International* **2004**, *45*, 1–10, doi:10.1016/j.neuint.2004.01.005.
423. Laurino, A.; Landucci, E.; Resta, F.; De Siena, G.; Pellegrini-Giampietro, D.E.; Masi, A.; Mannaioni, G.; Raimondi, L. Anticonvulsant and Neuroprotective Effects of the Thyroid Hormone Metabolite 3-Iodothyroacetic Acid. *Thyroid* **2018**, *28*, 1387–1397, doi:10.1089/thy.2017.0506.
424. Landucci, E.; Mazzantini, C.; Calvani, M.; Pellegrini-Giampietro, D.E.; Bergonzi, M.C. Evaluation of Conventional and Hyaluronic Acid-Coated Thymoquinone Liposomes in an In Vitro Model of Dry Eye. *Pharmaceutics* **2023**, *15*, 578, doi:10.3390/pharmaceutics15020578.

425. Buonvicino, D.; Ranieri, G.; Pratesi, S.; Guasti, D.; Chiarugi, A. Neuroimmunological Characterization of a Mouse Model of Primary Progressive Experimental Autoimmune Encephalomyelitis and Effects of Immunosuppressive or Neuroprotective Strategies on Disease Evolution. *Experimental Neurology* **2019**, *322*, 113065, doi:10.1016/j.expneurol.2019.113065.
426. Lana, D.; Landucci, E.; Mazzantini, C.; Magni, G.; Pellegrini-Giampietro, D.E.; Giovannini, M.G. The Protective Effect of CBD in a Model of In Vitro Ischemia May Be Mediated by Agonism on TRPV2 Channel and Microglia Activation. *IJMS* **2022**, *23*, 12144, doi:10.3390/ijms232012144.
427. Landucci, E.; Mazzantini, C.; Lana, D.; Giovannini, M.G.; Pellegrini-Giampietro, D.E. Neuronal and Astrocytic Morphological Alterations Driven by Prolonged Exposure with Δ9-Tetrahydrocannabinol but Not Cannabidiol. *Toxics* **2022**, *10*, 48, doi:10.3390/toxics10020048.
428. Cerbai, F.; Lana, D.; Nosi, D.; Petkova-Kirova, P.; Zecchi, S.; Brothers, H.M.; Wenk, G.L.; Giovannini, M.G. The Neuron-Astrocyte-Microglia Triad in Normal Brain Ageing and in a Model of Neuroinflammation in the Rat Hippocampus. *PLoS ONE* **2012**, *7*, e45250, doi:10.1371/journal.pone.0045250.
429. Rombaut, B.; Kessels, S.; Schepers, M.; Tiane, A.; Paes, D.; Solomina, Y.; Piccart, E.; Hove, D.V.D.; Brône, B.; Prickaerts, J.; et al. PDE Inhibition in Distinct Cell Types to Reclaim the Balance of Synaptic Plasticity. *Theranostics* **2021**, *11*, 2080–2097, doi:10.7150/thno.50701.
430. Kroker, K.S.; Mathis, C.; Marti, A.; Cassel, J.-C.; Rosenbrock, H.; Dorner-Ciossek, C. PDE9A Inhibition Rescues Amyloid Beta-Induced Deficits in Synaptic Plasticity and Cognition. *Neurobiology of Aging* **2014**, *35*, 2072–2078, doi:10.1016/j.neurobiolaging.2014.03.023.
431. Kelly, M.P.; Nikolaev, V.O.; Gobejishvili, L.; Lugnier, C.; Hesslinger, C.; Nickolaus, P.; Kass, D.A.; Pereira de Vasconcelos, W.; Fischmeister, R.; Brocke, S.; et al. Cyclic Nucleotide Phosphodiesterases as Drug Targets. *Pharmacological Reviews* **2025**, *77*, 100042, doi:10.1016/j.pharmr.2025.100042.
432. Corradini, E.; Burgers, P.P.; Plank, M.; Heck, A.J.R.; Scholten, A. Huntingtin-Associated Protein 1 (HAP1) Is a cGMP-Dependent Kinase Anchoring Protein (GKAP) Specific for the cGMP-Dependent Protein Kinase Iβ Isoform. *J Biol Chem* **2015**, *290*, 7887–7896, doi:10.1074/jbc.M114.622613.
433. Ahmad, F.; Murata, T.; Shimizu, K.; Degerman, E.; Maurice, D.; Manganiello, V. Cyclic Nucleotide Phosphodiesterases: Important Signaling Modulators and Therapeutic Targets. *Oral Dis* **2015**, *21*, e25-50, doi:10.1111/odi.12275.
434. Pilz, R.B.; Casteel, D.E. Regulation of Gene Expression by Cyclic GMP. *Circ Res* **2003**, *93*, 1034–1046, doi:10.1161/01.RES.0000103311.52853.48.
435. Laudette, M.; Zuo, H.; Lezoualc'h, F.; Schmidt, M. Epac Function and cAMP Scaffolds in the Heart and Lung. *J Cardiovasc Dev Dis* **2018**, *5*, 9, doi:10.3390/jcdd5010009.

436. Liu, S.; Wang, S.; Gu, R.; Che, N.; Wang, J.; Cheng, J.; Yuan, Z.; Cheng, Y.; Liao, Y. The XPO1 Inhibitor KPT-8602 Ameliorates Parkinson's Disease by Inhibiting the NF-κB/NLRP3 Pathway. *Front Pharmacol* **2022**, *13*, 847605, doi:10.3389/fphar.2022.847605.
437. Nagel, D.J.; Aizawa, T.; Jeon, K.-I.; Liu, W.; Mohan, A.; Wei, H.; Miano, J.M.; Florio, V.A.; Gao, P.; Korshunov, V.A.; et al. Role of Nuclear Ca2+/Calmodulin-Stimulated Phosphodiesterase 1A in Vascular Smooth Muscle Cell Growth and Survival. *Circulation Research* **2006**, *98*, 777–784, doi:10.1161/01.RES.0000215576.27615.fd.
438. Martinez, J.M.; Shen, A.; Xu, B.; Jovanovic, A.; De Chabot, J.; Zhang, J.; Xiang, Y.K. Arrestin-Dependent Nuclear Export of Phosphodiesterase 4D Promotes GPCR-Induced Nuclear cAMP Signaling Required for Learning and Memory. *Sci. Signal.* **2023**, *16*, eade3380, doi:10.1126/scisignal.ade3380.
439. Landry, I.S.; Aluri, J.; Schuck, E.; Ino, M.; Horie, K.; Boyd, P.; Reyderman, L.; Lai, R. Phase 1 Single Ascending and Multiple Ascending Dose Studies of Phosphodiesterase-9 Inhibitor E2027: Confirmation of Target Engagement and Selection of Phase 2 Dose in Dementia With Lewy Bodies Trial. *Alzheimer Dis Assoc Disord* **2022**, *36*, 200–207, doi:10.1097/WAD.0000000000000515.
440. Landucci, E.; Ribaudo, G.; Anyanwu, M.; Oselladore, E.; Giannangeli, M.; Mazzantini, C.; Lana, D.; Giovannini, M.G.; Memo, M.; Pellegrini-Giampietro, D.E.; et al. Virtual Screening-Accelerated Discovery of a Phosphodiesterase 9 Inhibitor with Neuroprotective Effects in the Kainate Toxicity In Vitro Model. *ACS Chem. Neurosci.* **2023**, *14*, 3826–3838, doi:10.1021/acschemneuro.3c00431.
441. Ribaudo, G.; Giannangeli, M.; Anyanwu, M.; Gianoncelli, A. Phosphodiesterase 9 Localization in Cytoplasm and Nucleus: The Gateway to Selective Targeting in Neuroprotection? *Neural Regeneration Research* **2025**, *20*, 1701–1702, doi:10.4103/NRR.NRR-D-24-00373.
442. Miller, G. Is Pharma Running Out of Brainy Ideas? *Science* **2010**, *329*, 502–504, doi:10.1126/science.329.5991.502.
443. Abbott, A. Novartis to Shut Brain Research Facility. *Nature* **2011**, *480*, 161–162, doi:10.1038/480161a.
444. Gribkoff, V.K.; Kaczmarek, L.K. The Need for New Approaches in CNS Drug Discovery: Why Drugs Have Failed, and What Can Be Done to Improve Outcomes. *Neuropharmacology* **2017**, *120*, 11–19, doi:10.1016/j.neuropharm.2016.03.021.
445. Morofuji, Y.; Nakagawa, S. Drug Development for Central Nervous System Diseases Using In Vitro Blood-Brain Barrier Models and Drug Repositioning. *CPD* **2020**, *26*, 1466–1485, doi:10.2174/1381612826666200224112534.
446. Miller, K.D.; Fidler-Benaoudia, M.; Keegan, T.H.; Hipp, H.S.; Jemal, A.; Siegel, R.L. Cancer Statistics for Adolescents and Young Adults, 2020. *CA A Cancer J Clinicians* **2020**, *70*, 443–459, doi:10.3322/caac.21637.
447. Bazi Alahri, M.; Jibril Ibrahim, A.; Barani, M.; Arkaban, H.; Shadman, S.M.; Salarpour, S.; Zarrintaj, P.; Jaberi, J.; Turki Jalil, A. Management of Brain Cancer

and Neurodegenerative Disorders with Polymer-Based Nanoparticles as a Biocompatible Platform. *Molecules* **2023**, *28*, 841, doi:10.3390/molecules28020841.
448. Fayazi, N.; Sheykhhasan, M.; Soleimani Asl, S.; Najafi, R. Stem Cell-Derived Exosomes: A New Strategy of Neurodegenerative Disease Treatment. *Mol Neurobiol* **2021**, *58*, 3494–3514, doi:10.1007/s12035-021-02324-x.
449. Khalil, B.; Linsenmeier, M.; Smith, C.L.; Shorter, J.; Rossoll, W. Nuclear-Import Receptors as Gatekeepers of Pathological Phase Transitions in ALS/FTD. *Mol Neurodegeneration* **2024**, *19*, 8, doi:10.1186/s13024-023-00698-1.
450. Gregory, J.V.; Kadiyala, P.; Doherty, R.; Cadena, M.; Habeel, S.; Ruoslahti, E.; Lowenstein, P.R.; Castro, M.G.; Lahann, J. Systemic Brain Tumor Delivery of Synthetic Protein Nanoparticles for Glioblastoma Therapy. *Nat Commun* **2020**, *11*, 5687, doi:10.1038/s41467-020-19225-7.
451. Freeman, B.B.; Yang, L.; Rankovic, Z. Practical Approaches to Evaluating and Optimizing Brain Exposure in Early Drug Discovery. *European Journal of Medicinal Chemistry* **2019**, *182*, 111643, doi:10.1016/j.ejmech.2019.111643.
452. Martin, I. Prediction of Blood–Brain Barrier Penetration: Are We Missing the Point? *Drug Discovery Today* **2004**, *9*, 161–162, doi:10.1016/S1359-6446(03)02961-1.
453. Giacomini, K.M.; Huang, S.-M.; Tweedie, D.J.; Benet, L.Z.; Brouwer, K.L.R.; Chu, X.; Dahlin, A.; Evers, R.; Fischer, V.; Hillgren, K.M.; et al. Membrane Transporters in Drug Development. *Nat Rev Drug Discov* **2010**, *9*, 215–236, doi:10.1038/nrd3028.
454. Md, S.; Bhattmisra, S.K.; Zeeshan, F.; Shahzad, N.; Mujtaba, M.A.; Srikanth Meka, V.; Radhakrishnan, A.; Kesharwani, P.; Baboota, S.; Ali, J. Nano-Carrier Enabled Drug Delivery Systems for Nose to Brain Targeting for the Treatment of Neurodegenerative Disorders. *Journal of Drug Delivery Science and Technology* **2018**, *43*, 295–310, doi:10.1016/j.jddst.2017.09.022.
455. Di, L.; Artursson, P.; Avdeef, A.; Ecker, G.F.; Faller, B.; Fischer, H.; Houston, J.B.; Kansy, M.; Kerns, E.H.; Krämer, S.D.; et al. Evidence-Based Approach to Assess Passive Diffusion and Carrier-Mediated Drug Transport. *Drug Discovery Today* **2012**, *17*, 905–912, doi:10.1016/j.drudis.2012.03.015.
456. Dickens, D.; Radisch, S.; Pirmohamed, M. Chapter 5. Drug Transporters at the Blood–Brain Barrier. In; pp. 151–183.
457. Stephens, R.H.; O'Neill, C.A.; Bennett, J.; Humphrey, M.; Henry, B.; Rowland, M.; Warhurst, G. Resolution of P-glycoprotein and non-P-glycoprotein Effects on Drug Permeability Using Intestinal Tissues from Mdr1a (−/−) Mice. *British J Pharmacology* **2002**, *135*, 2038–2046, doi:10.1038/sj.bjp.0704668.
458. Gomez-Zepeda, D.; Taghi, M.; Scherrmann, J.-M.; Decleves, X.; Menet, M.-C. ABC Transporters at the Blood–Brain Interfaces, Their Study Models, and Drug Delivery Implications in Gliomas. *Pharmaceutics* **2019**, *12*, 20, doi:10.3390/pharmaceutics12010020.

459. Hitchcock, S.A.; Pennington, L.D. Structure−Brain Exposure Relationships. *J. Med. Chem.* **2006**, *49*, 7559–7583, doi:10.1021/jm060642i.
460. Rankovic, Z. Designing CNS Drugs for Optimal Brain Exposure. In *Blood-Brain Barrier in Drug Discovery*; John Wiley & Sons, Ltd, 2015; pp. 385–424 ISBN 978-1-118-78852-3.
461. Upadhyay, R.K. Drug Delivery Systems, CNS Protection, and the Blood Brain Barrier. *BioMed Research International* **2014**, *2014*, 1–37, doi:10.1155/2014/869269.
462. Nau, R.; Sörgel, F.; Eiffert, H. Penetration of Drugs through the Blood-Cerebrospinal Fluid/Blood-Brain Barrier for Treatment of Central Nervous System Infections. *Clin Microbiol Rev* **2010**, *23*, 858–883, doi:10.1128/CMR.00007-10.
463. Lipinski, C.A.; Lombardo, F.; Dominy, B.W.; Feeney, P.J. Experimental and Computational Approaches to Estimate Solubility and Permeability in Drug Discovery and Development Settings 1PII of Original Article: S0169-409X(96)00423-1. The Article Was Originally Published in Advanced Drug Delivery Reviews 23 (1997) 3–25. 1. *Advanced Drug Delivery Reviews* **2001**, *46*, 3–26, doi:10.1016/S0169-409X(00)00129-0.
464. Gupta, M.; Feng, J.; Bhisetti, G. Experimental and Computational Methods to Assess Central Nervous System Penetration of Small Molecules. *Molecules* **2024**, *29*, 1264, doi:10.3390/molecules29061264.
465. Leeson, P.D.; Springthorpe, B. The Influence of Drug-like Concepts on Decision-Making in Medicinal Chemistry. *Nat Rev Drug Discov* **2007**, *6*, 881–890, doi:10.1038/nrd2445.
466. Hitchcock, S.A. Structural Modifications That Alter the P-Glycoprotein Efflux Properties of Compounds. *J. Med. Chem.* **2012**, *55*, 4877–4895, doi:10.1021/jm201136z.
467. Pajouhesh, H.; Lenz, G.R. Medicinal Chemical Properties of Successful Central Nervous System Drugs. *Neurotherapeutics* **2005**, *2*, 541–553, doi:10.1602/neurorx.2.4.541.
468. Hu, E.; Kunz, R.K.; Chen, N.; Rumfelt, S.; Siegmund, A.; Andrews, K.; Chmait, S.; Zhao, S.; Davis, C.; Chen, H.; et al. Design, Optimization, and Biological Evaluation of Novel Keto-Benzimidazoles as Potent and Selective Inhibitors of Phosphodiesterase 10A (PDE10A). *J. Med. Chem.* **2013**, *56*, 8781–8792, doi:10.1021/jm401234w.
469. Veber, D.F.; Johnson, S.R.; Cheng, H.-Y.; Smith, B.R.; Ward, K.W.; Kopple, K.D. Molecular Properties That Influence the Oral Bioavailability of Drug Candidates. *J. Med. Chem.* **2002**, *45*, 2615–2623, doi:10.1021/jm020017n.
470. Van De Waterbeemd, H.; Camenisch, G.; Folkers, G.; Chretien, J.R.; Raevsky, O.A. Estimation of Blood-Brain Barrier Crossing of Drugs Using Molecular Size and Shape, and H-Bonding Descriptors. *Journal of Drug Targeting* **1998**, *6*, 151–165, doi:10.3109/10611869808997889.
471. Kelder, J.; Grootenhuis, P.D.J.; Bayada, D.M.; Delbressine, L.P.C.; Ploemen, J.-P. Polar Molecular Surface as a Dominating Determinant for Oral Absorption and Brain

Penetration of Drugs. *Pharm Res* **1999**, *16*, 1514–1519, doi:10.1023/A:1015040217741.
472. McCoull, W.; Thomson, C.; Braybrooke, E.; Chan, C.; Colclough, N.; Cortés González, M.A.; Cosulich, S.; Davies, N.L.; Floc'h, N.; Greenwood, R.; et al. Highly Optimized CNS Penetrant Inhibitors of EGFR Exon20 Insertion Mutations. *J. Med. Chem.* **2025**, *68*, 3700–3748, doi:10.1021/acs.jmedchem.4c02811.
473. Chan, B.W.G.L.; Lynch, N.B.; Tran, W.; Joyce, J.M.; Savage, G.P.; Meutermans, W.; Montgomery, A.P.; Kassiou, M. Fragment-Based Drug Discovery for Disorders of the Central Nervous System: Designing Better Drugs Piece by Piece. *Front. Chem.* **2024**, *12*, 1379518, doi:10.3389/fchem.2024.1379518.
474. Kato, R.; Zhang, L.; Kinatukara, N.; Huang, R.; Asthana, A.; Weber, C.; Xia, M.; Xu, X.; Shah, P. Investigating Blood–Brain Barrier Penetration and Neurotoxicity of Natural Products for Central Nervous System Drug Development. *Sci Rep* **2025**, *15*, 7431, doi:10.1038/s41598-025-90888-2.
475. Yadav, A.; Pandey, D.; Ashraf, G.Md.; Rachana Peptide Based Therapy for Neurological Disorders. *CPPS* **2021**, *22*, 656–665, doi:10.2174/1389203722666210920151810.
476. Ayo, A.; Laakkonen, P. Peptide-Based Strategies for Targeted Tumor Treatment and Imaging. *Pharmaceutics* **2021**, *13*, 481, doi:10.3390/pharmaceutics13040481.
477. Raucher, D. Tumor Targeting Peptides: Novel Therapeutic Strategies in Glioblastoma. *Current Opinion in Pharmacology* **2019**, *47*, 14–19, doi:10.1016/j.coph.2019.01.006.
478. Kakinen, A.; Jiang, Y.; Davis, T.; Teesalu, T.; Saarma, M. Brain Targeting Nanomedicines: Pitfalls and Promise. *IJN* **2024**, *Volume 19*, 4857–4875, doi:10.2147/IJN.S454553.
479. Bose, M.; Farias Quipildor, G.; Ehrlich, M.E.; Salton, S.R. Intranasal Peptide Therapeutics: A Promising Avenue for Overcoming the Challenges of Traditional CNS Drug Development. *Cells* **2022**, *11*, 3629, doi:10.3390/cells11223629.
480. Parrasia, S.; Szabò, I.; Zoratti, M.; Biasutto, L. Peptides as Pharmacological Carriers to the Brain: Promises, Shortcomings and Challenges. *Mol. Pharmaceutics* **2022**, *19*, 3700–3729, doi:10.1021/acs.molpharmaceut.2c00523.
481. Parthsarathy, V.; McClean, P.L.; Hölscher, C.; Taylor, M.; Tinker, C.; Jones, G.; Kolosov, O.; Salvati, E.; Gregori, M.; Masserini, M.; et al. A Novel Retro-Inverso Peptide Inhibitor Reduces Amyloid Deposition, Oxidation and Inflammation and Stimulates Neurogenesis in the APPswe/PS1ΔE9 Mouse Model of Alzheimer's Disease. *PLoS ONE* **2013**, *8*, e54769, doi:10.1371/journal.pone.0054769.
482. Gregori, M.; Taylor, M.; Salvati, E.; Re, F.; Mancini, S.; Balducci, C.; Forloni, G.; Zambelli, V.; Sesana, S.; Michael, M.; et al. Retro-Inverso Peptide Inhibitor Nanoparticles as Potent Inhibitors of Aggregation of the Alzheimer's Aβ Peptide. *Nanomedicine: Nanotechnology, Biology and Medicine* **2017**, *13*, 723–732, doi:10.1016/j.nano.2016.10.006.

483. Offen, D.; AHARONY, I. Peptides for the Treatment of Neurodegenerative Diseases 2014.
484. Popiel, H.A.; Burke, J.R.; Strittmatter, W.J.; Oishi, S.; Fujii, N.; Takeuchi, T.; Toda, T.; Wada, K.; Nagai, Y. The Aggregation Inhibitor Peptide QBP1 as a Therapeutic Molecule for the Polyglutamine Neurodegenerative Diseases. *Journal of Amino Acids* **2011**, *2011*, 1–10, doi:10.4061/2011/265084.
485. Belwal, V.K.; Datta, D.; Chaudhary, N. The B-turn-supporting Motif in the Polyglutamine Binding Peptide QBP1 Is Essential for Inhibiting Huntingtin Aggregation. *FEBS Letters* **2020**, *594*, 2894–2903, doi:10.1002/1873-3468.13873.
486. Nath, A.; Pandey, S.; Nisar, K.S.; Tiwari, A.K. Gaining Insights into the Physicochemical Properties and Sequence Space of Blood–Brain Barrier Penetrating Peptides. *Egyptian Informatics Journal* **2024**, *28*, 100557, doi:10.1016/j.eij.2024.100557.
487. Mahipal, A.; Malafa, M. Importins and Exportins as Therapeutic Targets in Cancer. *Pharmacology & Therapeutics* **2016**, *164*, 135–143, doi:10.1016/j.pharmthera.2016.03.020.
488. Nofrini, V.; Di Giacomo, D.; Mecucci, C. Nucleoporin Genes in Human Diseases. *Eur J Hum Genet* **2016**, *24*, 1388–1395, doi:10.1038/ejhg.2016.25.
489. Strambio-De-Castillia, C.; Niepel, M.; Rout, M.P. The Nuclear Pore Complex: Bridging Nuclear Transport and Gene Regulation. *Nat Rev Mol Cell Biol* **2010**, *11*, 490–501, doi:10.1038/nrm2928.
490. Yang, Y.; Guo, L.; Chen, L.; Gong, B.; Jia, D.; Sun, Q. Nuclear Transport Proteins: Structure, Function and Disease Relevance. *Sig Transduct Target Ther* **2023**, *8*, 425, doi:10.1038/s41392-023-01649-4.
491. Pumroy, R.A.; Cingolani, G. Diversification of Importin-α Isoforms in Cellular Trafficking and Disease States. *Biochemical Journal* **2015**, *466*, 13–28, doi:10.1042/BJ20141186.
492. Pasha, T.; Zatorska, A.; Sharipov, D.; Rogelj, B.; Hortobágyi, T.; Hirth, F. Karyopherin Abnormalities in Neurodegenerative Proteinopathies. *Brain* **2021**, *144*, 2915–2932, doi:10.1093/brain/awab201.
493. Yoshimura, S.H.; Hirano, T. HEAT Repeats – Versatile Arrays of Amphiphilic Helices Working in Crowded Environments? *Journal of Cell Science* **2016**, *129*, 3963–3970, doi:10.1242/jcs.185710.
494. Milles, S.; Mercadante, D.; Aramburu, I.V.; Jensen, M.R.; Banterle, N.; Koehler, C.; Tyagi, S.; Clarke, J.; Shammas, S.L.; Blackledge, M.; et al. Plasticity of an Ultrafast Interaction between Nucleoporins and Nuclear Transport Receptors. *Cell* **2015**, *163*, 734–745, doi:10.1016/j.cell.2015.09.047.
495. Goodsell, D.S.; Dutta, S.; Zardecki, C.; Voigt, M.; Berman, H.M.; Burley, S.K. The RCSB PDB "Molecule of the Month": Inspiring a Molecular View of Biology. *PLoS Biol* **2015**, *13*, e1002140, doi:10.1371/journal.pbio.1002140.

496. Wing, C.E.; Fung, H.Y.J.; Chook, Y.M. Karyopherin-Mediated Nucleocytoplasmic Transport. *Nat Rev Mol Cell Biol* **2022**, *23*, 307–328, doi:10.1038/s41580-021-00446-7.
497. Barbato, S.; Kapinos, L.E.; Rencurel, C.; Lim, R.Y.H. Karyopherin Enrichment at the Nuclear Pore Complex Attenuates Ran Permeability. *Journal of Cell Science* **2020**, *133*, jcs238121, doi:10.1242/jcs.238121.
498. Conti, E.; Müller, C.W.; Stewart, M. Karyopherin Flexibility in Nucleocytoplasmic Transport. *Current Opinion in Structural Biology* **2006**, *16*, 237–244, doi:10.1016/j.sbi.2006.03.010.
499. Kim, Y.H.; Han, M.-E.; Oh, S.-O. The Molecular Mechanism for Nuclear Transport and Its Application. *Anat Cell Biol* **2017**, *50*, 77, doi:10.5115/acb.2017.50.2.77.
500. Springhower, C.E.; Rosen, M.K.; Chook, Y.M. Karyopherins and Condensates. *Current Opinion in Cell Biology* **2020**, *64*, 112–123, doi:10.1016/j.ceb.2020.04.003.
501. Çağatay, T.; Chook, Y.M. Karyopherins in Cancer. *Current Opinion in Cell Biology* **2018**, *52*, 30–42, doi:10.1016/j.ceb.2018.01.006.
502. Anyanwu, M.; Giannangeli, M.; Gianoncelli, A.; Ribaudo, G. Therapeutic Approaches Interfering with Nuclear Localization Signals: An Emerging Strategy for CNS-Related Diseases. *Current Neuropharmacology* **2025**, *23*, 1–15, doi:10.2174/011570159X384321250627071259.
503. Jans, D.A.; Martin, A.J.; Wagstaff, K.M. Inhibitors of Nuclear Transport. *Current Opinion in Cell Biology* **2019**, *58*, 50–60, doi:10.1016/j.ceb.2019.01.001.
504. Indrigo, M.; Morella, I.; Orellana, D.; d'Isa, R.; Papale, A.; Parra, R.; Gurgone, A.; Lecca, D.; Cavaccini, A.; Tigaret, C.M.; et al. Nuclear ERK1/2 Signaling Potentiation Enhances Neuroprotection and Cognition via Importinα1/KPNA2. *EMBO Mol Med* **2023**, *15*, e15984, doi:10.15252/emmm.202215984.
505. Marchi, M.; D'Antoni, A.; Formentini, I.; Parra, R.; Brambilla, R.; Ratto, G.M.; Costa, M. The N-Terminal Domain of ERK1 Accounts for the Functional Differences with ERK2. *PLOS ONE* **2008**, *3*, e3873, doi:10.1371/journal.pone.0003873.
506. Yang, S.N.Y.; Atkinson, S.C.; Wang, C.; Lee, A.; Bogoyevitch, M.A.; Borg, N.A.; Jans, D.A. The Broad Spectrum Antiviral Ivermectin Targets the Host Nuclear Transport Importin α/B1 Heterodimer. *Antiviral Research* **2020**, *177*, 104760, doi:10.1016/j.antiviral.2020.104760.
507. Atkinson, S.C.; Audsley, M.D.; Lieu, K.G.; Marsh, G.A.; Thomas, D.R.; Heaton, S.M.; Paxman, J.J.; Wagstaff, K.M.; Buckle, A.M.; Moseley, G.W.; et al. Recognition by Host Nuclear Transport Proteins Drives Disorder-to-Order Transition in Hendra Virus V. *Sci Rep* **2018**, *8*, 358, doi:10.1038/s41598-017-18742-8.
508. Wagstaff, K.M.; Rawlinson, S.M.; Hearps, A.C.; Jans, D.A. An AlphaScreen®-Based Assay for High-Throughput Screening for Specific Inhibitors of Nuclear Import. *SLAS Discovery* **2011**, *16*, 192–200, doi:10.1177/1087057110390360.

509. Kosyna, F.K.; Nagel, M.; Kluxen, L.; Kraushaar, K.; Depping, R. The Importin α/β-Specific Inhibitor Ivermectin Affects HIF-Dependent Hypoxia Response Pathways. *Biological Chemistry* **2015**, *396*, 1357–1367, doi:10.1515/hsz-2015-0171.
510. Kosugi, S.; Hasebe, M.; Entani, T.; Takayama, S.; Tomita, M.; Yanagawa, H. Design of Peptide Inhibitors for the Importin α/β Nuclear Import Pathway by Activity-Based Profiling. *Chemistry & Biology* **2008**, *15*, 940–949, doi:10.1016/j.chembiol.2008.07.019.
511. Zienkiewicz, J.; Armitage, A.; Hawiger, J. Targeting Nuclear Import Shuttles, Importins/Karyopherins Alpha by a Peptide Mimicking the NFκB1/P50 Nuclear Localization Sequence. *JAHA* **2013**, *2*, e000386, doi:10.1161/JAHA.113.000386.
512. Li, X.; Rasul, A.; Sharif, F.; Hassan, M. PIAS Family in Cancer: From Basic Mechanisms to Clinical Applications. *Front. Oncol.* **2024**, *14*, 1376633, doi:10.3389/fonc.2024.1376633.
513. Wirt, S.E.; Sage, J. P107 in the Public Eye: An Rb Understudy and More. *Cell Div* **2010**, *5*, 9, doi:10.1186/1747-1028-5-9.
514. Cansizoglu, A.E.; Lee, B.J.; Zhang, Z.C.; Fontoura, B.M.A.; Chook, Y.M. Structure-Based Design of a Pathway-Specific Nuclear Import Inhibitor. *Nat Struct Mol Biol* **2007**, *14*, 452–454, doi:10.1038/nsmb1229.
515. Hintersteiner, M.; Ambrus, G.; Bednenko, J.; Schmied, M.; Knox, A.J.S.; Meisner, N.-C.; Gstach, H.; Seifert, J.-M.; Singer, E.L.; Gerace, L.; et al. Identification of a Small Molecule Inhibitor of Importin β Mediated Nuclear Import by Confocal On-Bead Screening of Tagged One-Bead One-Compound Libraries. *ACS Chem. Biol.* **2010**, *5*, 967–979, doi:10.1021/cb100094k.
516. Soderholm, J.F.; Bird, S.L.; Kalab, P.; Sampathkumar, Y.; Hasegawa, K.; Uehara-Bingen, M.; Weis, K.; Heald, R. Importazole, a Small Molecule Inhibitor of the Transport Receptor Importin-β. *ACS Chem. Biol.* **2011**, *6*, 700–708, doi:10.1021/cb2000296.
517. Pathak, G.K.; Ornstein, H.; Aranda-Espinoza, H.; Karlsson, A.J.; Shah, S.B. Increases in Retrograde Injury Signaling Complex-Related Transcripts in Central Axons Following Injury. *Neural Plasticity* **2016**, *2016*, 1–13, doi:10.1155/2016/3572506.
518. Chen, W.-S.; Chen, Y.-J.; Huang, Y.-A.; Hsieh, B.-Y.; Chiu, H.-C.; Kao, P.-Y.; Chao, C.-Y.; Hwang, E. Ran-Dependent TPX2 Activation Promotes Acentrosomal Microtubule Nucleation in Neurons. *Sci Rep* **2017**, *7*, 42297, doi:10.1038/srep42297.
519. Sheng, K.L.; Pridham, K.J.; Sheng, Z.; Lamouille, S.; Varghese, R.T. Functional Blockade of Small GTPase RAN Inhibits Glioblastoma Cell Viability. *Front. Oncol.* **2019**, *8*, 662, doi:10.3389/fonc.2018.00662.
520. Zhu, Z.-C.; Liu, J.-W.; Li, K.; Zheng, J.; Xiong, Z.-Q. KPNB1 Inhibition Disrupts Proteostasis and Triggers Unfolded Protein Response-Mediated Apoptosis in Glioblastoma Cells. *Oncogene* **2018**, *37*, 2936–2952, doi:10.1038/s41388-018-0180-9.

521. Van Der Watt, P.J.; Chi, A.; Stelma, T.; Stowell, C.; Strydom, E.; Carden, S.; Angus, L.; Hadley, K.; Lang, D.; Wei, W.; et al. Targeting the Nuclear Import Receptor Kpnβ1 as an Anticancer Therapeutic. *Molecular Cancer Therapeutics* **2016**, *15*, 560–573, doi:10.1158/1535-7163.MCT-15-0052.
522. Ajayi-Smith, A.; Van Der Watt, P.; Mkwanazi, N.; Carden, S.; Trent, J.O.; Leaner, V.D. Novel Small Molecule Inhibitor of Kpnβ1 Induces Cell Cycle Arrest and Apoptosis in Cancer Cells. *Experimental Cell Research* **2021**, *404*, 112637, doi:10.1016/j.yexcr.2021.112637.
523. Liu, W.; Patouret, R.; Barluenga, S.; Plank, M.; Loewith, R.; Winssinger, N. Identification of a Covalent Importin-5 Inhibitor, Goyazensolide, from a Collective Synthesis of Furanoheliangolides. *ACS Cent. Sci.* **2021**, *7*, 954–962, doi:10.1021/acscentsci.1c00056.
524. Izumi, C.; Laure, H.J.; Barbosa, N.G.; Hassibe Thomé, C.; Aguiar Ferreira, G.; Paulo Barreto Sousa, J.; Peporine Lopes, N.; César Rosa, J. Sequesterpene Lactones Isolated from a Brazilian Cerrado Plant (Eremanthus Spp.) as Anti-Proliferative Compounds, Characterized by Functional and Proteomic Analysis, Are Candidates for New Therapeutics in Glioblastoma. *IJMS* **2020**, *21*, 4713, doi:10.3390/ijms21134713.
525. Wagstaff, K.M.; Headey, S.; Telwatte, S.; Tyssen, D.; Hearps, A.C.; Thomas, D.R.; Tachedjian, G.; Jans, D.A. Molecular Dissection of an Inhibitor Targeting the HIV Integrase Dependent Preintegration Complex Nuclear Import. *Cellular Microbiology* **2019**, *21*, e12953, doi:10.1111/cmi.12953.
526. Fraser, J.E.; Watanabe, S.; Wang, C.; Chan, W.K.K.; Maher, B.; Lopez-Denman, A.; Hick, C.; Wagstaff, K.M.; Mackenzie, J.M.; Sexton, P.M.; et al. A Nuclear Transport Inhibitor That Modulates the Unfolded Protein Response and Provides In Vivo Protection Against Lethal Dengue Virus Infection. *The Journal of Infectious Diseases* **2014**, *210*, 1780–1791, doi:10.1093/infdis/jiu319.
527. Wang, C.; Yang, S.N.Y.; Smith, K.; Forwood, J.K.; Jans, D.A. Nuclear Import Inhibitor N -(4-Hydroxyphenyl) Retinamide Targets Zika Virus (ZIKV) Nonstructural Protein 5 to Inhibit ZIKV Infection. *Biochemical and Biophysical Research Communications* **2017**, *493*, 1555–1559, doi:10.1016/j.bbrc.2017.10.016.
528. Lopez-Denman, A.J.; Russo, A.; Wagstaff, K.M.; White, P.A.; Jans, D.A.; Mackenzie, J.M. Nucleocytoplasmic Shuttling of the West Nile Virus RNA - dependent RNA Polymerase NS5 Is Critical to Infection. *Cellular Microbiology* **2018**, *20*, doi:10.1111/cmi.12848.
529. Li, C.; Zhang, Q.; Huang, W.; Huang, L.; Long, Q.; Lei, Y.; Jia, D.; Yang, S.; Yang, Y.; Zhang, X.; et al. Discovery of a Hidden Pocket beneath the NES Groove by Novel Noncovalent CRM1 Inhibitors. *J. Med. Chem.* **2023**, *66*, 17044–17058, doi:10.1021/acs.jmedchem.3c01867.
530. Kudo, N.; Matsumori, N.; Taoka, H.; Fujiwara, D.; Schreiner, E.P.; Wolff, B.; Yoshida, M.; Horinouchi, S. Leptomycin B Inactivates CRM1/Exportin 1 by

Covalent Modification at a Cysteine Residue in the Central Conserved Region. *Proc. Natl. Acad. Sci. U.S.A.* **1999**, *96*, 9112–9117, doi:10.1073/pnas.96.16.9112.
531. Sun, Q.; Carrasco, Y.P.; Hu, Y.; Guo, X.; Mirzaei, H.; MacMillan, J.; Chook, Y.M. Nuclear Export Inhibition through Covalent Conjugation and Hydrolysis of Leptomycin B by CRM1. *Proc. Natl. Acad. Sci. U.S.A.* **2013**, *110*, 1303–1308, doi:10.1073/pnas.1217203110.
532. Dey, A.; Tergaonkar, V.; Lane, D.P. Double-Edged Swords as Cancer Therapeutics: Simultaneously Targeting P53 and NF-κB Pathways. *Nat Rev Drug Discov* **2008**, *7*, 1031–1040, doi:10.1038/nrd2759.
533. Rodriguez, M.S.; Thompson, J.; Hay, R.T.; Dargemont, C. Nuclear Retention of IκBα Protects It from Signal-Induced Degradation and Inhibits Nuclear Factor κB Transcriptional Activation. *Journal of Biological Chemistry* **1999**, *274*, 9108–9115, doi:10.1074/jbc.274.13.9108.
534. Newlands, E.; Rustin, G.; Brampton, M. Phase I Trial of Elactocin. *Br J Cancer* **1996**, *74*, 648–649, doi:10.1038/bjc.1996.415.
535. Niu, M.; Wu, S.; Mao, L.; Yang, Y. CRM1 Is a Cellular Target of Curcumin: New Insights for the Myriad of Biological Effects of an Ancient Spice. *Traffic* **2013**, *14*, 1042–1052, doi:10.1111/tra.12090.
536. Theodoropoulos, N.; Lancman, G.; Chari, A. Targeting Nuclear Export Proteins in Multiple Myeloma Therapy. *Targ Oncol* **2020**, *15*, 697–708, doi:10.1007/s11523-020-00758-2.
537. Bonazzi, S.; Eidam, O.; Güttinger, S.; Wach, J.-Y.; Zemp, I.; Kutay, U.; Gademann, K. Anguinomycins and Derivatives: Total Syntheses, Modeling, and Biological Evaluation of the Inhibition of Nucleocytoplasmic Transport. *J. Am. Chem. Soc.* **2010**, *132*, 1432–1442, doi:10.1021/ja9097093.
538. Wach, J.-Y.; Güttinger, S.; Kutay, U.; Gademann, K. The Cytotoxic Styryl Lactone Goniothalamin Is an Inhibitor of Nucleocytoplasmic Transport. *Bioorganic & Medicinal Chemistry Letters* **2010**, *20*, 2843–2846, doi:10.1016/j.bmcl.2010.03.049.
539. Walker, J.S.; Hing, Z.A.; Harrington, B.; Baumhardt, J.; Ozer, H.G.; Lehman, A.; Giacopelli, B.; Beaver, L.; Williams, K.; Skinner, J.N.; et al. Recurrent XPO1 Mutations Alter Pathogenesis of Chronic Lymphocytic Leukemia. *J Hematol Oncol* **2021**, *14*, 17, doi:10.1186/s13045-021-01032-2.
540. Ferreira-Cerca, S.; Sagar, V.; Schäfer, T.; Diop, M.; Wesseling, A.-M.; Lu, H.; Chai, E.; Hurt, E.; LaRonde-LeBlanc, N. ATPase-Dependent Role of the Atypical Kinase Rio2 on the Evolving Pre-40S Ribosomal Subunit. *Nat Struct Mol Biol* **2012**, *19*, 1316–1323, doi:10.1038/nsmb.2403.
541. Beevers, C.S.; Chen, L.; Liu, L.; Luo, Y.; Webster, N.J.G.; Huang, S. Curcumin Disrupts the Mammalian Target of Rapamycin-Raptor Complex. *Cancer Research* **2009**, *69*, 1000–1008, doi:10.1158/0008-5472.CAN-08-2367.

542. Gradišar, H.; Keber, M.M.; Pristovšek, P.; Jerala, R. MD-2 as the Target of Curcumin in the Inhibition of Response to LPS. *Journal of Leukocyte Biology* **2007**, *82*, 968–974, doi:10.1189/jlb.1206727.
543. Zhang, Z.; Luo, D.; Xie, J.; Lin, G.; Zhou, J.; Liu, W.; Li, H.; Yi, T.; Su, Z.; Chen, J. Octahydrocurcumin, a Final Hydrogenated Metabolite of Curcumin, Possesses Superior Anti-Tumor Activity through Induction of Cellular Apoptosis. *Food Funct.* **2018**, *9*, 2005–2014, doi:10.1039/C7FO02048A.
544. Ramakrishna, R.; Diamond, T.H.; Alexander, W.; Manoharan, A.; Golombick, T. Use of Curcumin in Multiple Myeloma Patients Intolerant of Steroid Therapy. *Clinical Case Reports* **2020**, *8*, 739–744, doi:10.1002/ccr3.2735.
545. Liu, X.; Niu, M.; Xu, X.; Cai, W.; Zeng, L.; Zhou, X.; Yu, R.; Xu, K. CRM1 Is a Direct Cellular Target of the Natural Anti-Cancer Agent Plumbagin. *J Pharmacol Sci* **2014**, *124*, 486–493, doi:10.1254/jphs.13240FP.
546. Abedinpour, P.; Baron, V.T.; Chrastina, A.; Rondeau, G.; Pelayo, J.; Welsh, J.; Borgström, P. Plumbagin Improves the Efficacy of Androgen Deprivation Therapy in Prostate Cancer: A Pre-clinical Study. *The Prostate* **2017**, *77*, 1550–1562, doi:10.1002/pros.23428.
547. Jiang, Z.-B.; Xu, C.; Wang, W.; Zhang, Y.-Z.; Huang, J.-M.; Xie, Y.-J.; Wang, Q.-Q.; Fan, X.-X.; Yao, X.-J.; Xie, C.; et al. Plumbagin Suppresses Non-Small Cell Lung Cancer Progression through Downregulating ARF1 and by Elevating CD8+ T Cells. *Pharmacological Research* **2021**, *169*, 105656, doi:10.1016/j.phrs.2021.105656.
548. Sakakibara, K.; Saito, N.; Sato, T.; Suzuki, A.; Hasegawa, Y.; Friedman, J.M.; Kufe, D.W.; VonHoff, D.D.; Iwami, T.; Kawabe, T. CBS9106 Is a Novel Reversible Oral CRM1 Inhibitor with CRM1 Degrading Activity. *Blood* **2011**, *118*, 3922–3931, doi:10.1182/blood-2011-01-333138.
549. Wang, J.; Barve, M.; Chiorean, E.; LoRusso, P.; Courtney, K.; Qi, D.; Bullington, J.; Sardone, M.; Chen, J.; Brooks, C.; et al. 466P - Interim Results from Trial of SL-801, a Novel XPO-1 Inhibitor, in Patients with Advanced Solid Tumours. *Annals of Oncology* **2019**, *30*, v175, doi:10.1093/annonc/mdz244.028.
550. Sun, Q.; Chen, X.; Zhou, Q.; Burstein, E.; Yang, S.; Jia, D. Inhibiting Cancer Cell Hallmark Features through Nuclear Export Inhibition. *Sig Transduct Target Ther* **2016**, *1*, 16010, doi:10.1038/sigtrans.2016.10.
551. Daelemans, D.; Afonina, E.; Nilsson, J.; Werner, G.; Kjems, J.; De Clercq, E.; Pavlakis, G.N.; Vandamme, A.-M. A Synthetic HIV-1 Rev Inhibitor Interfering with the CRM1-Mediated Nuclear Export. *Proc. Natl. Acad. Sci. U.S.A.* **2002**, *99*, 14440–14445, doi:10.1073/pnas.212285299.
552. XPO1 Inhibitor Approved for Multiple Myeloma. *Cancer Discovery* **2019**, *9*, 1150–1151, doi:10.1158/2159-8290.CD-NB2019-085.
553. Peterson, T.J.; Orozco, J.; Buege, M. Selinexor: A First-in-Class Nuclear Export Inhibitor for Management of Multiply Relapsed Multiple Myeloma. *Ann Pharmacother* **2020**, *54*, 577–582, doi:10.1177/1060028019892643.

554. Ben-Barouch, S.; Kuruvilla, J. Selinexor (KTP-330) - a Selective Inhibitor of Nuclear Export (SINE): Anti-Tumor Activity in Diffuse Large B-Cell Lymphoma (DLBCL). *Expert Opinion on Investigational Drugs* **2020**, *29*, 15–21, doi:10.1080/13543784.2020.1706087.
555. Kasamon, Y.L.; Price, L.S.L.; Okusanya, O.O.; Richardson, N.C.; Li, R.-J.; Ma, L.; Wu, Y.-T.; Theoret, M.; Pazdur, R.; Gormley, N.J. FDA Approval Summary: Selinexor for Relapsed or Refractory Diffuse Large B-Cell Lymphoma. *The Oncologist* **2021**, *26*, 879–886, doi:10.1002/onco.13859.
556. Miao, H.; Qin, Y.; Shao, D.; Chen, Q.; Pan, Y.; Lei, M.; Wu, R.; Ye, X.; Wang, X.; Zhu, Y. Discovery of SZJK-0421: A Novel Potent, Low Toxicity, Selective Second Generation of CRM1 Inhibitor for the Treatment of Both Hematological and Solid Tumors. *J. Med. Chem.* **2024**, *67*, 20595–20618, doi:10.1021/acs.jmedchem.4c02169.
557. Lai, C.; Xu, L.; Dai, S. The Nuclear Export Protein Exportin-1 in Solid Malignant Tumours: From Biology to Clinical Trials. *Clinical & Translational Med* **2024**, *14*, e1684, doi:10.1002/ctm2.1684.
558. Lassman, A.B.; Wen, P.Y.; Van Den Bent, M.J.; Plotkin, S.R.; Walenkamp, A.M.E.; Green, A.L.; Li, K.; Walker, C.J.; Chang, H.; Tamir, S.; et al. A Phase II Study of the Efficacy and Safety of Oral Selinexor in Recurrent Glioblastoma. *Clinical Cancer Research* **2022**, *28*, 452–460, doi:10.1158/1078-0432.CCR-21-2225.
559. Hoosemans, L.; Vooijs, M.; Hoeben, A. Opportunities and Challenges of Small Molecule Inhibitors in Glioblastoma Treatment: Lessons Learned from Clinical Trials. *Cancers* **2024**, *16*, 3021, doi:10.3390/cancers16173021.
560. National Cancer Institute (NCI) *A Phase 1 and Randomized Phase 2 Trial of Selinexor and Temozolomide in Recurrent Glioblastoma*; clinicaltrials.gov, 2025;
561. Karyopharm Therapeutics Inc *A Phase 2 Study Evaluating the Efficacy and Safety of Selinexor (KPT-330) in Patients With Recurrent Gliomas*; clinicaltrials.gov, 2023;
562. Camphausen, K. *A Phase I Clinical Trial of Selinexor (KPT-330) in Combination With Temozolomide and Radiation Therapy in Patients With Newly Diagnosed Glioblastoma*; clinicaltrials.gov, 2024;
563. Cornell, R.F.; Baz, R.; Richter, J.R.; Rossi, A.; Vogl, D.T.; Chen, C.; Shustik, C.; Alvarez, M.J.; Shen, Y.; Unger, T.J.; et al. A Phase 1 Clinical Trial of Oral Eltanexor in Patients with Relapsed or Refractory Multiple Myeloma. *American J Hematol* **2022**, *97*, doi:10.1002/ajh.26420.
564. Chari, A.; Vogl, D.T.; Gavriatopoulou, M.; Nooka, A.K.; Yee, A.J.; Huff, C.A.; Moreau, P.; Dingli, D.; Cole, C.; Lonial, S.; et al. Oral Selinexor–Dexamethasone for Triple-Class Refractory Multiple Myeloma. *N Engl J Med* **2019**, *381*, 727–738, doi:10.1056/NEJMoa1903455.
565. Lei, Y.; An, Q.; Shen, X.; Sui, M.; Li, C.; Jia, D.; Luo, Y.; Sun, Q. Structure-Guided Design of the First Noncovalent Small-Molecule Inhibitor of CRM1. *J. Med. Chem.* **2021**, *64*, 6596–6607, doi:10.1021/acs.jmedchem.0c01675.

566. Klahn, P.; Fetz, V.; Ritter, A.; Collisi, W.; Hinkelmann, B.; Arnold, T.; Tegge, W.; Rox, K.; Hüttel, S.; Mohr, K.I.; et al. The Nuclear Export Inhibitor Aminoratjadone Is a Potent Effector in Extracellular-Targeted Drug Conjugates. *Chem. Sci.* **2019**, *10*, 5197–5210, doi:10.1039/C8SC05542D.
567. Jian, L.; Zscherp, R.; Beutling, U.; Shen, X.; Xu, S.; Zhang, X.; Brönstrup, M.; Klahn, P.; Sun, Q. Discovery of Aminoratjadone Derivatives as Potent Noncovalent CRM1 Inhibitors. *J. Med. Chem.* **2023**, *66*, 11940–11950, doi:10.1021/acs.jmedchem.3c00549.
568. Huang, W.; Wang, J.-X.; Shen, X.; Lei, Y.; Chen, X.; Jia, D.; Zhang, X.; Sun, Q. Searching for Novel Noncovalent Nuclear Export Inhibitors through a Drug Repurposing Approach. *J. Med. Chem.* **2023**, *66*, 1574–1582, doi:10.1021/acs.jmedchem.2c01772.
569. Saavedra, A.; Giralt, A.; Arumí, H.; Alberch, J.; Pérez-Navarro, E. Regulation of Hippocampal cGMP Levels as a Candidate to Treat Cognitive Deficits in Huntington's Disease. *PLoS ONE* **2013**, *8*, e73664, doi:10.1371/journal.pone.0073664.
570. Kalaria, R.N. Neuropathological Diagnosis of Vascular Cognitive Impairment and Vascular Dementia with Implications for Alzheimer's Disease. *Acta Neuropathol* **2016**, *131*, 659–685, doi:10.1007/s00401-016-1571-z.
571. Susmi, T.F.; Rahman, A.; Khan, Md.M.R.; Yasmin, F.; Islam, Md.S.; Nasif, O.; Alharbi, S.A.; Batiha, G.E.-S.; Hossain, M.U. Prognostic and Clinicopathological Insights of Phosphodiesterase 9A Gene as Novel Biomarker in Human Colorectal Cancer. *BMC Cancer* **2021**, *21*, 577, doi:10.1186/s12885-021-08332-3.
572. Kim, K.M.; Girdhar, A.; Cicardi, M.E.; Kankate, V.; Hayashi, M.; Yang, R.; Carey, J.L.; Fare, C.M.; Shorter, J.; Cingolani, G.; et al. NLS-Binding Deficient Kapβ2 Reduces Neurotoxicity via Selective Interaction with C9orf72-ALS/FTD Dipeptide Repeats. *Commun Biol* **2025**, *8*, 2, doi:10.1038/s42003-024-07412-x.
573. Abramson, J.; Adler, J.; Dunger, J.; Evans, R.; Green, T.; Pritzel, A.; Ronneberger, O.; Willmore, L.; Ballard, A.J.; Bambrick, J.; et al. Accurate Structure Prediction of Biomolecular Interactions with AlphaFold 3. *Nature* **2024**, *630*, 493–500, doi:10.1038/s41586-024-07487-w.
574. Ocana, A.; Pandiella, A.; Privat, C.; Bravo, I.; Luengo-Oroz, M.; Amir, E.; Gyorffy, B. Integrating Artificial Intelligence in Drug Discovery and Early Drug Development: A Transformative Approach. *Biomark Res* **2025**, *13*, 45, doi:10.1186/s40364-025-00758-2.
575. Tintore, M.; Vidal-Jordana, A.; Sastre-Garriga, J. Treatment of Multiple Sclerosis - Success from Bench to Bedside. *Nat Rev Neurol* **2019**, *15*, 53–58, doi:10.1038/s41582-018-0082-z.
576. Atanasov, A.G.; Zotchev, S.B.; Dirsch, V.M.; Supuran, C.T. Natural Products in Drug Discovery: Advances and Opportunities. *Nat Rev Drug Discov* **2021**, *20*, 200–216, doi:10.1038/s41573-020-00114-z.

577. Singh, M.; Kaur, M.; Chadha, N.; Silakari, O. Hybrids: A New Paradigm to Treat Alzheimer's Disease. *Mol Divers* **2016**, *20*, 271–297, doi:10.1007/s11030-015-9628-9.
578. Tsuno, N. Donepezil in the Treatment of Patients with Alzheimer's Disease. *Expert Review of Neurotherapeutics* **2009**, *9*, 591–598, doi:10.1586/ern.09.23.
579. Mahase, E. Lecanemab: European Drug Agency Rejects Alzheimer's Drug amid Debate over Efficacy and Safety. *BMJ* **2024**, q1692, doi:10.1136/bmj.q1692.
580. Ribaudo, G.; Memo, M.; Gianoncelli, A. Multi-Target Natural and Nature-Inspired Compounds against Neurodegeneration: A Focus on Dual Cholinesterase and Phosphodiesterase Inhibitors. *Applied Sciences* **2021**, *11*, 5044, doi:10.3390/app11115044.
581. Ali, S.; Venkatesan, L.S. How Do Natural Products Work for Alzheimer's Disease Management? *Natural Product Research* **2024**, 1–2, doi:10.1080/14786419.2024.2414403.
582. Apaza Ticona, L.; Sánchez Sánchez-Corral, J.; Zou Shi, Y.; Montoto Lozano, N.; Slowing Barillas, K. Pentacyclic Triterpenes as Bioactive Compounds Isolated from *Mauritia Flexuosa* L. f. Acting against the Alzheimer's Disease. *Natural Product Research* **2024**, 1–10, doi:10.1080/14786419.2024.2412839.
583. Grabić, J.; Ljevnaić-Mašić, B.; Zhan, A.; Benka, P.; Heilmeier, H. A Review on Invasive False Indigo Bush (*Amorpha Fruticosa* L.): Nuisance Plant with Multiple Benefits. *Ecology and Evolution* **2022**, *12*, e9290, doi:10.1002/ece3.9290.
584. Cui, X.; Guo, J.; Lai, C.-S.; Pan, M.-H.; Ma, Z.; Guo, S.; Liu, Q.; Zhang, L.; Ho, C.-T.; Bai, N. Analysis of Bioactive Constituents from the Leaves of Amorpha Fruticosa L. *Journal of Food and Drug Analysis* **2017**, *25*, 992–999, doi:10.1016/j.jfda.2016.10.006.
585. Samardžić, S.; Đorđić Crnogorac, M.; Petković, M.; Arsenijević, J.; Stanojković, T.; Maksimović, Z. Cytotoxic Prenylated Phenols of False Indigo-Bush (*Amorpha Fruticosa* L.). *Natural Product Research* **2025**, *39*, 5066–5069, doi:10.1080/14786419.2024.2353912.
586. Liu, Y.; Zhao, Y.; Chen, H.; Wang, W.; Zou, M. Isolation, Purification, and Biological Activities of Polysaccharides from *Amorpha Fruticosa* Flowers. *Natural Product Research* **2025**, *39*, 4701–4708, doi:10.1080/14786419.2024.2346272.
587. Moon, S.W.; Kim, J.Y.; Lee, S.H.; Im, S.Y.; Lee, G.; Park, K.H. New Class of Tyrosinase Inhibitors, Rotenoids, from *Amorpha Fruticosa*. *ACS Omega* **2023**, *8*, 31870–31879, doi:10.1021/acsomega.3c03396.
588. Jankovská, D.; Jurčová, N.; Kubínová, R.; Václavík, J.; Švajdlenka, E.; Mascellani, A.; Maršík, P.; Bouzková, K.; Malaník, M. Anticholinesterase Activity of Methanolic Extract of Amorpha Fruticosa Flowers and Isolation of Rotenoids and Putrescine and Spermidine Derivatives. *Plants* **2024**, *13*, 1181, doi:10.3390/plants13091181.
589. Kozuharova, E.; Matkowski, A.; Woźniak, D.; Simeonova, R.; Naychov, Z.; Malainer, C.; Mocan, A.; Nabavi, S.M.; Atanasov, A.G. Amorpha Fruticosa – A

Noxious Invasive Alien Plant in Europe or a Medicinal Plant against Metabolic Disease? *Front. Pharmacol.* **2017**, *8*, 333, doi:10.3389/fphar.2017.00333.
590. Đorđević Zlatković, M.R.; Stojanović, N.M.; Zlatković, D.B.; Randjelović, P.J.; Radulović, N.S. Chemodiversity and Antinociceptive Activity of Amorpha Fruticosa L. Essential Oil. *Plants* **2024**, *13*, 3045, doi:10.3390/plants13213045.
591. Shelepova, O.V.; Galkina, M.A.; Vinogradova, Y.K. Phytochemical Composition of the Alien Invasive Species Amorpha Fruticosa at the Northern Edge of Its Secondary Distribution Range—In the Arboretum of the Main Botanical Garden of the Russian Academy of Sciences. *JZBG* **2024**, *5*, 805–816, doi:10.3390/jzbg5040053.
592. Zheleva-Dimitrova, D. Antioxidant and Acetylcholinesterase Inhibition Properties of Amorpha Fruticosa L. and Phytolacca Americana L. *Phcog Mag* **2013**, *9*, 109, doi:10.4103/0973-1296.111251.
593. Tu, Y.; Wu, C.; Kang, Y.; Li, Q.; Zhu, C.; Li, Y. Bioactivity-Guided Identification of Flavonoids with Cholinesterase and β-Amyloid Peptide Aggregation Inhibitory Effects from the Seeds of Millettia Pachycarpa. *Bioorganic & Medicinal Chemistry Letters* **2019**, *29*, 1194–1198, doi:10.1016/j.bmcl.2019.03.024.
594. Daina, A.; Michielin, O.; Zoete, V. SwissADME: A Free Web Tool to Evaluate Pharmacokinetics, Drug-Likeness and Medicinal Chemistry Friendliness of Small Molecules. *Sci Rep* **2017**, *7*, 42717, doi:10.1038/srep42717.
595. Daina, A.; Michielin, O.; Zoete, V. SwissTargetPrediction: Updated Data and New Features for Efficient Prediction of Protein Targets of Small Molecules. *Nucleic Acids Research* **2019**, *47*, W357–W364, doi:10.1093/nar/gkz382.
596. Zhang, Y.; Kua, J.; McCammon, J.A. Role of the Catalytic Triad and Oxyanion Hole in Acetylcholinesterase Catalysis: An Ab Initio QM/MM Study. *J. Am. Chem. Soc.* **2002**, *124*, 10572–10577, doi:10.1021/ja020243m.
597. Zhou, Y.; Wang, S.; Zhang, Y. Catalytic Reaction Mechanism of Acetylcholinesterase Determined by Born−Oppenheimer Ab Initio QM/MM Molecular Dynamics Simulations. *J. Phys. Chem. B* **2010**, *114*, 8817–8825, doi:10.1021/jp104258d.
598. Winder, C.; Azzi, R.; Wagner, D. The Development of the Globally Harmonized System (GHS) of Classification and Labelling of Hazardous Chemicals. *Journal of Hazardous Materials* **2005**, *125*, 29–44, doi:10.1016/j.jhazmat.2005.05.035.
599. Olsen, L.; Montefiori, M.; Tran, K.P.; Jørgensen, F.S. SMARTCyp 3.0: Enhanced Cytochrome P450 Site-of-Metabolism Prediction Server. *Bioinformatics* **2019**, *35*, 3174–3175, doi:10.1093/bioinformatics/btz037.
600. Djoumbou-Feunang, Y.; Fiamoncini, J.; Gil-de-la-Fuente, A.; Greiner, R.; Manach, C.; Wishart, D.S. BioTransformer: A Comprehensive Computational Tool for Small Molecule Metabolism Prediction and Metabolite Identification. *J Cheminform* **2019**, *11*, 2, doi:10.1186/s13321-018-0324-5.
601. Wishart, D.S.; Tian, S.; Allen, D.; Oler, E.; Peters, H.; Lui, V.W.; Gautam, V.; Djoumbou-Feunang, Y.; Greiner, R.; Metz, T.O. BioTransformer 3.0—a Web Server

for Accurately Predicting Metabolic Transformation Products. *Nucleic Acids Research* **2022**, *50*, W115–W123, doi:10.1093/nar/gkac313.
602. Durosini, E.; Anyanwu, M.; Vendrame, T.; Ribaudo, G. Mechanistic Investigation on Compounds from Amorpha Fruticosa L. Targeting Acetylcholinesterase. **2025**, doi:DOI:%2010.1080/14786419.2025.2495856.
603. Pettersen, E.F.; Goddard, T.D.; Huang, C.C.; Couch, G.S.; Greenblatt, D.M.; Meng, E.C.; Ferrin, T.E. UCSF Chimera?A Visualization System for Exploratory Research and Analysis. *J. Comput. Chem.* **2004**, *25*, 1605–1612, doi:10.1002/jcc.20084.
604. Hanwell, M.D.; Curtis, D.E.; Lonie, D.C.; Vandermeerschd, T.; Zurek, E.; Hutchison, G.R. Avogadro: An Advanced Semantic Chemical Editor, Visualization, and Analysis Platform. *J Cheminform* **2012**, *4*, 1-17, doi:10.1186/1758-2946-4-17/FIGURES/14.
605. Trott, O.; Olson, A.J. AutoDock Vina: Improving the Speed and Accuracy of Docking with a New Scoring Function, Efficient Optimization, and Multithreading. *J. Comput. Chem.* **2009**, NA-NA, doi:10.1002/jcc.21334.
606. Banerjee, P.; Eckert, A.O.; Schrey, A.K.; Preissner, R. ProTox-II: A Webserver for the Prediction of Toxicity of Chemicals. *Nucleic Acids Research* **2018**, *46*, W257–W263, doi:10.1093/nar/gky318.
607. Banerjee, P.; Kemmler, E.; Dunkel, M.; Preissner, R. ProTox 3.0: A Webserver for the Prediction of Toxicity of Chemicals. *Nucleic Acids Research* **2024**, *52*, W513–W520, doi:10.1093/nar/gkae303.
608. Kannaiyan, R.; Shanmugam, M.K.; Sethi, G. Molecular Targets of Celastrol Derived from Thunder of God Vine: Potential Role in the Treatment of Inflammatory Disorders and Cancer. *Cancer Letters* **2011**, *303*, 9–20, doi:10.1016/j.canlet.2010.10.025.
609. Allison, A.C.; Cacabelos, R.; Lombardi, V.R.M.; Álvarez, X.A.; Vigo, C. Central Nervous System Effects of Celastrol, a Potent Antioxidant and Antiinflammatory Agent. *CNS Drug Reviews* **2000**, *6*, 45–62, doi:10.1111/j.1527-3458.2000.tb00137.x.
610. Der Sarkissian, S.; Cailhier, J.; Borie, M.; Mansour, S.; Hamet, P.; Stevens, L.; Noiseux, N. Celastrol as a Novel Cardioprotective Drug. *Canadian Journal of Cardiology* **2013**, *29*, S331, doi:10.1016/j.cjca.2013.07.563.
611. Yang, G.; Wang, K.; Song, H.; Zhu, R.; Ding, S.; Yang, H.; Sun, J.; Wen, X.; Sun, L. Celastrol Ameliorates Osteoarthritis via Regulating TLR2/NF-κB Signaling Pathway. *Front. Pharmacol.* **2022**, *13*, 963506, doi:10.3389/fphar.2022.963506.
612. Jang, S.Y.; Jang, S.-W.; Ko, J. Celastrol Inhibits the Growth of Estrogen Positive Human Breast Cancer Cells through Modulation of Estrogen Receptor α. *Cancer Letters* **2011**, *300*, 57–65, doi:10.1016/j.canlet.2010.09.006.
613. Jin, H.Z.; Hwang, B.Y.; Kim, H.S.; Lee, J.H.; Kim, Y.H.; Lee, J.J. Antiinflammatory Constituents of *Celastrus o Rbiculatus* Inhibit the NF-κB Activation and NO Production. *J. Nat. Prod.* **2002**, *65*, 89–91, doi:10.1021/np010428r.

614. Zhang, T.; Li, Y.; Yu, Y.; Zou, P.; Jiang, Y.; Sun, D. Characterization of Celastrol to Inhibit Hsp90 and Cdc37 Interaction. *Journal of Biological Chemistry* **2009**, *284*, 35381–35389, doi:10.1074/jbc.M109.051532.
615. Wong, V.K.W.; Qiu, C.; Xu, S.; Law, B.Y.K.; Zeng, W.; Wang, H.; Michelangeli, F.; Dias, I.R.D.S.R.; Qu, Y.Q.; Chan, T.W.; et al. Ca $^{2+}$ Signalling Plays a Role in Celastrol-mediated Suppression of Synovial Fibroblasts of Rheumatoid Arthritis Patients and Experimental Arthritis in Rats. *British J Pharmacology* **2019**, *176*, 2922–2944, doi:10.1111/bph.14718.
616. Gravallese, E.M.; Firestein, G.S. Rheumatoid Arthritis - Common Origins, Divergent Mechanisms. *N Engl J Med* **2023**, *388*, 529–542, doi:10.1056/NEJMra2103726.
617. Lv, Q.; Zhang, W.; Shi, Q.; Zheng, W.; Li, X.; Chen, H.; Wu, Q.; Jiang, W.; Li, H.; Gong, L.; et al. Comparison of Tripterygium Wilfordii Hook F with Methotrexate in the Treatment of Active Rheumatoid Arthritis (TRIFRA): A Randomised, Controlled Clinical Trial. *Annals of the Rheumatic Diseases* **2015**, *74*, 1078–1086, doi:10.1136/annrheumdis-2013-204807.
618. Nasra, S.; Bhatia, D.; Kumar, A. Recent Advances in Nanoparticle-Based Drug Delivery Systems for Rheumatoid Arthritis Treatment. *Nanoscale Adv.* **2022**, *4*, 3479–3494, doi:10.1039/D2NA00229A.
619. Crescenzi, V.; Cornelio, L.; Di Meo, C.; Nardecchia, S.; Lamanna, R. Novel Hydrogels via Click Chemistry: Synthesis and Potential Biomedical Applications. *Biomacromolecules* **2007**, *8*, 1844–1850, doi:10.1021/bm0700800.
620. Kolb, H.C.; Sharpless, K.B. The Growing Impact of Click Chemistry on Drug Discovery. *Drug Discov Today* **2003**, *8*, 1128–1137, doi:10.1016/s1359-6446(03)02933-7.
621. Saxon, E.; Armstrong, J.I.; Bertozzi, C.R. A "Traceless" Staudinger Ligation for the Chemoselective Synthesis of Amide Bonds. *Org Lett* **2000**, *2*, 2141–2143, doi:10.1021/ol006054v.
622. Saxon, E.; Bertozzi, C.R. Cell Surface Engineering by a Modified Staudinger Reaction. *Science* **2000**, *287*, 2007–2010, doi:10.1126/science.287.5460.2007.
623. Klaić, L.; Morimoto, R.I.; Silverman, R.B. Celastrol Analogues as Inducers of the Heat Shock Response. Design and Synthesis of Affinity Probes for the Identification of Protein Targets. *ACS Chem. Biol.* **2012**, *7*, 928–937, doi:10.1021/cb200539u.
624. Luo, P.; Liu, D.; Zhang, Q.; Yang, F.; Wong, Y.-K.; Xia, F.; Zhang, J.; Chen, J.; Tian, Y.; Yang, C.; et al. Celastrol Induces Ferroptosis in Activated HSCs to Ameliorate Hepatic Fibrosis via Targeting Peroxiredoxins and HO-1. *Acta Pharmaceutica Sinica B* **2022**, *12*, 2300–2314, doi:10.1016/j.apsb.2021.12.007.
625. Feng, Y.; Wang, W.; Zhang, Y.; Fu, X.; Ping, K.; Zhao, J.; Lei, Y.; Mou, Y.; Wang, S. Synthesis and Biological Evaluation of Celastrol Derivatives as Potential Anti-Glioma Agents by Activating RIP1/RIP3/MLKL Pathway to Induce Necroptosis. *European Journal of Medicinal Chemistry* **2022**, *229*, 114070, doi:10.1016/j.ejmech.2021.114070.

626. Li, N.; Chen, C.; Zhu, H.; Shi, Z.; Sun, J.; Chen, L. Discovery of Novel Celastrol-Triazole Derivatives with Hsp90-Cdc37 Disruption to Induce Tumor Cell Apoptosis. *Bioorganic Chemistry* **2021**, *111*, 104867, doi:10.1016/j.bioorg.2021.104867.
627. He, Q.-W.; Feng, J.-H.; Hu, X.-L.; Long, H.; Huang, X.-F.; Jiang, Z.-Z.; Zhang, X.-Q.; Ye, W.-C.; Wang, H. Synthesis and Biological Evaluation of Celastrol Derivatives as Potential Immunosuppressive Agents. *J. Nat. Prod.* **2020**, *83*, 2578–2586, doi:10.1021/acs.jnatprod.0c00067.
628. Axer, A.; Hermann, S.; Kehr, G.; Clases, D.; Karst, U.; Fischer-Riepe, L.; Roth, J.; Fobker, M.; Schäfers, M.; Gilmour, R.; et al. Harnessing the Maltodextrin Transport Mechanism for Targeted Bacterial Imaging: Structural Requirements for Improved in Vivo Stability in Tracer Design. *ChemMedChem* **2018**, *13*, 241–250, doi:10.1002/cmdc.201700543.
629. Pang, C.; Luo, J.; Liu, C.; Wu, X.; Wang, D. Synthesis and Biological Evaluation of a Series of Novel Celastrol Derivatives with Amino Acid Chain. *Chemistry & Biodiversity* **2018**, *15*, e1800059, doi:10.1002/cbdv.201800059.
630. Toyoshima, C.; Nomura, H. Structural Changes in the Calcium Pump Accompanying the Dissociation of Calcium. *Nature* **2002**, *418*, 605–611, doi:10.1038/nature00944.
631. Daina, A.; Michielin, O.; Zoete, V. SwissADME: A Free Web Tool to Evaluate Pharmacokinetics, Drug-Likeness and Medicinal Chemistry Friendliness of Small Molecules. *Sci Rep* **2017**, *7*, 42717, doi:10.1038/srep42717.
632. Axer, A.; Hermann, S.; Kehr, G.; Clases, D.; Karst, U.; Fischer-Riepe, L.; Roth, J.; Fobker, M.; Schäfers, M.; Gilmour, R.; et al. Harnessing the Maltodextrin Transport Mechanism for Targeted Bacterial Imaging: Structural Requirements for Improved in Vivo Stability in Tracer Design. *ChemMedChem* **2018**, *13*, 241–250, doi:10.1002/cmdc.201700543.
633. Xie, Y.; Kuan, H.; Wei, Q.; Gianoncelli, A.; Ribaudo, G.; Coghi, P. (2R,4aS,6aS,12bR,14aS,14bR)10-Hydroxy-N-(4-((6-Methoxyquinolin-8-Yl)Amino)Pentyl)-2,4a,6a,9,12b,14a-Hexamethyl-11-Oxo-1,2,3,4,4a,5,6,6a,11,12b,13,14,14a,14b-Tetradecahydropicene-2-Carboxamide. *Molbank* **2023**, *2023*, M1716, doi:10.3390/M1716.
634. Sharma, R.; Singla, R.K.; Banerjee, S.; Sharma, R. Revisiting Licorice as a Functional Food in the Management of Neurological Disorders: Bench to Trend. *Neuroscience & Biobehavioral Reviews* **2023**, *155*, 105452, doi:10.1016/j.neubiorev.2023.105452.
635. Sharma, R.; Singla, R.K.; Banerjee, S.; Sinha, B.; Shen, B.; Sharma, R. Role of *Shankhpushpi* (*Convolvulus Pluricaulis*) in Neurological Disorders: An Umbrella Review Covering Evidence from Ethnopharmacology to Clinical Studies. *Neuroscience & Biobehavioral Reviews* **2022**, *140*, 104795, doi:10.1016/j.neubiorev.2022.104795.
636. Zorzan, M.; Collazuol, D.; Ribaudo, G.; Ongaro, A.; Scaroni, C.; Zagotto, G.; Armanini, D.; Barollo, S.; Galeotti, F.; Volpi, N.; et al. Biological Effects and

Potential Mechanisms of Action of *Pistacia Lentiscus* Chios Mastic Extract in Caco-2 Cell Model. *Journal of Functional Foods* **2019**, *54*, 92–97, doi:10.1016/j.jff.2019.01.007.

637. Ahmad, R.; Almubayedh, H.; Ahmad, N.; Naqvi, A.A.; Riaz, M. Ethnobotany, Ethnopharmacology, Phytochemistry, Biological Activities and Toxicity of Pistacia Chinensis Subsp. Integerrima: A Comprehensive Review. *Phytotherapy Research* **2020**, *34*, 2793–2819, doi:10.1002/ptr.6720.
638. Rauf, A.; Uddin, G.; Latif, A.; Muhammad, N. Pistagremic Acid, a Novel Antimicrobial and Antioxidant Isolated from Pistacia Integerrima. *Chem Nat Compd* **2014**, *50*, 97–99, doi:10.1007/s10600-014-0875-2.
639. Lee, W.; Woo, E.-R.; Lee, D.G. Effect of Apigenin Isolated from *Aster Yomena* against *Candida Albicans*: Apigenin-Triggered Apoptotic Pathway Regulated by Mitochondrial Calcium Signaling. *Journal of Ethnopharmacology* **2019**, *231*, 19–28, doi:10.1016/j.jep.2018.11.005.
640. Yan, X.; Qi, M.; Li, P.; Zhan, Y.; Shao, H. Apigenin in Cancer Therapy: Anti-Cancer Effects and Mechanisms of Action. *Cell Biosci* **2017**, *7*, 50, doi:10.1186/s13578-017-0179-x.
641. Stompor, M. A Review on Sources and Pharmacological Aspects of Sakuranetin. *Nutrients* **2020**, *12*, 513, doi:10.3390/nu12020513.
642. Chen, Y.-H.; Wu, J.-X.; Yang, S.-F.; Yang, C.-K.; Chen, T.-H.; Hsiao, Y.-H. Anticancer Effects and Molecular Mechanisms of Apigenin in Cervical Cancer Cells. *Cancers (Basel)* **2022**, *14*, 1824, doi:10.3390/cancers14071824.
643. Uddin, G. Broad Spectrum Anticancer Activity of Pistagremic Acid. *Chemotherapy* **2013**, *2*, doi:10.4172/2167-7700.1000117.
644. Rauf, A.; Uddin, G.; Raza, M.; Ahmad, A.; Jehan, N.; Ahmad, B.; Nisar, M.; Molnar, J.; Csonka, A.; Szabo, D.; et al. Reversal of Multidrug Resistance and Computational Studies of Pistagremic Acid Isolated from Pistacia Integerrima. *Asian Pac J Cancer Prev* **2016**, *17*, 2311–2314, doi:10.7314/apjcp.2016.17.4.2311.
645. Jenkins, J.L.; Bender, A.; Davies, J.W. *In Silico* Target Fishing: Predicting Biological Targets from Chemical Structure. *Drug Discovery Today: Technologies* **2006**, *3*, 413–421, doi:10.1016/j.ddtec.2006.12.008.
646. Vilar, S.; Costanzi, S. Predicting the Biological Activities Through QSAR Analysis and Docking-Based Scoring. In *Membrane Protein Structure and Dynamics: Methods and Protocols*; Vaidehi, N., Klein-Seetharaman, J., Eds.; Humana Press: Totowa, NJ, 2012; pp. 271–284 ISBN 978-1-62703-023-6.
647. Colloc'h, N.; Hajji, M.E.; Bachet, B.; L'Hermite, G.; Schiltz, M.; Prangé, T.; Castro, B.; Mornon, J.-P. Crystal Structure of the Protein Drug Urate Oxidase-Inhibitor Complex at 2.05 Å Resolution. *Nat Struct Mol Biol* **1997**, *4*, 947–952, doi:10.1038/nsb1197-947.
648. He, S.; Qiao, X.; Zhang, S.; Xia, J.; Wang, L.; Liu, S. Urate Oxidase from Tea Microbe Colletotrichum Camelliae Is Involved in the Caffeine Metabolism Pathway

and Plays a Role in Fungal Virulence. *Front Nutr* **2022**, *9*, 1038806, doi:10.3389/fnut.2022.1038806.
649. Islam, S.; Hosen, M.A.; Ahmad, S.; ul Qamar, M.T.; Dey, S.; Hasan, I.; Fujii, Y.; Ozeki, Y.; Kawsar, S.M.A. Synthesis, Antimicrobial, Anticancer Activities, PASS Prediction, Molecular Docking, Molecular Dynamics and Pharmacokinetic Studies of Designed Methyl α-D-Glucopyranoside Esters. *Journal of Molecular Structure* **2022**, *1260*, 132761, doi:10.1016/j.molstruc.2022.132761.
650. Retailleau, P.; Colloc'h, N.; Vivarès, D.; Bonneté, F.; Castro, B.; El-Hajji, M.; Mornon, J.P.; Monard, G.; Prangé, T. Complexed and Ligand-Free High-Resolution Structures of Urate Oxidase (Uox) from Aspergillus Flavus: A Reassignment of the Active-Site Binding Mode. *Acta Crystallogr D Biol Crystallogr* **2004**, *60*, 453–462, doi:10.1107/S0907444903029718.
651. Santos, E. da S.; Nogueira, K.A.B.; Fernandes, L.C.C.; Martins, J.R.P.; Reis, A.V.F.; Neto, J. de B.V.; Júnior, I.J. da S.; Pessoa, C.; Petrilli, R.; Eloy, J.O. EGFR Targeting for Cancer Therapy: Pharmacology and Immunoconjugates with Drugs and Nanoparticles. *Int J Pharm* **2021**, *592*, 120082, doi:10.1016/j.ijpharm.2020.120082.
652. Abourehab, M.A.S.; Alqahtani, A.M.; Youssif, B.G.M.; Gouda, A.M. Globally Approved EGFR Inhibitors: Insights into Their Syntheses, Target Kinases, Biological Activities, Receptor Interactions, and Metabolism. *Molecules* **2021**, *26*, 6677, doi:10.3390/molecules26216677.
653. Guo, Y.; Du, Z.; Shi, T. Structural Analysis of Interactions between Epidermal Growth Factor Receptor (EGFR) Mutants and Their Inhibitors. *Biophysica* **2023**, *3*, 203–213, doi:10.3390/biophysica3010013.
654. Stamos, J.; Sliwkowski, M.X.; Eigenbrot, C. Structure of the Epidermal Growth Factor Receptor Kinase Domain Alone and in Complex with a 4-Anilinoquinazoline Inhibitor. *J Biol Chem* **2002**, *277*, 46265–46272, doi:10.1074/jbc.M207135200.
655. Kiyama, R. Estrogenic Flavonoids and Their Molecular Mechanisms of Action. *J Nutr Biochem* **2023**, *114*, 109250, doi:10.1016/j.jnutbio.2022.109250.
656. Pham, T.H.; Page, Y.L.; Percevault, F.; Ferrière, F.; Flouriot, G.; Pakdel, F. Apigenin, a Partial Antagonist of the Estrogen Receptor (ER), Inhibits ER-Positive Breast Cancer Cell Proliferation through Akt/FOXM1 Signaling. *International Journal of Molecular Sciences* **2021**, *22*, 470, doi:10.3390/ijms22010470.
657. Rauf, A.; Anyanwu, M.; Aliiri, A.A.; Alanazi, H.A.H.; Alharbi, A.M.A.; Wadood, A.; Aljohani, A.S.M.; Muhammad, N.; Samad, A.; Shah, S.U.A.; et al. Antifungal and Antiproliferative Activity of Pistagremic Acid and Flavonoids Extracted from the Galls of Pistacia Chinensis Subsp. Integerrima. *Chemistry and Biodiversity* **2024**, *21*, doi:10.1002/cbdv.202301815.
658. Arfan, M.; Rauf, A.; Tahir, M.N.; Ali, M.; Uddin, G. 2-Methyl-6-(4,4,10,13,14-Penta-Methyl-3-Oxo-2,3,4,5,6,7,10,11,12,13,14,15,16,17-Tetra-Deca-Hydro-1H-Cyclo-Penta-[a]Phenanthren-17-Yl)Hept-2-Enoic Acid. *Acta Crystallogr Sect E Struct Rep Online* **2011**, *67*, o711, doi:10.1107/S1600536811006283.

659. Khurm, M.; Chaudhry, B.A.; Uzair, M.; Janbaz, K.H. Antimicrobial, Cytotoxic, Phytotoxic and Antioxidant Potential of Heliotropium Strigosum Willd. *Medicines* **2016**, *3*, 20, doi:10.3390/medicines3030020.
660. Nordin, M.-A.-F.; Wan Harun, W.H.A.; Abdul Razak, F. Antifungal Susceptibility and Growth Inhibitory Response of Oral Candida Species to Brucea Javanica Linn. Extract. *BMC Complement Altern Med* **2013**, *13*, 342, doi:10.1186/1472-6882-13-342.
661. Nili Ahmadabadi, M.; Rezaee, E.; Nematpour, M.; Karami, L.; Mokhtari, S.; Kobarfard, F.; Tabatabai, S.A. Synthesis, Molecular Dynamics Simulation, and In-Vitro Antitumor Activity of Quinazoline-2,4,6-Triamine Derivatives as Novel EGFR Tyrosine Kinase Inhibitors. *Iran J Pharm Res* **2022**, *21*, e133840, doi:10.5812/ijpr-133840.
662. Retailleau, P.; Colloc'h, N.; Vivarès, D.; Bonneté, F.; Castro, B.; El Hajji, M.; Mornon, J.-P.; Monard, G.; Prangé, T. Complexed and Ligand-Free High-Resolution Structures of Urate Oxidase (Uox) from *Aspergillus Flavus* : A Reassignment of the Active-Site Binding Mode. *Acta Crystallogr D Biol Crystallogr* **2004**, *60*, 453–462, doi:10.1107/S0907444903029718.